Transport and Seismoelectric Properties of Porous Permeable Rock: Numerical Modeling and Laboratory Measurements

by

Xin Zhan

Submitted to the Department of Earth, Atmospheric and Planetary Sciences in

Partial Fulfillment of the Requirements for the Degree of

Doctor of Philosophy

at the

Massachusetts Institute of Technology

February 2010

ARCHIVES
MASSACHUSETTS INSTITUTE OF TECHNOLOGY
MAY 0 5 2010
LIBRARIES

© Massachusetts Institute of Technology, 2010. All rights reserved.

Signature of Author: _____

Department of Earth, Atmospheric and Planetary Sciences
December 21, 2009

Certified by: _____

M. Nafi Toksöz
Robert R. Shrock Professor of Geophysics
Thesis Supervisor

Accepted by: _____

Maria T. Zuber
E.A. Griswold Professor of Geophysics
Head, Department of Earth, Atmospheric and Planetary Sciences

Transport and Seismoelectric Properties of Porous Permeable Rock: Numerical Modeling and Laboratory Measurements

by

Xin Zhan

Submitted to the Department of Earth, Atmospheric and Planetary Sciences

on December 21, 2009 in partial fulfillment of the requirements for the degree of

Doctor of Philosophy

Abstract

The objective of this thesis is to better understand the transport and seismoelectric (SE) properties of porous permeable rock. Accurate information of rock transport properties, together with pore geometry, can aid us to better quantify the frequency dependence of its SE coupling coefficient. With the development of micro-CT (μCT) scanners, microstructure of the sedimentary rock can now be obtained in three dimensions at micron level resolution. Pore scale modeling on the rock 3-D μCT images provides us the ability to obtain different rock properties all at once and without much ambiguity.

In this thesis, we build numerical tools to compute a range of transport properties and pore geometry parameters (e.g., porosity, electrical conductivity, hydraulic permeability, pore surface area) on the microstructures from basic physical laws. A staggered-grid finite difference (FD) scheme is used to solve the Laplace equation for electrical conductivity and the Stokes equation for hydraulic conductivity. The Laplace solver can handle different levels of conductivity contrast so that different saturations (gas, oil and brine) can be modeled. A three-phase conductivity model developed on the binary representation of the microstructure, which is based on the geometric average of free electrolyte conductance and surface conductance in the EDL, is illustrated. Two different edge detection methods are applied to recognize surface voxel in a binary image. One is a gradient based, first order differential method and the second one is a connectivity-number-based edge detection (CNED) method.

Computations are done for a family of synthetic sand packs – Finney pack with low, medium to high porosities – to provide a benchmark of numerical tools and to compare with analytic solutions. Then, the numerical methods are used to calculate properties of Berea Sandstone 500 (BS500) with 23.6% porosity, whose 3-D microtomograms with 2.8 micron resolution are available. Using the numerical methods, rock porosity, pore surface area,

electrical conductivity and permeability are calculated. These are compared with the laboratory measurements made on the same rock. The numerical and laboratory values compare very well. Impact of various aspects of numerical modeling on the accuracy of results are evaluated. It is demonstrated that increasing the sample used in the computation improves the match between the numerical values and laboratory measurements. Reducing the spatial resolution (i.e. increasing grid size), most affects the accuracy of electrical conductivity and hydraulic permeability.

Seismoelectric measurements are carried out at 10 kHz – 120 kHz range for the BS500 sample. Both single sine pulse and five-cycle sine burst are adopted as acoustic source wavelets. Streaming potential is collected on freshly cut BS500 cylinder core samples saturated with different brine conductivities under the same experimental condition as the AC measurements. With the transport and geometrical parameters previously obtained from μCT image and laboratory measurements, the frequency dependent coupling coefficient of BS500 is theoretically calculated using available rock properties. Comparison between the theoretical prediction and the experimental data is found to be promising. This experiment extends our ability to conduct quantitative seismoelectric measurements at frequency ranges applied for field and laboratory acoustic borehole logging.

Thesis supervisor: M. Nafi Toksöz

Title: Robert R. Shrock Professor of Geophysics

Acknowledgements

I would like to thank many people for their help towards the completion of this thesis in the Earth Resources Laboratory at MIT.

First of all, I would like to thank my thesis advisor, Professor M. Nafi Toksöz for his support and guidance throughout my study at MIT. I always feel lucky to meet and work with such a reputable scientist as Professor Toksöz, who offered me the chance to enter MIT as well as the field of geophysics. Besides his scientific guidance, the most important thing I learned from him is to think and research independently. His broad knowledge and his generosity continue to impress me.

Special thanks are given to Dr. Zhenya Zhu. This thesis would have been impossible without his help. Through the discussion with him, I learned a lot about borehole acoustic and electrokinetic conversion as well as the right attitude towards the scientific research. His sincere encouragements help me to survive the difficult time in my study and work.

I would also like to take this opportunity to thank my thesis committee. Professor Dale Morgan is the world leading expert on electrochemistry and the pioneer in the research area of electrokinetics at MIT. Besides his insightful directions on my research, he has always been a great person to talk to and share ideas with on different aspects of life. I also thank him for sharing his experience on how to write, organize and present a scientific work with us. Dr.

Lawerence Schwartz from Schlumberger – Doll Research, I'm grateful to his intensive help during my last two years of studies. His in depth knowledge on electric and fluid conduction as well as great scientific writing skill is the most direct help. Professor Thomas Herring is the advisor for my second general topic. It's a great pleasure to work with Thomas on GPS modeling, which is also my favorate research topic in my undergraduate study. His patience and support has helped me through many difficult times. I would appreciate Professor Brian Evans for his time and interest in my work as well as his courage to me.

Earth Resources Laboratory is the home of my study at MIT. This environment has been a tremendous resource for both my academic study and research work. Without the well equipped Ultrasonic Lab, I couldn't have finished the laboratory experiments in this thesis. Also, many academic events are held here weekly or monthly to give me the opportunity to hear the voices from both academy and industry. Besides the scientific topics, many social issues are discussed here, which help me to better understand the American life and culture. ERL has also taught me the importance of communication and cooperation which is of great importance besides the individual work.

I would like to take this opportunity to thank many of the former and current students and staff of ERL and Green Building, who give me a lot of technical help and spiritual encouragement. Dr. Dan Burns is always a source of encouragement and a good organizer at ERL. I thank him for always being ready to give help. I appreciate Dr. Rama Rao for his technical support. His knowledge on acoustic LWD and his Matlab codes on dispersion analysis and semblance analysis helped me greatly during the procession of the laboratory

data in this thesis. I also owe many thanks to Dr. Shimon Chi. I benefited a lot from his guidance on using the FORTRAN code for borehole acoustic modeling. He has been always generous to teach me how to solve the numerical problems. His abundant experience in borehole acoustic and petroleum engineering also helped me a lot.

Youshun Sun is the big brother for all the students at ERL. He is always willing to share his experience of living and studying here at MIT. Burke Kinsley discussed with me on many topics from general physics to COMSOL workshops. He always came up with so many good ideas. Rongrong Lu gave me a lot of advice and hand on help on signal processing, coding and PowerPoint presentation. He is a huge and ready resource on many technical aspects. A lot of appreciation will be given to Yang Zhang, who came to MIT the same year as me. Our discussions range from course study to research work to daily life. His sincerity and enthusiasm on research impresses me a lot. Fuxian Song has become a great friend to me. His friendship brings me a lot of fun out of the stressful life at MIT. Fred Pearce is a great colleague to consult on a variety of things ranging from research to home furniture. Junlun Li always shares a lot of information from good deal to interesting course and good food with everyone in my office. I would also like to thank Haijiang Zhang, who has offered me a lot of general help and provided many feedback on my work, Hussam Busfar, Nasruddin Nazerali and Abdulaziz Al-Muhaidib, who are great officemates, Yulia Agramakova, who brings me nice Russian gift and food, Huajian Yao gives me a lot of good suggestions on the final organization of the thesis, Ping Wang, Chang Li, Oleg Poliannikov, Samantha Grandi,

Victoria Briggs, Xu Li, Bill Rodi, Mark Wills, Jonathan Ajo-Franklin, Mary Krasovec, Sophie Michelet, Sudipta Sarkar, Edmund Sze, Xander Campman and Joongmoo Byun.

Many thanks to Liz Henderson and Sue Turbak, who take good care of everyone at ERL and Linda Meinke, who guarantees the smooth running of my computer. Ms. Carol Sprague and Ms. Vicki McKenma in the Departement Education Office give me a lot of prompt help. I want to thank Macia Taylor for her considerate aid during my last year at MIT.

Besides the people at ERL, I would like to acknowledge Schlumberger Doll Research for their support and cooperation on my thesis work. I want to thank Wave Smith for his intensive help on the laboratory measurements and interpretation, Peter Tilke for providing me the rock μCT images and Jeffery Tarvin for his helpful discussions on electrical and seismoelectric measurement. Many appreciations are given to Schlumberger Data and Consulting Services for offering my first summer internship. I want to thank Dr. Patrick J. Hooyoman for his support and trust, Colin Sayers for his mentoring and helpful discussions. Sheila Noeth, Saad Kisra, T. J, Zsolt Nagy are all great colleagues and offer me a lot of help during my summer internship at SDC. Deep appreciations are given to Michael Payne, Wenjie Dong, Stefan Hussenoeder and Alex Martinez for providing me the opportunity to work with ExxonMobil. I want to thank Shiyu Xu, Enru Liu for their mentoring and support during my summer internship at ExxonMobil; Xiaojun Huang, Xiaoxia Xu, Yaping Zhu, Xinyou Lu for their help on my work and life in Houston. Those experiences not only broaden my view but also help to cultivate the maturity in my personality.

I owe a lot of thanks to all my friends at MIT and other places in the world. I see many of them are pursuing their goals untiringly and never give up on the way. The courage and friendship they give me are so powerful. With their chats, email and phones, the life at MIT is no longer so stressful.

In the end, I can't forget to express my deepest appreciation to my family. Thanks my mother, who witnessed my growth and shared every moment in my life with me. My father, the tutor and role model for me, helps me to build up my character and set my life goals. He always encourages me to go abroad for advanced education and gain more life experience. Many thanks to my uncle and aunt who offer me the most direct and endless technical and spiritual support. Their care and regard let me strongly feel the warmth of family. Next-to-last is Jinchao Yuan, a great companion and friend, who is always there to support and back me up in all the up and downs. His intelligence and comfot brings me a lot of strength throughout this journey.

I will try my best in my future career as requital to everyone who has ever helped and supported me in my life.

Contents

List of Figures

List of Tables

Chapter 1

Introduction

1.1 Objective

The overall goal of this thesis is to better understand the transport properties and seismoelectric[1] (SE) response of porous permeable rock. Accurate information of rock transport properties, together with pore geometry, will aid us to better quantify the frequency dependence of its SE coupling coefficient. Nowadays, pore scale modeling on the rock 3-D μCT (i.e., micro-CT) images opens a new avenue to better quantify and understand rock. It allows us to simulate many natural processes by conducting numerical simulations to predict massive rock petrophysical properties, with a clear description of the structure and connectivity of the pore space. Specifically, this work is divided into two parts to cover different aspects.

The first part of the thesis is concerned with the transport properties (electrical conductivity and hydraulic permeability) of fluid saturated porous media. Besides transport

[1]In this thesis, seismoelectric (abbreviated as SE) method refers to the collection of the electric field induced by seismic (acoustic) waves.

properties, pore geometry information (such as pore surface area and Λ parameter, which represents a weighted pore surface to volume ratio (Johnson et al., 1986)) is also studied. We build numerical tools to calculate those rock physical properties on 3-D microtomograms from basic physical laws. A three phase electrical conductivity model is developed on the segmented microtomogram to account for surface conduction. Laboratory measurements of those rock properties are collected on the core samples to verify our numerical computations. Cross-correlations between different computed properties are also established. Two numerical issues are addressed: image resolution and computation sample size. The importance of these is illustrated when we compare the pore scale computation with the laboratory measurements on the cm^3 core samples. This first part of the thesis provides a complete and systematic study of different transport properties of porous permeable rock. For the same rock, consistency between different computed transport properties is shown by their agreement with laboratory measurements and cross-correlation. In this study, we consider not only the structural information but also the material property, which is particularly important for electrical transport. Rock matrix, pore fluid and rock–fluid interface are the three phases taking effect in the electrical conduction. We use the state-of-the-art computation size in our simulations to better represent the rock sample. Moreover, we optimize the computation algorithm to handle large system calculations, as well as to improve computation efficiency.

The second part of the thesis is concerned with the seismoelectric properties of porous, permeable rock. Quantitative high frequency AC (10 kHz to 120 kHz) seismoelctric signals are recorded on rock samples with the aid of high-frequency, high-pressure acoustic transient

and wavelet techniques. Acoustic and converted seismoelectric signals collected in a water tank are analyzed in both the time and frequency domain. Both single sine pulse and five-cycle sine burst are adopted as acoustic source wavelets. The clean recorded waveforms presented in this thesis are rarely achieved in similar research. With precisely known transport properties and pore geometry, we are able to calculate the frequency dependent seismoelectric coupling coefficient using Pride's model (Pride, 1994). The majority of the measured frequency SE response follows the trend predicted by Pride's model. This extends our ability to conduct quantitative SE measurements at frequency ranges applied to acoustic borehole logging in the field and laboratory. The overall data quality is better for single sine pulse than five-cycle sine burst due to its higher resolution and simplicity in time domain. It is optimistic for the field application where the high pressure transient is commonly adopted as the source wavelet.

This thesis combines two basic scientific approaches: numerical simulation and laboratory measurement. For pore scale calculation of rock transport properties (except hydraulic permeability) and geometrical information of the pore space, we introduce new calculation methods which differ from previous works. Quantitative AC seismoelectric measurement at high frequencies (10 kHz to 120 kHz) is another innovation explored in this thesis. Details of previous research and our research are discussed in a later section of this chapter.

1.2 Previous Research and Our Research

1.2.1 Computational Rock Physics

The field of studies associated with characterization of and computation on the rock microstructure is known as computational rock physics. It has been a growing field in the past decade. The core idea of computational rock physics is first to image the details of the rock microstructure and then to compute the physical properties from its governing laws. Comprehensive application of this idea, in recent years, is contributed to the fast development of micro-CT scanners and powerful computational hardware and software, i.e., high performance compilers suitable for 32-bit, 64-bit and multicore processors supporting automatic parallelization and computer clusters. Direct measurements of the complex morphology of the pore space of sedimentary rock can be obtained in three dimensions at resolution down to one micron using synchrotron and X-ray CT scanners. Numerical experiments can be carried out to simulate electric current, fluid flow (including multi-phase flow) and elastic deformation on the rock μCT image. Though not yet possible to theoretically mimic the full complexity of the microstructure, there has been quite a bit of success in simulating electrical current, single and multiphase flow (Dvorkin, et al., 2008).

On the electrical modeling, a number of researches have been developed based on solving the Laplace equation on the binary representation of rock microstructure (Auzerais et al., 1996; Keehm et al., 2001; Arns, 2001, 2005; Devarajan, 2006). A fluid saturated rock is modeled as a two-component medium: insulating solid grain (with zero conductivity) and conducting brine in the pore space (with unit conductivity). Effective conductivity of the

saturated rock is obtained from the solution of the Laplace equation and Ohm's law. The underlying assumption is that the electrolyte conductivity is uniform, and mobile ions are uniformly distributed throughout the pore space. However, the surface of the grains, which compose the solid matrix of sand, sandstone and clay, is typically charged when it is in contact with an electrolyte. Anions from the electrolyte are chemically adsorbed to the surface of the matrix leaving behind a net excess of cations distributed near the surface. The adsorbed layer and diffuse layer together constitute the electric double layer (EDL). The surface that separates the diffuse layer from the adsorbed layer is called the "shear plane". Zeta potential, ζ, is the electric potential at the shear plane, and the electric potential in neutral electrolyte (no excess charge) is defined to be zero (Bockris and Reddy, 1972; Morgan et al., 1989; Pride and Morgan, 1991). Zeta potentials are usually obtained in experimental studies. Theoretical determination of ζ remains problematic due to the complexity of the adsorbed layer (Pride and Morgan 1991). Surface conduction within this electric double layer can contribute substantially to rock conductivity at low salinity, high temperature and high shaliness environment. 'Electrokinetic phenomena', such as electroosmosis, electrophoresis, and streaming potential are caused by the movement of the mobile charges in the EDL.

The simple two phase conductivity model is insufficient to capture the impact of surface conduction. Recent researchers have devoted considerable attention to modeling surface conduction at pore scale (Devarajan, 2006; Jin et al., 2007; Motealleh et al., 2007). In their researches, 'shaly sand' is modeled as surface-conductive clay coating the grains. To represent 'shale', all the grains are assumed to be conductive clays. However, all these works

are conducted on synthetic porous medium-sphere packs with a single type of clay minerals. Furthermore, no experimental proof is given in those works to verify their simulation. Real rocks are known to have much more complex composition and pore geometry. Thus, one of the objectives of this thesis is to numerically model surface conductivity on real rock microstructure. In addition, laboratory data are collected to verify the numerical calculation.

For fluid flow simulation, a lot of work has been done to solve the linear Stokes or Navier-Stokes equation on the microstructure (Martys and Garboczi, 1992; Schwartz et al., 1993; Keehm et al., 2001; Kameda, 2004; Arns, et al., 2005). Fluid viscosity in the pore space is assigned, and distributions of velocity and pressure fields are computed on the microstructure. Hydraulic permeability is obtained using Darcy's law. Multi-phase flow analysis provides two-phase relative permeability, which includes water-oil, gas-oil and water-gas displacement at different wetability indices and viscosity values. In this study, we simulate the single phase fluid flow and compute the hydraulic permeability following the traditional method. To obtain other geometrical parameters, such as pore surface to volume ratio, statistical methods, e.g., two-point correlation function, spatial correlation functions (Berryman, 1985; Torquato and Stillinger, 2001) are mostly adopted. Using different statistical functions (e.g., different correlation functions) can lead to different results. In this study, two different edge detection methods are introduced to detect the surface voxels on the binary image. One is gradient based edge detection and the other is connectivity-number-based edge detection. The pore surface area obtained from the two different methods is close and the mean value of the two methods is taken to be the final result. Especially, the

connectivity based method examines only the pore phase instead of the entire structure, which is efficient for large size images. Calculated permeability and surface to volume ratio are compared with corresponding laboratory measurements collected on the rock core samples as well.

1.2.2 Electrokinetic Studies

For the study of electrokinetic coupling in the porous medium, much experimental work has been done in the DC or low to intermediate frequency AC (a few Hz to a few hundred Hz) range in the past forty years. Streaming potential, seismoelectric conversion and electroosmosis have been measured on different materials. Fundamental studies, e.g., the impact of PH value, temperature, electrolyte conductivity, pressure and mineral types on the streaming coupling coefficient and zeta potential, are carried out on crushed rock samples in the laboratory (Ishido and Mizutani, 1981; Morgan et al., 1989). Later laboratory works begin to combine streaming potential and electroosmosis to determine rock properties, such as permeability, pore size, etc. The studied materials include glass capillary, fused glass beads, sandstones and carbonates (Sharma et al., 1986; Pengra and Wong, 1995; Pengral et al., 1999; Reppert, 2000; Reppert and Morgan, 2002). Field experiments also measure the electric signal excited by seismic waves on the surface (Thompson and Gist, 1993) and Stoneley waves in the borehole (Mikhailov et al., 2000) to detect the underground fractured zone. The seismic source in these two field studies is put on the surface with tens of Hz to a few hundred Hz frequency range. Thus, the penetration depth is confined to be within a few hundred meters.

On the theoretical side, the first theoretical development of electrokinetic transport equations is attributed to Helmholtz and Smoluchowski (Helmholtz, 1879; Smoluchowski, 1903). Later, Packard deduced the frequency-dependent coupling coefficient for capillary geometry and verified his theory with experiments on capillary samples (Packard, 1953). He was able to achieve a maximum frequency of 200Hz and perform the measurements on capillaries of large radii (0.589 -2.083 *mm*). In 1994, the macroscopic governing equations controlling the coupled acoustics and electromagnetics of porous media were derived by Pride (1994). The low frequency limit and high frequency limit of the electrokinetic coupling coefficient are jointed by a smooth curve. Porosity, permeability, tortuosity and Λ parameter (defined by Johnson et al., 1987) are the four key independent parameters used to determine the frequency dependence in Pride's model.

Pride's coupling coefficient has been validated by Reppert (Reppert, 2000; Reppert and Morgan, 2002) and compared with Packard's model on glass capillary, porous filters with pore diameters ranging from 34 micrometers to 1 millimeter. Both Packard's and Pride's models fit the frequency dependent streaming potential capillary and porous filter data. Theoretically, when using capillary geometry terms and neglecting second-order effects, Pride's model is identical to Packard's model when the series and asymptotic approximations are used (Reppert, 2000). Reppert also measured the frequency dependent coupling coefficient on one rock sample, Boise sandstone, which has an estimated permeability of 2.89 Darcy and equivalent pore radius of 17 micrometers using the Walsh-Brace permeability

model (Reppert, 2000). Pride's theory is compared with the rock experimental data in the frequency range below 1 kHz.

Due to the small amplitude of the coupling coefficient, researchers began to seek the application of electokinetics in borehole logging, instead of putting the seismic source on the surface survey, to evaluate formation properties at depth (Hunt and Worthington, 2000; Singer et al., 2006). Numerical modeling has also been developed to couple the acoustic wave and electromagnetic wave in layered media (Haartsen, 1995; Haartsen and Pride, 1997) and in open borehole (Singer et al., 2006; Guan and Hu, 2008). Applicability of the seismoelectric signal in the acoustic logging frequency range (a few kHz to a few hundred kHz), which can go above the transition frequency of a variety of rocks, is proven by those numerical studies. In recent years, seismoelectric signal at high frequency range (a few kHz to a few hundred kHz) has been successfully recorded in sandstones, experimentally (Zhu et al., 2000, 2008; Zhu and Toksöz, 2003, 2005; Singer et al., 2006), with effective pressure generating devices. Different types of acoustic waves (P-wave, S-wave, Stoneley wave, etc.) and their converted electric signals are well identified and distinguished in the waveforms. These studies verify that the recorded electric signals are generated from seismoelectric conversion in the fluid saturated rock. However, those experiments remain at the qualitative stage due to the difficulty to quantify the acoustic wave fields in their models. In this research, we carry out quantitative seismoelectric measurements at high frequencies (10 kHz to 120 kHz). Delicate quantification of acoustic wave field is done prior to seismoelectric measurement.

Quantitative SE measurement enables us to exam the dependence of SE coupling coefficient on fluid conductivity and frequency.

1.3Outline of Thesis

This thesis contains five chapters, which delineate the two objectives mentioned above.

In Chapter 1, the background and previous studies related to this thesis are reviewed and the thesis objectives are stated.

Chapter 2 describes the numerical methods used to compute different physical properties on the 3-D microstructure. All the numerical methods are applied to a family of synthetic sand pack – Finney pack (Finney, 1968; 1970) with low-, medium- to high- porosities. Numerical calculations of electrical conductivity (with and without the presence of surface conductivity), permeability, surface area and hydraulic radius are compared with analytic solutions. A staggered-grid finite difference (FD) scheme is applied to solve the Laplace equation for electrical conduction and the Stokes equation for hydraulic conduction. Each grid is one voxel in the 3-D digital image of the microstructure. The Laplace solver can handle different levels of conductivity contrast so that different saturations (gas, oil and brine) can be modeled. Details of the finite difference formulation and numerical benchmarks for the Laplace solver are given in Appendix A, and the Stokes solver is given in Appendix B. Two different edge detection methods are applied to recognize surface voxel in the binary image. One is a gradient based, first order differential method, and the second one is connectivity-number-based edge detection (CNED) method. A three phase conductivity

model developed on the binary representation of the microstructure, which is based on the geometric average of free electrolyte conductance and surface conductance in the EDL, is illustrated. Cross-correlation between the formation factor and permeability is established using specific surface area and Λ parameter. We examine the influence of image resolution on calculations of different properties using a well established method – *majority rule* (Arns, 2001; Arns et al., 2005). The bulk of this chapter is under revision as:

Zhan X., L. M. Schwartz. and M. N. Toksöz.: 2009, Estimating transport properties of granular porous media, under revision for *Journal of Applied Physics*.

Chapter 3 implements the numerical methodologies described in Chapter 2 to the 3-D μCT microtomography of a 23.6% porosity Berea Sandstone 500 (BS500) with 2.8 micron resolution. Five 400^3 sub-sets at different locations within the whole 1840^3 volume are selected as representative computation units based on the porosity distribution. Heterogeneity at 400^3 (physical size of $1mm^3$) scale is observed from the computed properties. Averaged electrical conductivity, permeability, specific surface area and surface conductivity are compared with corresponding laboratory measurements collected on the cm^3 BS500 core sample. The values of EDL length and counter-ion mobility are chosen according to the experimental electrolyte type and salinity. With the experimental measurement of the cation exchange capacity *(CEC)* for BS500, the saturated rock conductivity as a function of saturation brine conductivity is forward predicted and compares with laboratory measurements on freshly cut core samples. Formation factor and permeability of five sub-sets

are cross-correlated using surface area and Λ parameter. Resolution impacts on different properties are addressed by downscaling the digital image using *majority rule*. In the end, we increase the computation sample volume and obtain a better match to laboratory measurements. Large sample provides a better representation of the rock. The bulk of this chapter has been accepted as:

Zhan X., L. M. Schwartz., M. N. Toksöz., W. C. Smith. and F. D. Morgan.: 2009, Pore scale modeling of rock properties and comparison to laboratory measurements, accepted by *Geophysics*.

Chapter 4 moves on to the experimental study of seismoelectric response in the brine saturated BS500 block. Quantitative AC seismoelectric signal (10 kHz to 120 kHz) is collected on the saturated BS500 plate in a solution tank to simplify the acoustic wave field. We use single sine plus and five-cycle sine burst as source wavelets. The "pro" of using single sine plus is to obtain better resolution in the time domain. Transmitted and reflected waves can be distinguished and separated from noise in time domain waveforms. The "con" of single plus is the complication in the frequency domain. On the contrary, the five-cycle sine wave is simple in frequency content while difficult to distinguish different arrivals in the time domain. Received acoustic and electric signals are analyzed in both time domain and frequency domain excited by different source wavelets. Precautions, such as electrically shielding the acquisition system and securely holding the sample and electrodes, are taken to ensure the data quality. Abundant stacking of recorded data effectively enhances the signal to noise ratio. We measure the streaming potential (electric voltage) across the freshly cut BS500 cylinder

core samples saturated with different brine conductivities and under different static pressure gradients. The frequency dependent coupling coefficient of BS500 is theoretically calculated using Pride's equation with the parameters previously obtained from μCT image and laboratory measurements. Comparison between the experimentally obtained coupling coefficients and theoretical calculation is made in the end. The bulk of this chapter is:

In preparation to be submitted to *Geophysics*.

Chapter 5 summarizes the results and conclusions of this thesis and is followed by five appendices.

Appendix A describes the finite difference formulation of the Laplace equation, benchmark of the FD solver and application on a 3-D Fontainbleau Sandstone μCT microtomography.

Appendix B describes the finite difference formulation of the Stokes equation and benchmark of the FD solver with Lattice-Boltzmann method on a 2-D SEM image of sandstone.

Appendix C describes the semi-empirical relationship between clay content and cation exchange capacity.

Appendix D describes Pride's formula for coupled electromagnetic and acoustic fields of a fluid-filled porous medium.

Appendix E describes a geophysical application of seismoelectric conversion in borehole logging while drilling model. The bulk of this appendix has been published as:

Zhan X., Z. Zhu., S. Chi. and M. N. Toksöz.: 2009, Elimination of LWD (logging while drilling) tool modes using seismoelectric data, *Communications in Computational Physics,* **7**, 47-63.

1.4 References

Alkafeef, S. F. and Alajmi, A. F.: 2006, Streaming potentials and conductivities of reservoir rock cores in aqueous and non-aqueous liquids, *Colloids and Surfaces A*, **289**, 141-148.

Arns, C. H.: 2001, The influences of morphology on physical properties of reservoir rock, *Ph.D. thesis, Univ. of New South Wales*.

Arns, C.H., Bauget, F., Ghous, A., Sakellariou, A., Senden, T.J., Sheppard, A.P., Sok, R.M., Pinczewski,W.V., Kelly, J.C. and Knackstedt, M.A.: 2005, Digital core Laboratory: Petrophysical analysis from 3D imaging of reservoir core fragments, *Petrophysics*, **46**, 260-277.

Auzerais, F. M., Dunsmuir, J., Ferréol, B. B., Martys, N., Olson, J., Ramakrishnan, T. S., Rothman, D. H. and Schwartz, L. M.: 1996, Transport in sandstone: a study based on three dimensional microtomography, *Geophysical Research Letters*, **23**, 70E-708.

Berryman, J. G.: 1985, Measurement of spatial correlation functions using image processing techniques, *J. Appl. Phys,* **57**, 2374-2384.

Bockris, J. O'M. and Reddy, A. K. X.: 1972, Modern aspects of electrochemistry, *Plenum, New York.*

Devarajan, S., Toumelin, E. and Torres-Verdín, C.: 2006, Pore scale analysis of the Waxman-Smits shaly sand conductivity model, *SPWLA 47th Annual Logging Symposium*, June 4-7.

Dvorkin, J., Armbruster, M., Baldwin, C., Fang, Q., Derzhi, N., Gomez, C., Nur, B., Nur, A. and Mu, Y.: 2008, The future of rock physics: computational methods vs. lab testing, *Petroleum Geology*, **26**, 63-68.

Finney, J.: 1968, Random packings and structure of the liquid state, *Ph.D. thesis, Univ. of London.*

Finney, J.: 1970, Random packings and the structure of the liquid state, *Proc. Roy. Soc,* **319A**, 479.

Garbozi, E.J. and J. F. Douglas, 1996, Intrinsic conductivity of objects having arbitrary shape and conductivity, Physical Review E, 53, 6169-6180.

Guan, W. and Hu, H.: 2008, Finite-difference modeling of the electroseismic logging in a fluid-saturated porous formation, *Journal of Computational Physics*, 227, 5633-5648.

Haartsen, M. W.: 1995, Coupled electromagnetic and acoustic wavefield modeling in poro-elastic media and its application in geophysical exploration, *Ph.D. thesis, Massachusetts Institute of Technology.*

Haartsen, M. W. and Pride, S. R.: 1997, Electroseismic waves from point sources in layered media, *Journal of Geophysical Research*, **102(B11),** 2474E-24769.

Helmholtz, H. V.:1879, Studien über electrische grenschichten, *Ann. Der Phys. und Chem.*, **7**, 337-387.

Hunt, C. W. and Worthington, M. H.: 2000, Borehole electrokinetic response in fracture dominated hydraulically conductive zones, *Geophysical Research Letters*, **27**, 131E-1318.

Ishido, T. and Mizutani, H.: 1981, Experimental and theoretical basis of electrokinetics phenomena in rock-water systems and its applications to geophysics, *Journal of Geophysical Research*, **86**, 1763-1775.

Jin, G. D., C. Torres-Verdín., S. Devarajan., E. Toumelin. and E. C. Thomas, 2007, Pore-scale analysis of the Waxman-Smits shaly sand conductivity model, Petrophysics, 48, 104-120.

Johnson, D. L., Koplik, J. and Dashen, R.: 1987, Theory of dynamic permeability and tortuosity in fluid-saturated porous media, *Journal of Fluid Mechanics*, **176**, 379-402.

Kameda, A., 2004, Permeability evolution in sandstone: digital rock approach: Ph.D. thesis, Stanford University.

Keehm, Y., Mukerji, T. and Nur, A.: 2001, Computational rock physics at the pore scale: transport properties and diagnosis in realistic pore geometries.

Martys, N. and E. J. Garboczi, 1992, Length scales in relating fluid permeability and electrical conductivity in random two-dimensional model porous media: Physical Review B, 46, 6080.

Mikhailov, O. V., Queen, J., and Toksöz, M. N.: 2000, Using borehole electroseismic measurements to detect and characterize fractured (permeable) zones, *Geophysics*, **65**, 1098-1112.

Mizutani, H., Ishido, T., Yokokura, T. and Ohnishi, S.: 1976, Electrokinetic phenomena associated with earthquakes, *Geophysical Research Letters*, **3**, 36E-368.

Morgan, F.D., Williams, E.R. and Madden, T.R.: 1989, Streaming potential properties of westerly granite with applications, *Journal of Geophysical Research,* **94,** 12449-12461.

Motealleh, S., Gladkikh, M., Bespalov, A., Herrick, D. C. and Bryant, S. L.: 2007, Grain-scale modeling of electrical resistivity of 'shaly sands', *SPWLA 48th Annual Logging Symposium*, June 3-6.

Packard, R. G.: 1953, Streaming potentials across glass capillaries for sinusoidal pressure, *Journal of Chemical Physics*, **21**, 303-307.

Pengra, D. and Wong, P.: 1995, Pore size, permeability and electrokinetic phenomena, Access in Nanoporous Materials, pp.29E- 317, *Springer, New York.*

Pengra, D. B., Li, S. X. and Wong, P.: 1999, Determination of rock properties by low-frequency AC electrokinetics, *Journal of Geophysical Research*, **104**, 2948E-29508.

Pride, S. R. and Morgan, F. D.: 1991, Electrokinetic dissipation induced by seismic waves, *Geophysics*, **56**, 914-925.

Pride, S. R.: 1994, Governing equations for the coupled electromagnetics and acoustics of porous media, *Physical Review B*, **50**, 15678-15696.

Reppert, P. M.: 2000, Electrokinetics in the earth, *Ph.D. thesis, Massachusetts Institute of Technology.*

Reppert, P. M. and Morgan, F. D.: 2002, Frequency-dependent electroosmosis, *Journal of Colloid and Interface Science*, **254**, 372-383.

Revil, A., Cathles III, L.M., Losh, S. and Nunn, J.A.: 1998, Electrical conductivity in shaly sands with geophysical applications, *Journal of Geophysical Research*, **103**, n. B10, 2392E-23936.

Revil, A. and Glover P. W. J.: 1998, Nature of surface electrical conductivity in natural sands, sandstone, and clays, *Geophysical Research Letters,* **25,** 691-694.

Schwartz, L.M., N. S, Nunn, D. P. Bentz, E. J. Bentz, and S. Torquato, 1993, Cross-property relations and permeability estimation in model porous media: Physical Review E, 48, 4584-4591.

Sharma, M. M., Kuo, J. F. and Yen, T. F.: 1986, Further investigation of the surface charge properties of oxide surfaces in oil-bearing sands and sandstones, *Journal of Colloid and Interface Science*, **115,** 9-16.

Singer, J., Hollway, L. Stuart-Bruges, W., Manson, G.: 2006, Electrokinetic logging has the potential to measure permeability, *Petrophysics,* **47**, 427-441.

Smoluchowski, M. von.: 1903, Contribution a la theorie de l'endosmose electrique et de quelques phenomenes correlatifs, *Bull. International de l'Academie des Sciences de Cracovie*, **8**, 182-200.

Thompson, A. and Gist, G.: 1993, Geophysical applications of electrokinetic conversion, *The Leading Edge*, **12**, 1169-1173.

Torquato, S. and Stillinger, F. H.: 2001, Multiplicity of generation, selection, and classification procedure for Jammed Hard-Particle packing, *J. Phys.Chem. B.,* **105 (47)**, 11849-11853.

Zhu, Z., Haartsen, M. W. and Toksöz, M. N.: 2000, Experimental studies of electrokinetic conversions in fluid-saturated porous media, *J. Geophys. Res.,* **105**, 1349-1356.

Zhu, Z. and Toksöz, M. N.: 2003, Crosshole seismoelectric measurements in borehole models with fractures, *Geophysics,* **68**, 1519-1524.

Zhu, Z. and Toksöz, M. N.: 2005, Seismoelectric and electroseismic measurements in fractured borehole models, *Geophysics,* **70**, F4E-F51.

Zhu, Z., Toksöz, M. N. and Burns, D. R.: 2008, Electroseismic and seismoelectric measurements of rock samples in a water tank, *Geophysics,* **73,** E153-E164.

Chapter 2

Pore Scale Modeling of Physical Properties of Granular Porous Media[1]

Abstract

Transport properties, such as permeability, electrical conductivity, are important in many geophysical and petroleum applications. The microstructure of porous media and physical characteristics of the solid and fluids that occupy the pore space determine the macroscopic transport properties of the medium. The purpose of this chapter is to test the applicability to numerically calculate the geometrical and transport properties (electrical conductivity, permeability, specific surface area and surface conductivity) of porous media given its microstructure. We calculate geometrical and transport properties (electrical conductivity, permeability, specific surface area and surface conductivity) of a family of model granular porous media from an image based representation of its microstructure. The models are based

[1] (the bulk of this Chapter is) Under revision as: Zhan X., L. M. Schwartz. and M. N. Toksöz.: 2009, Estimating transport properties of granular porous media, for *Journal of Applied Physics*.

on the packing described by Finney and cover a wide range of porosities. Finite difference (FD) scheme is applied to solve Laplace equation for electrical problem and Stokes equation for hydraulic problem. Two image processing methods are used to identify pore-grain interface. Cross-correlation linking permeability to formation factor through pore geometric parameter, hydraulic radius, computed from the digitized image is established. A three phase conductivity model is developed to compute surface conductivity present at grain-pore fluid interface. Numerical calculations of electrical conductivity (with and without presence of surface conductivity), formation factor, permeability and surface area on the Finney pack compare well against analytic models over the entire porosity range studied. In addition to physical aspect, we examine the influence of image resolution on our calculations using majority rule.

2.1 Introduction

The transport properties of porous media are important in many geophysical, environmental, chemical and bio-medical applications. Generally, the interaction between the solid matrix and the pore fluids at the microscopic scale is crucial to the interpretation of macroscopic measurements. Computational physics has grown with recent advances in micro and nano-scale imaging. Given an accurate digital representation of the microstructure at the pore scale, physical properties can, in principle, be computed with confidence (Hazlett, 1995; Coles et al., 1996; Pal et al., 2002; Kameda et al., 2006). In practice, one must deal with

uncertainties due to the imaging technique (e.g. proper segmentation) and with questions associated with image resolution and sample size.

In this study, we use the 3-D digital structure of overlapping spherical grains based on a familiar dense random packing (a dense pack of spheres of uniform radius) (Finney, 1968, 1970) (Fig. 2-1) to compute electrical conductivity, permeability and specific surface area. This model has several attractive features. First, it provides reasonable first approximation to well-sorted sandstones. Finney pack has been successfully applied to simulate different geological process, such as sedimentation, compaction and grain growth (Roberts and Schwartz, 1985; Schwartz and Banavar, 1989; Bryant et al., 1993). Second, the entire structure is completely specified by the radii and the spatial locations of the constituent grains; there are no issues related to image segmentation or the inappropriate closing of narrow pores due to improper assignment of discrete voxels. Third, changing the porosity on Finney pack is relatively easy by the uniform expansion of the grain radius. Fourth, there are analytic models available for sphere packs; these provide a useful benchmark of our numerical calculations.

FD techniques are employed to solve the Laplace equation for electrical conduction and the Stokes equation for single phase fluid flow (Roberts and Garboczi, 2000). In addition to the effective values of conductivity and hydraulic permeability, our calculations also yield the current and flow field distributions at each voxel within the3-D structure. This provides the basis for solving multi-physics coupled problems such as electrokinetic phenomena (Pride et al., 1997).

The electrical formation factor, F, is the ratio between conductivity of a fluid saturated porous solid, σ_{eff}, and the conductivity of the fluid, σ_f. When thinking about a family of related porous media (e.g. sintered glass beads or rocks from the same well or quarry) a useful empirical relation is Archie's law (Archie, 1942):

$$\mathrm{F} = \frac{\sigma_f}{\sigma_{eff}} = \mathrm{a}\phi^{-\mathrm{m}}. \tag{2-1}$$

Here ϕ is the porosity (the pore volume fraction), m is known as the cementation exponent, and $a \approx 1$ is a fitting parameter. This relationship assumes that the mobile ions in the pore fluid (electrolyte) are distributed uniformly. A fluid saturated rock can therefore be modeled as a two-component medium: solid grains (volume fraction $1 - \phi$) and saline water (volume fracti ϕ) (Arns et al., 2001, 2005; Pal et al., 2002). However in many porous media there is an additional conducting mechanism at the pore-grain interface (e.g. clay minerals in sandstones or modified porosity in mortars). Quite often this enhanced surface conduction is confined to a layer whose thickness is very small compared to typical pore dimensions. For example, in sandstones where the pore size is typically 10 -50 μm, the electrical double layer (Debye and Hückel., 1923; Morgan et al., 1989; Pride and Morgan, 1991) extends 30 to 3000 Å from the mineral surface into the neutral electrolyte. Formally, conductivity can be written as the sum of the normal ionic brine conductivity σ_f and a near surface term σ_{surf} due to the double layer. Here, we present a three phase conductivity model to include surface conduction in our numerical calculations. Finally, we examine the influence of image resolution on the various quantities we have calculated.

2.2 Numerical Calculations

We begin with original Finney pack, which has porosity , $\phi = 36.2\%$, when spheres are just touching each other. Given the coordinates of sphere centers and grain radius, the complete description of solid matrix and pore space is obtained without ambiguity (Fig. 2-2). A 3-D binary digital image is obtained according to the center of the voxel is inside (solid matrix) or outside of any sphere (pore space). We assign solid matrix to be phase *1* and pore to be phase *0*. By increasing the sphere radii without altering their center positions, generate a series of 14 porous media with porosities *4.02%, 6.24%, 7.85%, 9.91%, 12.54%, 15.79%, 19.80%, 22.32%, 24.16%, 25.13%, 26.12%, 28.02%, 31.52%* and *36.2%* , respectively. The lower bound of porosity, *4.02%,* is slightly higher than the percolation threshold, which is just above *3%* (Roberts and Schwartz, 1985; Bryant et al., 1993). When the size of the sampling cube in the finney pack exceeds four-grain radii, the fluctuation in both porosity and permeability is negligible (Kameda et al., 2006). To reduce the computation cost, we took a sub-set with cube size of E-grain radii right in the middle of the whole finney pack , which is composed of 8000 spheres in total. Our calculations are done on 200^3 cube whose edge length equals of $1/20$ of the original grain radii.

2.2.1 Electrical Conductivity Calculation

The effective dc conductivity of a random medium can be calculated by Ohm's Law. The conductivity value σ of a composite n-phase material is a function of location *r*. For a steady

state conductivity problem, where the currents are steady in time, the charge conservation equation possesses the form of the Laplace equation as:

$$\nabla \cdot \vec{J}(r) = -\nabla \cdot \left(\sigma(r) \cdot \nabla \vec{V}(r)\right) = 0, \tag{2-2}$$

where J is the current density, σ is the electric conductivity and V is the electric potential. At boundaries between materials with different conductivities, the boundary conditions require that the current density normal to the interface and the potential are continuous. We calculate the macroscopic conductivity of the random material by applying an electric potential gradient across the sample. The volume averaged current density is used to compute the effective conductivity from Ohms' law.

For numerical calculation, we use a staggered-grid finite difference scheme with 2nd order accuracy in space (Moon and Spencer, 1953; Garbozi et al., 1996; Zwillinger, 1997). Our finite difference electrical conductivity programs can handle isotropic materials as well as conductivity tensors. To deal with high contrast conductivity values for neighboring grids, we adopt a gradual relaxation method (Press et al., 1990). The Laplace solver has been benchmarked with a commercial finite element software package FEMLAB (see Details in Appendix A). For formation factor calculation, we assign the conductivity values to be 0 (solid matrix) and 1 (pore fluid). The normalized fluid filled rock conductivity , $\sigma_{eff,}$ gives the formation factor. By using the solid matrix and saturation fluid conductivities, we can calculate the absolute value for the fluid filled rock conductivity.

2.2.2 Hydraulic Permeability Calculation

The representation of fluid flow is given by the Navier-Stokes equation. For the case of laminar (slow, incompressible) flow, the fluid flow can be conveniently described by the linear Stokes equations:

$$\eta\nabla^2\vec{u}(r) = \nabla P(r), \tag{2-3}$$

$$\nabla \cdot \vec{u}(r) = 0, \tag{2-4}$$

where u and P are the local velocity vector and pressure fields at position r, η is the dynamic viscosity of the fluid. We can calculate the macroscopic permeability of the porous medium by applying a pressure gradient across the sample. The permeability, κ, of the porous medium is calculated by volume averaging the local fluid velocity (in the direction of the flow) and applying the Darcy equation:

$$u = -\frac{\kappa}{\eta}\frac{\Delta P}{L}, \tag{2-5}$$

where u is the average fluid velocity in the direction of the flow for the porous media and L is the length of the sample porous medium across which there is an applied pressure gradient of ΔP.

To solve the hydraulic problem, we use a modified Stokes solver based on an industry standard finite difference (FD) code developed at NIST (National Institute of Standards and Technology, Gaithersburg, MD 20899-8621, U.S.A; ftp://ftp.nist.gov/pub/bfrl/bentz/permsolver/) (see details in Appendix B). This Stokes solver was first designed to study the relationship between microstructure and permeability in porous cement (Martys and Garboczi, 1992). More recently, the code has been utilized on a wide

variety of applications in study of three-dimensional microstructures (Schwartz et al., 1993; Nicos et al., 1994; Bentz and Martys, 2007) using a uniform FD scheme .

2.2.3 Surface Area Calculation

The coordinates of the Finney pack are known and we construct a family of consolidated porous media by increasing the grain radii while holding the grain centers fixed. On these models we impose a high resolution digital grid; each voxel is assigned to be part of the grain (or pore) population depending on whether (or not) its center lies within a grain. Compared to X-ray CT images on real physical samples, the present images are binary images free of any uncertainty associated with the segmentation of gray-scale data. To quantify the surface area from the binary image, we need to identify pixels at the pore-grain interface. Two different edge detection methods are adopted. Generally speaking, the aim of edge detection on the binary images is to classify the pixels into two classes: edge versus non-edge. The key problem is how to construct an operator to detect the edge pixels of the images.

The first method is a gradient based method – first order differential method of edge detection (Canny, 1986; Pathegama et al., 2004). Most edge detection methods work on the assumption that an edge occurs where there is a discontinuity in the intensity function or a very steep intensity gradient in the image (e.g. *0* and *1*). Using this assumption, if we take the derivative of the intensity values across the image and find points where the derivative is a maximum, we will have marked our edges. In a discrete image of pixels we can calculate the gradient by simply taking the difference of intensity values between adjacent pixels. An odd

symmetric filter $\begin{bmatrix} -1 & 0 & -1 \\ -1 & 0 & -1 \\ -1 & 0 & -1 \end{bmatrix}$ approximates a first derivative, peaks in the convolution output determine the edges.

The second one is an connectivity-number-based edge detection (CNED) method (Zahn, 1971; Zhang and Wang, 2005). This method is based on tracing phase connectivity to identify a phase change. Connectivity-number is sought as detector; those pixels that have zero-connectivity-number are eliminated as inner pixels from the image. In binary images, the connectivity number of the *0* phase is the number of the connected *0* phase pixels passed when it moves around its neighbor (Zahn and Roskies, 1972). Checking the connectivity of the *0* phase to the *0* phase in its 8 neighbors in 3-D, the zero-connectivity pixels are inner points or isolated points. Eliminating those inner and isolated points from the original image gives the surface (edge) pixel (Zahn, 1971).

There are only 7 typical zero-CN 8-neighbors as shown in Fig. 2-3. The above 7 types have 17 different combination forms. Taking the central black pixel to be *0,* from row to columns, one can find the regular forms in Tab. 2-1. These 17 combinations form the edge detectors. The CNED algorithm could be described as following:

Step 1 Read in the 3-D binary image *F* in a 1-D numbering labeling scheme. The *(i, j ,k)* label for a pixel gives its position in a 3-D lattice.

Step 2 Initialize a temple array *f(8).* Calculate function *f* for each black pixel (phase *0*) based on the formula below (Eq. 2-6):

$$f(0) = F(i+1, j), \quad f(1) = F(i+1, j-1), \tag{2-6}$$

$$f(2) = F(i, j-1),\ f(3) = F(i-1, j-1),$$
$$f(4) = F(i-1, j),\ f(5) = F(i-1, j+1),$$
$$f(6) = F(i, j+1),\ f(7) = F(i+1, j+1).$$

Step 3 Calculate the CN for each black pixel according to Tab. 2-1, the result is set to be *CN(i, j, k)*.

Step 4 Eliminate the inner and isolated pixels with zero-CN and pick out the edge pixels (surface pixels between two phases).

Because only the black pixels participate in the iterative computing, the CNED algorithms execute time strictly relies on the number of black pixels of the binary image. Thus, this edge detection method works more efficient for the low porosity finny pack than the high porosity packs. Compared with the first method we mentioned – first order differential methods of edge detection (Canny, 1986; Pathegama et al., 2004), the execution time is less since the first method needs to calculate the convolution at each pixel location. This CNED method is more efficient especially for large volume images.

The difference between results from the two methods is within 8% for medium to high porosity Finney pack (*19.80%, 22.32%, 24.16%, 25.13%, 26.12%, 28.02%, 31.52%* and *36.2%*). For low to medium low porosity Finney pack (*4.02%, 6.24%, 7.85%, 9.91%, 12.54%, 15.79%*), the difference is within 12%. We take the average of the two methods as our count of the surface pixels. Specific surface area, which is the pore surface area to pore volume ratio, could be simply calculated as:

$$S = \frac{S_P}{V_P} = \frac{\phi_s}{\phi L}, \tag{2-7}$$

where S_P is the pore surface area, V_P is the pore volume, ϕ_s is the volume fraction of the surface pixels, ϕ is the total porosity, and L is the grid size.

2.3 Summary of Results

2.3.1 Electrical and Fluid Flow

The inverse of formation factor (the ratio between the saturated rock conducticit and saturation brineconductivity, $1/F = \sigma_{eff}/\sigma_f$) is plotted for different porosities packing in Fig. 2-4. We solve Eq. 2-2 by assigning conductivity values to be 0 for the solid matrix and 1 for the pore space. For systems composed of spherical grains, the cementation factor, m, in Eq. 2-1 is estimated to be *1.5* (Sen et al., 1981; Sen and Kan. 1987). Good agreement is seen between our numerical calculations and this analytic result except at the lowest porosities where influence of percolation threshold is apparent (Roberts and Schwartz, 1985; Bryant et al., 1993). The finite difference Laplace solver is written in an energy form and solved using conjugate gradient method (see details in Appendix A). The condition of the global matrix to be solved is less good in case of low porosity, when conducting phase becomes sparsely connected. Especially close to the percolation threshold, the numerical accuracy is expected to be less good.

The calculated permeabilities (κ) by solving Eq. 2-3, Eq. 2-4, normalized to that of the original packing with *36.2%* porosity (κ_0), are shown in Fig. 2-5. Shown also is a curve representing the Kozeny-Carman relationship (Kozeny, 1927; Carman, 1938, 1961) modified to include a percolation threshold (Mavko and Nur, 1997):

$$\kappa = \frac{1}{72}\frac{(\phi - \phi_p)^3 d^2}{[1-(\phi-\phi_p)]^2 \phi F}. \quad (2\text{-}8)$$

Here d is the grain diameter, ϕ_p is the percolation threshold (*3%* for Finney pack) and F is the electrical formation factor. Good agreement between the FD calculation and Kozeny-Carman relationship holds for the entire porosity range.

2.3.2 Specific Surface Area

The identified surface voxels are shown in red along the pore (shown in blue) – grain (shown in green) boundary in Fig. 2-6 for one of our models (*19.80%* porosity Finney pack) using the CNED method described before. Our calculated specific surface area, S (the average of two edge detection methods), is compared with the analytic expression for spheres with diameter, d, ϕ is porosity:

$$S = \frac{6(1-\phi)}{d}. \quad (2\text{-}9)$$

The original Finney pack with *36.2%* porosity, when the spheres are just touching, has a specific surface area of $3.82/d$ according to Eq. 2-9. The computed specific surface area of *36.2%* Finney pack, which is the mean value of two edge detection method, on the 200^3 image with grid size being $1/20$ the grain radii is found to be $4.02/d$.

2.4 Formation Factor and Permeability Correlation

Correlating hydraulic permeability to other physical properties of the porous media is a long standing subject. In practices, direct in-situ permeability measurement is difficult to make. The correlations to measurements of other properties, such as porosity, electrical

conductivity, mercury porosimetry, and NMR response have been used to estimate permeability (Wong et al., 1984; Katz and Thompson, 1986; Kenyon, 1992; Schwartz et al., 1993). The most popular one is to relate permeability with electrical conductivity through pore volume to surface area (V_P/S). We have numerically calculated electrical conductivity, permeability and surface area on the same structure. What we want to test next is whether we can establish the correlation among those computed physical properties on the same geometry.

A consistent development of the equivalent channel model for both fluid flow and electrical conduction in porous media leads to the expression:

$$\kappa = \frac{CR^2}{F}, \tag{2-10}$$

where k is permeability, F is formation factor, C is a geometrical factor and R is so called hydraulic radius (Brace, 1977; Paterson, 1983; Walsh and Brace, 1984). This equation is valid under the assumption that the fluid is electrically conducting and the solid parts not and that the electrical and fluid stream lines are identical. C is in the range of $1/2$ for circular pores to $1/3$ for a slot, which cover the widest range of aspect ratio of most porous media (Wyllie and Gregory, 1955).

The concept of hydraulic radius first developed for pipes of non-circular section where it is defined by the ratio of the cross-sectional area to the perimeter under the assumption of uniformity along the length. Its use for porous media extends this notion, with the aid of dimensional arguments, to a situation where many local conduits acting more or less in parallel make up an equivalent channel but where the local conduits are varying in actual

cross-section and direction along their length and are branching (Paterson, 1983). In porous media, hydraulic radius R can be determined by the ratio of porosity and specific surface area (ϕ/S). Thus, R represents an equivalent (or average) hydraulic radius of the exceedingly complicated flow channels. From this empirical relationship, we could see that permeability is inverse proportional to the formation factor.

Now we have two ways to estimate permeability from the microstructure. One is by directly solving Stokes equation on digital image. The other is combing the computed electrical conductivity by solving Laplace equation and computed specific surface area to calculate permeability using Eq. 2-10. We cross plot the numerically computed permeability, $k_{numerical,}$ which is solved from Stokes equation (Eq. 2-3, Eq. 2-4) with estimated permeability, $k_{image,}$ which is computed from Eq. 2-10 (Fig. 2-7). All the permeability values here are normalized permeability (with respect to *36.2%* porosity Finney pack) as described before. Permeabilities calculated from two different methods are in good agreement with each other. Thus, cross-correlation between different transport properties of the same structure could be established numerically.

2.5 Surface Conductivity Calculation

So far, we have assumed so far that the solid grains are insulating and that the electrolyte conductivity arises from mobile ions that are uniformly distributed throughout pore space. Modeling the porous medium as a two-component structure: solid grains (volume fraction $1-\phi$) and saline water filled up the pore space (volume fraction ϕ) can provide a good

estimate of formation factor. As we mentioned in the introduction (section 2.1), an electrical double layer is developed at the interface of pore and grain, which composes the solid matrix of porous media (Waxman and Smit, 1968; Clavier et al., 1977; Johnson et al., 1986; Sen and Kan, 1987; Lima and Sharma, 1990; Revil et al., 1998; Devarajan, 2006). In this section, we introduce a three phase electrical conductivity model, which includes the surface conduction, and illustrate it on the microstructure of Finney pack. The calculated result from three phase conductivity model is compared with analytic formula. We will implement this method on a Berea sandstone microtomograhpy. Physical values of grain property and the electrolyte conductivity will be adopted to be compared with laboratory experiment in Chapter 3.

A three phase model is proposed to include the surface conductivity originated in a very thin layer at grain-electrolyte boundary. Surface pixels at the pore-grain boundary are defined to be the third phase. Numerical representation of the porous rock is changed to a three phase model as illustrated in Fig. 2-8. The third phase voxels (shown in red in Fig. 2-8) contains an EDL whose thickness, χ_d, is at the nanometer scale (Debye and Hückel., 1923; Morgan et al., 1989; Pride and Morgan, 1991). By contrast, the image voxels in most naturally occurring porous media are at the micron scale ($1/20$ of the original grain radii in our numerical representation of Finney pack). In this case, the first kind of grid cell has the conductivity of σ_1 equal to the rock matrix conductivity. The second kind of grid cell has the conductivity of σ_2 equal to the free electrolyte conductivity in the pore space. The third kind of grid cell is the boundary grid containing an EDL at fluid-solid interface with the conductivity σ_3. The conductivity model in the third kind of grid is illustrated in Fig. 2-9. We calculate σ_3 by

geometrically averaging the surface conductivity, Σ_{surf}, within the double layer thickness χ_d with free electrolyte conductance , Σ_2 , in the remainder, $L - \chi_d$, of the surface voxel. Based on the thin EDL assumption, surface conductivity in the EDL and the free electrolyte in the pore space can be treated as two conductors in parallel for the first order approximation. Thus, this geometric average is physically reasonable and σ_3 can be expressed as

$$\sigma_3 = \frac{\Sigma_{surf} + \sigma_2 . (L - \chi_d)}{L}. \tag{2-11}$$

The effective conductivity of fluid saturated rock could be computed from Ohm's law and be expressed at micro-scale as:

$$\frac{1}{F} = \frac{\sigma_{eff}}{\sigma_f} = \left(\frac{l}{\Delta V}\right)\frac{1}{A}\iint_S (-\vec{z} \cdot \vec{\nabla} V)\, ds. \tag{2-12}$$

Here, l is the length of the sample, ΔV is the electrical potential across the sample, A is the cross-section, and S is the pore area over which the integration is made. With the surface conductance, $\sum_{surf}$, localized within the double layer, Eq. 2-12 should be expanded as (Guéguen and Palciauskas, 1997):

$$\sigma_{eff} = \frac{1}{F}\left(\sigma_f + \frac{2\Sigma_{surf}}{\Lambda}\right) = \frac{\sigma_f}{F}(1 + X), \tag{2-13}$$

where $\Lambda/2$ is a dynamic length scale related to the pore volume to surface area ratio (Johnson et al., 1986, 1987). Λ is a parameter characteristic of the geometry of the porsou medium and independent of fluid property, which is rigorously given by (Johnson et al., 1986):

$$\frac{2}{\Lambda} = \frac{\int |\nabla \psi(r)|^2 dS_P}{\int |\nabla \psi(r)|^2 dV_P}. \tag{2-14}$$

Integration on the numerator of Eq. 2-14 is over the walls of the pore-grain interface (S); that in the denominator is over the pore volume (V_P). Thus, $\Lambda/2$ is an effective surface-to-volume

ratio wherein each area or volume element is weighted according to the local value of the electric field, which would exist in the absence of surface mechanism.

For a given X, we have $\sum_{surf} = \frac{\Lambda X \sigma_2}{2}$ from Eq. 2-13 (σ_2 and σ_f are exchangeable, both of them indicate the bulk electrolyte conductivity) , and Λ can be written as (Johnson et al., 1986), which is an analog form of Eq. 2-14:

$$\frac{2}{\Lambda} = \mathrm{m}(\phi)\frac{\mathrm{S}}{\mathrm{V_P}}, \tag{2-15}$$

where m is the exponent in Archie's law (Eq. 2-1). For Finney pack, we have$m(\phi) \approx 1.5$, especially in the high porosity region (Sen et al., 1981). Thus, Eq. 2-15 takes the form:

$$\Lambda = \frac{4\mathrm{V_P}}{3\mathrm{S_P}} = \frac{4\Phi}{3\Phi_s}\mathrm{L}. \tag{2-16}$$

We illustrate these ideas with the *19.80%* finney pack. The surface detection methods described before gives $\phi_S = 6.7\%$. Realistic values of χ_d, which is at nanometer scale, can, in principle, be calculated as a function of the ionic strength of the saturating electrolyte(Debye and Hückel., 1923; Morgan et al., 1989; Pride and Morgan, 1991). Here, we take χ_d to be two orders smaller than $L(L/100)$. Substituting from Eq. 2-15 into Eq. 2-11, we have:

$$\sigma_3 \approx \frac{\sum_{surf}}{\mathrm{L}} + \sigma_2 = (\frac{2\Phi X}{3\Phi_s} + 1)\sigma_2, \tag{2-17}$$

We can now compute σ_3 as a function of σ_2 and put it into the surface voxel in the image (red in Fig. 2-8). for the rest of porosity the conductivity value isσ_2. Realistic values of X at low values of salinity vary from 2-10 (Devarajan, 2006). Taking X=3, we have $\sigma_3 = 6.91\sigma_2$.

Solving Laplace equation (Eq. 2-2) with conductivity value at different location within the Finney pack, we get $\sigma_{eff} = \frac{3.68}{F}\sigma_2$, which is close to the result from Eq. 2-13 as $\sigma_{eff} = \frac{4}{F}\sigma_2$.

The determination of $\sum_{surf}$ in real porous rock will depend on microstructure, mineralogy and the saturation brine. We will implement the same method described here on a Berea sandstone microtomgrahpy and compare with the laboratory measurements in the next Chapter.

2.6 Impact of Image Resolution

The fact that we are using finite size voxel limits our ability to resolve the smallest features of the pore space. This image resolution issue will impact the numerical calculation of physical properties, especially transport properties. We will demonstrate the method to estimate image resolution impact on different properties using the *19.80%* porosity finney pack. A sequence of models with successively poorer resolution could be generated by doubling the voxel edge length. Beginning with a 400^3 grid, we can combine 8 voxels into one new voxel with twice the edge length. The new voxel is assigned to be grain or pore by a *majority rule*. If more than 4 of the original voxels were in the pore (grain) space, the new voxel is assigned to be pore (grain); if the breakdown of the original voxels is 4 grain and 4 pore, then the new voxel is assigned randomly. Repeating this process four times, the original 400^3 cube model is reduced to models of size 200^3, 100^3, 50^3 and 25^3 (Fig. 2-10). clearly, the pore structure is distorted and connectivity of the pore space is reduced as the resolution is degraded.

Porosity, permeability, formation factor and surface area have been calculated for the four downscaled models; the results relative to the values calculated for the original 400^3 cube model are defined as fractional changes as plotted in Fig. 2-11. The electrical conductivity is most affected by this process. This is expected since using coarser grids to resolve a structure tends to close narrow pore throats. Closure of the narrow throats impacts the electrical current more severely than hydraulic current. The contribution of small channels to electrical current flow is important so their connectivity must be described properly. By contrast, fluid flow is considerably less *democratic* and is controlled by the largest connected channels (Auzerais et al., 1996). Another observation is that our results do not exhibit the simple linear trend described by Arns et al (2001) (see their Fig. 1c.) in their analysis of calculations based on Fontainebleau sandstone micro-tomograms. When the voxel edge length (image resolution) exceeds the characteristic length of the porous medium, a more dramatic drop in the transport properties is expected. Thus, a non-linear trend should be observed. For Finney pack, we have the expression for the specific surface area S (Eq. 2-9). Thus, the hydraulic radius can be written as:

$$R = \frac{\phi}{S} = \frac{\phi \cdot d}{6(1-\phi)}, \tag{2-18}$$

where d is grain diameter and ϕ is porosity. For *19.80%* porosity Finney pack, the characteristic length, which is twice the hydraulic radii, should be 0.16 times the original grain radius computed from Eq. 2-18. Compared with the edge size, which is $1/20$ of the original grain radii, the characteristic length is about 3 times the edge size (L). In Fig. 2-11, a marked decrease in permeability and electrical conductivity can be observed when the grid

size exceeds $4L$. An advantage or working with the Finney pack is that we can focus entirely on errors associated with image resolution, there is no additional uncertainty due to improper segmentation.

In Fig. 2-12, we exam the impact of image resolution on models with a wide range of porosities [*6.24%, 9.91%, 15.79%, 19.80%, 25.13%* and *31.52%*]. The fractional change in the electrical conductivity was computed at four resolution levels for each porosity. Clearly, the lower the porosity, the more sensitive are the calculated transport properties to reduced resolution.

2.7 Summary

In this chapter, we present the numerical computation method of different physical properties on Finney pack at pore scale. A uniform finite difference (FD) scheme is applied to solve Laplace equation for electrical problem and Stokes equation for hydraulic problem. Laplace solver is modified to handle different level of conductivity contrast. Two different edge detection methods are applied to recognize surface voxel in the digital binary image. One is a gradient based – first order differential method. The second one is an connectivity-number-based edge detection (CNED) method.

1. Binary image of 200^3 cube Finney packs whose edge length equals of $1/20$ of the original grain radii is generated for computation. Numerical results on 14 Finney packs with low, medium to high porosities compare well with the analytic rock physics models for formation factor, permeability and specific surface area.

2. A three phase conductivity model is proposed to include the surface conduction along the pore-grain boundary. Three different conductivity values are assigned to the 19.80% Finney pack microstructure. Numerically computed effective conductivity is close to the analytic solution.

3. The effects of image resolution on computed physical properties are investigated using *majority rule*. Decreased resolution leads to decreased permeability and electrical conductivity. Image resolution has larger impact on low porosity microstructure than high porosity microstructure.

Acknowledgements

This work was supported by the Schlumberger – Doll Research and MIT Earth Resources Laboratory Founding Member Consortium. We thank Dr. Lawrence M. Schwartz for providing us the coordinates for Finney pack and his directing advice on this work.

2.8 References

Amaefule, J.O., Wolfe, K., Walls, J.D., Ajufo, A.O. and Paterson, E.: 1986, Laboratory determination of effective liquid permeability in low-quality reservoir rocks by the pulse decay technique, *paper SPE 15149 presented at the 56th California Regional Meeting, Soc. Of Pet. Eng., Oakland, Calif,* April 2-4.

Archie, G.E.: 1942, The electrical resistivity log as an aid in determining some reservoir characteristics, *Trans. AIME*, **146**, 54-62.

Arns, C. H.: 2001, The influences of morphology on physical properties of reservoir rock, *Ph.D. thesis, Univ. of New South Wales.*

Arns, C.H., Bauget, F., Ghous, A., Sakellariou, A., Senden, T.J., Sheppard, A.P., Sok, R.M., Pinczewski,W.V., Kelly, J.C. and Knackstedt, M.A.: 2005, Digital core Laboratory: Petrophysical analysis from 3D imaging of reservoir core fragments, *Petrophysics*, **46**, 260-277.

Asquith, G.B.: 1990, Log evaluation of shaly sandstones: a practical guide, *AAPG continuing education course note series #31*, 59P

Auzerais, F.M., Dunsmuir, J., Ferréol, B.B., Martys, N., Olson, J., Ramakrishnan, T.S., Rothman, D.H. and Schwartz, L.M.: 1996, Transport in sandstone: A study based on three dimensional microtomography, *Geophysical Research Letters,* **23,** 70E-708.

Brace, W.F.: 1977, Permeability from resistivity and pore shape, *J.Geophys.Res*, **82**, 3343-3349.

Carman, P.C.: 1938, The determination of the specific surface of powders, *J.Soc. Chem. Ind. Trans*, **57**, 225.

Brown, R. J. S.: 1980, Connection between formation factor for electrical resistivity and fluid-solid coupling factor in Biot's equations for acoustic waves in fluid-filled porous media, *Geophyics*, **45**,1269-1275.

Carman, P. C.: 1961, L'écoulement des gaz à travers les milieux poreus, Bibliothèque des Sciences et des Techniques nucléaires, P.U. F, 52.

Canny, J.: 1986, A computational approach to edge detection, *IEEE Trans. Pattern Analysis and Machine Intelligence*, **8**, 679-714.

Coles, M. E., Hazlett, R.D, Muegge, E.L. Jones, K.W., Andrews, B., Siddons, P., Peskin, A. and Soll, W.E.: 1996, Developments in synchrotron X-Ray microtomography with applications to flow in porous media, paper SPE 36531, *Proc. 1996 SPE Annual Technical Conference and Exhibition, Denver*, Oct 6-9.

Debye, P. and Hückel, E.: 1923, Zur theorie der electrolyte, *Phys. Z*, **24,** 18E-206.

Devarajan, S., Toumelin, E. and Torres-Verdín, C.: 2006, *SPWLA 47th Annual Logging Symposium*, June 4-7.

Finney, J.: 1968, Random packings and structure of the liquid state, *Ph.D. thesis, Univ. of London.*

Finney, J.: 1970, Random packings and the structure of the liquid state, *Proc. Roy. Soc,* **319A**, 479.

Garbozi, E.J.: 1998, Finite Element and Finite Difference Programs for Computing the Linear Electric and Elastic Properties of Digital Image of Random Materials, *NISTIR* **6269**.

Guéguen, Y. and Palciauskas, V.: 1997, Introduction to the physics of rocks, *Princeton University Press*.

Hazlett, R.D.: 1995, Simulation of capillary dominated displacements in microtomographic images of reservoir rocks, *Transport in Porous Media*, **20,** 21-35.

Johnson, D.L., Koplik, J. and Schwartz, L.M.: 1986, New pore-size parameter characterization transport in pours media, *Physical Review Letters*, 57, **n.20**, 2564-2567.

Johnson, D.L., Koplik, J. and Dashen, R.: 1987, Theory of dynamic permeability and tortuosity in fluid-saturated porous media, *Journal of Fluid Mechanics*, **176**, 379-402.

Kameda, A.: 2004, Permeability evolution in sandstone: digital rock approach, *Ph.D. thesis, Stanford University.*

Kameda, A., Dvorkin, J., Keehm, Y., Nur, A. and Bosl, W.: 2006, Permeability-porosity transforms from small sandstone fragments, *Geophyics*, **71**, N11-N19.

Kan, R. and Sen, P.N.: 1987, Electrolytic conduction in periodic arrays of insulators with charges, *J. Chem. Phys*, **86,** 5748-5756.

Katz, A. J. and Thompson, A. H.: 1986, Quantitative prediction of permeability in porous rock, *Physical Review B*, **34**, 8179-8181.

Kenyon, W. E.: 1992, Nuclear magnetic resonance imaging- technology for the 21st century, *Nuclear Geophysics*, **6**, 153-168.

Klinkenberg, R.L.: 1941, The permeability of porous media to liquids and gases, *Drill. Prod. Pract,* **8**, 200-213.

Knackstedt, M.A., Arns, C.H., Limaye, A., Sakellariou, A., Senden, T.J., Sheppard, A.P., Sok, R.M., Pinczewski, W.V. and Bunn, G.F.: 2004, Digital Core Laboratory: Properties of reservoir core derived from 3D images, SPE-87009; *presented at the 2004 Asia Pacific Conference on Integrated Modelling for Asset Management, Kuala Lumpur.*

Kozeny, J.: 1927, Ueber kapillare letiung des Wassers im Boden, *Wien. Akad. Wiss*, **136 (2a),** 271.

Li, S.X., Pengra, D.B. and Wong, P. Z.: 1995, Onsager's reciprocal relation and the hydraulic permeability of porous media, *Phys. Rev. E,* **59,** 2049-2059.

Lima, O.A.L. and Sharma, M.M.: 1990, A grain conductivity approach to shaly sandstones, *Geophysics*, **55**, n.10, 1347-1356.

Mavko, G and Nur, A.:1997, The effect of a percolation threshold in the Kozeny-Carman relation, *Geophysics*, **62**, 1480-1482.

Morgan, F.D., Williams, E.R. and Madden, T.R.: 1989, Streaming potential properties of westerly granite with applications, *Journal of Geophysical Research,* **94,** 12449-12461.

Minnis, M.M.: 1984, An automatic point-counting method for mineralogical assessment, *The American Association of Petroleum Geologists Bulletin*, **68,** P744-752.

Neasham, J.W.: 1977, The morphology of dispersed clay in sandstone reservoirs and its effect on sandstone shaliness, pore space and fluid flow properties, *SPE paper,* **6858**.

Nelson, P.H.: 2000, Evolution of permeability-porosity trends in sandstones: *Society of Professional Well Log Analysts 41st Annual Logging Symposium*, June 4-7.

Pal, E.R., Stig, B.: 2002, Process based reconstruction of sandstones and prediction of transport properties, *Transport in Porous Media*, **46,** 311-343.

Patchett, J.G.: 1975, An investigation of shale conductivity, *SPWLA*, *16th Annual Logging Symposium*, Paper **U,** 40pp.

Paterson, M.S.: 1983, The Equivalent Channel Model for Permeability and Resistivity in Fluid Saturated Rock-a Re-appraisal, *Mechanics of Materials*, **2**, 34E-351.

Pathegama, M. and Göl, Ö.: 2004, Edge-based image segmentation, *Proceedings of the International Conference on Computational Intelligence,* ISBN **97E-98458-0-6**.

Pike, J.D.: 1981, Feldspar diagenesis in Yowlumne sandstone, Kem County, California: *M.S. thesis, Texas A&M University, College Station, TX*

Pride, S. R. and Morgan, R. D.: 1991, Electrokinetic dissipation induced by seismic waves, *Geophysics*, **56**, 914-925.

Press, W.H., Flannery, B.P., Teukolsky, S.A. and Vetterling, W.T.: 1990, Numerical Recipes, *Cambridge University Press, Cambridge.*

Revil, A. and Glover P. W. J.: 1997, Theory of ionic-surface electrical conduction in porous media, *Phys. Rev. B,* **55,** 1757-1773.

Revil, A. and Glover P. W. J.: 1998, Nature of surface electrical conductivity in natural sands, sandstone, and clays, *Geophysical Research Letters,* **25,** 691-694.

Revil, A., Cathles III, L.M., Losh, S. and Nunn, J.A.: 1998, Electrical conductivity in shaly sands with geophysical applications, *Journal of Geophysical Research*, **103**, n. B10, 2392E-23936.

Revil, A. and Leroy, P.: 2001, Hydroelectric coupling in a clayey material, *Geophysical Research Letters,* **28,** 1643-1646.

Roberts, J. and Schwartz, L.: 1985, Grain consolidation and electrical conductivity in porous media, *Phys. Rev. B*, **31**, 5990.

Schwartz, L. M. and Banavar, J.: 1989, Transport properties of disordered continuum systems, *Phys. Rev. B*, **39**, 11965.

Schwartz, L. M., Martys, N., Bentz, D. P., Garboczi, E.J. and Torquato, S.: 1993, Cross-property relations and permeability estimation in model porous media, *Physical Review B*, **48**, 4584-4591.

Sen, P.N., Scala, C. and Cohen, M.H.: 1981, A self-similar model for sedimentary rocks with application to the dielectric constant of fused glass beads, *Geophysics*, **46**, 781-795.

Sen, P.N. and Kan, R.: 1987, Electrolytic conduction in porous media with charges, *Phys. Rev. Lett*, **58**, 778-780.

Bryant, S.L., Mellor D.W. and Cade, C.A.: 1993, Physically representative network models of transport in porous media, *AIChE Journal*, **39**, 387-396.

Wu, T.: 2004, Permeability prediction and drainage capillary pressure simulation in sandstone reservoirs, *Ph.D. thesis, Texas A&M University.*

Toumelin, E. and Torres-Verdín, C.: 2008, Objected-oriented approach for the pore-scale simulation of DC electrical conductivity of two-phase saturated porous media, *Geophysics*, **73**, E67-E79.

Walsh, J. B. and Brace, W. F.: 1984, The effect of pressure on porosity and transport properties of rock, *J.Geophy. Res,* **89**, 942E-9431.

Waxman, M. H. and Smits, L.J.M.: 1968, Electrical conduction in oil-bearing sands, *Society of Petroleum Engineers Journal*, **8**, 107-122.

Wong, P. Z., Koplik, J. and Tomanic, J. P.: 1984, Conductivity and permeability of rocks, *Physical Review B*, **30**, 6606-6614.

Wyllie, M.R.J. and Gregory, A.R.: 1955, Fluid flow through unconsolidated porous aggregates. Effect of porosity and particle shape on Kozeny-Carman constants, *Ind. Eng. Chem*, **47**, 1379.

Zahn, C. T.: 1971, Graph-Theoretic Methods for Detecting and Describing Gestalt Clusters, *IEEE Trans. Computers*, **20**, 68–86.

Zahn, C. T. and Roskies, P. Z.: 1972, Fourier descriptions for plane closed curve, *IEEE Trans.*, **Vol C 21**, 269-281.

Zhan, X.: 2005, A study of seismoelectric signals in measurement while drilling, *M.S. thesis, Massachusetts Institute of Technology.*

Zhang, W. M. and Wang, S. A.: 2005, An efficient connectivity-number-based edge detection method for binary images, *Proceedings of the Fourth International Conference on Machine Learning and Cybernetics*, 18-21.

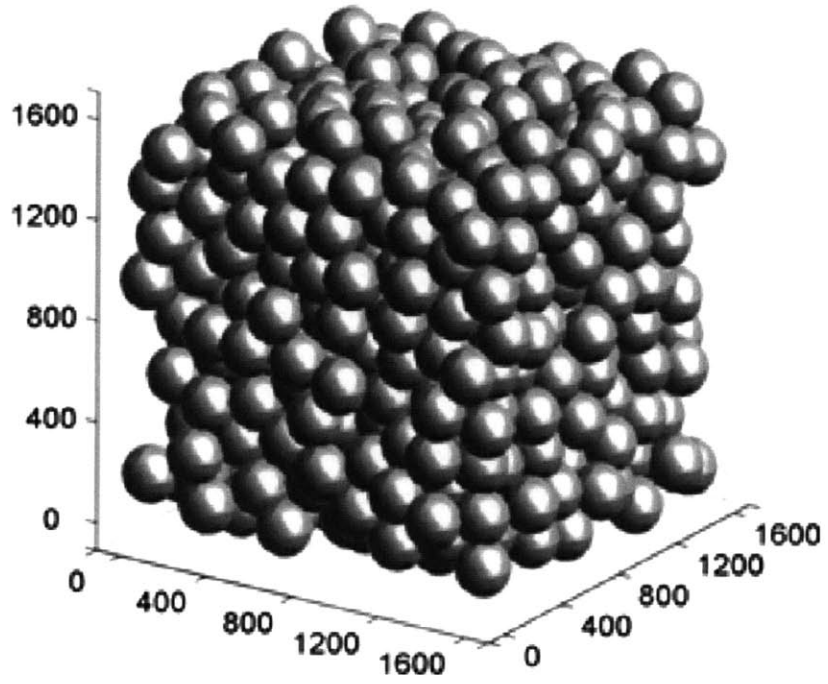

Figure 2-1: An example of a 1000-grain cubic subset from the *20% porosity* Finney pack with grain diameter to be 200 (dimensionless) (Toumelin and Torres-Verdín, 2008, Fig 1.a).

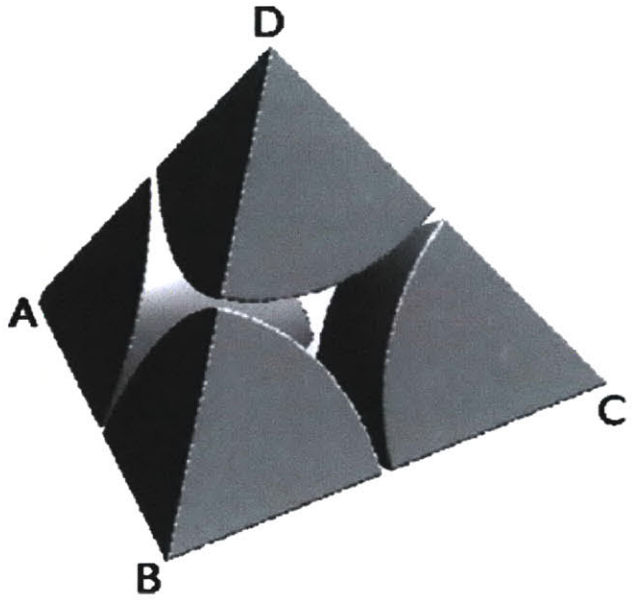

(a)

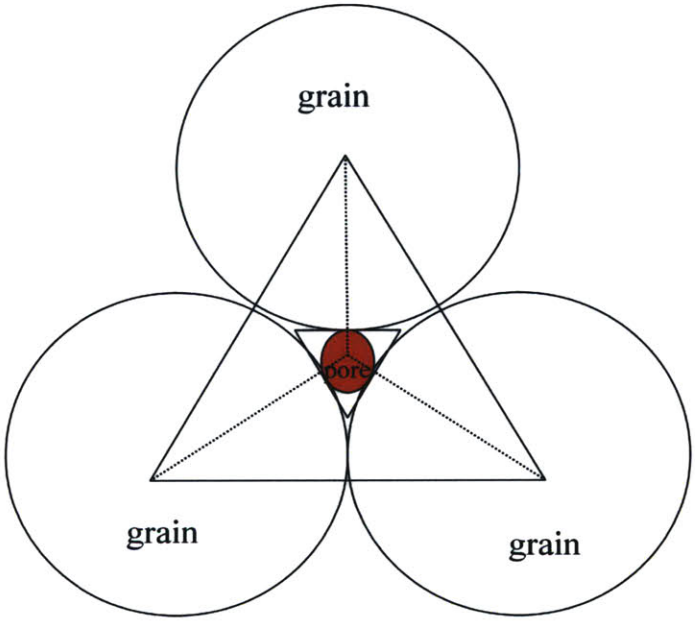

(b)

Figure 2-2: (a) 3D view of one pore bounded by four grains. (b) Pore section through A-C plane. The grain and pore space is well defined by the sphere center and grain radii.

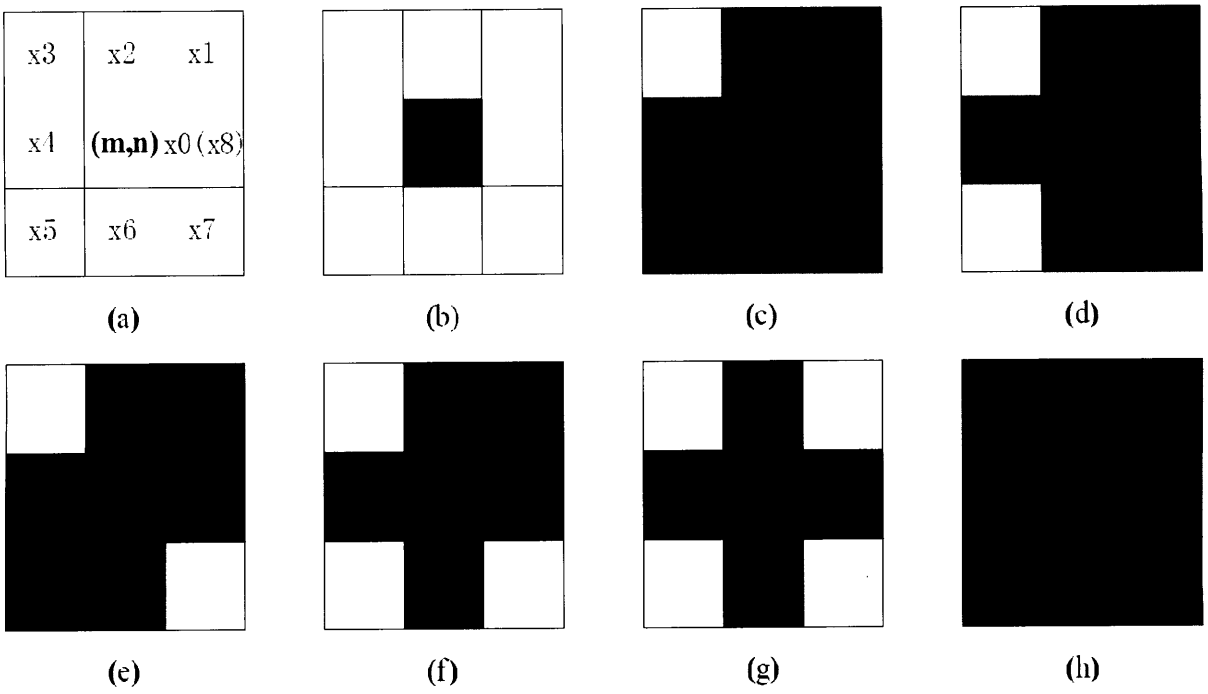

Figure 2-3: typical zero-CN 8-neighbors. Central pixel (m,n) and 8 neighbors 3D is shown in (a). The black pixel in the center is defined as an inner or isolated pixel in case of (b), (c), (d), (e), (f), and (g), (h).

Image No. in Fig. 2-3	Different Neighbor Combination Forms			
b	1111 1111			
c	1000 0000	0010 0000	0000 0100	0000 0001
d	1010 0000	0010 0001	00000101	1000 0100
e	1000 0001	0010 0100		
f	1010 0001	1010 0100	1000 0101	0010 0101
g	1010 0101			
h	0000 0000			

Table 2-1: Combinations of zero-CN 8-neighbors corresponding to (b), (c), (d), (e), (f), (g), (h) in Fig. 2-3. The black central pixel in (a) of Fig. 2-3 is defined to be phase *0*.

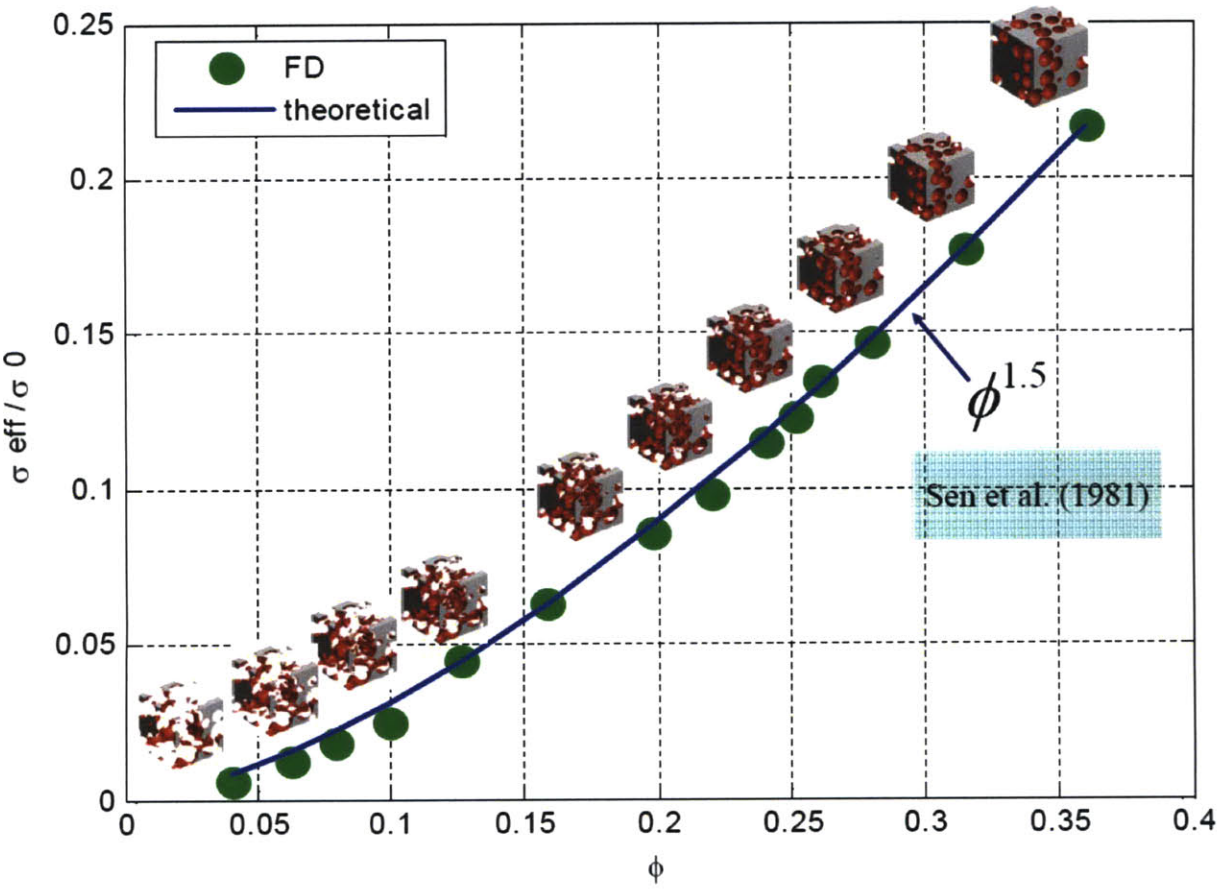

Figure 2-4: The inverse of formation factor as a function of porosity for 14 granular packings with porosities ranging from *4.02%* to *36.2%*. Green dots are the numerical results by solving Laplace equation using FD scheme. Blue curve is the analytic rock physics model (Sen et al., 1981). The 3D pore structures of the Finney pack are also illustrated in the figure (pore cast is shown in red). 36.2% porosity is when the spheres are just in contact with each other.

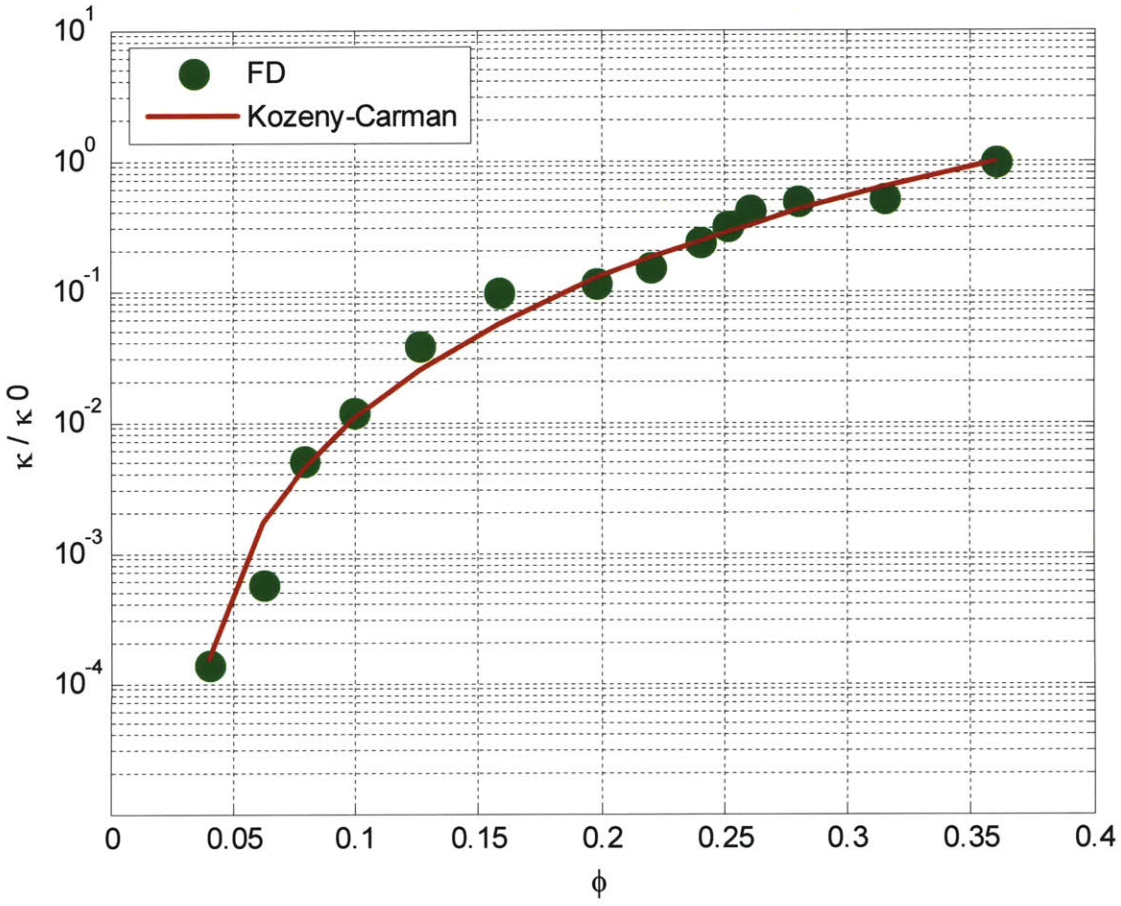

Figure 2-5: Normalized permeability (κ/κ_0) as a function of porosity for 14 granular systems with porosities ranging from 4.02% to 36.2%. $\kappa_0$stands for the permeability of the original 36.2% porosity Finney pack. Green dots are the numerical results by solving Stokes equation using FD scheme. Red curve is Kozeny-Carman relationship (Eq. 2-8). At 36.2% porosity, $\kappa_0 = 6.85e^{-5} \cdot d^2$, where d is the grain diameter.

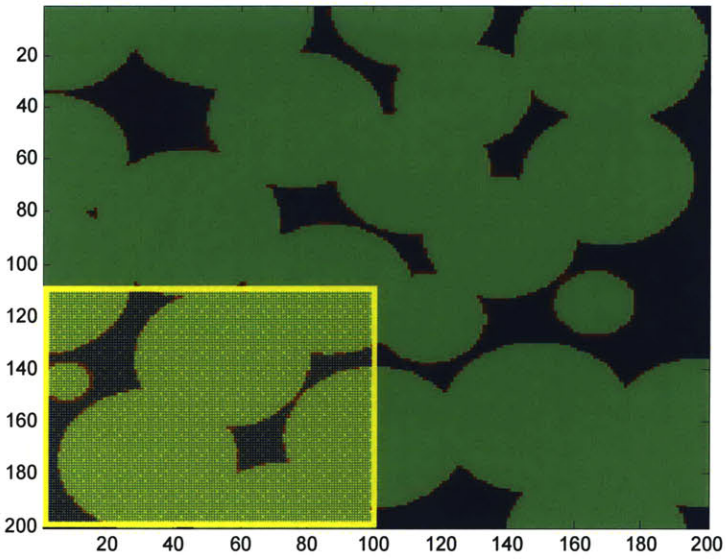

(a)

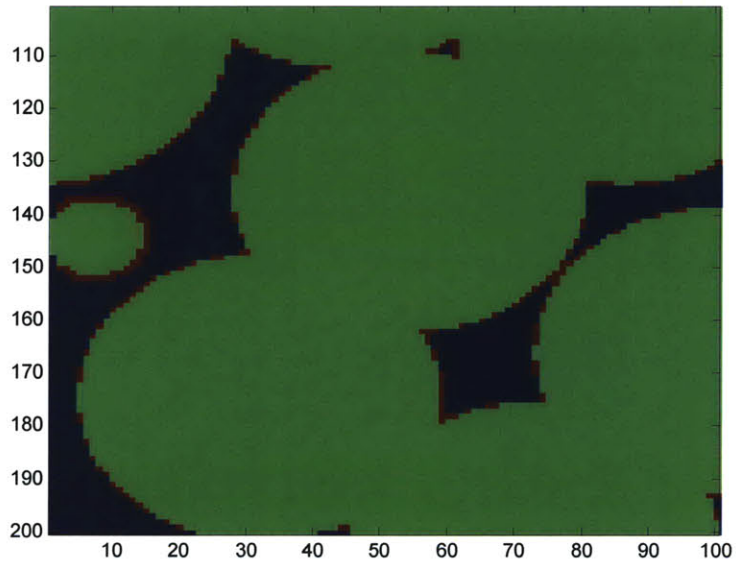

(b)

Figure 2-6: (a) Surface pixels (red) are shown along the pore (blue) – grain (green) boundary. Here gradient based image processing was used on the *19.80%* porosity Finney pack. (b) Enlarged view of shadowed area (yellow square) in (a).

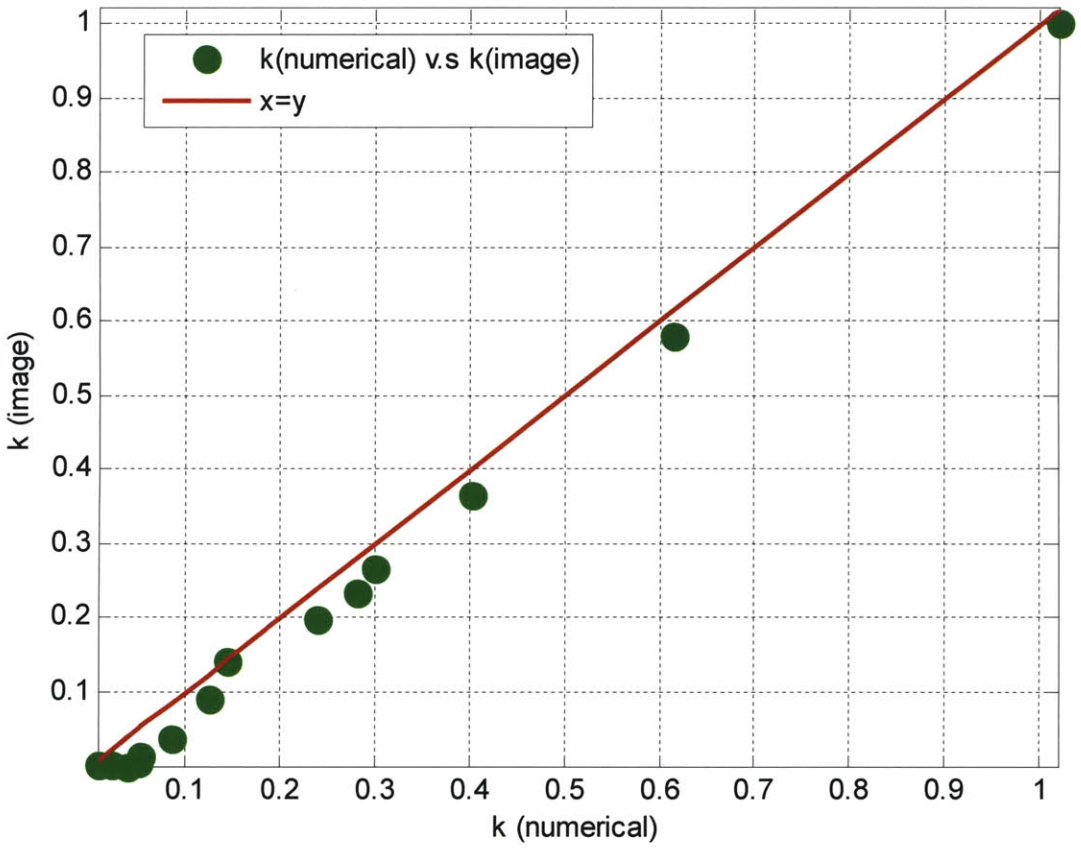

Figure 2-7: Cross-plot of numerically calculated permeability, $k_{numerical,}$ from Stokes equation *vs.* the permeability, k_{image}, calculated from Paterson-Walsh-Brace relationship (Eq. 2-10).

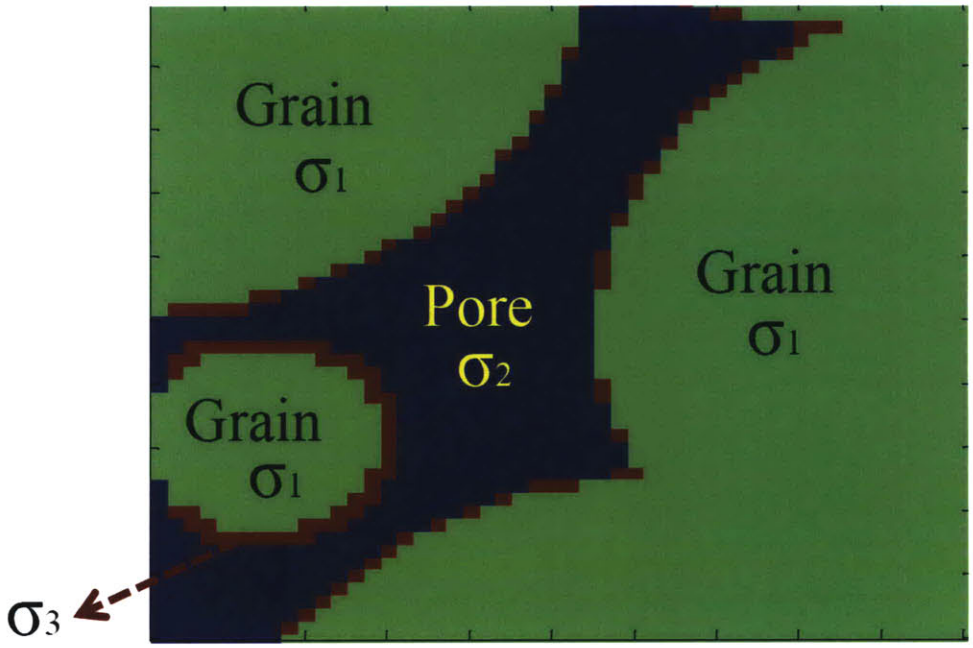

Figure 2-8: Three-phase representation of the porous rock. σ_1 is solid grain (shown in green) conductivity, σ_2 is the free electrolyte (shown in blue) conductivity in the pore space. σ_3 is the conductivity for the surface grid at grain-fluid interface (shown in red), which contains both free electrolyte and bound water.

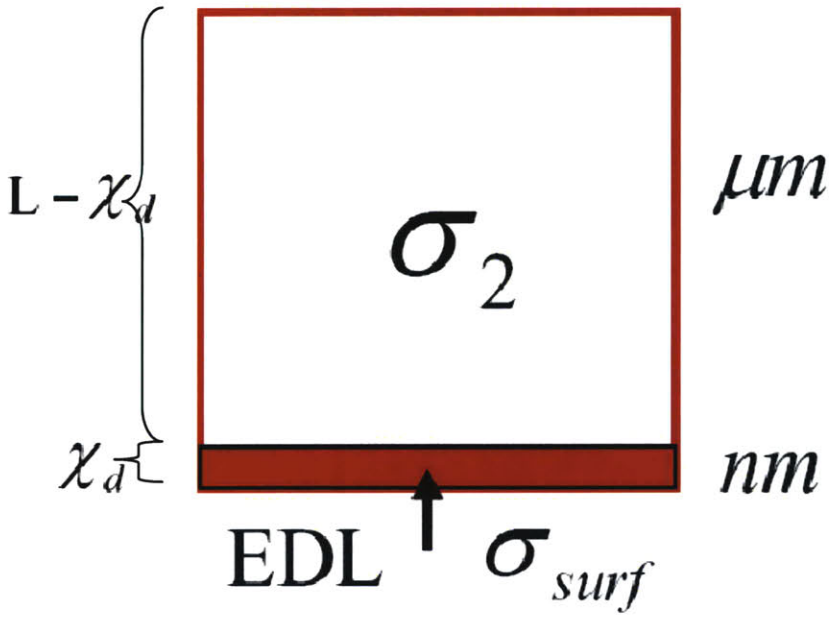

Figure 2-9: Conductivity model for the surface grids at grain-electrolyte interface (σ_3 in Fig. 2-9). Gird size is L and grid conductivity is σ_3. An electric double layer (EDL) with length χ_d at nanometer scale is included in the grid with surface conductivity, σ_{surf}. The remainder of the grid $(L - \chi_d)$ has conductivity of σ_2, which is the free electrolyte conductivity in the pore space.

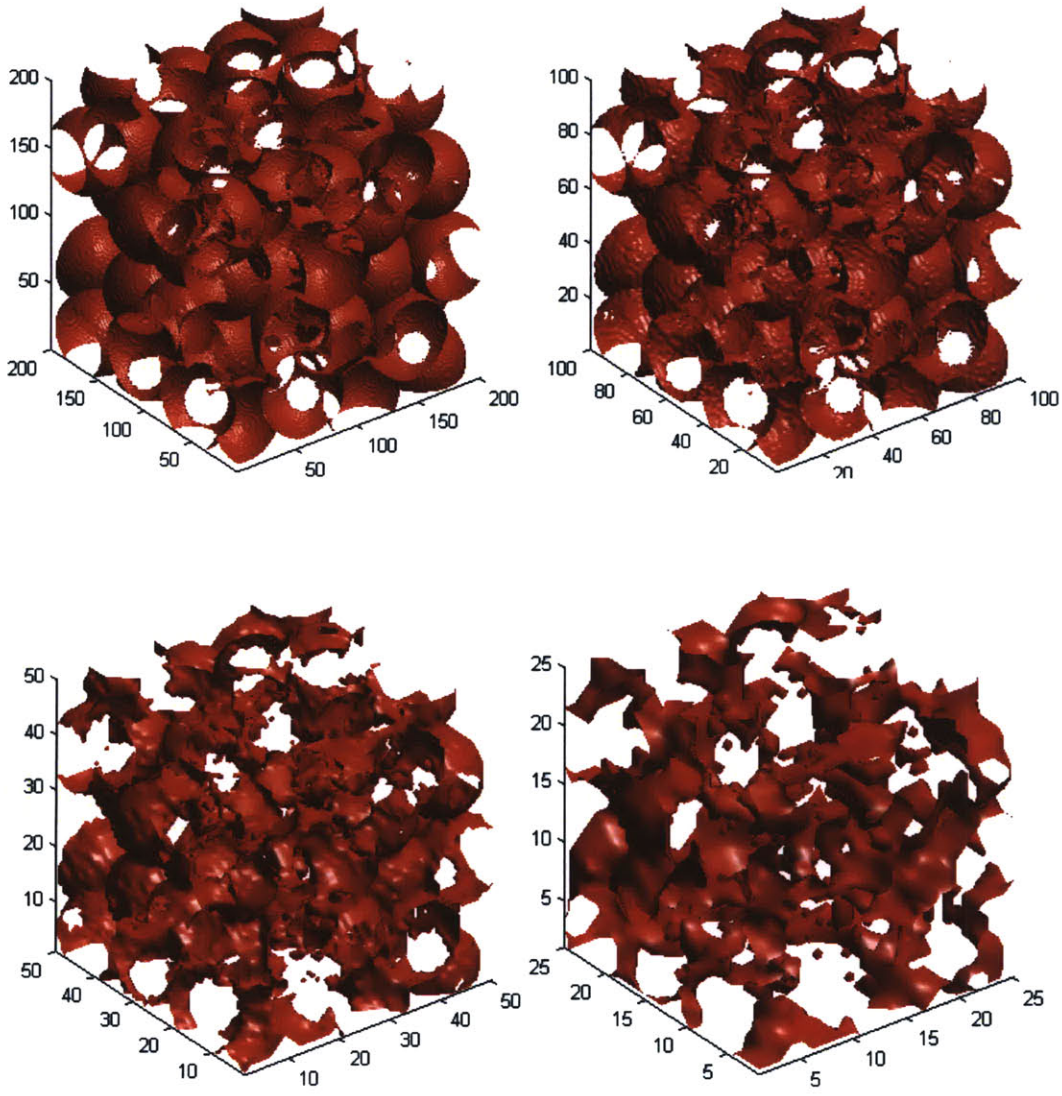

Figure 2-10: 3-D pore structure of the downscaled 200^3, 100^3, 50^3 ,25^3 cubes of *19.8%* porosity Finney pack from original 400^3 cube. As the resolution decreases, the connectivity of the pore space significantly reduced.

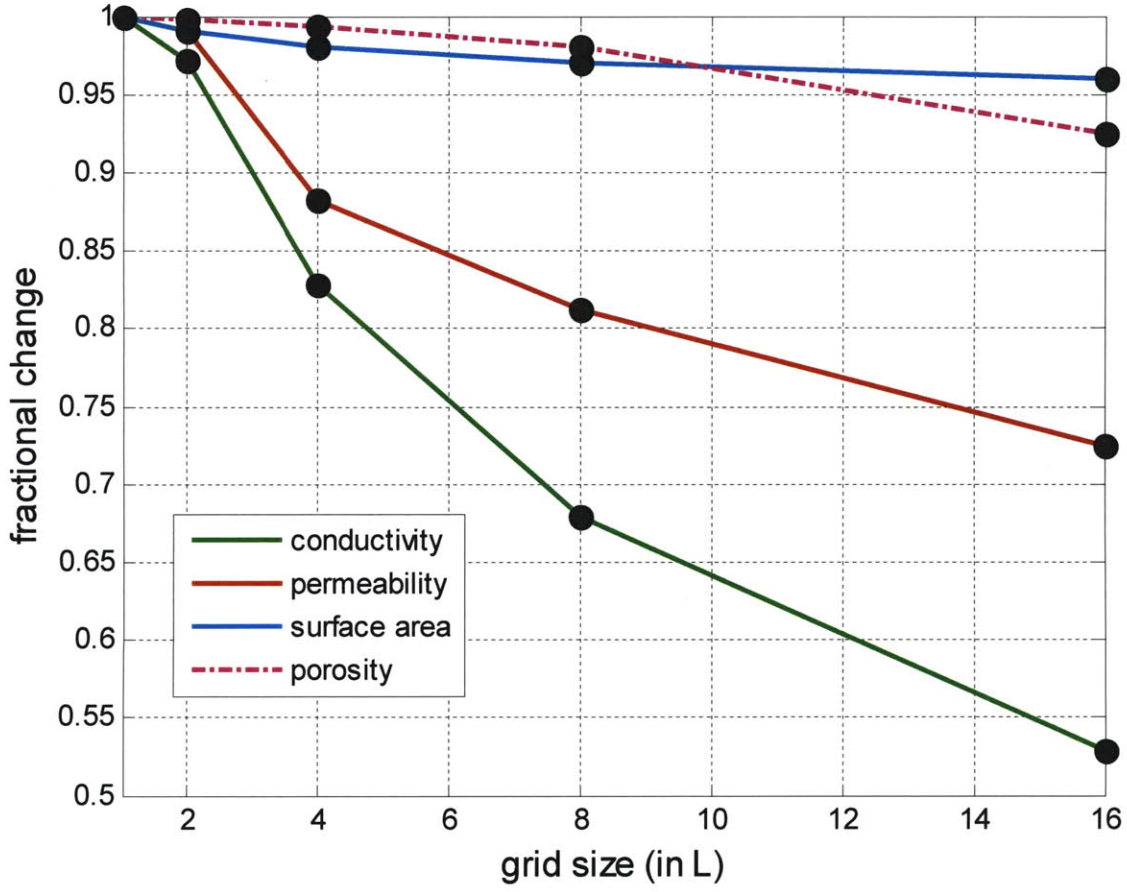

Figure 2-11: Fractional change in numerically computed porosity, electrical conductivity, permeability and surface area from 400^3 cube with grid size of L to 25^3 cubes with grid size of $16L$. The fractional changes in all quantities are with respect to their values for 400^3 cube with grid size of L.

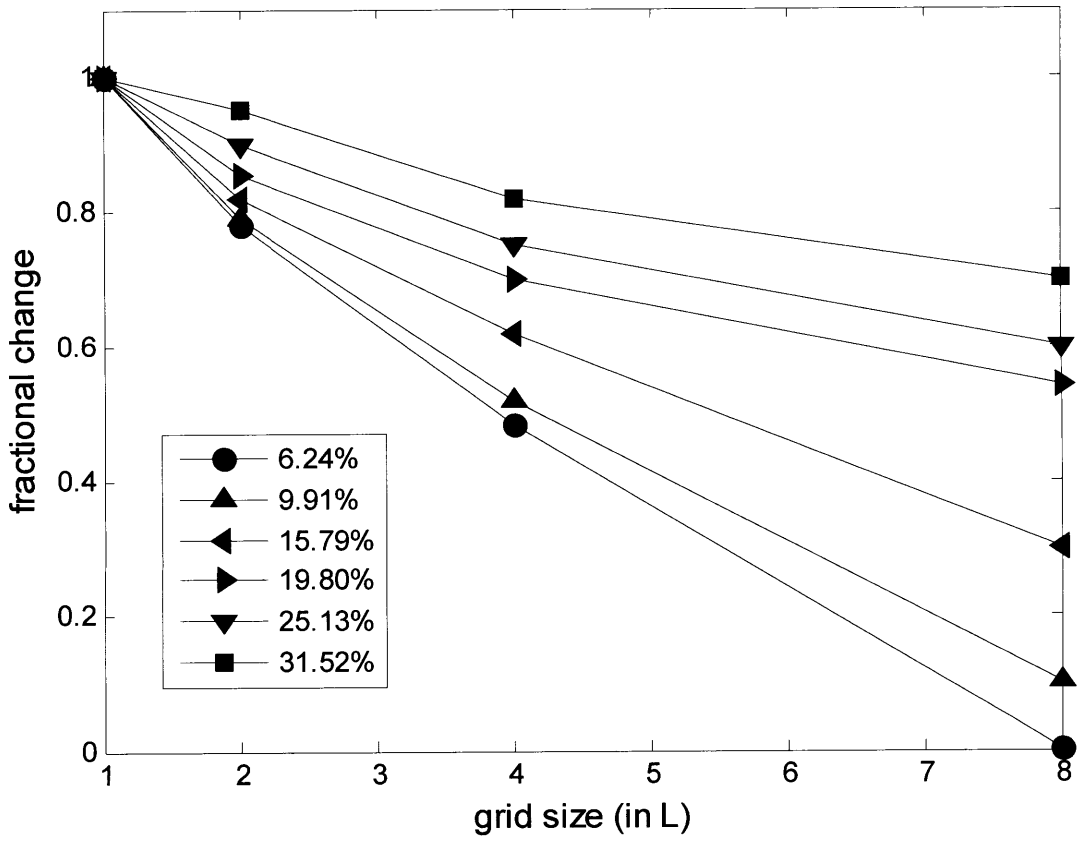

Figure 2-12: Fractional changes in numerically computed electrical conductivity from 200^3 cube with grid size L to 25^3 cube with grid size $8L$. The fractional changes in all quantities are with respect to their values for 200^3 cube with grid size of L.

Chapter 3

Pore Scale Modeling of Electrical and Fluid Transport in Berea Sandstone[2]

Abstract

The purpose of this chapter is to test how well the numerical calculations can predict transport properties of porous permeable rock, given its 3-D digital microtomography (μCT) image. For this study, we use a Berea 500 sandstone sample, whose μCT images have been obtained with 2.8μm resolution. The porosity, electrical conductivity, permeability, surface area is calculated from the μCT image and compare with laboratory measured values. For transport properties (electrical conductivity, permeability), a finite difference scheme is adopted. The calculated and measured properties compare quite well. Electrical transport in Berea 500 is complicated by the presence of surface conduction in the electric double layer at

[2] (the bulk of this Chapter has been) accepted as: Zhan X., L. M. Schwartz, M. N. Toksöz., W. C. Smith. and F. D. Morgan.: 2009, Pore scale modeling of rock properties and comparison to laboratory measurements, accepted by *Geophysics*.

grain-electrolyte boundary. A three phase conductivity model is proposed to compute surface conduction on the rock μCT image. We also investigate the effects of image resolution and computation sample size on the accuracy of numerical predictions. Reducing the resolution (i.e., increasing the voxel dimensions) decreases the calculated values of electrical conductivity and hydraulic permeability. Increasing the computation sample volume gives a better match between the laboratory measurements and numerical results. Large sample provides a better representation of the rock.

3.1 Introduction

Understanding the interaction between rock matrix and pore fluids at the microscopic scale is essential for the interpretation of macroscopic geophysical measurements. With the development of modern imaging techniques, such as X-ray CT and laser confocal microscopy, direct images, with micron resolution, of the 3-D pore structure of sedimentary rocks are now available. Accurate digital representations of the pore structure allow us to compute rock properties from basic physical laws (Hazlett, 1995; Coles et al., 1996; Pal et al., 2002). Computational rock physics has become a significant complement to core-derived laboratory measurements and empirical relationships in the interpretation of borehole measurements.

In this study, we use finite difference (FD) techniques to solve the Laplace equation for electrical conductivity and the Stokes equation for single phase fluid flow (Roberts and Garboczi, 2000). A number of authors have used μCT images to calculate the electrical formation factors of by treating the fluid filled porous rock as a two phase system (Auzerais

al., 1996; Arns et al., 2001, 2005; Pal et al., 2002). The solid matrix is non-conductive and the pore fluid has a uniform conductivity. In this case, Archie's law (Archie, 1942) describes the linear relationship between the fluid conductivity, σ_f, and saturated rock conductivity, σ_{eff}. In its simplest form, this is:

$$F = \frac{\sigma_f}{\sigma_{eff}} = \phi^{-m}. \tag{3-1}$$

Here F is known as the formation factor, Φ is the porosity and m is the cementation exponent which depends on lithology. This relationship is based on the assumption that the mobile ions are uniformly distributed throughout the pore space. Once the basic quantities of electrical and fluid flow are in hand, we go on to consider two issues related to the pore grain interface (i.e. the grain surface). While F depends only on the porosity, the fluid permeability, k, depends in addition on the absolute dimensions of the pore space. Two of the simplest length scales are the pore volume to surface area ratio, V_p/S and the Λ parameter, a dynamic length derived from the solution of the conductivity problem (Johnson et al., 1986). We show that both V_p/S and Λ can be used to estimate k.

In addition to bulk conduction, there is also the mechanism of interface conduction. The surface of both quartz and clay grains becomes charged when in contact with an electrolyte. Surface conductivity is confined to a thin layer known as the electric double layer (EDL) (Debye and Hückel., 1923; Morgan et al., 1989). One of the most popular empirical models to treat surface conductivity is the Waxman-Smits model (Waxman and Smits, 1968). They assume that interfacial and bulk conduction can simply be added in parallel:

$$\sigma_{eff} = \frac{1}{F^*}(\sigma_f + BQ_v), \tag{3-2}$$

where F^* is the formation factor in the low resistivity limit, Q_v is the cation concentration per unit pore volume (meq ml^{-1}) and B is the average mobility of the counterions close to the grain surface (mho cm^2 meq^{-1}). The value of B can be adjusted to capture the nonlinear (convex-upward) behavior of σ_{eff} vs. σ_f for shaly sands.

Recent authors have devoted considerable attention to treating surface conduction at the pore scale (Devarajan, 2006; Jin et al., 2007; Motealleh, 2007). In these work shaly sands are modeled with surface-conductive clay coating the grains. To represent shale the grains are assumed to be comprised entirely of conductive clays. However, all these calculations are based on synthetic porous media, sphere packs with a single type of clay mineral. Real rocks are known to have much more complex composition, mineral distribution and pore geometry. Thus, one of the main objectives of this work is to numerically model surface conductivity on real rock microstructure. In addition, laboratory data are collected to verify our numerical calculations.

3.2 Sample Description and Laboratory Measurements

3.2.1 BS500 Core Sample and μCT Image

Our studied sample is a Berea Sandstone 500 (BS500) core with 23.6% porosity. A 3-D microtomography image is obtained from the Australia National University (ANU) Digital Core Lab Consortium. This sample contains some clay. The gray-scale image with brightness corresponding to X-ray attenuation is binarized by ANU to give clear distinction of pore space and rock matrix using anisotropic diffusion filtering. Intensity histogram of the core sample is shown in Fig. 3-1 (provided by ANU). The two peaks in Fig. 3-1 correspond to void and grain in the microstructure. Normally, a clear binary image separating pore from mineral phase is expected. The presence of low-density pore inclusions (e.g., microporosity, clay, feldspars decaying into grains, etc.) leads to the spread in the low density signal (intermediate portion of the histogram between the two peaks) (Knackstedt et al., 2005; Arns et al., 2005). This core sample is digitized into 1840^3 voxel tomogram with 2.8 micron resolution.

BS500 contains some clay; its mineralogy is listed in Tab. 3-1 using FTIR (Fourier Transform InfraRed Sepctroscopy). The image shown in Fig. 3-2 a is an example; the solid phase is divided into quartz (white) and non-quartz minerals (grey). Identification and classification of clay types using petrographic analysis are generally impossible due to the small clay particle size (Minnis, 1984; Knackstedt et al., 2005). The current X-ray μCT imaging technique is capable of indentifing clay types for determining the volume content for clay minerals (Pike, 1981; Minnis, 1984; Arns, 2005). The ability to determine the spatial relationship of minerals and the size of small particles is still limited by the image resolution

and image processing techniques, such as accurate boundary detection between low-contrast regions. Accordingly, we have chosen to work with the segmented image which represents well the porosity of the interconnected pore volume and contains negligible intra-granular porosity (Nelson, 2000; Wu, 2004). This is a reasonable and reliable starting point for determining transport properties.

3.2.2 Laboratory Measurements

Laboratory measurements are made on a cylindrical BS500 core sample of length ~3.7cm and diameter ~2.5cm. The formation factor was obtained using a NaCl brine with conductivity $0.2S/m$ at 25°C. Two permeability measurements were carried out. Gas permeability is measured using Nitrogen (N_2); the result, 858 mD, can be converted to liquid permeability using the Klinkenberg correction (Klinkenberg, 1941; Tanikawa and Shimamoto, 2006), which is 430mD. Direct liquid permeability is also measured using NaCl brine with $0.2S/m$ conductivity at 25 °C by the steady state flow method in the pressure range of $0.05atm$ ~ $0.2atm$, and it is close to 450mD. A rubber jacket is used to prevent flow around outside of the cylindrical plug. The BET (Brunauer, Emmett and Teller, 1938) surface area measurement is based on the volume of Krypton (Kr) gas adsorbed at a sequence of pressure points (relative pressure range (P/P_0) is between 0.06 ~ 0.19). All the laboratory measurement results are compared with numerical calculations in the next section.

A special purpose laboratory procedure is designed to measure the electrical conductivity, σ_{eff}, on saturated BS500 core sample. A particular concern when saturating

with highly resistive electrolytes is chemical changes in the sample, such as clay swelling and liberation (Waxman and Smits, 1968; Sen et al., 1981; Sen and Kan. 1987). To avoid this problem, we used one freshly cut samples for each salinity. Samples are cut into cylinders of *~2cm* length and *~2.5cm* in diameter from the same BS500 block. Ten samples are saturated with NaCl brines of conductivity 0.001*S/m*, 0.005*S/m*, 0.01*S/m*, 0.025*S/m*, 0.05*S/m*, 0.1*S/m*, 0.2*S/m*, 0.4*S/m*, 1*S/m* and 2*S/m*, respectively. Each sample is first vacuumed for a couple of hours to expel air and then to be vacuumed-impregnated with brines in order to be fully saturated. Saturated samples are held by a rubber jacket to prevent it from falling apart and never allowed to dry out during the conductivity measurements, in a manner similar to the permeability measurement. Non-polarized *Ag/AgCl* electrode disks (Perrier et al., 1997; Petiau, 2000; Minsley, 2007) are made using electroplating of silver mesh following the procedure described by Minsley (2007, Appendix C of Minsely, 2007). The silver mesh is soaked in a *NaCl* solution of 1M to be electroplated. The current needed is estimated to be 1 Coulomb per square cm of silver mesh. After a stable *AgCl* coating is formed on the surface on the silver mesh. The mesh is rinsed in de-ionized (DI) water and set aside to dry. Measured electrical conductivities of saturated BS500 are compared with numerical modeling results in next section.

3.3 Numerical Results and Comparison to Laboratory Measurements

The same numerical methods will be applied to the 3-D microtomography of BS500 as described in Chapter 2. Finite difference Laplace solver (Chapter 2.2.1, Appendix A) and Stokes solver (Chapter 2.2.2, Appendix B) will be used to compute formation factor and permeability. The two edge detection methods (Chapter 2.2.3) will be used to calculate specific surface area.

3.3.1 Porosity, Formation Factor, Permeability and Surface Area

Five 400^3 sub-volumes at different locations are selected in the total 1840^3 volume as shown in Fig. 3-2 a. We choose the samples away from the edge in all three dimensions (where the rock fragment could be damaged during cutting, Fig. 3-3). Sub-volume 3 is in the middle of the sample (slice 920- slice 1319 in Z direction (axial direction of the core sample)). Sub-volumes 1, 2, 4 and 5 are located, respectively, northwest, northeast, southwest and southeast of sub-volume 3 to capture both vertical and horizontal heterogenerity. The choice of representative sub-cube is first based on the porosity. Variation in porosity for five 400^3 sub-fragments is within 3% and the porosity difference between each 400^3 sub-cube and the full core is also within 3%. As we go to smaller size, the porosity variation among sub-cubes and the porosity difference from the full core is getting larger (Fig. 3-4). Thus, we will start our computation from the 400^3 sub-cubes. The hydraulic flux (u in Eq. 2-5, with unit of m/s) and electrical current density (J in in Eq. 2-2, with unit of A/m^2) for one slice in sub-volume 3

are color mapped (on a logarithmic scale) in Fig. 3-5. For display purposes, we chose a 200^3 sub-volume in the middle of 3 (Fig. 3-5.a); the most complex pore geometry was found to be in the X-Y plane (Fig. 3-5.b). The electrical current shows higher amplitude than the hydraulic flux in the thin and narrow pores (Fig. 3-5.c and Fig. 3-5.d).

We could compute the effective conductivity of BS500 sample with different saturation phases, such as gas, oil and brines with different salinity based on our modified Laplace solver. For the saturation phase, we use the realistic conductivity value for different fluids instead of *1* as a normalized conductivity, which is the case in previous studies. The grains could be given the quartz conductivity of $10^{-14}\,S/m$ instead of *0.* To compute the formation factor, we could use either *0* v.s *1* or more physically, use highly conductive brine $10^{-1}\,S/m$ v.s $10^{-14}\,S/m$system. The saturated rock conductivities, σ_{eff}, with different saturation phases are listed in Tab. 3-2. Similar to Fig. 3-5.c, Fig. 3-6.a and Fig. 3-6.b correspond to the electrical current density with oil and gas saturation, respectively. With an increase of the conductivity contrast between the saturating fluid and the solid grain phase, the boundary between the pore space and grain becomes sharper. It is obvious that larger contrasts can better resolve the details of the structure. The example of picked surface pixels at grain-void interface is shown in Fig. 3-7.

Porosity, formation factor, permeability and surface area of the five sub-volumes computed from the 3D tomography are listed in Tab. 3-3. The total variation in porosity is about 3% for five 400^3 sub-fragments, which indicates our calculation size is representative. Heterogeneity of the geometry at different locations of the core sample is reflected in both

formation factor and permeability. An isolated inclusion, small in volume, could block the flow without much impact on the porosity (Kameda, 2004). Distribution of the conducting fluid phase also affects electrical conductivity.

We calculate the mean value and variance for those five sets of data and compare these with the laboratory measurements in Tab. 3-4. The calculated mean value compare well with the laboratory measurements. The experimental data is provided with a range to account for the experimental errors. Some experiments are repeated a few times on different BS500 core plugs, such as porosity, formation factor and surface area experiment. Berea sandstone is generally accepted to be homogenous enough that the experiments are repeatable from plug to plug. The slight difference in composition and size among plugs can lead to the small fluctuation in the measured values. As can be observed from Tab. 3-4, the match between experimental and numerical is best for porosity. Our numerical calculations and the low pressure BET measurements both provide the surface area of the sandstone skeleton. The surface area is usually expressed as square meters of surface per gram of solid. By multiplying the grain density (2.65 g/cm^3), we could transfer the numerically solved surface area from square meter per cube meter of solid to per gram of solid as expressed in the laboratory measurements. Numerical result of formation factor is higher than the experimental value. This is very like to be due to the unresolved pores (e.g., micropores and thin pore throat) below image resolution. The calculated permeability is higher than the experimental value. In general, coarse gridding or poor resolution leads to an over-estimation of the hydraulic flux within the grid. This is a numerical artifact observed by both finite difference and Lattice

Boltzmann (Kameda, 2004) simulation for fluid flow. Without distortion of the structure, the hydraulic permeability computed from the discredited image could be higher than the one obtained from continuum object. When the digitized image is downscaled, the distortion of the structure (e.g., loose of the thin features and connectivities in 3D) could take effect. Overall speaking, the calculated property values compare well with the laboratory measurements.

3.3.2 Formation Factor – Permeability Correlation and Λ parameter

Correlating hydraulic permeability to other physical properties of the porous media is a long standing and important subject. The most popular correlation relates permeability with electrical conductivity, based on the assumption that electrical and fluid stream lines are identical. On physical grounds we have to introduce a length scale because permeability has dimensions of area. Typically, the proposed correlations have the form (same as Eq. 2-10):

$$\kappa = \frac{CR^2}{F}, \tag{3-3}$$

where C is a dimensionless constant and R is a length related to the size of the connected pore pathways. The permeability estimated from formation factor F is denoted as κ_{est}. In the simplest approach, we can use $R = V_p/S$, the pore volume to surface ratio. In a related but generally better approximation, V_p/S is replaced by the Λ parameter (Johnson et al, 1986) in which the value of the local square magnitude of the electric field is used to weight the average over the pore volume and the pore–grain interface. Because we have a complete solution of the Laplace equation, we can calculate Λ; its value for each sub-volume is given in

Tab. 3-3. In Fig. 3-8, these two estimates for the permeability are compared to the results of our FD calculations. The agreement is good except for sub-volume 4. In this sub-volume we see that the formation factor is quite low while κ_{calc} is only slightly high and both V_p/S and Λ are large. This indicates a system with a large number of narrow channels which promote electrical transport but have relatively little influence on fluid flow. Another way to see this is to notice that in Tab. 3-3, the sub-volumes with the largest (smallest) F values have the largest (smallest) surface area. Also, the characteristic pore size, Λ, is larger than the 2.8 μm image resolution for all five sub-volumes. Thus, a reasonable prediction of the transport properties is expected with our current image resolution for BS500 core sample.

3.3.3 Surface Conductivity

Our aim is to calculate surface conduction based on the realistic pore and grain shapes defined by the BS500 μCT image. By contrast, in previous studies the solid grains were modeled as spheres (Johnson et al., 1986; Lima and Sharma, 1990; Devarajan, 2006; Motealleh, 2007; Toumelin, 2008). Given the sparse distribution of non-quartz minerals in BS500 (grey in Fig. 3-2 a), the dominant mechanism for surface conduction is the electric double layer (EDL) lying along the entire grain-electrolyte interface.

As before, our calculations are carried out on cells with edge length 2.8 microns. The pore fluid is divided into free water and bound water which exists along all the grain-electrolyte boundary. Thus surface voxels form a third phase in our conductivity calculations as illustrated in Fig. 3-9 a. In this model the first kind of cell has $\sigma_1 = 0.$ for the

insulating rock matrix, the second kind of cell has conductivity σ_2 corresponding to the bulk electrolyte and the third kind of cell, containing the EDL and located at the fluid-solid interface, has conductivity σ_3. Based on the thin EDL assumption, the two conduction paths in the interface cells can be treated, to first order, as conductors in parallel (Fig. 3-9 b). The surface conductance, Σ_{surf}, in the EDL and the bulk conductance, Σ_{bulk} in the rest of the cell can be summed to give the conductance of surface voxel. And σ_3 is expressed as:

$$\sigma_3 = \frac{\Sigma_{surf} + \Sigma_{bulk}}{L} = \frac{\Sigma_{surf} + \sigma_2.(L - \chi_d)}{L}. \quad (3\text{-}4)$$

Here χ_d is the thickness of the EDL, L is the length of the cell edge and Σ_{surf} is surface conductance (with units of S) over the pore-grain interface (Schwartz et al., 1989).

To quantify surface conductance, we adopt a practical method which directly uses the CEC value of the rock sample (Kan and Sen, 1987; Sen et al., 1990; Revil et al., 1998):

$$\Sigma_{surf} = \frac{2}{3}\left[\frac{\phi}{1-\phi}\right]\beta_s Q_v \Lambda, \quad Q_v = \rho_m[(1-\phi)\phi]CEC. \quad (3\text{-}5)$$

Here, ρ_m is grain density, ϕ is the porosity and β_S is the surface mobility of the counterions, which is independent of electrolyte conductivity (at least above 10^{-3} mol L^{-1}) and clay mineralogy (Shubin et al., 1993; Revil et al., 1998; Mojid and Cho, 2008). The *CEC* indicates the maximum number of exchange counterions per unit mass of the rock. Q_V, which appears in Eq. E-2, is the cation concentration per unit pore volume. In this way, we transfer the Q_V value (in per unit pore volume) to Σ_{surf} (in per unit pore surface area) through Λ which is a weighted surface to volume ratio (O'Konski, 1961; Kan and Sen, 1987; Schwartz et al., 1989). This is compatible with our assumption that every surface voxel has the same effective conductivity. The Λ parameter also gives the proper geometrical factors that map conduction

in the EDL and the bulk effectively into two conductors in parallel (Kan and Sen, 1987). For sodium chloride electrolyte, the counterions in the electrolyte are Na^+ with a surface mobility, $\beta_S = 5.14 \times 10^{-9}\ m^2\ s^{-1}\ V^{-1}$ at 25°C (Patchett, 1975). We substitute the measured *CEC* value [*0.27 meg/100g*] and the computed Λvalue (listed in Tab. 3-4) into Eq. E-5 to calculate the surface conductance, Σ_{surf}.

The last parameter to be determined is the EDL thickness (the Debye length) (Morgan et al., 1989; Pride and Morgan, 1991; Zhan, 2009):

$$\chi_d = \sqrt{\varepsilon_f \kappa_B T / e^2 z^2 N} \quad . \tag{3-6}$$

Here ε_f is the fluid permittivity, κ_B is the Boltzman constant, T is the absolute temperature, e is the electric charge, z is the ionic valence of the solution, and N is the ion concentration defined as N = 6.022 x 10^{26} x molarity. The Debye lengths for different values of the brine conductivity were computed from Eq. E-6 and are listed in Tab. 3-5. Also given in Tab. 3-5 are the corresponding values of the surface conductivity, σ_3. These results comprise the input data for our three phase solutions of the Laplace equation within the μCT structure; we have calculated σ_{eff} for a wide range of salinities.

Laboratory measurements (triangles) and numerical calculations (dashed and solid red lines) are shown in Fig. 3-10. In the high salinity region, the two-phase model works well to predict the linear relationship between the saturated rock conductivity, σ_{eff} and the electrolyte conductivity,σ_f. In this regime the ratio σ_f/σ_{eff} is the formation factor. When the electrolyte conductivity is low and surface conductivity cannot be neglected, the three-phase model is needed to match the experimental data and the concave upward shape of

the σ_{eff} vs. σ_f curve. Also shown in Fig. 3-10 is a curve based on the Waxman Smits equation (solid green line). Here we have taken their parameters for B in Eq. E-2: $B = 0.046[1 - 0.6\exp(-\sigma_f/(0.013))]$, where σ_f is expressed in mho cm^{-1}. This choice leads to an over estimate of rock conductivity at low salinities. The form of B was chosen by Waxman and Smits to fit conductivity data at mostly medium to high salinities (above 0.2 *S/m*). The decrease of B with salinity described by their model is also controversial (Schwartz, 1989; Revil et al., 1998).

Besides using the practical models, in which *Qv* (or alternatively, *CEC*) is the key parameter, we have also examed the most basic electrochemical model adopted by Morgan (Morgan et al., 1989). The surface conductance Σ_{surf} is obtained by the multiplication of σ_f, and EDL thickness χ_d with a hyperbolic function of the normalized zeta potential (Overbeek, 1952; Morgan et al., 1989). With an estimated zeta potential as a function of σ_f, (Pride and Morgan, 1991; zeta potential expression is given in Appendix D), we obtain a constant Σ_{surf} value using Morgan's method at low salinities (less than 0.2S/m). This is consistent with the result from our calculations using Eq. E-5. The basic mechanisms of surface conduction, especially in the low salinity regime, remain the subject of active research. Our approach is based on: (1) the measured CEC value, (2) the Λ parameter obtained by resolving the electric field in the microstructure, (3) a constant value for the surface mobility, β_S and (4) an interface conduction path along the entire grain-electrolyte boundary.

3.4 Impact of Image Resolution

The fact that we are using finite size voxels limits our ability to resolve the smallest features of the pore space. To test the importance of this effect we have generated a sequence of models with successively poorer resolution by doubling the voxel edge length. Eight high resolution voxels form one low resolution voxel with a simple majority rule used to assign the new voxel to be either pore or grain. If more than 4 of the original voxels were in the pore (grain) space, the new voxel is assigned to be pore (grain); if the breakdown of the original voxels is 4 grain and 4 pore, then the new voxel is assigned randomly. [Note that this is slightly different than the procedure used by Jin (Jin et al., 2009); they assign the 4-4 case to the grain space which leads to decreasing porosity as the resolution is degraded.] The five models then vary from the original 400^3 with 2.8 μm resolution to 25^3 with 44.8 μm resolution. Four downscaled cubes from the original 400^3 cube (sub-set #3 in Fig. 3-2 a) are shown in Fig. 3-11. The connectivity of pore space is largely reduced with decreasing resolution. The structure of the medium is severely compromised in the model with cell size 44.8 μm.

Porosity, permeability, formation factor and surface area were calculated for the five models; their fractional change relative to the original 400^3 with 2.8 μm resolution is plotted in Fig. 3-12. We note that the purely geometric parameters (porosity and surface area) are relatively unaffected while the electrical conductivity is most affected. This is expected since using coarser cells to resolve a structure tends to describe the curved grain boundaries inaccurately and to close narrow pores. While closing a few narrow channels will not affect

surface area greatly, the impact on transport properties is dramatic. As discussed in connection with Fig. 3-5 c and Fig. 3-5 d, electrical current is more severely affected than hydraulic current. We note that our results do not exhibit the simple linear trend described by Arns et al. (2001; see their Fig. 1c.) in their analysis of calculations based on Fontainebleau sandstone micro-tomograms. This non-linear trend is expected because when the image resolution is degraded to the point where the voxel edge is larger than typical channel diameters (Tab. 3-4), the estimation of transport properties is quite poor. A marked decrease in permeability and electrical conductivity is observed when the cell size goes from 5.6 μm to 11.2 μm. By contrast, when we go from 2.8 to 5.6 μm, there is relatively little change in the transport properties because the pore throats are fairly well resolved.

3.5 Impact of Computation Size

From the properties calculated on five 400^3 sub-fragments, we can observe the heterogeneity of all properties at 400^3 scale. This corresponds to $1.1mm^3$ for physical size. Now, we consider the effect computation size by enlarging our model from 400^3 to 800^3, both with 2.8 μm resolution. The Laplace solver is optimized to allow dynamic allocation of memory. One 800^3 sub-fragment is chosen from the total 1840^3 based on the criteria of porosity (Fig. 3-13). A single conductivity run at 800^3 cube scale requires ~10 Gbytes of memory and 15 CPU hours to complete on a Intel Quad-Core Xeon 3GHz processor. In the 800^3 model, we get ***13.75*** for electrical formation factor, which is much closer to the experimental value than taking the mean value of five 400^3 sub-volumes. Thus, the choice of

representative computation cell size is important. Within the capacity of computational power, large sampling volume is always preferable.

Of course, boosting the computation to larger volume will increase the computation expanse. Optimization of the computation algorithm and more powerful hardwares (e.g., cluster) are required. Thus, we should run the image resolution effect analysis on the specific core sample and the CT image. Finding an optimal resolution to run a large volume within the computational capacity will help to give the best computable physical size.

3.6 Summary

In this chapter, electrical and fluid transport properties of a Berea Sandstone with 23.6% porosity are computed from an X-ray μCT image and are compared with laboratory measurements. Finite difference techniques are used to solve Laplace's equation for electrical conductivity and Stokes' equation for viscous fluid flow. Two different image processing methods are applied to identify surface voxels in the digital binary image.

1. For computation, we chose five 400^3 sub-volumes at different locations within the core. Each corresponds to a physical sample (1 mm^3). The computed physical properties varied between samples: formation factor by a factor of two (12 to 22), permeability by a factor of three (0.38 darcy to 1.05 darcy) and surface area from $0.69\, m^2/g$ to $0.88\, m^2/g$. These variations are due to the heterogeneity of the BS500 at the *mm* scale.

2. The average values of properties calculated for five samples compared well with laboratory measured values. To obtain representative values of physical properties, it is necessary to do calculations on several sub-samples.

3. Optimization of our computation algorithm enabled us to perform calculations on a large (800^3) 3D volume; this calculation gives better results for the electrical formation factor.

4. The effects of image resolution on computed physical properties were investigated. Decreased resolution leads to sharply decreased permeability and electrical conductivity.

5. Good results were obtained to support a correlation linking permeability to electrical conductivity through the calculated geometric and dynamic length scales.

6. A three phase conductivity model was developed to treat surface conduction based on the rock μCT image. This model agrees with experimental data and provides a better fit than the Waxman-Smits equation.

Acknowledgements

This work was supported by the Schlumberger – Doll Research and MIT Earth Resources Laboratory Founding Member Consortium. We thank Dr. Peter Tilke from Schlumberger-Doll Research for providing us the μCT image of BS500 core sample. We thank Wave Smit from Schlumberger-Doll Research for providing us the laboratory measurements, the BS500 core plug and interpretation of the laboratory results. We would

also like to thank Dr. Jeffery Tarvin from Schlumberger-Doll Research for his helpful discussion on electrical conductivity and permeability measurements.

3.7 References

Amaefule, J.O., Wolfe, K., Walls, J.D., Ajufo, A.O. and Paterson, E.: 1986, Laboratory determination of effective liquid permeability in low-quality reservoir rocks by the pulse decay technique, *paper SPE 15149 presented at the 56th California Regional Meeting, Soc. Of Pet. Eng.,Oakland,Calif,* April 2-4.

Archie, G.E.: 1942, The electrical resistivity log as an aid in determining some reservoir characteristics, *Trans. AIME*, **146**, 54-62.

Armstead, C. G., Tyler, A. J., Hambleton, F. H., Mitchell, S. A. and Hockey, J. A.:1969, The surface hydroxylation of silica, *Journal of Physical Chemistry B,* **73**, 3947-3952.

Arns, C. H.: 2001, The influences of morphology on physical properties of reservoir rock, *Ph.D. thesis, Univ. of New South Wales.*

Arns, C.H., Bauget, F., Ghous, A., Sakellariou, A., Senden, T.J., Sheppard, A.P., Sok, R.M., Pinczewski,W.V., Kelly, J.C. and Knackstedt, M.A.: 2005, Digital core Laboratory: Petrophysical analysis from 3D imaging of reservoir core fragments, *Petrophysics*, **46**, 260-277.

Asquith, G.B.: 1990, Log evaluation of shaly sandstones: a practical guide, *AAPG continuing education course note series #31*, 59P.

Auzerais, F.M., Dunsmuir, J., Ferréol, B.B., Martys, N., Olson, J., Ramakrishnan, T.S., Rothman, D.H. and Schwartz, L.M.: 1996, Transport in sandstones: A study based on three dimensional microtomography, *Geophysical Research Letters*, **23**, 70E-708.

Bentz, D.P. and Martys, N.S.: 2007, A stokes permeability solver for three-dimensional porous media, *NISTIR 7416, U.S. Department of Commerce.*

Blair, S. C., Berge, P. A. and Berryman, J. G.: 1996, Using two-point correlation functions to characterize microgeometry and estimate permeability of synthetic and natural sandstones, *Jounral of Geophysical Research*, **101**, 20359-20375.

Bockris, J. O'M. and Reddy, A. K. X.: 1972, Modern aspects of electrochemistry, *Plenum, New York.*

Brace, W.F.: 1977, Permeability from resistivity and pore shape, *J. Geophys. Res*, **82**, 3343-3349.

Brunauer, S., Emmett, P. H. and Teller, E.: 1938, Adsorption of gases in multimolecular layers, *J. Am. Chem. Soc.*, **60**, 309-319.

Canny, J.: 1986, A computational approach to edge detection, *IEEE Trans. Pattern Analysis and Machine Intelligence*, **8**, 679-714.

Clavier, C., Coates, G. and Dumanoir, J.: 1984, Theoretical and experimental bases for the dual-water model for interpretation of shaly sands, *Soc. Pet. Eng. J.*, **24**, 153-168.

Coles, M. E., Hazlett, R.D., Muegge, E.L., Jones, K.W., Andrews, B., Siddons, P., Peskin, A. and Soll, W.E.: 1996, Developments in synchrotron X-Ray microtomography with applications to flow in porous media, paper SPE 36531, *Proc. 1996 SPE Annual Technical Conference and Exhibition, Denver*, Oct 6-9.

Debye, P. and Hückel, E.: 1923, Zur theorie der electrolyte, *Phys. Z*, **24,** 18E-206.

Devarajan, S., Toumelin, E. and Torres-Verdín, C.: 2006, *SPWLA 47th Annual Logging Symposium*, June 4-7.

Finney, J.: 1970, Random packings and the structure of the liquid state, *Proc. Roy. Soc,* **319A**, 479.

Garbozi, E.J. and Douglas, J.F.: 1996, Intrinsic conductivity of objects having arbitrary shape and conductivity, *Physical Review E*, **53**, 6169-6180.

Garbozi, E.J.: 1998, Finite Element and Finite Difference Programs for Computing the Linear Electric and Elastic Properties of Digital Image of Random Materials, *NISTIR* **6269**.

Hazlett, R.D.: 1995, Simulation of capillary dominated displacements in microtomographic images of reservoir rocks, *Transport in Porous Media*, **20,** 21-35.

Iler, R. K.: 1979, The chemistry of silica, *Wiley, New York.*

Jin, G., Torres-Verdín, C. and Toumelin, E.:2009, Comparison of NMR simulations of porous media derived from analytical and voxelized representations, *Journal of Magnetic Resonance*, **200,** 313-320.

Johnson, D.L., Koplik, J. and Schwartz, L.M.: 1986, New pore-size parameter characterization transport in pours media, *Physical Review Letters*, 57, **n.20**, 2564-2567.

Juhász, I.: 1981, Normalized Qv – The key to shaley sand evaluation using Waxman-Smits equation in the absence of core data, *Trans. Soc. Prof. Well Log Analysts, 22nd Annual Logging Symposium,* Paper Z.

Kameda, A.: 2004, Permeability evolution in sandstone: digital rock approach, *Ph.D. thesis, Stanford University.*

Kan, R. and Sen, P.N.: 1987, Electrolytic conduction in periodic arrays of insulators with charges, *J. Chem. Phys*, **86,** 5748-5756.

Klinkenberg, L.J.: 1941, The permeability of porous media to liquids and gases, *Drill. Prod. Pract,* **8**, 200-213.

Knackstedt, M.A., Arns, C.H., Limaye, A., Sakellariou, A., Senden, T.J., Sheppard, A.P., Sok, R.M., Pinczewski, W.V. and Bunn, G.F.: 2004, Digital Core Laboratory: Properties of reservoir core derived from 3D images, SPE-87009; *presented at the 2004 Asia Pacific Conference on Integrated Modelling for Asset Management, Kuala Lumpur.*

Lai, T. M. and Mortland, M. M.: 1960, Self-diffusion of exchangeable ions in bentonite, *Porc. Ninth Natl. Conf.,* Clays and Clay Minerals, Pergamon Press, Ltd. The Macmillan Co., New York, 229.

Li, S. X., Pengra, D.B. and Wong, P. Z.: 1995, Onsager's reciprocal relation and the hydraulic permeability of porous media, *Phys. Rev. E,* **59,** 2049-2059.

Lima, O.A.L. and Sharma, M.M.: 1990, A grain conductivity approach to shaly sandstones, *Geophysics*, **55**, n.10, 1347-1356.

Marr, D. and Hildreth, E. C.: 1980, Theory of edge detection, *Proceeding of the Royal Society, London B,* **207,** 187-217.

Martys, N. and Garboczi, E.J.: Length scales in relating fluid permeability and electrical conductivity in random two-dimensional model porous media, *Physics Review B,* **46,** 6080 .

Minnis, M.M.: 1984, An automatic point-counting method for mineralogical assessment, *The American Association of Petroleum Geologists Bulletin*, **68,** P744-752.

Minsley, B. J.: 2007, Modeling and inversion of self-potential data, *Ph.D. thesis, Massachusetts Institute of Technology.*

Moon, P. and Spencer, D.E.: 1953, Recent investigations of the separation of Laplace's equation, *Proc. Amer. Math. Soc*, **4**, 302.

Morgan, F.D., Williams, E.R. and Madden, T.R.: 1989, Streaming potential properties of westerly granite with applications, *Journal of Geophysical Research,* **94,** 12449-12461.

Motealleh, S., Gladkikh, M., Bespalov, A., Herrick, D. C. and Bryant, S. L.: 2007, Grain-scale modeling of electrical resistivity of 'shaly sands', *SPWLA*, *48th Annual Logging Symposium*, Paper **SSS,** 1-9.

Neasham, J.W.: 1977, The morphology of dispersed clay in sandstone reservoirs and its effect on sandstone shaliness, pore space and fluid flow properties, *SPE paper,* **6858**.

Nelson, P.H.: 2000, Evolution of permeability-porosity trends in sandstones: *Society of Professional Well Log Analysts 41st Annual Logging Symposium*, June 4-7.

Nicos, S., Martys, N.S., Torquato, S. and Bentz, D.P.: 1994, Universal scaling of fluid permeability for sphere packings, *Phys. Rev. E*, **50**, 403-408.

Pal, E.R., Stig, B.: 2002, Process based reconstruction of sandstones and prediction of transport properties, *Transport in Porous Media*, **46,** 311-343.

Patchett, J. G.: 1975, An investigation of shale conductivity, *SPWLA*, *16th Annual Logging Symposium*, Paper **U,** 40pp.

Paterson, M.S.: 1983, The Equivalent Channel Model for Permeability and Resistivity in Fluid Saturated Rock-a Re-appraisal, *Mechanics of Materials*, **2**, 34E-351.

Pathegama, M. and Göl, Ö.: 2004, Edge-based image segmentation, *Proceedings of the International Conference on Computational Intelligence,* ISBN **97E-98458-0-6**.

Perrier, F. E., Petiau, G., Clerc, G., Bogorodsky, V.: 1997, A one-year systematic studies of electrodes for long period measurements of the electric field in geophysical environments, *J. Geomag, Geolectr.*, **49,** 1677-1696.

Petiau, G.: 2000, Second generation of lead-lead chloride electrodes for geophysical applications, *Pure. Appl. Geophys.*, **157,** 357-382.

Pike, J. D.: 1981, Feldspar diagenesis in Yowlumne sandstone, Kem County, California: *M.S. thesis, Texas A&M University, College Station, TX*

Press, W. H., Flannery, B.P., Teukolsky, S.A. and Vetterling, W.T.: 1990, Numerical Recipes, *Cambridge University Press, Cambridge.*

Pride, S. R. and Morgan, F. D.: 1991, Electrokinetic dissipation induced by seismic waves, *Geophysics*, **56**, 914-925.

Revil, A. and Glover P. W. J.: 1997, Theory of ionic-surface electrical conduction in porous media, *Phys. Rev. B,* **55,** 1757-1773.

Revil, A. and Glover P. W. J.: 1998, Nature of surface electrical conductivity in natural sands, sandstone, and clays, *Geophysical Research Letters,* **25,** 691-694.

Revil, A., Cathles III, L.M., Losh, S. and Nunn, J.A.: 1998, Electrical conductivity in shaly sands with geophysical applications, *Journal of Geophysical Research*, **103**, n. B10, 2392E-23936.

Revil, A. and Leroy, P.: 2001, Hydroelectric coupling in a clayey material, *Geophysical Research Letters,* **28,** 1643-1646.

Richman, D. and Thomas, H.C.: 1956, Self-diffusion of sodium ion in a cation exchange resin, *J. Phys. Chem,* 60**,** 237.

Sakellariou, A., Sawkins, T, J, Senden, T. J. and Limaye, A.: 2004, X-ray tomography for mesoscale physics applications, *Physica A,* **339,** 152-158.

Schwartz, L.M., Martys, N.S, Bentz, D.P., Garboczi, E.J. and Torquato, S.: 1993, Cross-property relations and permeability estimation in model porous media, *Phys. Rev. E,* **48,** 4584-4591.

Schwartz, L. M., Sen, P. N. and Johnson, D. L.: 1989, Influence of rough surface on electrolytic conduction in porous media, *Phys. Rev. B,* **40,** 2450-2458.

Sen, P.N. and Kan, R.: 1987, Electrolytic conduction in porous media with charges, *Phys. Rev. Lett*, **58**, 778-780.

Sen, P.N., Straley, C., Kenyon, W.E. and Whittingham, M.S.: 1990, Surface-to-volume ratio, charge density, nuclear magnetic relaxation, and permeability in clay-bearing sandstones, *Geophysics*, **55**, 61-69.

Spanne, P., J. Thovert, J. Jacquin, W. B. Lindquist, K. Jones, and D. Coker.: 1994, Synchotron computed microtomorgraphy of porous media: topology and transport, *Phys. Rev. Lett,* **73,** 2001-2004.

Tanikawa, W. and Shimamoto, T.: 2006, Kinkenberg effect for gas permeability and its comparison to water permeability for porous sedimentary rocks, *Hydrology and Earth System Sciences Discussions*, **3**, 131E-1338.

Toumelin, E. and Torres-Verdín, C.: 2008, Objected-oriented approach for the pore-scale simulation of DC electrical conductivity of two-phase saturated porous media, *Geophysics*, **73**, E67-E79.

Wu, T.: 2004, Permeability prediction and drainage capillary pressure simulation in sandstone reservoirs, *Ph.D. thesis, Texas A&M University.*

Walsh, J. B. and Brace, W. F.: 1984, The effect of pressure on porosity and transport properties of rock, *J.Geophy. Res,* **89**, 942E-9431.

Waxman, M.H and Smits, L.J.M.: 1968, Electrical conduction in oil-bearing sands, *Society of Petroleum Engineers Journal*, **8**, 107-122.

Wyllie, M.R.J. and Gregory, A.R.: 1955, Fluid flow through unconsolidated porous aggregates. Effect of porosity and particle shape on Kozeny-Carman constants, *Ind. Eng. Chem*, **47**, 1379.

Zahn C.: 1971, Graph-Theoretic Methods for Detecting and Describing Gestalt Clusters, *IEEE Trans. Computers*, **20**, 68–86.

Zhan, X.: 2005, A study of seismoelectric signals in measurement while drilling, *M.S. thesis, Massachusetts Institute of Technology.*

Zhan, X., Zhu, Z., Chi, S. H. and Toksöz, M. N.: 2009, Elimination of LWD (logging while drilling) tool modes using seismoelectric data, *Communications in Computational Physics,* **7**, 47-63.

Zhang, W. M. and Wang, S. A.: 2005, An efficient connectivity-number-based edge detection method for binary images, *Proceedings of the Fourth International Conference on Machine Learning and Cybernetics*, 18-21.Zwillinger, D.: 1997, Handbook of Differential Equations, 3rd Ed, Boston, MA, *Academic Press.*

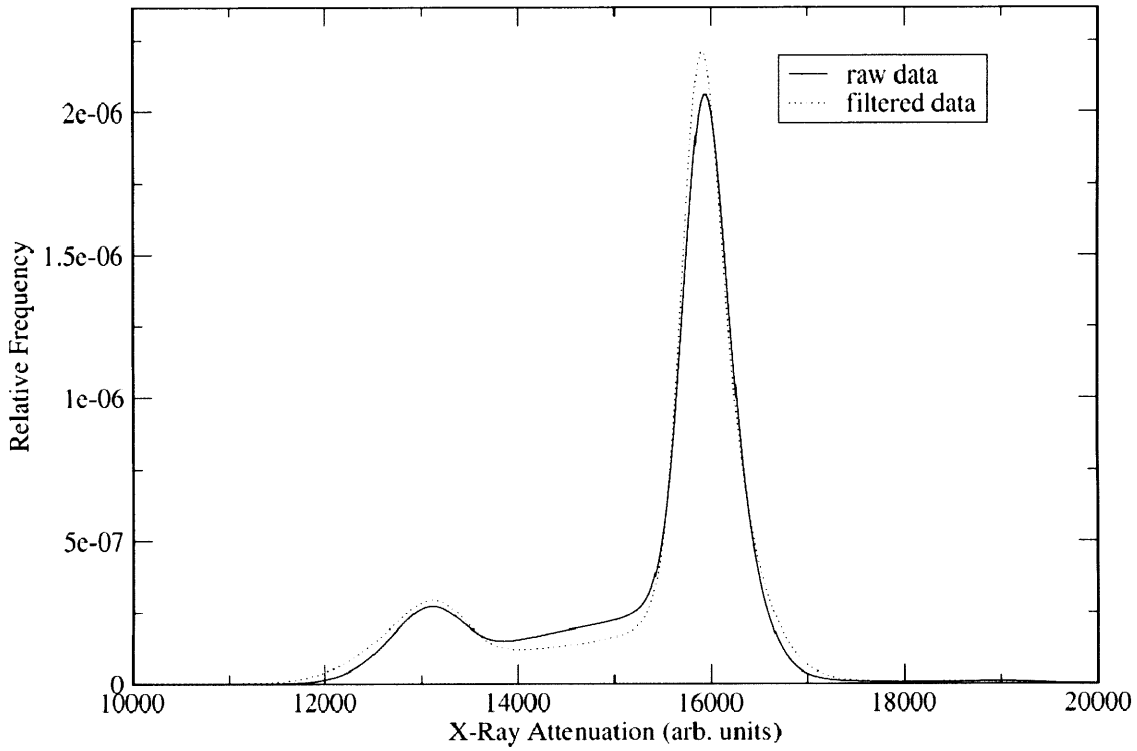

Figure 3-1: Intensity (i.e. X-ray attenuation) histogram before and after application of the anisotropic diffusion filter on BS500 core sample (provided by ANU). The first peak on the left hand side corresponds to void space of the microstructure. The second peak on the right hand side corresponds to the grains. The intermediate portion of the curve between the two peaks corresponds to the low density pore inclusions (e.g., microporosity, clays, feldspars, etc.).

Composition	Weight Fraction (%)
Quartz	88.9
Clay	3.9
Feldspar	3.4
Carbonate	2.2
Evaporite	0.5
Others	1.1

Table 3-1: Composition of Berea Sandstone 500 core sample (provided by Schlumberger Doll Research).

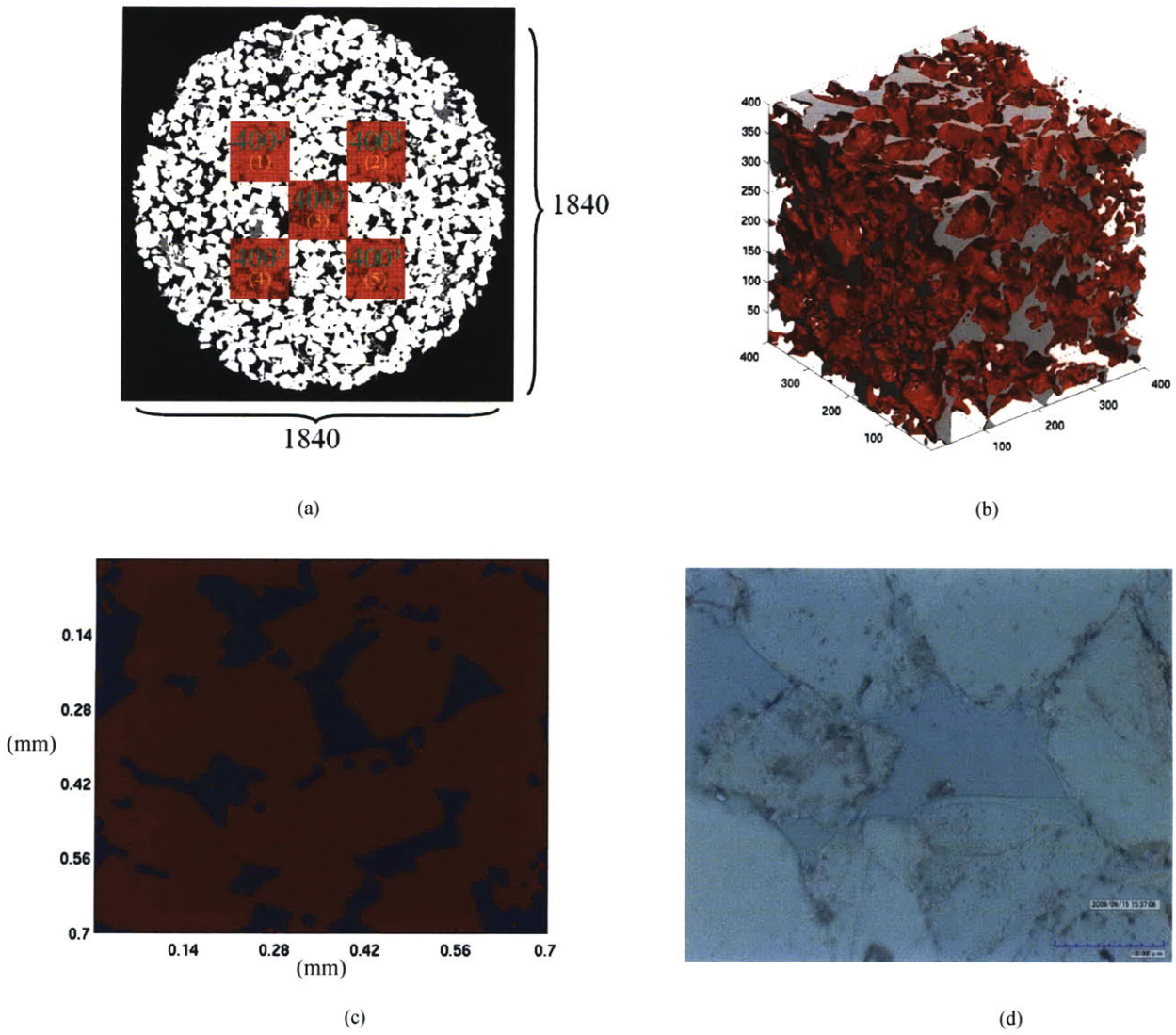

Figure 3-2: (a) View of selected five 400^3 sub-volumes at different locations in the total 1840^3 BS500 core sample with 2.8 micron resolution. X-ray intensity values are encoded in grey shades with brightness corresponding to increased intensity. (b) Pore-cast for sub-volume 3 from the middle of the total volume. (c) 200^2 subset from sub-volume 3 showing absolute units. (d) Thin section for Berea 500 showing quartz grains and additional mineral inclusions.

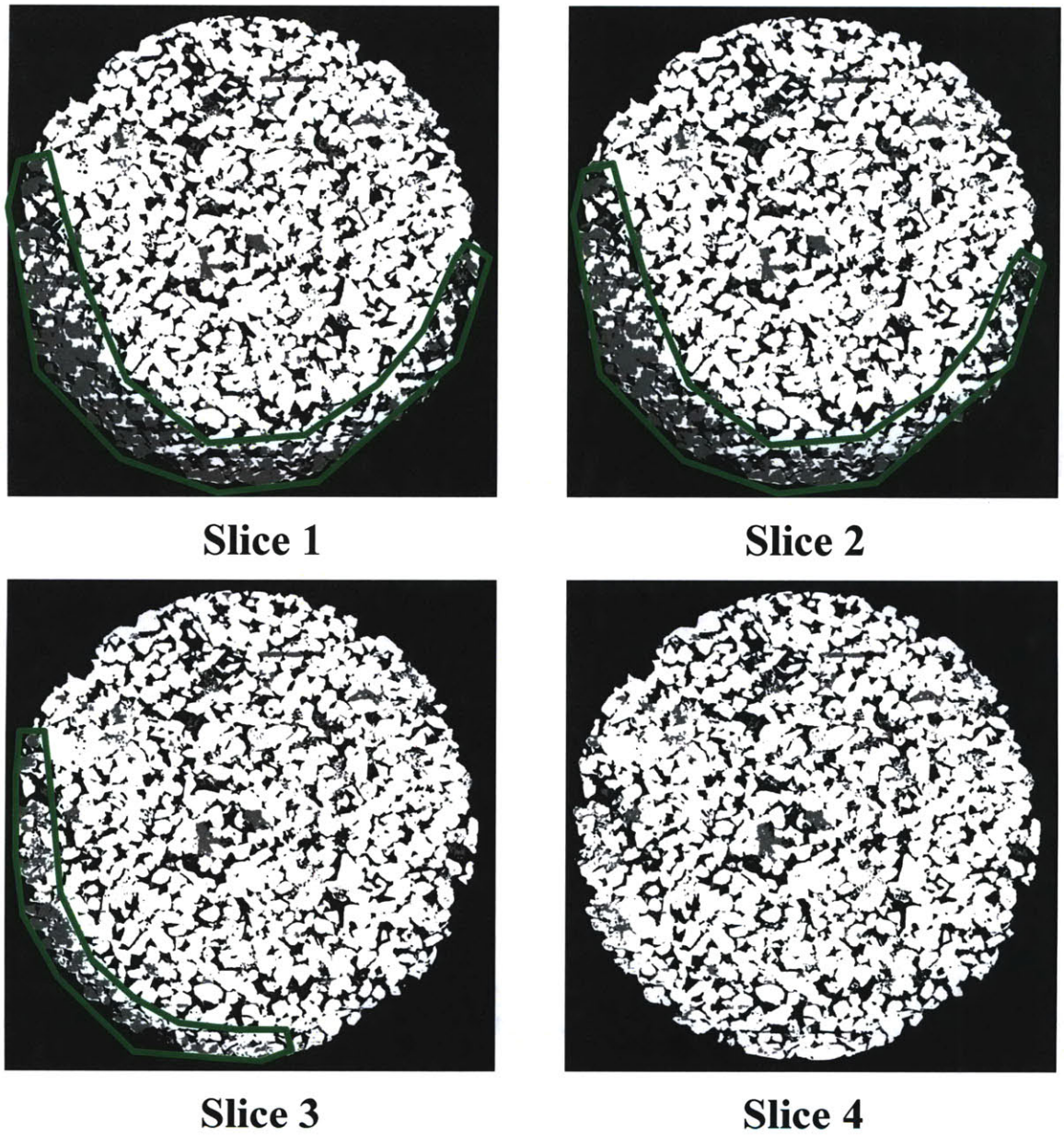

Figure 3-3: Slice 1, 2, 3, 4 in the total 1840^3 volume in Z direction. The shaded area (circled out in green) in slice 1, 2, 3 is very likely due to the cutting damage. The image quality is getting better moving towards the center of the core.

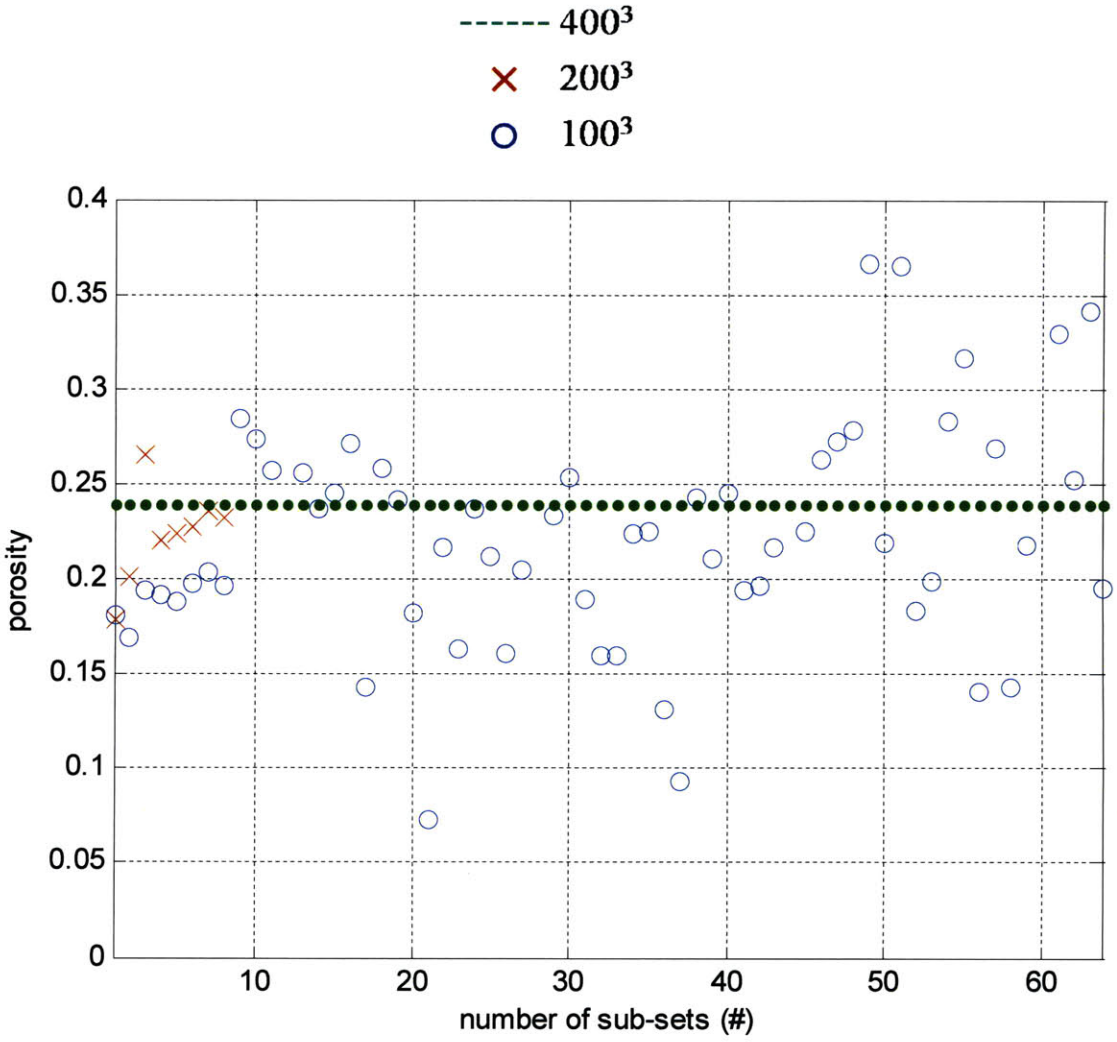

Figure 3-4: Porosity distribution of different size of sub-cubes. 400^3 cube is the #3 sub-volume in Fig. 3-2 with 23.81% porosity (shown in green line). The porosities of eight 200^3 cube and sixty-four 100^3 cube within the 400^3 cube (# 3 in Fig. 3-2) are shown in red cross and blue circles, respectively.

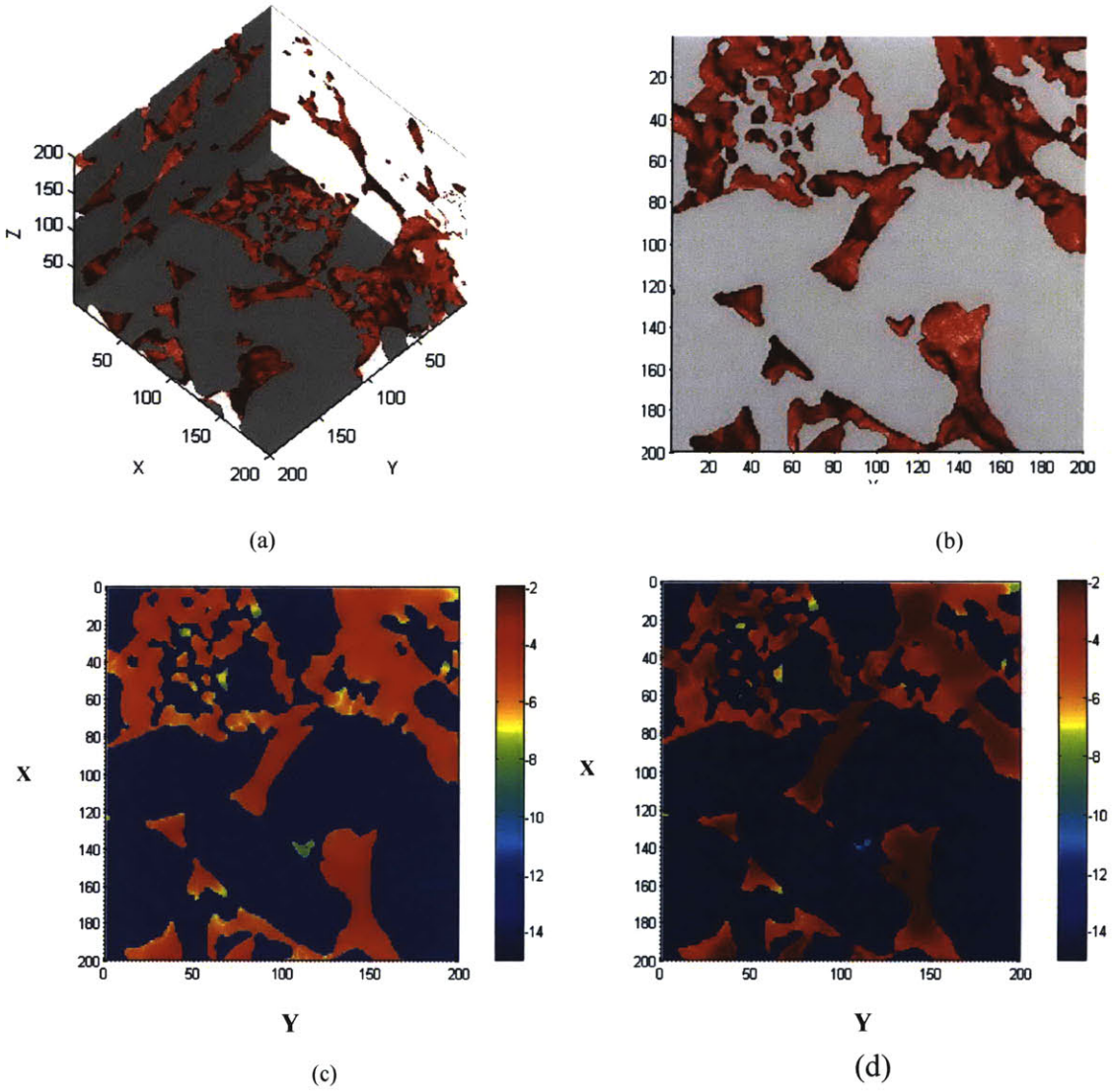

Figure 3-5: (a) 3D tilted view of a 200^3 cube in #3 sub-volume in Fig. 3-2 (red indicates pore space, grey indicates grain) (b) X-Y plane of the first slice in Fig. 3-2. a. (c) Electrical current density (with the units of A/m^2) of Fig. 3-2.b in logarithm scale. (d) Hydraulic flux (with the units of m/s) of Fig. 3-2.b in logarithm scale.

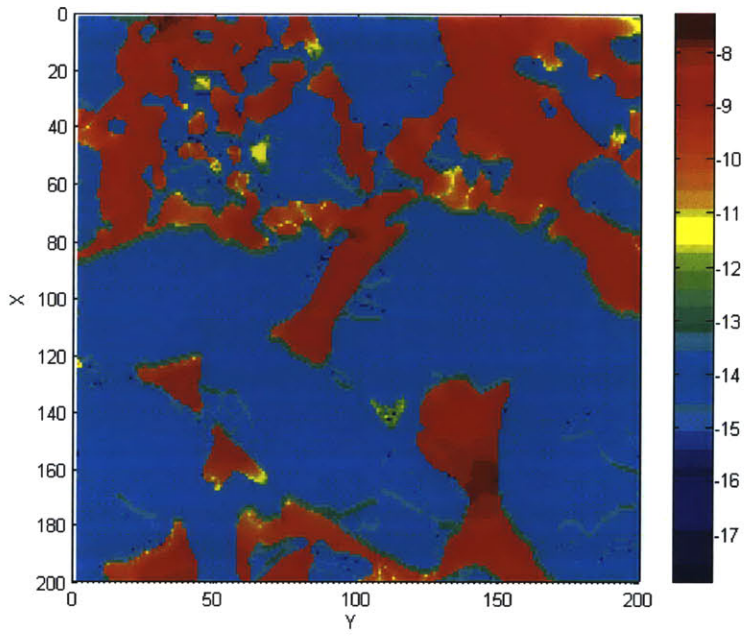

(a)

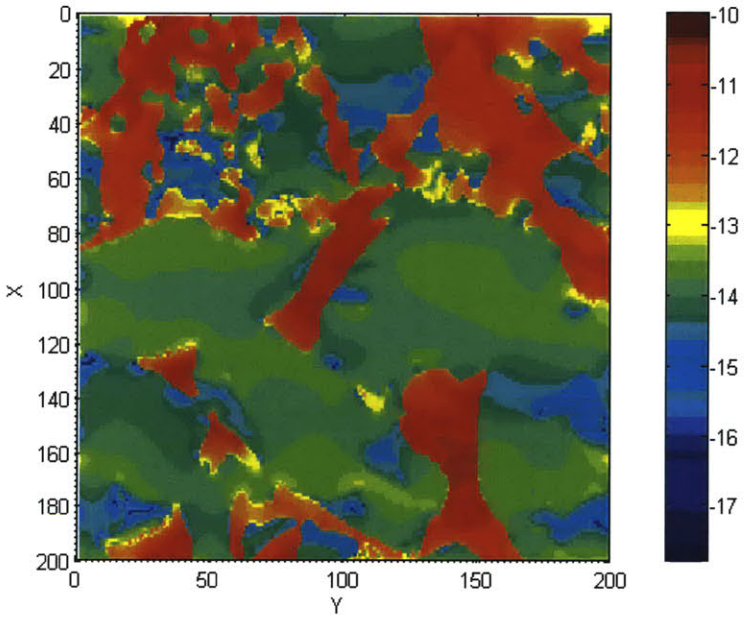

(b)

Figure 3-6: (a) Electrical current density (with the units of A/m^2) of Fig. 3-2.b saturated with oil in (base 10) logarithm scale. (b) Electrical current density of Fig. 3-2.b saturated with gas in (base 10) logarithm scale.

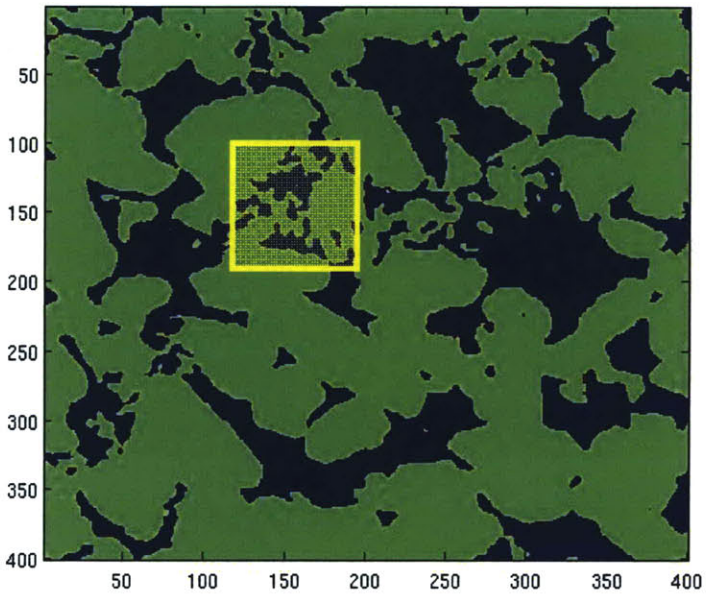

(a)

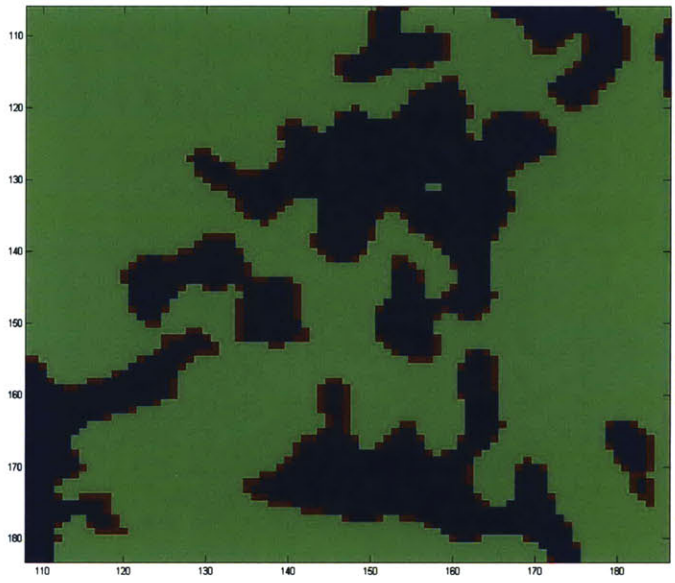

(b)

Figure 3-7: (a) Surface pixel (red) along pore (blue) – grain (green) boundary using gradient based image processing method. This is one slice in sub-volume #3. (b) Enlarged view of shadowed area (yellow square) in (a). Surface pixels are shown in red, pore in blue and grain in green.

Saturation Phase	**Gas**	**Oil**	**Saline Water**			
Saturation Fluid Conductivity (S/m)	$1e^{-11}$	$5e^{-9}$	$1e^{-1}$	1	10	100
Effective Conductivity (S/m)	$6.16e^{-13}$	$3.01e^{-11}$	$7.63e^{-3}$	$7.75e^{-2}$	$7.32e^{-1}$	7.95

Table 3-2: The effective conductivity of BS500 saturated with gas, oil and saline water. For highly conductive brine in the table, saturated rock conductivity and electrolyte conductivity obeys Archie's law. The ratio between electrolyte conductivity and saturated rock conductivity is a constant, formation factor, given in Tab. 3-3.

	#1	#2	#3	#4	#5
Porosity (%)	22.98	23.33	23.81	24.10	23.60
Formation Factor	22.23	18.69	16.11	11.98	16.31
Permeability (Darcy)	0.38	0.61	0.75	1.05	0.83
Surface Area (m^2/g)	0.88	0.81	0.78	0.69	0.77
Pore Volume to Surface Ratio (μm)	6.57	7.19	7.46	8.4	7.52
Λ (μm)	6.48	7.51	8.24	10.18	8.18

Table 3-3: Numerically computed porosity, permeability, formation factor and surface area, pore volume to surface area ratio and Λ parameter for the five selected sub-volumes in Fig. 3-2 a.

	Laboratory	Numerical
Porosity (%)	23.56 ~ 23.97	***23.64*** ± 0.43
Formation Factor	12.68 ~ 13.84	***16.40*** ± 3.76
Permeability (Darcy)	0.43 ~ 0.46	***0.60*** ± 0.23
Surface Area (m^2/g)	0.87 ~ 0.93	***0.77***± 0.02

Table 3-4: Comparison of laboratory measurements with calculated values. The numerical values are the mean value (bold italicized number in column 3) and variance for the five sub-volumes. The laboratory measurements are provided with a range to account for the experimental error. Some experiments are done multiple times on different BS500 core plugs, such as formation factor and surface area.

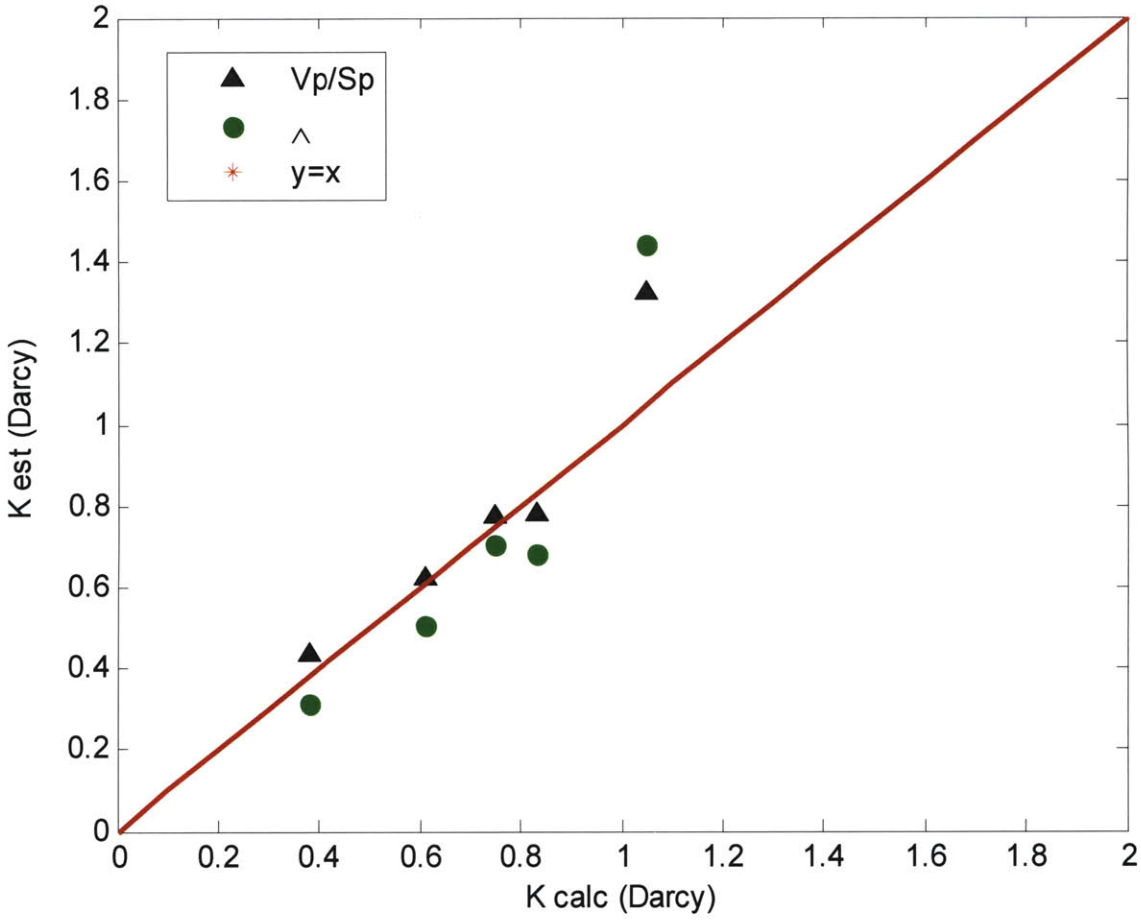

Figure 3-8: Numerically calculated permeability vs. estimated permeability. In the estimate based on V_p/S the value of $C = 0.225$; in the Λ estimate, $C = 0.167$.

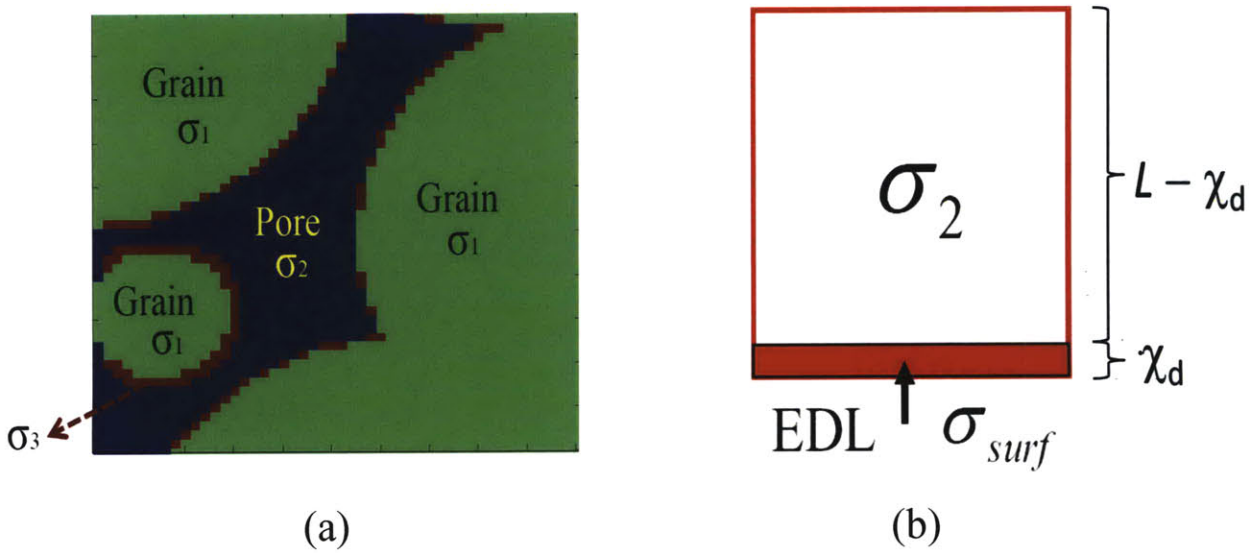

Figure 3-9: The three-phase representation of a porous rock is shown in (a): σ_1 is the conductivity of solid grain, σ_2 is the free electrolyte conductivity and σ_3 is the conductivity assigned to interface cells containing both free electrolyte and bound water. Our model for the interface cells is shown in (b). The cell edge is L and the EDL thickness is χ_d. Within the EDL the conductivity is σ_{eff}. The remainder of the cell has conductivity of σ_2.

Brine Conductivity (σ_2, *S/m*)	Debye Length (χ_d, Å)	Surface Cell Conductivity (σ_3, *S/m*)
0.005	240	0.012
0.01	166	0.015
0.025	105	0.030
0.05	74	0.055
0.1	52	0.114
0.2	37	0.205
0.4	26	0.4
1	16	1
2	12	2
10	5.3	10
50	2.4	50

Table 3-5: Debye length (χ_d), free electrolyte conductivity (σ_2) and surface cell conductivity (σ_3) values used in the three phase conductivity model.

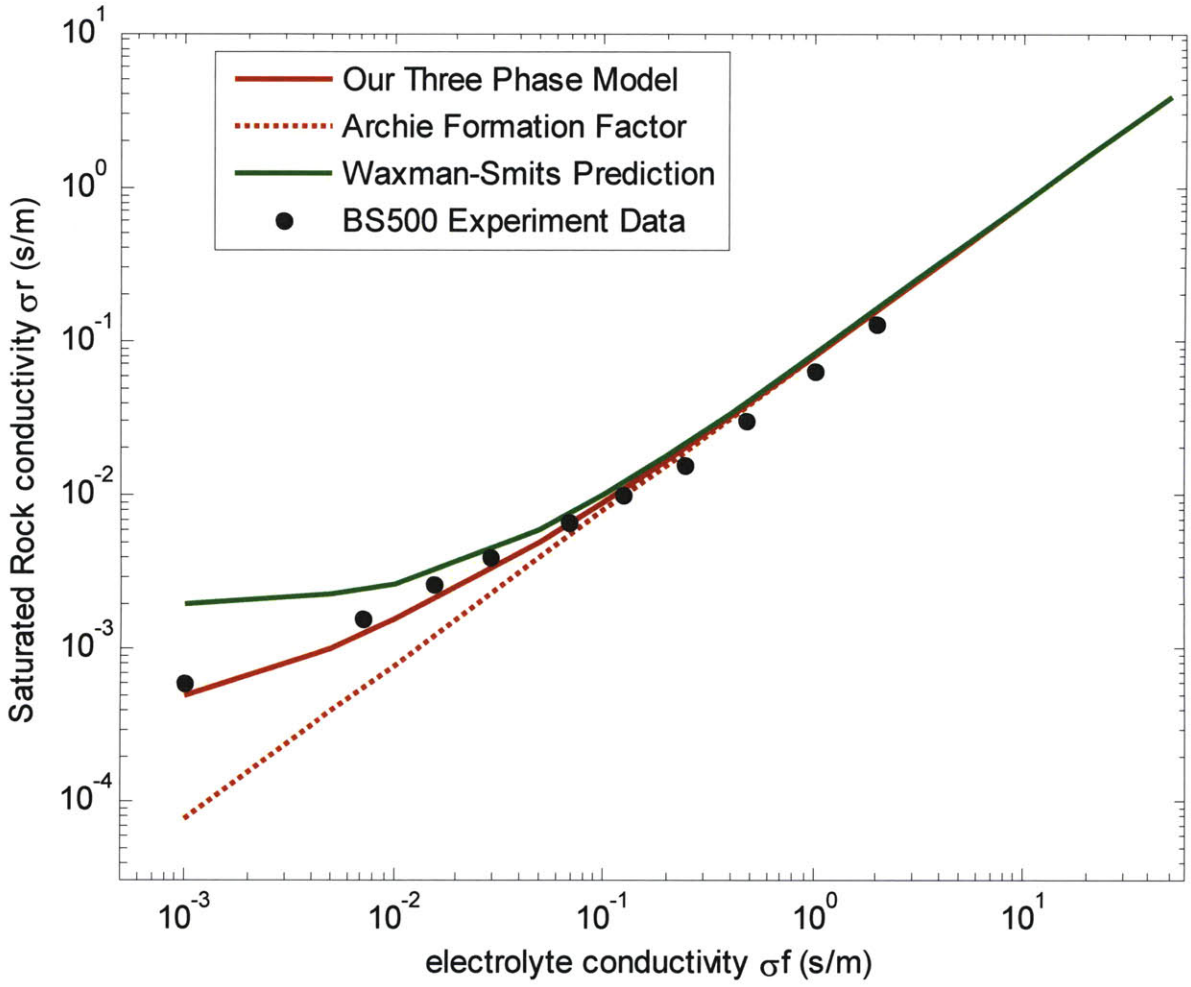

Figure 3-10: Three phase conductivity calculations of the effective BS500 conductivity (solid red line) are compared to the Waxman Smits prediction (solid green line) and experimental data for ten brine salinities (black circles). Each calculation is based on one row of data in Table 4. Red dashed line is the linear relationship (with Archie's formation factor) between electrolyte conductivity and saturated rock conductivity.

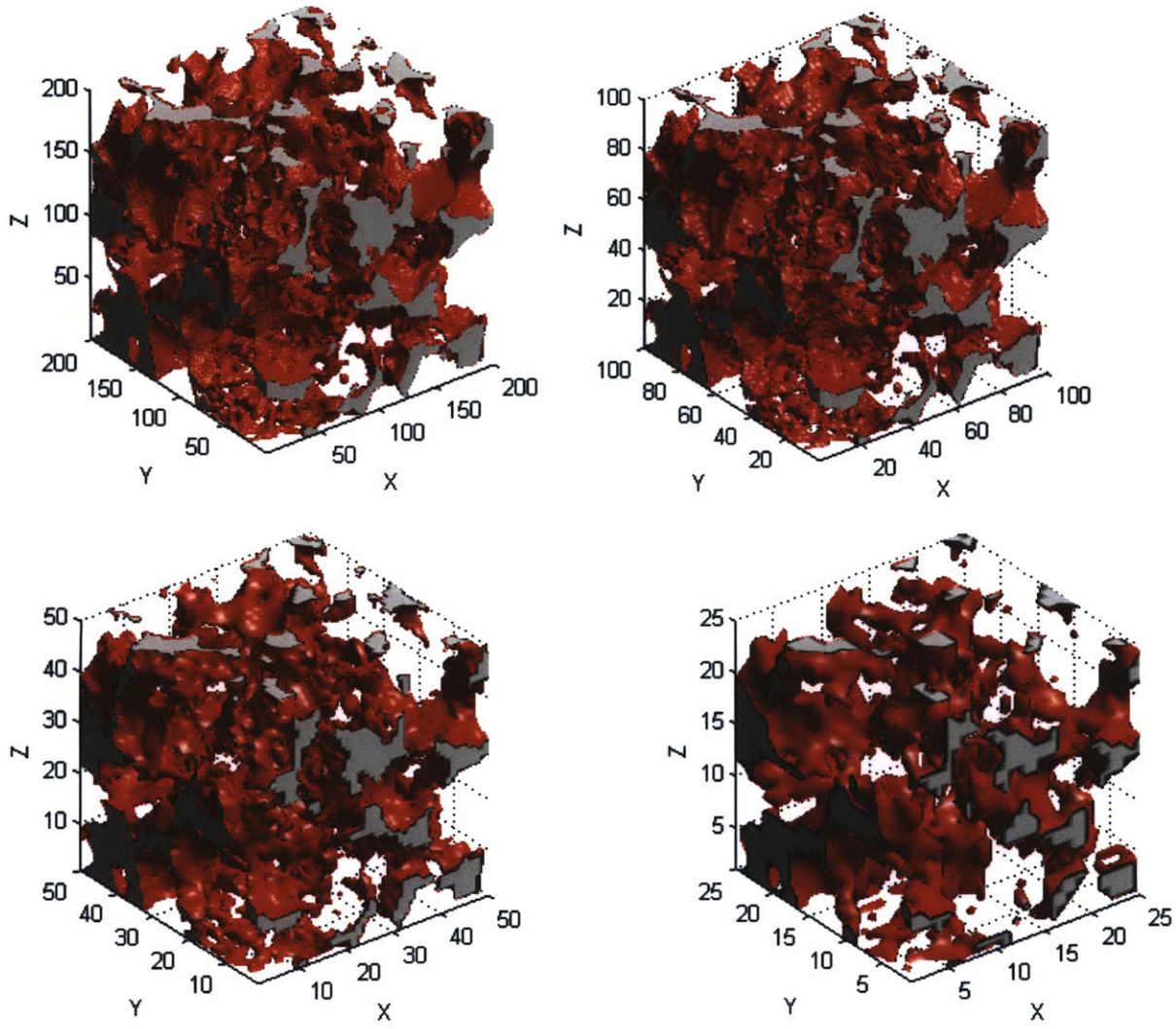

Figure 3-11: 3D pore structure of the downscaled cubes from original 400^3 cube (Fig 3-3.b) using majority rule. Connectivity of the pore space and thin pore throat is getting lost with decreasing image resolution.

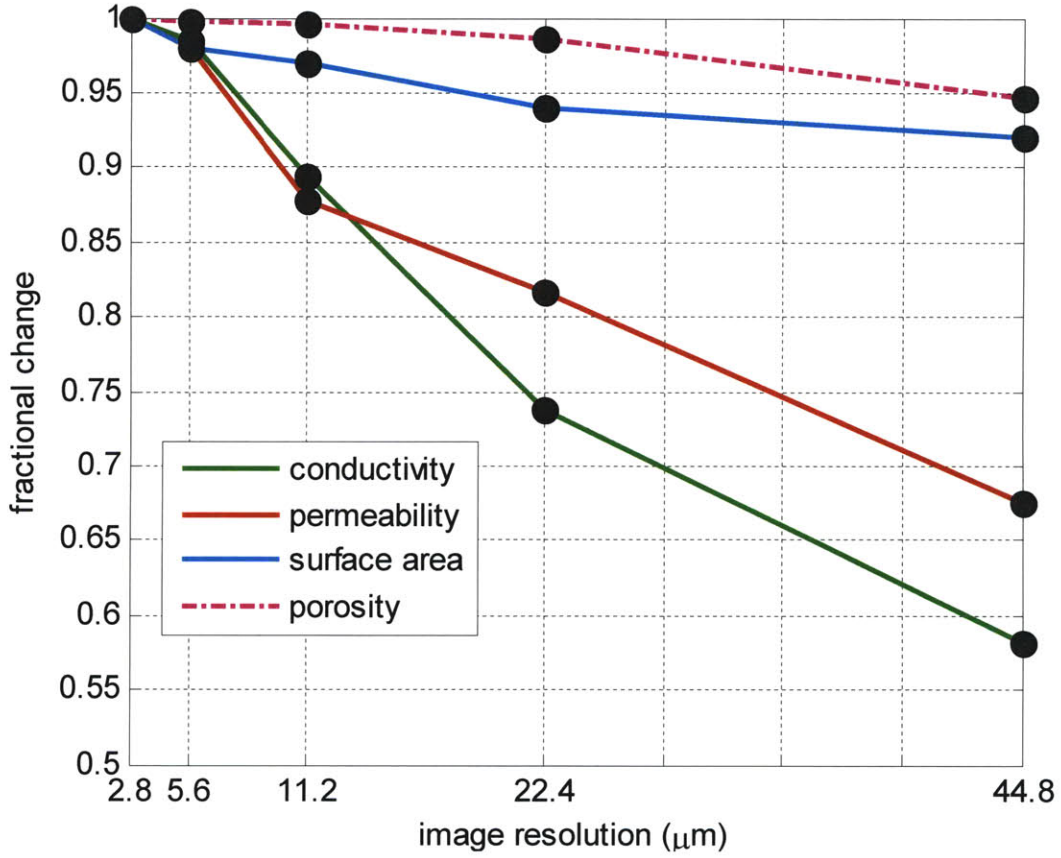

Figure 3-12: Fractional change in numerically computed porosity, electrical conductivity, permeability and surface area from 400^3 cube with 2.8 micron resolution to 25^3 cube with 44.8 micron resolution. Marked decrease could be observed in conductivity and permeability when the image resolution exceeds 5.6 micron.

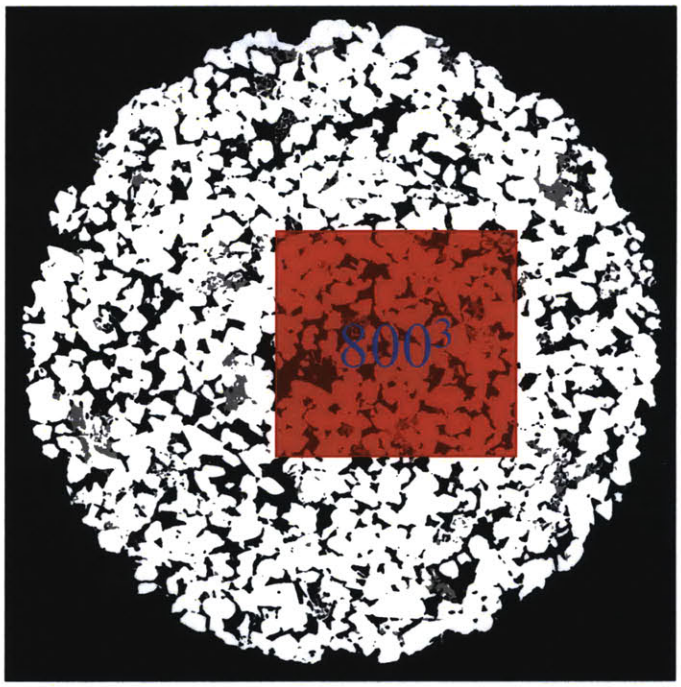

Formation Factor (F)		
800^3	Ave (400^3)	Lab
13.5	16.4 ± *3.7*	13.0

Figure 3-13: A 800^3 cube is chosen within the whole volume based on the criteria of porosity (above). The formation factor calculated on the 800^3 cube is closer to the experimental result than the mean value for five 400^3 sub-sets (below). The laboratory value is the mean value for multiple measurements in Tab. 3-4.

Chapter 4

Quantitative High Frequency AC Seismoelectric Measurement on Berea Sandstone[3]

Abstract

In brine-saturated rock, the existence of mobile charge within a thin layer along the fluid-solid interface, which is known as electric double layer (abbreviated as EDL) leads to electrokinetic phenomena. DC streaming potential is the electric potential induced by the fluid flow under constant pressure across a fluid filled porous rock. The alternating electric field induced by an acoustic wave propagating through the porous rock is the so called seismoelectric signal. In this chapter, we present quantitative AC seismoelectic measurement at high frequencies (10 kHz to 120 kHz) on Berea 500 sandstone (BS500) rock samples. In a solution tank, we measure the seismoelectric signals induced by acoustic waves at 10 kHz to 120 kHz on BS500 plate saturated with 0.01*S/m* to 0.4*S/m* NaCl brines. We use single sine

[3] In preparation to be submitted to *Geophysics*.

pulse and five-cycle sine burst as the acoustic source wavelets. Received acoustic and electric signals are analyzed in both time domain and frequency domain. DC streaming potential is also measured on BS500 cylinders with the same brine saturations as in AC experiments. Given the BS500 rock μCT image and experiment measurements, we can quantify the porosity, permeability, tortuosity and Λ parameter. The frequency dependence of the coupling coefficient with respect to its DC limit is calculated theorectically using Pride's model. The majority of the measured AC seismoelectric voltage coupling coefficient follows the trend predicted by Pride's model. The high frequency, high pressure transient and wavelet techniques presented in this work extend our ability to conduct quantitative SE measurements at acoustic borehole logging frequencies applied in the field and laboratory. The overall data quality is better for single sine pulse than five-cycle sine burst due to its higher resolution and simplicity in the time domain. This is optimistic for field application where the high pressure transient is commonly adopted as the source wavelet.

4.1 Introduction

Electrokinetic phenomena, which occur in the fluid saturated porous media, are a consequence of a mobile space charge region that exists at the interfacial boundary of two different phases (pore fluid and solid matrix). This region is commonly referred to as the electric double layer (EDL) (Debye and Hückel., 1923; Morgan et al., 1989; Pride and Morgan, 1991). Among several possible models of the electric double layer, the Gouy-Stern model, which has been improved by many authors, is generally accepted (Dukhin and

Derjaguin, 1974; Bockris and Reddy, 2000). The Gouy-Stern EDL model is depicted in Fig. 4-1 (Overbeek, 1952; Bockris and Ready, 1970; Pride and Morgan, 1991). The first layer of cations is bound to the anion–solid surface through both Van-der-Waals and electrostatic forces. They are bound so strongly that they are assumed to be immobile. The partially fixed part of the EDL is called the Stern layer and is, in general, further divided into two layers: one is the inner Helmholtz plane (IHP) and the other is the outer Helmholtz plane (OHP). Beyond this first layer of bound cations, there is a diffuse distribution of mobile cations whose position is determined by a balance between electrostatic attraction to the absorbed layer and diffusion toward the neutral electrolyte. This diffuse part of the EDL is called the Gouy diffuse layer. The Gouy-Stern is therefore a composite of a Stern layer and a Gouy diffusion zone. The separation between the mobile and immobile charge is called the shear plane. The zeta potential, ζ, is the electric potential at the shear plane, and the electric potential in neutral electrolyte (no excess charge) is defined to be zero (Bockris and Reddy, 1970; Pride and Morgan, 1991).

It is normally assumed that the diffuse distribution of mobile charge alone gives rise to the electrokinetic phenomena and the absorbed layer does not contribute to the electrokinetic phenomena. The only role of the immobile charge absorbed onto the surface is to fix the value of the electric potential at the shear plane (the zeta potential). Zeta potentials are usually obtained in experimental studies. Theoretical determination of ζ remains problematic due to the complexity of the adsorbed layer (Pride and Morgan 1991; Haartsen, 1995). This zeta

potential is the quantitative index of intensity for the EDL and differs in different material-electrolyte systems.

When fluid flows through a porous medium under certain pressure, the movement of the ions forms an electric current. We can measure the pressure induced electric potential. The ratio between the resulting potential and exerted pressures is referred to as the potential coupling coefficient. If the driving force is a constant pressure, we call the resulting voltage a DC streaming potential. If the driving force is seismic or acoustic wave, we call the resulting voltage a seismoelectric potential.

Streaming potential has been quantitatively measured in laboratories in the DC or low to medium AC (a few Hz to a few hundred Hz) frequency range (Ahmed, 1964; Ishido and Mizutani, 1981; Morgan et al., 1989; Pengral et al., 1999; Reppert and Morgan, 2002). Field seismoelectric researches have also been carried out at low to medium frequency range (a few Hz to a few hundred Hz) in the surface survey (Thompson and Gist, 1993; Garambois and Dietrich, 2001) and borehole (Mikhailov et al., 2000; Hunt and Worthington, 2000) by putting the source on the surface. The illumination depth is confined to be within a few hundred meters. In the recent a few years, high frequency seismoelectric signals (higher than 1kHz) have also been recorded and analyzed in laboratory experiments (Zhu and Toksöz, 2005; Block and Harris, 2006; Singer et al., 2006; Zhu et al., 2008) with effective pressure generating devices. These researches provide strong evidence that the received electric signals are generated from seismoelectric conversion in the fluid saturated rock at frequencies higher than 1 kHz. The intention is trying to move SE measurement into the wellbore to evaluate

formation properties (e.g., permeability) and detect fractured zone at depth. However, those high frequency experiments remain at the qualitative stage due to the difficulty in the quantification of the acoustic wave field at different frequencies. The frequency dependent acoustic and electric fields provided in those studies are normalized with respect to the values at a certain frequency.

The first theoretical development of electrikinetic transport equations is attributed to Helmholtz and Smoluchowski (Helmholtz, 1879; Smoluchowski, 1903). The DC streaming potential coupling coefficient for capillary geometry is deduced by equating the convection and conduction currents. Later, Packard deduced the frequency-dependent coupling coefficient for capillary geometry and verified his theory with experiments on capillary samples (Packard, 1953). Neev and Yeatts (1989) postulated sets of equations that attempt to model the interaction between mechanical waves and electric fields due to electrokinetics. However, their work did not solve the full set of Maxwell's equations which ignore the electromagnetic disturbances induced by shear wave. In 1994, Pride proposed a generalized theory for frequency dependent seismoelctric potentials for porous media (Pride, 1994). Pride's final equations have the form of Maxwell's equations coupled to Biot's equations. The pore scale flow and electric fields are first integrated to give the high- and low-frequency definition of the coupling coefficient. The two limits are then connected by a simple postulated function (Pride, 1994). The frequency dependence in the coupling coefficients is obtained following the procedure outlined by Johnson, Koplik and Dashen (Johnson et al., 1987). Thus, Pride's model parameters are rock porosity, permeability, tortuosity and Λ

parameter, which is the weighted surface to volume ratio defined by Johnson (Johnson et al., 1987).

Pride's model has been validated by Reppert (Reppert, 2000; Reppert and Morgan, 2002) and compared with Packard's model on glass capillary, glass filters with pore diameters ranged from 34 micrometers to 1 millimeter. Real and imaginary parts of frequency dependent streaming potentials are both measured by Reppert for the first time. Both Packard's and Pride's models fit the frequency dependent streaming potential capillary and porous filter data. Theoretically, when using capillary geometry terms and neglecting second-order effects, Pride's model is identical to Packard's model when the series and asymptotic approximations are used (Reppert, 2000). Reppert also measured the frequency dependent coupling coefficient on one rock sample, Boise sandstone, which has an estimated permeability of 2.89 Darcy and equivalent pore radius of 17 micrometers (Reppert, 2000). Pride's theory is compared with the rock experimental data in the frequency range below 1 kHz.

The present study is motivated by the recognition that, with the ability to effectively generate and quantify the acoustic wave field excited by high frequency transient and wavelet, we can extend the SE measurement to the frequency range applied in borehole acoustic logging. In this research, we present the laboratory set-up for quantitative high frequency (10 kHz to 120 kHz) seismoelectric measurement. The rock sample we use is BS500 plate with 0.5 Darcy permeability. Quantification of the acoustic wave field is done prior to the seismoelectric measurement. Both single sine pulse and five-cycle sine burst are excited as

the acoustic source wavelets. DC streaming potentials are measured on BS500 saturated with NaCl electrolyte in the conductivity range of $0.01S/m$ to $0.4S/m$. The transport and geometrical parameters of BS500 are quantified from rock μCT image and laboratory measurements. The theoretically calculated frequency dependent coupling coefficient using Pride's equation can be obtained without any approximation on the rock properties. Finally, the comparison between theoretical prediction and laboratory measurements are made.

4.2 DC Streaming Potential Measurements on BS500

4.2.1 Experiment Apparatus

Streaming potentials are measured across the cylindrical BS500 core samples saturated with different NaCl conductivities ($0.01S/m$ to $0.4S/m$) in the pressure range of $0.05atm$ to $0.2atm$. If a pressure difference ΔP applied across across the sample causes brine to flow, the streaming current will carry charge from one end of the sample to the other. The resulting streaming potential ΔV can be measured. The streaming potential opposes the streaming current which flows along the pore surface and sends conduction current back through the pore volume. When the system reaches steady state, the streaming potential ΔV is linearly proportional to the applied pressure difference ΔP. The proportionality constant is the streaming potential coupling coefficient Ks_0.

A $10cm$ length and $2.5cm$ diameter BS500 cylinder is cut into five $2cm$ samples. Each core sample is saturated with one conductivity NaCl brine. Thus, each sample can be retreated as 'intact rock' equally prior to measurement. Each sample is first vacuumed for several hours

to expel air and then is vacuumed-impregnated with brine in order to be fully saturated. Saturated samples are held by a rubber jacket to prevent them from falling apart and are never allowed to dry out during the measurements.

We measure the flow rate and streaming potential simultaneously. The experiment apparatus is shown in Fig. 4-2. Twenty liters of NaCl solution is poured into the solution tank in Fig. 4-2. The exerted pressure is determined by the vertical distance between the top of the rock and the top of the water in the tank. The diameter of the water tank is 26 cm, which is large enough to ensure a steady flow. The pressure range we use in this experiment is from $0.05atm$ –$0.2atm$. In theory, the streaming potential coupling coefficient Ks_0 should be a constant. However, a number of factors can cause the change in Ks_0 for a particular experiment system. For example, high applied pressure can cause changes in pore geometry (Amaefule et al., 1986) and turbulent effect at high flow rates (Geertsma, 1974). If the sample has a rigid structure and permeability that is not too low, Ks_0 can persist to be a constant with applied pressure as large as 100kPa and perhaps higher (Ishido and Mizutani, 1981; Jouniaux and Pozzi, 1995). Thus, $0.05atm$–$0.2atm$ should be a suitable pressure range for our BS500 core sample with approximately $450mD$ liquid permeability. And this is verified in the linearity of pressure gradient–flow rate cross plot described in the next section. To minimize the electrode polarization (Perrier et al., 1997; Petiau, 2000; Minsley, 2007) and electrode drift (Morgan et al., 1989; Gusev and Horváth; 2002), we use freshly made $Ag/AgCl$ electrodes to measure the DC streaming potential. The multimeter we use has a maximum sensitivity of $0.02mV$, an input resistance of 1MΩ.

4.2.2 Data and Results

The volume flow rate Q_f is determined by measuring the weight of the brine flowing through the sample per unit time under pressure drop ΔP. Darcy velocity u_f is found from $u_f = Q_f/A$, where A is the sample's cross sectional area. The pressure gradient ∇P is obtained by the division of ΔP by the sample length l. Permeability is computed as $\kappa = \eta/m$, where η is the fluid viscosity and m is the slope of the line fitted to the crossplot of ∇P and u_f. We show the pressure gradient and Darcy velocity crossplot for one sample saturated with $0.2S/m$ brine in Fig. 4-3 soon after the saturation. The estimated permeability from Fig. 4-3 is $390.9mD$. From the linearity of the experimental data, we can assume the persistence of the rock structure in the applied pressure range.

The pore-fluid system is a closed system in which the rock is dissolving (Reppert 2000). The time to conduct the streaming potential measurements varies from a few hours to one or two months after saturation for different rock-electrolyte systems and different experiment purposes (Ishido and Mizutani, 1981; Morgan et al., 1989; Jouniaux and Pozzi, 1995; Pengra et al., 1999; Reppert 2000). For our BS500 core sample, which contains a traceable amount of clay minerals (Tab. 3-2), the swelling and liberation of clay can cause geometrical and chemical change of the rock (Waxman and Smits, 1968; Sen and Kan. 1987), especially when the saturation electrolyte is dilute. We use one BS500 core sample saturated with $0.012S/m$ NaCl brine and monitor the time evolution of the rock-brine system. The permeability of BS500 greatly decreased after it was immersed in $0.012S/m$ NaCl brine for 48 hours. However, it kept close to $390.9mD$ at the first three to four hours after saturation. We know

that the frequency dependence of the coupling coefficient is closely related to the permeability of the rock. Thus, we chose to conduct the streaming potential and AC seismoelectric potential measurement soon after the saturation. In this case, both DC and AC experiments are conducted under the same experimental conditions without much change in the rock permeability.

Five *2cm* samples are saturated in NaCl brines with electric conductivities of 0.012*S/m*, 0.048*S/m*, 0.095*S/m*, 0.2*S/m* and 0.4*S/m*, respectively. For each conductivity, we measure the streaming potentials ΔV at four water heights (the vertical distance from the water level in the bottle and the surface of the sample) of 70*cm*, 120*cm,* 170*cm* and 220*cm*. The streaming potential coupling coefficient is obtained as the slope of ΔV and ΔP crossplot best fitted through the four data points. Measured streaming potential coupling coefficients for five conductivity brines are given in Fig. 4-4. The streaming potential coupling coefficient for 0.4*S/m* NaCl brine in Fig.4-4 is 26 nV/Pa. This is close to the value of 34 nV/Pa measured by Pengra (Pengra et al., 1999, Fig. 4 and Fig. 9) on BS500 (Pengra et al., 1999, Tab. 1) with 0.5*S/m* NaCl brine. The Berea Sandstone 500 in their study had slightly higher permeability (κ=*571mD*) and lower formation factor (*F=11.8*) than our BS500 core sample. Their measurements are taken within the first two days of saturation using a low frequency AC (0-70Hz) driving force (Pengra et al., 1999). The NaCl brine conductivity range in their research is from 0.5 *S/m* to 6.38*S/m*. Electric signals with high signal to noise ratio are recorded; even the saturation brine has a high conductivity of 6.38*S/m*.

4.3 High Frequency AC Seismoelectric Measurements on BS500

4.3.1 Experiment Apparatus

To measure the seismoelectric signals induced by high frequency acoustic waves (10 kHz to 120 kHz), we use a plate sample of BS500. A rectangular BS500 plate, 2.54*cm* in width and 15 cm in height and length, is taken from the same Berea Sandstone 500 block as the cylindrical core samples used for the DC streaming potential measurement. The plate sample is held by two thin Lucite boards, one on each side, and placed stably in a water tank. Fig. 4-5 shows the schematic of the experiment set-up. The size of the water tank is large enough to separate the seismoelectric signals induced in the rock sample and reflections from the tank walls. Mesh *Ag/AgCl* electrodes are glued to the plate to record voltages between the electrode and the ground. This strong coupling between the rock and electrode minimizes the vibration of the electrode induced by the acoustic wave.

The acoustic source (Hydrophone Celesoc, model LC-34) excites a sine wave in 10 kHz to 120 kHz frequency range. A high power function generator (HP3314A) forms the initial sine burst. This signal goes through a linear power amplifier (AC Techron, 3620 Linear Amplifier) and the signals are amplified up to 100*V*. The high voltage signals are applied to the source hydrophone to generate an acoustic sine wave in the water container. The sampling rate is 1000 ns. For each trace we record 512 points. The filter range is set from 300 Hz to 500 kHz, which is broad enough to include all the dominant acoustic and electric signals. To reduce random noise, we use the averaging function of the oscilloscope. Each trace in the

electric array data is the average of 512 sweeps. Good shielding, to eliminate the outside noise, is also very important for weak signal detection. Some good practices include the following: effectively grounding the computers, oscilloscope, and the shielding line of the point electrode; placing the transducers and electrodes completely in water; shutting down unnecessary electric sources and grounding the water tank.

4.3.2 Quantification of Acoustic Pressures

Prior to the seismoelectric measurements, we first need to quantify the acoustic wave field in our model. Two aspects are examined: 1) frequency dependent voltage sensitivity of the receiver hydrophone; 2) choice of source wavelet.

Fig. 4-6 shows the set-up for to calibrate the frequency dependent voltage sensitivity of the receiver hydrophone. We use a newly purchased Brüel & Kjær Type 8103 hydrophone, whose sensitivity chart is given in Fig. 4-7, as a standard receiver. This standard hydrophone gives stable voltage sensitivity in the frequency range of 10 kHz to 100 kHz. There are some fluctuations beyond 100 kHz as observed in Fig. 4-7. The accurate voltage sensitivities for individual frequencies are given in Tab. 4-1.The transformation between the acoustic pressure *Pa* and recorded electric voltage *V* is given as:

$$k = 20 \log_{10} \frac{K_1}{K_0}. \tag{4-1}$$

Here, k is the voltage sensitivity listed in Tab. 4-1 for each frequency. K_1 is the ratio of V/μPa at each frequency and K_0 is 1V/μPa. We place the receiver hydrophone right behind

the front Lucite board as shown in Fig. 4-6. The distance between the source hydrophone and receiver hydrophone is 21.5*cm*.

Choice of the source wavelet is another important issue in the determination of acoustic wave field. The high power function generator (HP3314A) can generate a continuous sine wave, single sine pulse and multi-cycle sine bust (e.g., five-cycle sine burst and ten-cycle sine burst) as shown in Fig. 4-8. The continuous wave represents a monochromatic signal. However, a standing wave can be generated in the water tank when we excite a continuous wave. In this case, the amplitude of the acoustic wave field is very sensitive to the location of the receiver and frequency. The acoustic pressure at the receiver location can vary dramatically at different frequencies due to the standing wave.

The "pro" of using single sine plus is to obtain better resolution in the time domain. Transmitted and reflected waves can be distinguished and separated in time domain waveforms. The "con" of single plus is the complexity in the frequency domain. On the contrary, the five-cycle sine wave is simple in frequency content while more difficult to pick direct arrivals in time domain.

When the source wavelet is a single sine pulse with center frequency of 10 kHz to 120 kHz, Fig. 4-9 shows the waveforms recorded by the receiver hydrophone. In the time domain, direct arrival at 0.14*ms* can be clearly identified. Reflections from the water tank walls are also shown in the later part of the waveform at around 0.2*ms* 0.44*ms*. All traces in Fig. 4-9 are normalized with the same scaling factor. In Fig. 4-10, we show the transferred acoustic pressure at the receiver location as a function of frequency. Pressure (with the unit of *Pa*) is

calculated from the amplitude of direct arrivals (with the unit of V) in Fig. 4-9 using the voltage sensitivity chart listed in Tab. 4-1.

The curve in Fig. 4-10 shows the system response for acoustic pressure, which convolves the frequency response of source hydrophone, receiver hydrophone and receiving system. Given the frequency response curve in Fig. 4-7 from 10 kHz to 120 kHz for the receiver hydrophone, we can deduce the source hydrophone has a central frequency around 60kHz to 80 kHz from Fig. 4-10. Received acoustic pressures above 40 kHz are larger in magnitude than those below 40 kHz. Similarly, Fig. 4-11 shows the received acoustic waveforms with five sine burst excitation. For the frequencies above 100 kHz, direct arrivals (at about 0.14ms) can be clearly distinguished from the later reflections (at about 0.2ms) in time domain. Below 100 kHz, the superposition of reflection on the 3rd to 4th cycles of direct arrivals can be observed. Below 40 kHz, the amplitude of direct arrivals is small and reflections are superposed on the 1st to 2nd cycle of direct arrivals. It is difficult to distinguish different components for five-cycle sine burst in time domain, especially in the low frequency range. In the range of 40 kHz to 100 kHz, we can use the signals before 0.2ms to determine the acoustic amplitude. Below 40 kHz, we find the 3rd and 4th cycle have the most stable and similar amplitude. Thus, we always use the mean of the 3rd and 4th cycle as the picked pressure value.

4.3.3 Quantification of Seismoelectric Signal

We now analyze the converted electric field recorded by the mesh electrode, which is placed at the same location as the acoustic hydrophone (shown in Fig. 4-5). As we have

mentioned before (section 4.3.1), the electrode is glued very close to the surface of the rock plate to minimize its vibration induced by the acoustic wave. Taking away the rock plate in Fig. 4-5, we hang the mesh electrode in the water at the same location. When the acoustic wave hits the electrode, we could barely record any signal with amplitude above the noise level. The influence of the earth's magnetic field has also been experimentally proved to be negligible (Zhu and Toksöz, 2003).

Received electric signals excited by single sine pulse in 10 kHz to 120 kHz frequency range are shown in Fig. 4-12 with 0.012*S/m* NaCl brine. All traces in Fig. 4-12 are normalized with the same scaling factor, which is 1000 in the absolute value (26 is equivalent to 1μV). At the very front of the waveform, there is a sine wavelet coming at almost time zero with large amplitude. This is an induced electric signal from the excitation of the source wavelet. This induced electric signal possesses a similar shape to the source wavelet in time domain. A clear arrival at around 0.14*ms* can be observed in the later part of the waveform. This electric signal has a time shift with respect to the corresponding direct arrival in acoustic waveform (Fig. 4-10). From the arrival time and shape, we can tell it is the seismoelectric signal converted from the acoustic wave. Reflections in the later part of the waveform also generate seismoelectric signals. Compared with direct arrivals, those reflections from the water tank walls are much smaller in amplitude. Thus, the corresponding converted electric signals are not quite observable in the electric waveform.

Similarly, received electric signal excited by five cycle sine burst is shown in Fig. 4-13 with 0.012S/m NaCl brine. Electric influence from the source is clearly shown at the very

beginning in all the traces. Electric signals are converted from the direct arrivals at around 0.14*ms*. Reflections are smaller in amplitude and superimposed on direct arrivals. Below 40 kHz, electric influence at the very front begins to interfere with the converted seismoelectric signals at 0.14*ms*. This makes it difficult to accurately determine the amplitude of seismoelectric signals in the time domain in low frequency range. Fortunately, there exists a similarity among different cycles of five cycle sine bust, especially the 3rd and 4th cycles. Below 40 kHz, we first recover a complete five cycle for the induced electric signal arriving at time zero by duplicating the 3rd cycle twice. Then we can subtract the constructed complete five cycles from the original wavetrain in the time domain. In this way, seismoelectric signals are decomposed from the electric influence from the source. Similar to acoustic signals, we always use the mean value of cycles 3 and 4 as the picked electric signal amplitude below 40 kHz. The same processing is done for the seismoelectric signals collected with 0.048*S/m*, 0.95*S/m*, 0.2*S/m* and 0.4*S/m* conductivity NaCl brines.

4.4 Experimental SE Coupling Coefficients and Comparison with Pride's Theory

4.4.1 Experimental AC Voltage Coupling Coefficients

We have quantified the absolute values of acoustic pressure and its converted seismoelectric voltage from the time domain waveforms. The seismoelectric voltage coupling coefficients can be calculated by the picked electric voltage divided by the acoustic pressure

for each frequency. As we have mentioned before, calculations in time domain are more reliable. Especially for single sine pulse, different components can be easily distinguished. Now we look at the frequency composition of the received signals excited by two different wavelets. We enlarge the seismoelectric signal arriving at around $0.14ms$ excited by 80 kHz sine pulse (trace No. 12 in Fig. 4-12) and plot it in Fig. 4-14 (a). Its frequency spectrum is shown in Fig. 4-14 (b). The seismoelectric signal excited by 80 kHz five cycle sine burst is also shown in time domain (Fig. 4-15 (a)) and frequency domain (Fig. 4-15 (b)). Five cycle sine bust gives more accurate representation in frequency. Its FFT is close to a delta function with a peak at 80 kHz. Single sine pulse, on the other hand, contains more frequency content. Its FFT is close to a Sinc function with peak frequency at 75 kHz. This slight shift in the central frequency is caused by the transient nature of single sine pulse. For five cycle sine burst, we can simply assign the seismoelectric voltage coupling coefficients to each excitation frequency. For single sine burst, we assign the seismoelectric voltage coupling coefficients to the peak frequency in its spectrum, which may vary slightly from its excitation frequency.

4.4.2 Pride's Formula for AC SE Coupling Coefficient

The macroscopic governing equations controlling the coupled acoustics and electromagnetic of porous media are derived from first principles by Pride in 1994 (Pride, 1994). His approach is to volume average the equations in the fluid and solid phases while allowing the boundary conditions that exist on the fluid-solid interface. Derived equations have the form of Maxwell's equations coupled to Biot's equations with coupling occurring in

the flux-force (or transport) relations (see detail in Appendix D). His version of the frequency dependent electrokinetic coupling coefficient is expressed as:

$$\frac{L(\omega)}{L_o} = [1 - i\frac{\omega}{\omega_c}\frac{m}{4}(1 - 2\frac{\chi_d}{\Lambda})^2(1 - i^{\frac{3}{2}}\frac{\chi_d}{\delta})^2]^{-\frac{1}{2}}, \quad (4\text{-}2)$$

where L_o is the low frequency limit of the coupling coefficient, $\omega_c = \phi\eta/\alpha_\infty \kappa_0 \rho_f$ is the so-called transition frequency, ϕ is porosity, κ_0 is DC permeability, α_∞ is the tortuosity, η is the fluid viscosity, *m* is a dimensionless parameter defined as $m = \phi\Lambda^2/\alpha_\infty \kappa_0$, Λ is the weighted volume to surface ratio as introduced previously, $\delta = \sqrt{\eta/\omega\rho_f}$ is so-called viscous skin depth, χ_d is the Debye length as introduced previously.This electrokinetic coupling coefficient, L, equals to the multiplication of voltage coupling coefficient Ks by the brine saturated rock conductivity.

From Eq. 4-2, we can see that the frequency dependence of the seismoelectric coupling coefficient is closely related to the transport and geometrical parameters of the porous medium. The four key parameters are ϕ, κ_0, α_∞ and Λ, which are independent of each other. Although each individual parameter could vary greatly from rock to rock, the dimensionless parameter *m* is relatively stable for different porous media. Both laboratory and numerical evidence suggests that when ϕ, κ_0, α_∞ and Λ are independently measured, *m* lies in the range $4 \leq m \leq 8$ (Johnson et al., 1986, 1987; Charlarix et al., 1988; Kostek, 1992; Pride, 1993, 1994) for a variety of porous media raging from grain packings to networks of variable radii tubes. Based on the thin electric double layer assumption, the correction term $1 - 2\chi_d/\Lambda$ represents, at most, a few percent correction. Thus, to the first order, the frequency

dependent coupling coefficient (Ks or L) is determined by the transition frequency ω_c and their DC value (Ks_o or L_o).

For BS500, we have the laboratory measurements value of ϕ and κ_0, which has been listed in Tab. 3-5. For Λ parameter, we calculated it from the electric field distribution in the μCT image (shown in Tab. 3-4). Tortuosity, $\alpha_{\infty,}$ is calculated as the multiplication of formation factor, F, and porosity, ϕ (Brown, 1980). We use the laboratory values for formation factor, F, and porosity (Tab. 3-5) to get a tortuosity value of *2.96*. Debye length is calculated as a function of electrolyte concentration using Eq. 3-8 and is shown in Tab. 3-5. Taking all the parameters into Eq. 4-2, we can quantify the frequency dependence of the coupling coefficient with respect to their DC values in our experiment.

4.4.3 Comparisons and Discussions

We have experimentally determined DC voltage coupling coefficients Ks_o for BS500 saturated with 0.012*S/m*, 0.048*S/m*, 0.95*S/m*, 0.2*S/m* and 0.4*S/m* NaCl brines (Fig. 4-4). Combined with the frequency dependence determined by Eq. 4-2, the high frequency seismoelectric voltage coupling coefficient, $Ks(\omega)$, and DC voltage coupling coefficients, Ks_o, is predicted as the blue lines in Fig. 4-17 for different conductivity brines. The low frequency limit is essentially the DC voltage coupling coefficientsKs_o. Together plotted are the experimental results of seismoelectric coupling coefficients in the 10 kHz to 120 kHz frequency range using single sine pulse (colored dots in Fig. 4-17). Similarly, five cycle results are compared with theoretical predictions in Fig. 4-18.

It appears that the best match between experimental data and theoretical prediction is in the 40 kHz to 100 kHz frequency range for both sine pulse and five-cycle burst. This is due to the large acoustic pressure amplitude within this frequency range (Fig. 4-10). Below 40 kHz, the acoustic pressure greatly drops and consequently the seismoelectric signals are weak. This can be observed in the 1st to the 7th trace in Fig. 4-12 and Fig. 4-13. Especially for the five cycle sine burst, it is more difficult to pick the amplitude of converted electric signal under the superposition of source electric influence. In Fig. 4-18, we can see the discontinuity between the front part (10 kHz to 40 kHz) and the back part (50 kHz to 120 kHz) of the experimental data.

However, for single sine pulse, we observe a convex-up-trend in the experimental data above 100 kHz. This is consistently shown for all five conductivities. One explanation for this is that single sine pulse is not monochromatic in the frequency domain. Higher frequency sine pulse has a broader frequency spectrum. Thus, the non-central frequency components will contribute more in the high frequency range. Also the central frequency of seismoeletric signals can be slightly different from the excitation central frequency due to the transient nature of single sine pulse. This convex-up-trend is not observed in the five-cycle experimental data above 100 kHz. Five cycle sine burst gives better resolution and accurate representation in the frequency domain.

We plot the results for each conductivity separately in Fig. 4-19 to Fig. 4-23. Overall speaking, single sine pulse data gives a better match to the theoretical curve than five sine burst at all five conductivities. Experimental values are closer to theoretical values for low

conductivity brines than high conductivity brines. In the high conductivity region, some of the experimental data can differ from the theoretical value by a factor of two to three, especially for those under 40kHz. This is also due to the smaller coupling coefficient at high brine conductivity and consequently the weaker seismoelectric signals.

4.5 Summary

In this Chapter, we study the seismoelectric response of a fluid saturated porous permeable rock. Quantitative AC seismoelectic measurement at high frequencies (10 kHz to 120 kHz) on a rock sample is the main innovation in this Chapter. This work extends the quantitative SE measurement to the frequency range applied for acoustic borehole logging in the field and laboratory. DC and high frequency AC seismoelectric voltage coupling coefficients are measured on the BS500 cylinders and plate sample under the same experimental conditions in a water tank. We vary the saturation NaCl brine conductivities to be 0.012*S/m*, 0.048*S/m*, 0.095*S/m*, 0.2*S/m* and 0.4*S/m*. Both single sine pulse and five-cycle sine burst are excited as acoustic source wavelets. Recorded acoustic and seismoelectric signals are analyzed in both time and frequency domains. Given the BS500 rock μCT image and experimental measurements, we can quantify the four key rock parameters, which are ϕ, κ_0, α_∞ and Λ. Thus, the frequency dependence of the coupling coefficient can be determined theoretically using Pride's formula with respect to its DC value. The majority of the experimental data between 40kHz and 100kHz frequency range, where the source hydrophone transmit high amplitude acoustic pressure, are found to follow the theoretical

curve. Though the seismoelectric coupling coefficient decreases with the increasing frequency and brine conductivity, a measurable seismoelectric signal can still be recorded using effective high pressure generating devices. Conducting the acoustic and SE measurements in a water tank helps us to quantify the acoustic pressure transmitted into the rock. The overall data quality is better for single sine pulse than five-cycle sine burst due to its higher resolution and simplicity in the time domain. This is optimistic for field application where the high pressure transient is commonly adopted as the source wavelet.

Acknowledgements

We thank Professor Dale Morgan for his directions on the streaming potential measurements. We thank Dr. Peter Tilke from Schlumberger-Doll Research for providing us the μCT image of BS500 core sample. We thank Wave Smith from Schlumberger-Doll Research for providing us the BS500 cylinders and plate sample. We would also like to thank Dr. Jeffery Tarvin from Schlumberger-Doll Research for his helpful discussion on streaming potential measurements.

4.6 References

Amaefule, J. O., Wolfe, K., Walls, J. D., Ajufo, A. O. and Peterson, E.: 1986, Laboratory determination of effective liquid permeability in low-quality reservoir rocks by the pulse decay technique, *paper SPE 15149,* presented at the 56th California Regional Meeting, Soc. of Pet. Eng., Oakland, Calif, April 2-4.

Ahmed, M. U.: 1964, A laboratory study of streaming potentials, *Geophysics Prospect*, **12,** 49-64.

Block, G. I. and Harris, J. G.: 2006, Conductivity dependence of seismoelectric wave phenomena in fluid-saturated sediments, *Journal of Geophysical Research*, **111**, B01304.

Bockris, J. O'M. and Reddy, A. K. X.: 1972, Modern aspects of electrochemistry, *Plenum, New York.*

Brown, R. J. S.: 1980, Connection between formation factor for electrical resistivity and fluid-solid coupling factor in Biot's equations for acoustic waves in fluid-filled porous media, *Geophysics*, **45**, 1269-1275.

Charlaix, E., Kushnick, A.P. and Kojima, H.: 1988, Experimental study of dynamic permeability in porous media, *Phys. Rev. Letter,* **61**, 159E-1598.

Debye, P. and Hückel, E.: 1923, Zur theorie der electrolyte, *Phys. Z,* **24,** 18E-206.

Dukhin, S. S. and Derjaguin, B. V.: 1974, Electrokinetic phenomena, *John Wiley and Sons, Inc.*

Debye, P. and Hückel, E.: 1923, Zur theorie der electrolyte, *Phys. Z,* **24,** 18E-206.

Garambois, S. and Dietrich, M.: 2001, Seismoelectric wave conversions in porous media: Field measurements and transfer function analysis, *Geophysics*, **66**, 1417-1430.

Geertsma, J.: 1974, Estimating the coefficient of inertial resistance in fluid flow through porous media, *Soc. Pet. Eng. J.*, **14**, 44E-450.

Gusev, I. and Horváth, C.: 2002, Streaming potential in open a packed fused-silica capillaries, *Journal of Chromatography A*, **948**, 203-223.

Helmholtz, H. V.:1879, Studien über electrische grenschichten, *Ann. Der Phys. und Chem.*, **7**,

337-387.

Ishido, T. and Mizutani, H.: 1981, Experimental and theoretical basis of electrokinetics phenoma in rock-water systems and its applications to geophysics, *Journal of Geophysical Research*, **86**, 1763-1775.

Johnson, D.L., Koplik, J. and Schwartz, L.M.: 1986, New pore-size parameter characterization transport in pours media, *Physical Review Letters*, 57, **n.20**, 2564-2567.

Johnson, D. L., Koplik, J. and Dashen, R.: 1987, Theory of dynamic permeability and tortuosity in fluid-saturated porous media, *Journal of Fluid Mechanics*, **176**, 379-402.

Jouniaux, L. and Pozzi, J. P.: 1995, Steraming potential and permeability of saturated sandstones under triaxial stress: Consequences for electrotelluric anomalies prior to earthquakes, *J. Geophys. Res.*, **100**, 10197-10209.

Kostek, S., Schwartz, L. M. and Johnson, D. L.: 1992, Fluid permeability in porous media: Comparison of electrical estimates with hydrodynamical calculations, *Phy. Rev. B.*, **45**, 186-195.

Minsley, B. J.: 2007, Modeling and inversion of self-potential data, *Ph.D. thesis, Massachusetts Institute of Technology.*

Morgan, F.D., Williams, E.R. and Madden, T.R.: 1989, Streaming potential properties of westerly granite with applications, *Journal of Geophysical Research,* **94,** 12449-12461.

Neev, J. and Yeatts, F. R.: 1989, Electrokinetic effects in fluid-saturated poroelastic media, *Physical Reviews B*, **40**, 913E-9141.

Overbeek, J. Th. G.: 1952, Electrochemistry of the double layer. In: *Colloid Science, Vol. 1, Irreversible Systems,* pp 11E-193. Elsevier, New York.

Packard, R. G.: 1953, Streaming potentials across glass capillaries for sinusoidal pressure, *Journal of Chemical Physics*, **21**, 303-307.

Perrier, F. E., Petiau, G., Clerc, G., Bogorodsky, V.: 1997, A one-year systematic studies of electrodes for long period measurements of the electric field in geophysical environments, *J. Geomag, Geolectr.*, **49,** 1677-1696.

Petiau, G.: 2000, Second generation of lead-lead chloride electrodes for geophysical applications, *Pure. Appl. Geophys.*, **157,** 357-382.

Pride, S. R. and Morgan, R. D.: 1991, Electrokinetic dissipation induced by seismic waves, *Geophysics*, **56**, 914-925.

Pride, S. R., Morgan, F. D. and Gangi, A. F.: 1993, Drag forces of porous-medium acoustics, *Phys. Rev. B.*, **45,** 4964-4978.

Reppert, P. M.: 2000, Electrokinetics in the earth, *Ph.D. thesis, Massachusetts Institute ofTechnology.*

Reppert, P. M. and Morgan, F. D.: 2002, Frequency-dependent electroosmosis, *Journal of Colloid and Interface Science*, **254**, 372-383.

Smoluchowski, M. von.: 1903, Contribution a la theorie de l'endosmose electrique et de quelques phenomenes correlatifs, *Bull. International de l'Academie des Sciences de Cracovie*, **8**, 182-200.

Sen, P.N. and Kan, R.: 1987, Electrolytic conduction in porous media with charges, *Phys. Rev. Lett*, **58**, 778-780.

Waxman, M. H and Smits, L. J. M.: 1968, Electrical conduction in oil-bearing sands, *Society of Petroleum Engineers Journal*, **8**, 107-122.

Zhu, Z. and Toksöz, M. N.: 2003, Seismoelectric measurements in cross-borehole models with fractures, *Proceedings of 6th SEGJ International Symposium,* Tokyo, Japan, 342-347.

Zhu, Z. and Toksöz, M. N.: 2005, Seismoelectric and electroseismic measurements in fractured borehole models, *Geophysics,* **70**, F4E-F51.

Zhu, Z., Toksöz, M. N. and Burns, D. R.: 2008, Electroseismic and seismoelectric measurements of rock samples in a water tank, *Geophysics,* **73,** E153-E164.

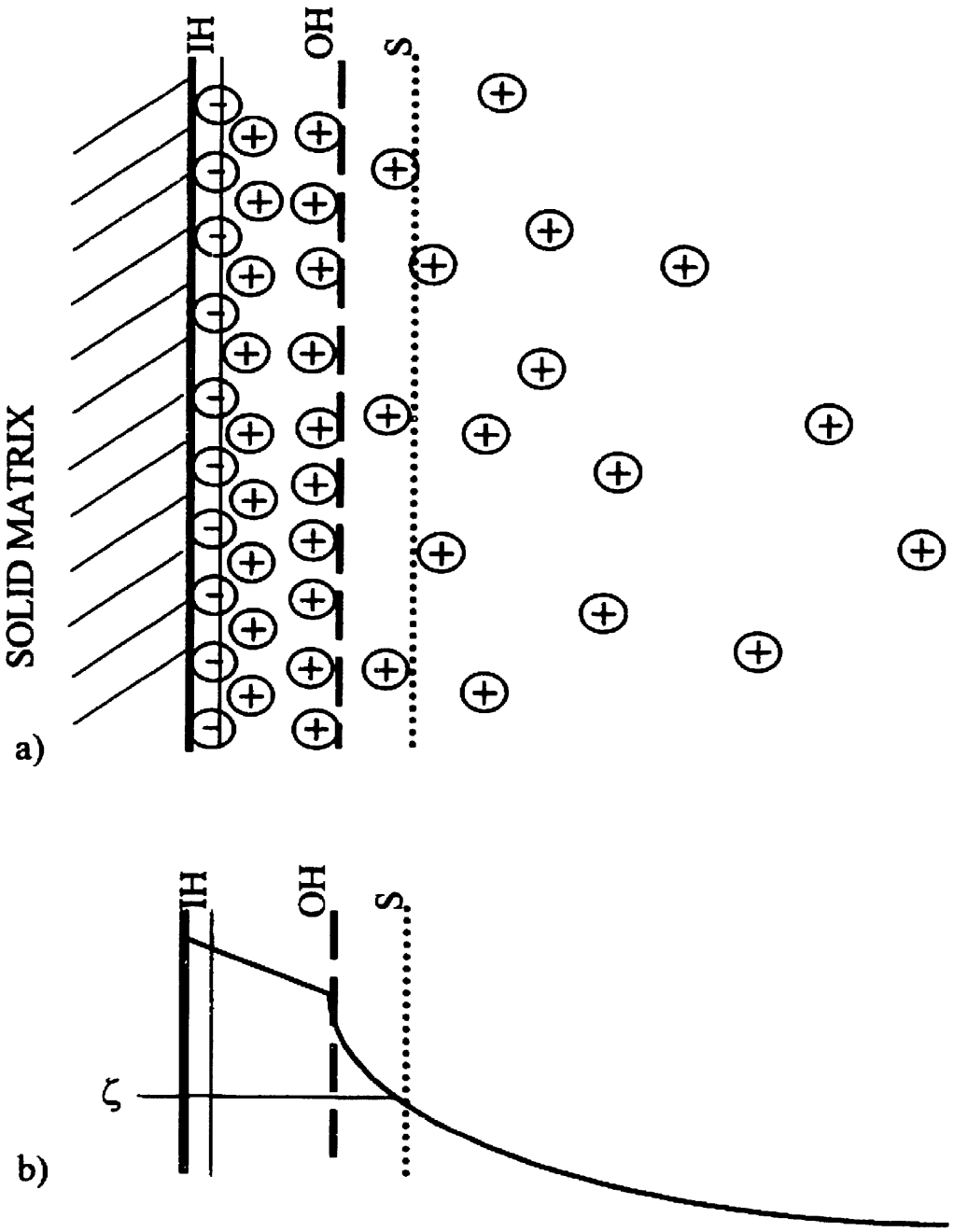

Figure 4-1: a) The Gouy-Stern EDL model. b) Potential distributions of the EDL model. The zeta potential, ζ, is the electric potential at the shear plane.

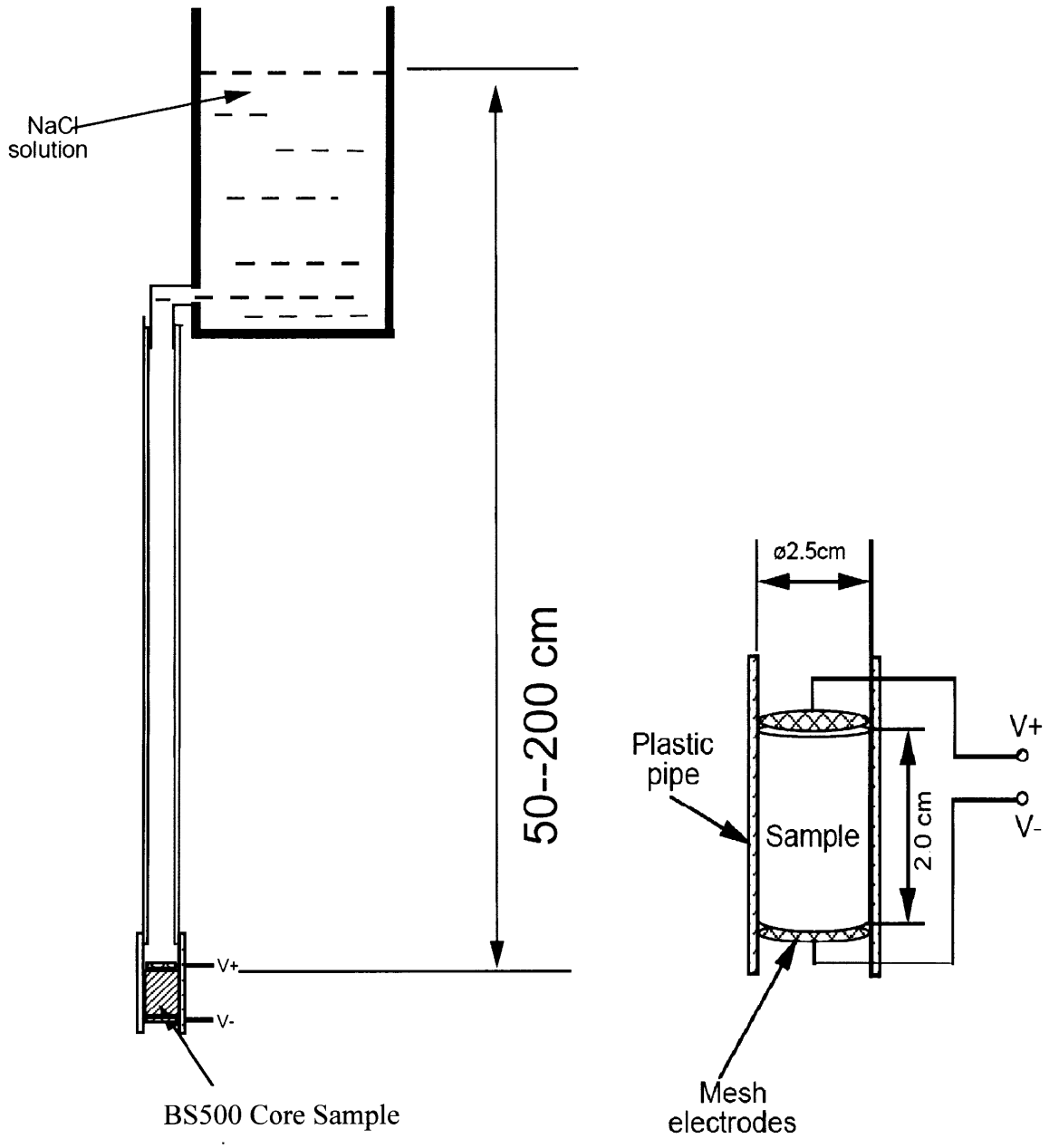

Figure 4-2: (a) Experimental system for measuring streaming potential, fluid rate, and sample resistance. The vertical distance between the top level of the sample and the top level in the bottle can be changed from 50cm to 200 cm. The streaming potential is measured between the Ag/AgCl mesh electrodes V+ and V-. (b) BS500 cylindrical core sample.

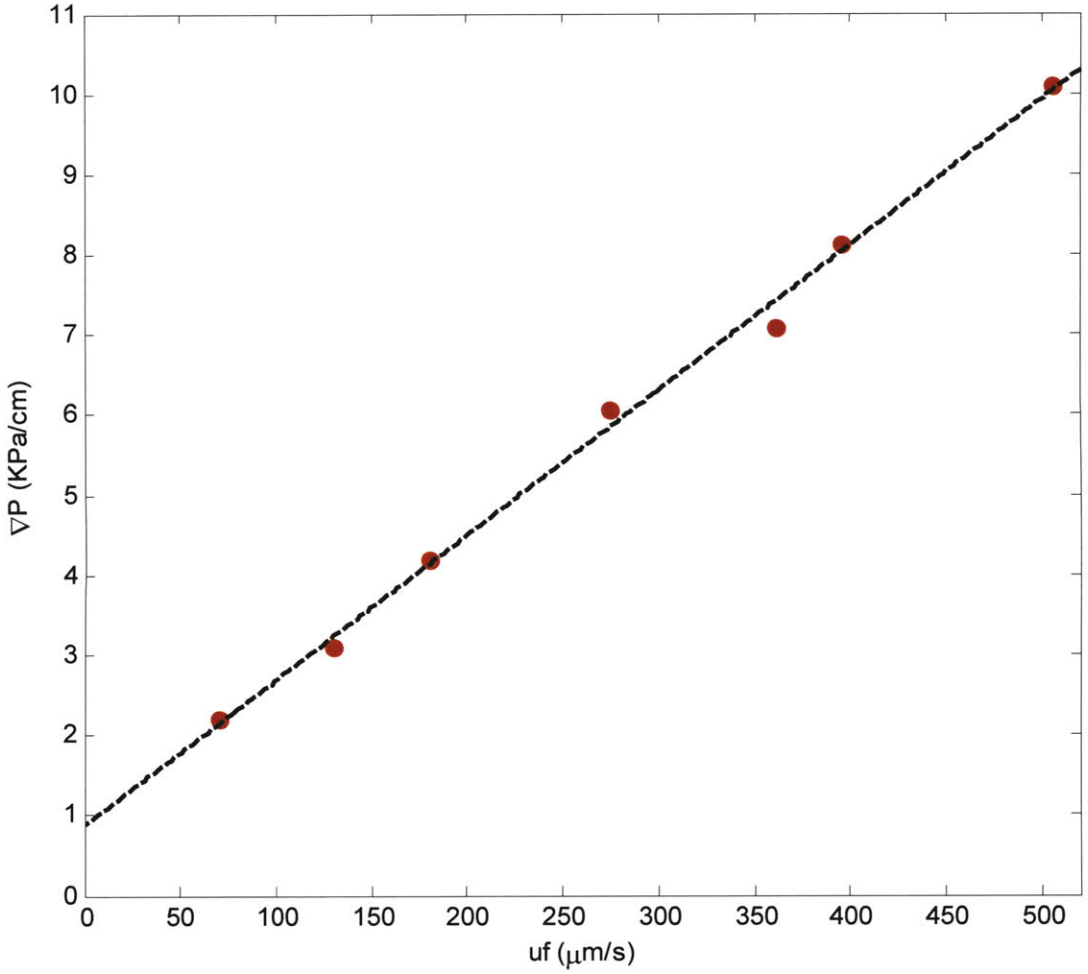

Figure 4-3: Cross plot of exerted pressure gradient ∇P (KPa/cm) and resulting Darcy velocity u_f ($\mu m/s$). The red circles are the measurements. All the permeability measurements are done within the first four hours after the saturation. Permeability can be extracted from the slope of the line fitted to the measured data (black dashed line) to be 390.9mD.

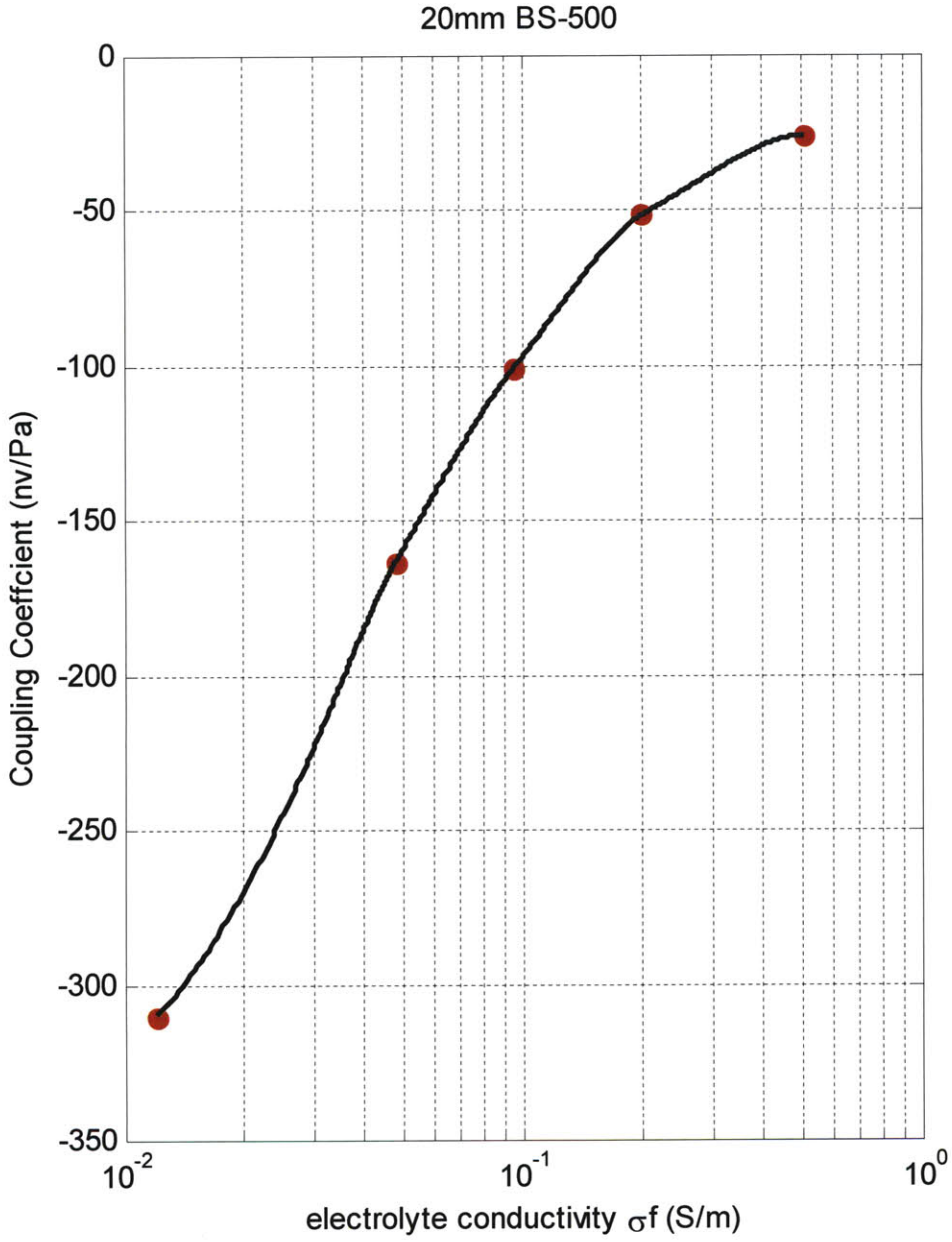

Figure 4-4: DC streaming potential coupling coefficients (with the unit of nV/Pa) as a function of NaCl brine conductivities (with the unit of S/m). Red circles are the experimental data points with the black curve smoothly connecting them.

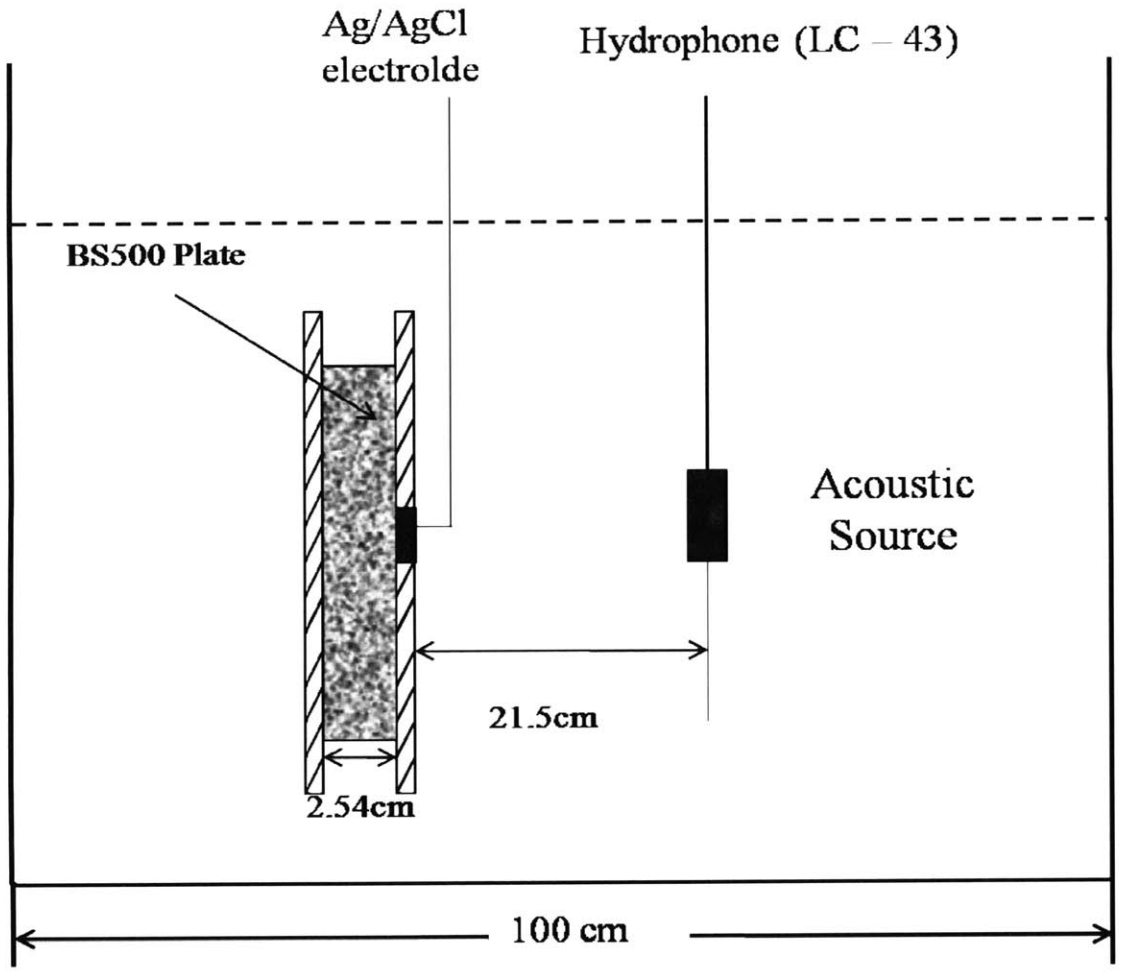

Figure 4-5: (a) Schematic of high frequency AC seismolectric experiment in a water tank. The length of the tank is 100*cm*. BS500 plate is held by two thin Lucite board stably in the water tank. Mesh *Ag/AgCl* electrodes are attached to both sides of the plate to record voltages between the electrodes and the ground. The acoustic source (Hydrophone LC-34) excites sine wave in 10 kHz to 120 kHz frequency range.

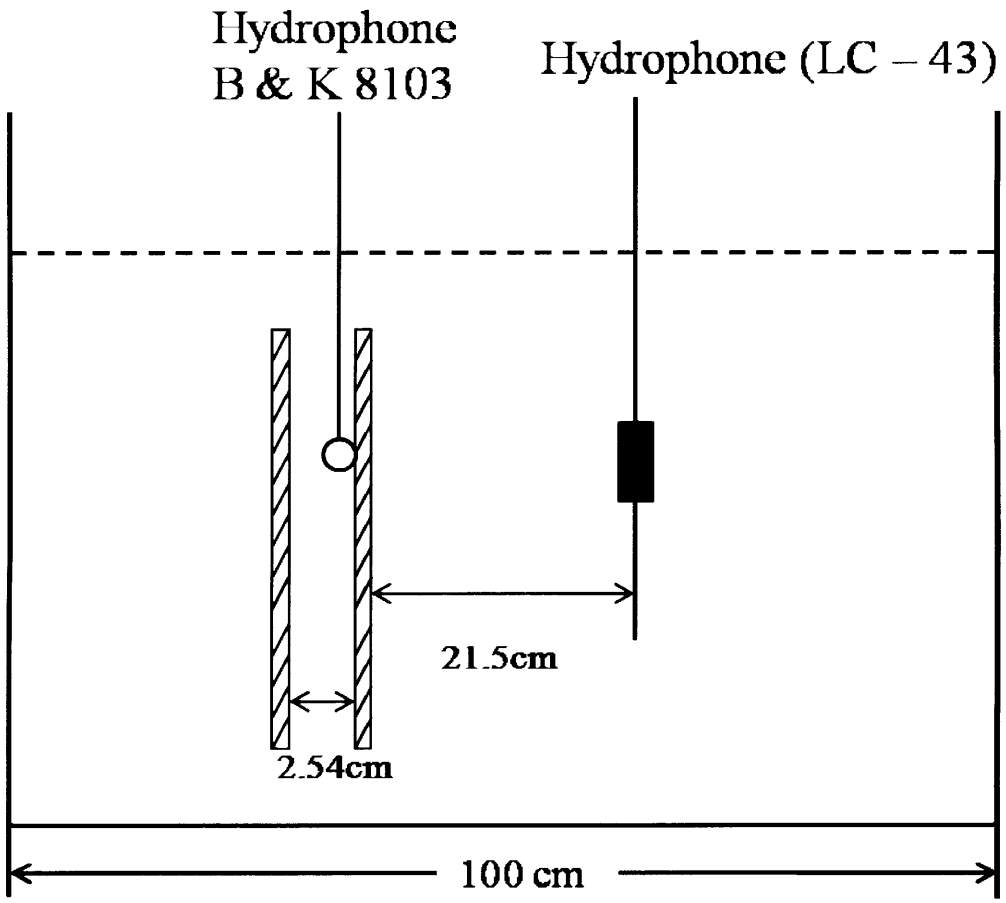

Figure 4-6: Calibration of the acoustic pressures at different excitation frequencies using standard hydrophone B&K 8103 before the seismoelectric measurements.

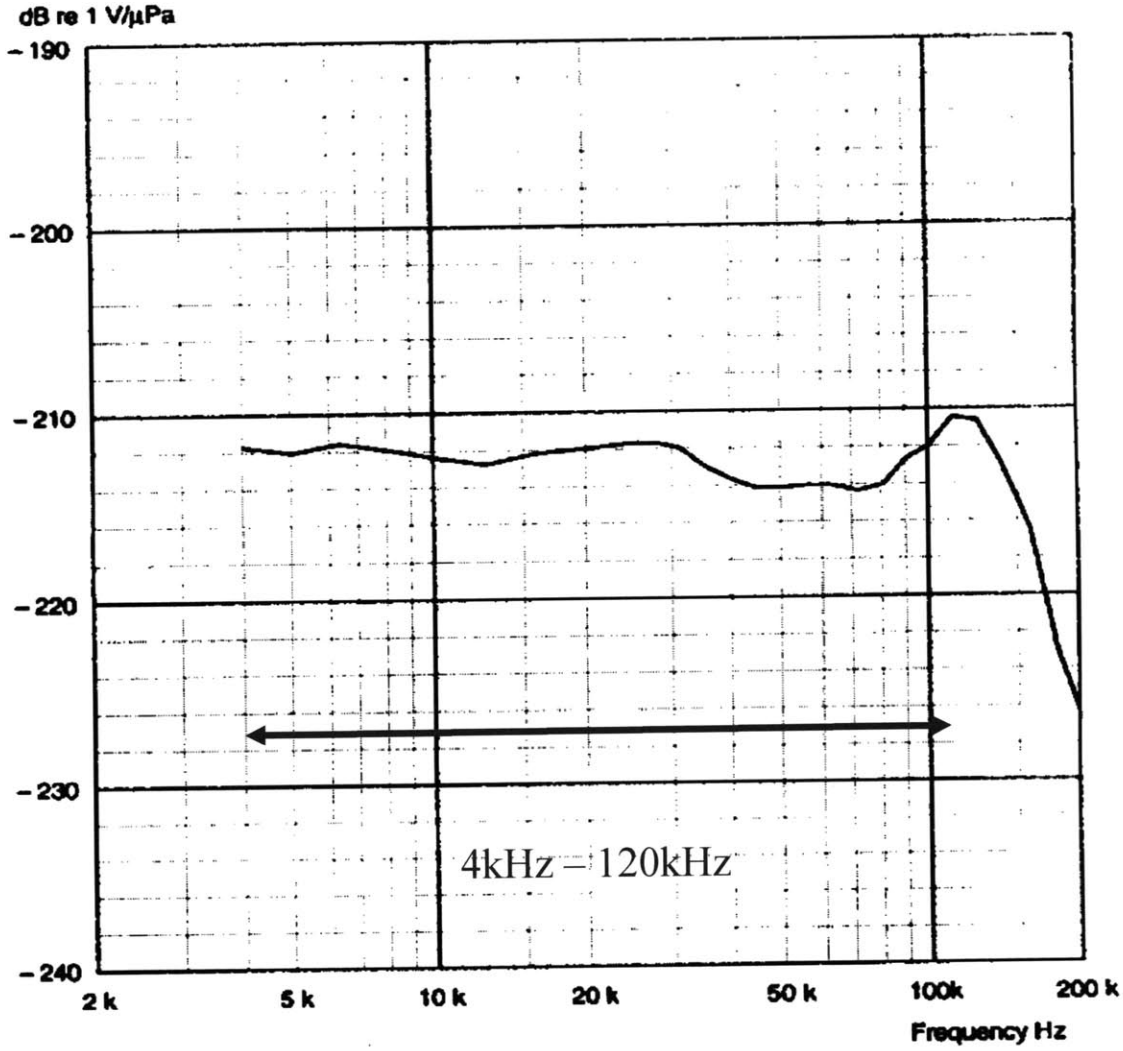

Fig 4-7. Voltage sensitivity response of Brüel & Kjær Type 8103 hydrophone in 4 kHz to 200 kHz frequency range.

Frequency (kHz)	Sensitivity (dB re 1V/μPa)		Frequency (kHz)	Sensitivity (dB re 1V/μPa)
4.0	**-211.2**		**50.0**	**-214.1**
5.0	**-211.7**		**56.1**	**-214.0**
6.3	**-211.3**		**63.0**	**-213.9**
8.1	**-211.7**		**71.0**	**-214.0**
10.0	**-211.9**		**80.0**	**-213.9**
12.5	**-212.1**		**90.0**	**-212.9**
16.0	**-212.1**		**100.0**	**-212.2**
20.0	**-212.0**		**112.0**	**-210.2**
25.0	**-212.0**		**125.1**	**-210.8**
28.0	**-212.1**		**140.0**	**-213.3**
31.5	**-212.2**		**160.0**	**-217.1**
35.5	**-213.0**		**180.0**	**-224.6**
40.1	**-213.5**		**200.1**	**-221.5**
45.1	**-214.1**			

Table 4-1: Voltage sensitivity for individual frequencies in 4kHz to 200kHz frequency range.

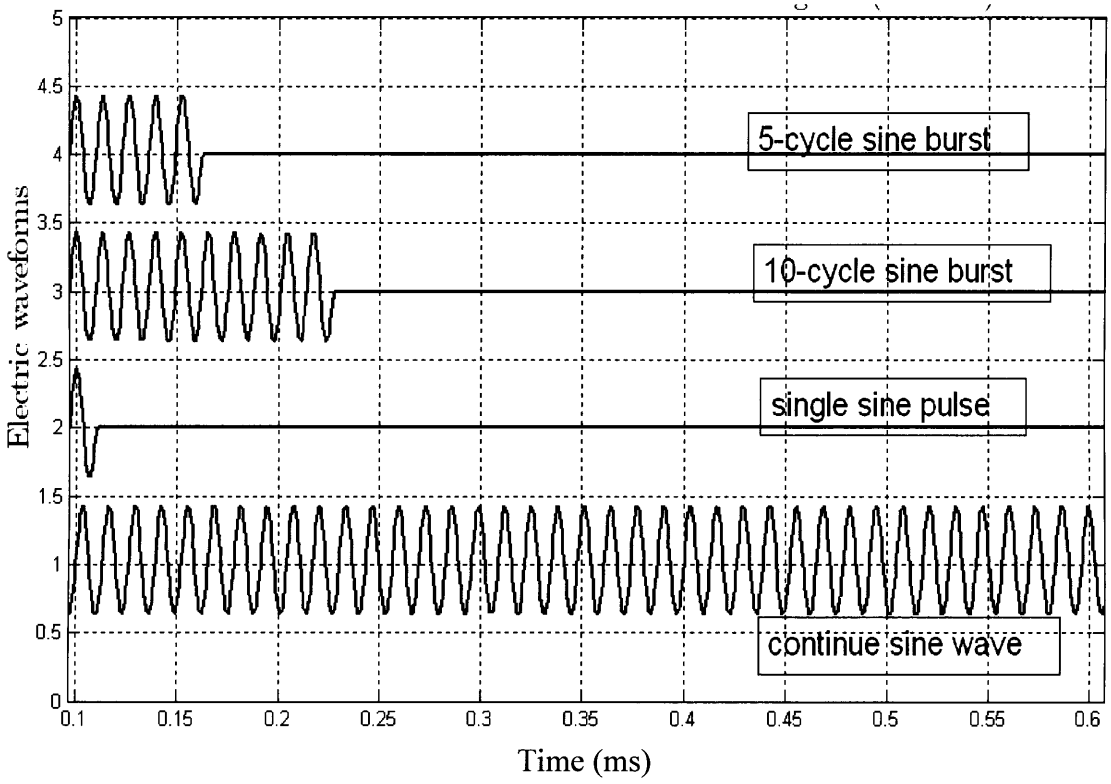

Figure 4-8: The high power function generator (HP3314A) can generate continuous sine waves, single sine pulse and multi-cycle sine bust (e.g., five-cycle sine burst and ten-cycle sine burst) in time domain.

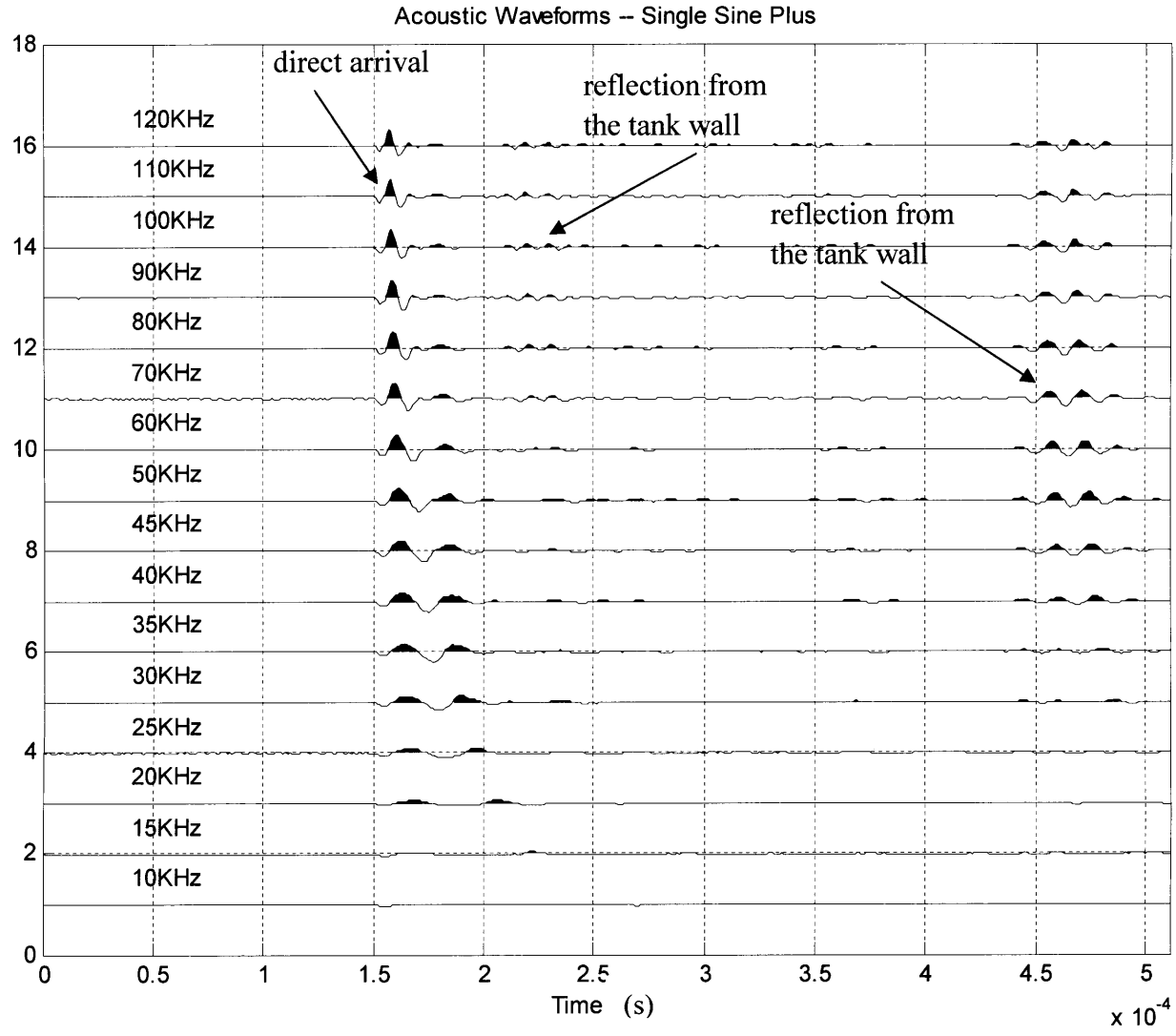

Figure 4-9: Acoustic waveforms received by B&K 8103 receiver hydrophone in Fig. 4-6. The source wavelet is a single sine pulse excited by LC-43 source hydrophone in Fig. 4-6. Source wavelet has a center frequency of 10 kHz to 120 kHz.

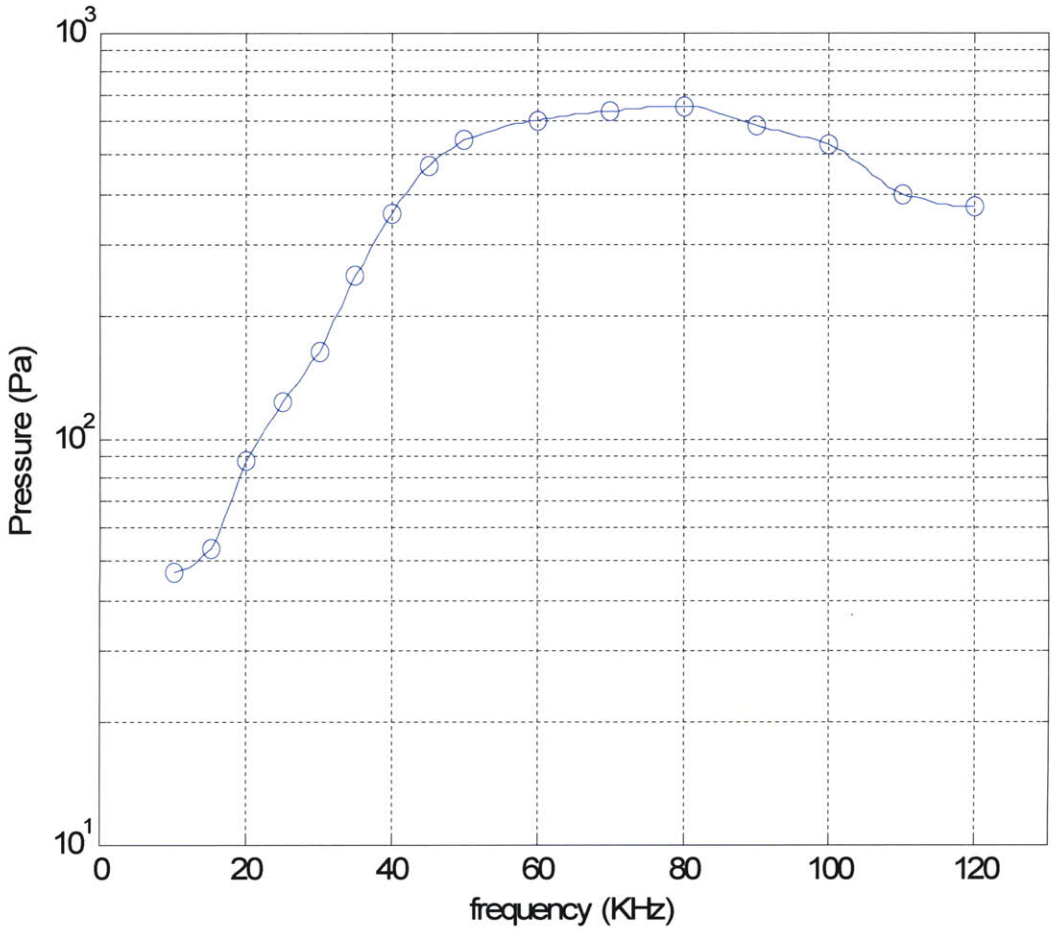

Figure 4-10: Received acoustic pressure (*Pa*) by hydrophone B&K 8103, which is calculated from the amplitude of the direct arrivals in Fig. 4-8 using the voltage sensitivity chart in Tab 4-1.

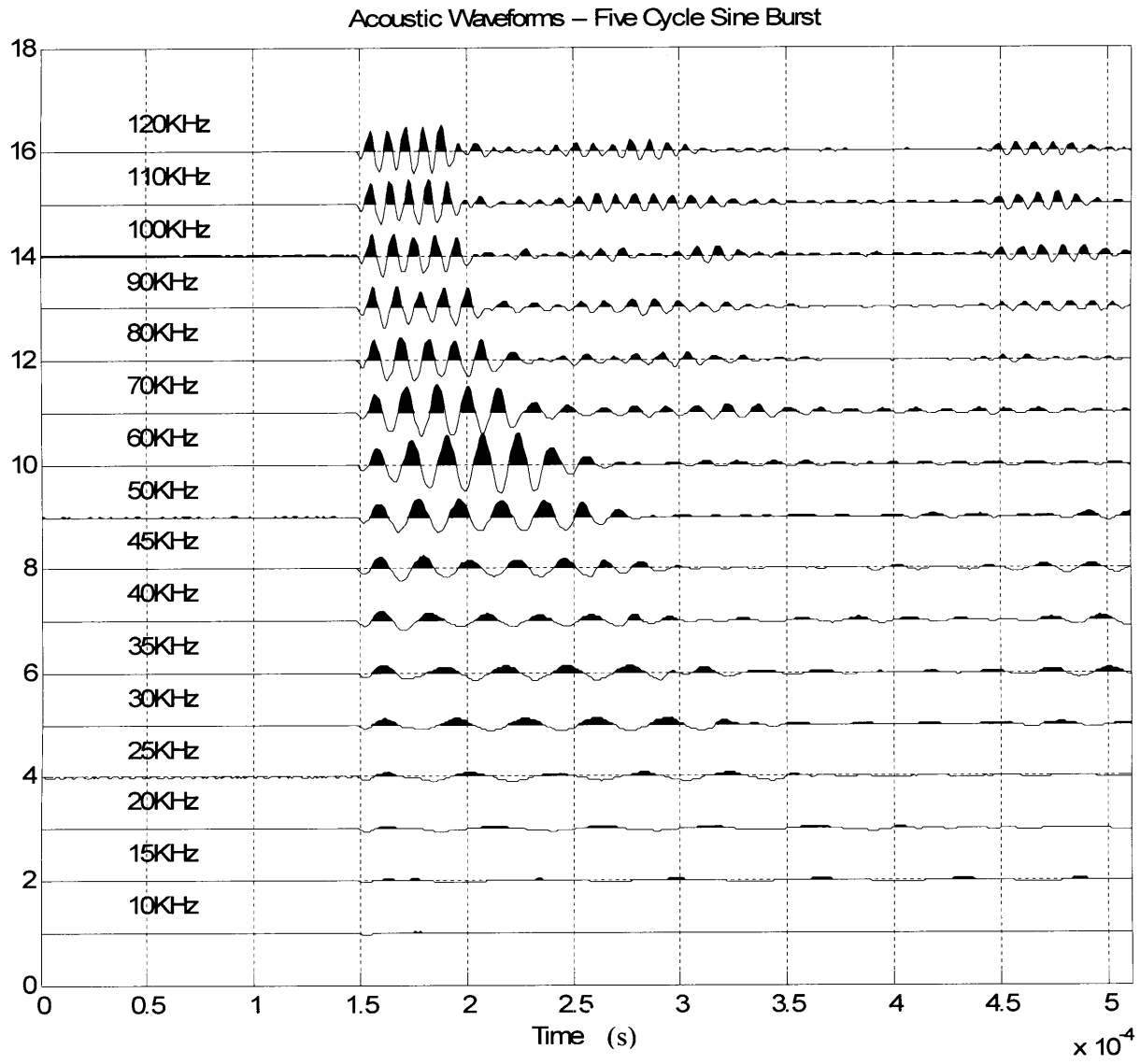

Figure 4-11: Acoustic waveforms received by B&K 8103 receiver hydrophone in Fig. 4-6. The source wavelet is a five-cycle sine burst. Source wavelet has a center frequency of 10 kHz to 120 kHz.

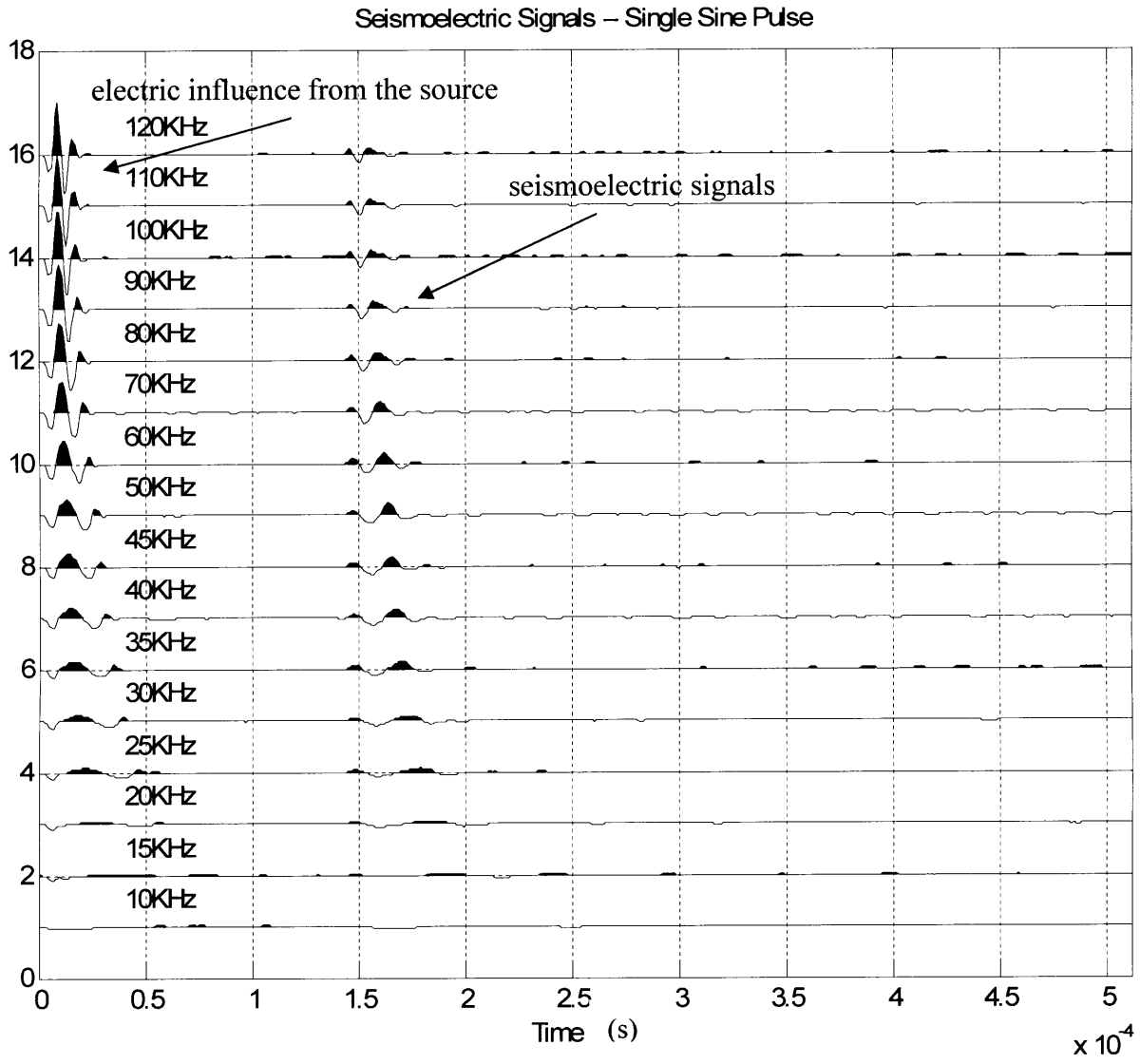

Figure 4-12: Seismoelectric signals recorded by the positive electrode (V+) in Fig. 4-5 for 0.012 *S/m* NaCl using single sine pulse from 10 kHz to 120 kHz. The electric influence from the acoustic source is recorded at the front of the waveforms. Seismoelectric signals converted from the direct arrivals in Fig. 4-9 are recorded at 1.4*ms*.

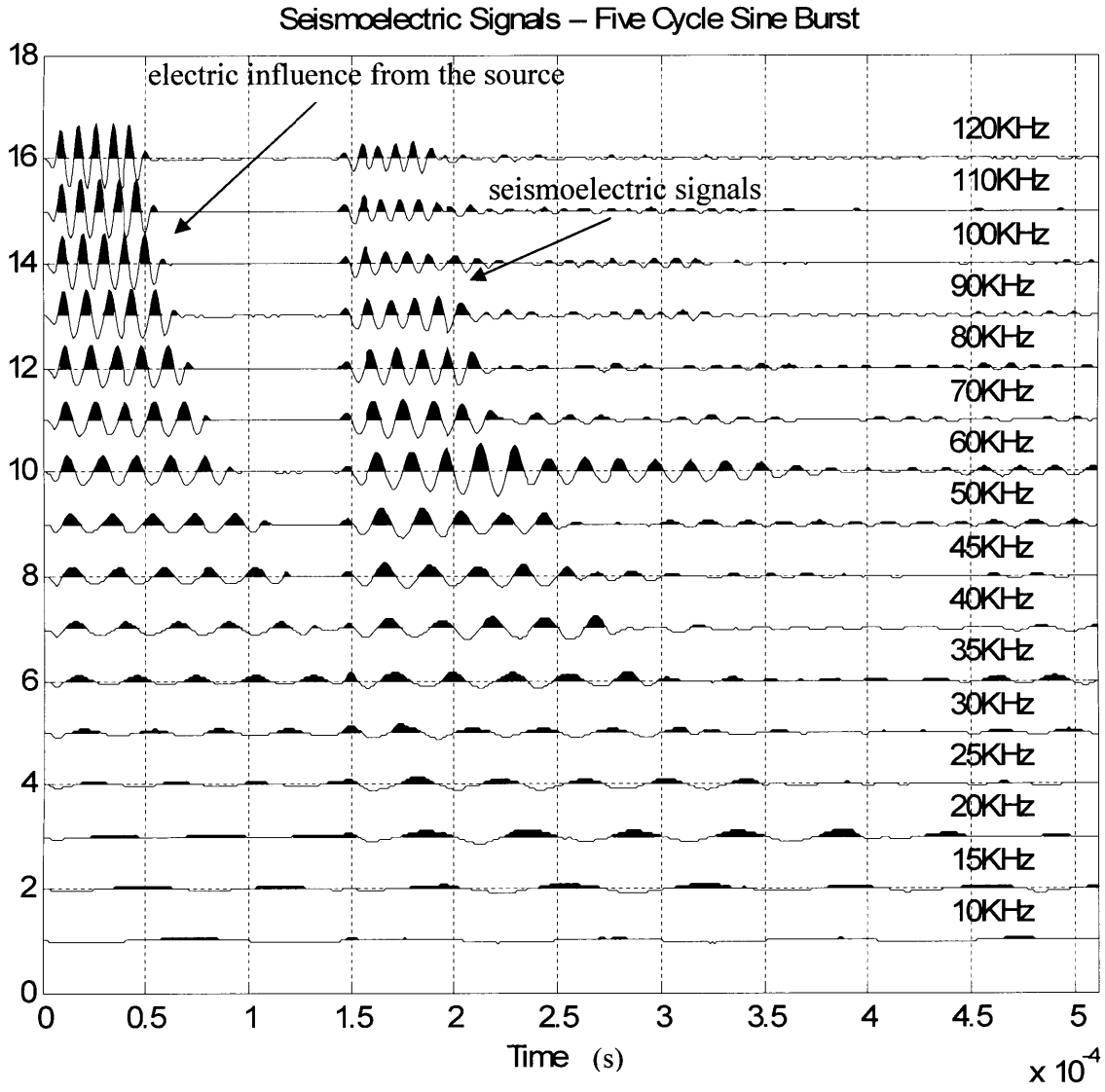

Figure 4-13: Seismoelectric signals recorded by the positive electrode (V+) in Fig. 4-5 for 0.012 *S/m* NaCl using five-cycle sine burst from 10 kHz to 120 kHz. The electric influence from the acoustic source is recorded at the front of the waveforms. Converted seismoelectric signals are recorded at 1.4*ms*.

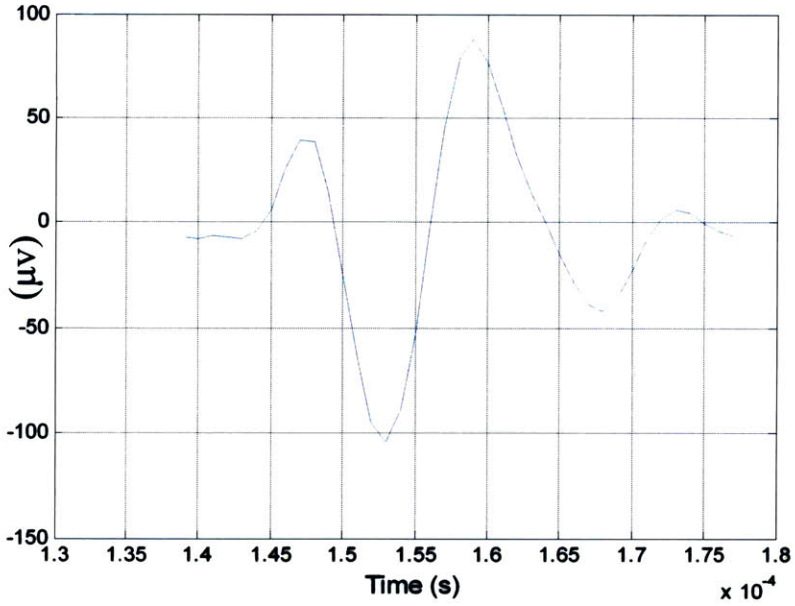

(a)

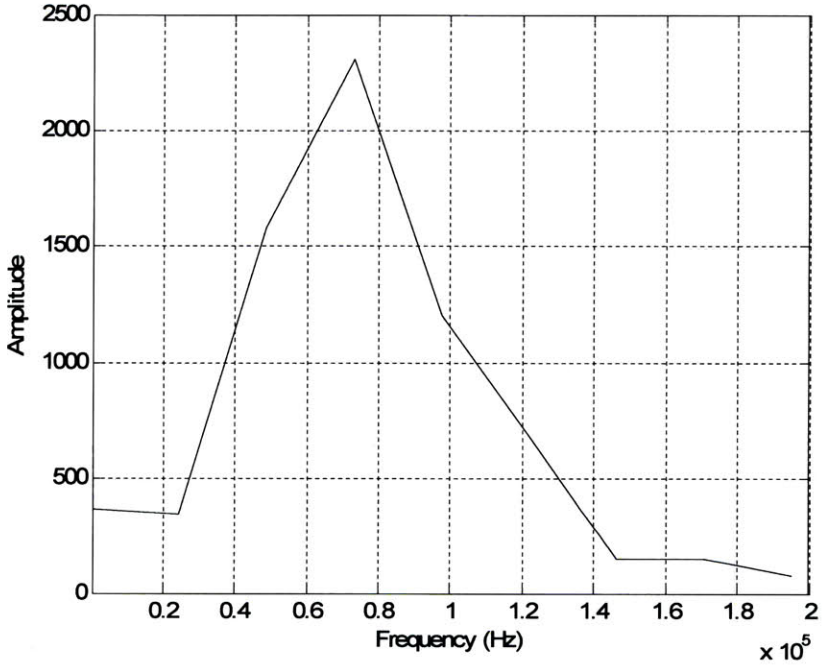

(b)

Figure 4-14: Seismoelectric signals of trace 12 in Fig, 4-12, which are excited by single sine pulse with center frequency of 80 kHz in the time domain (a) and frequency domain (b).

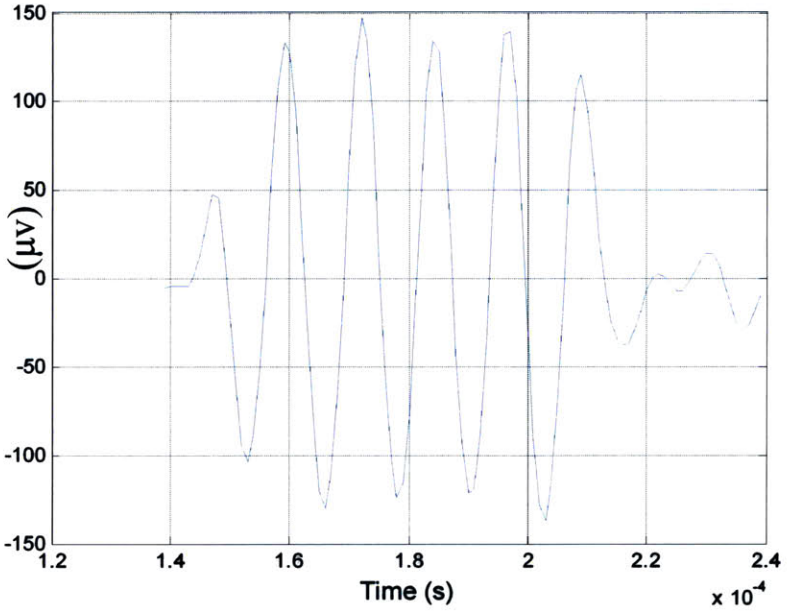

(a)

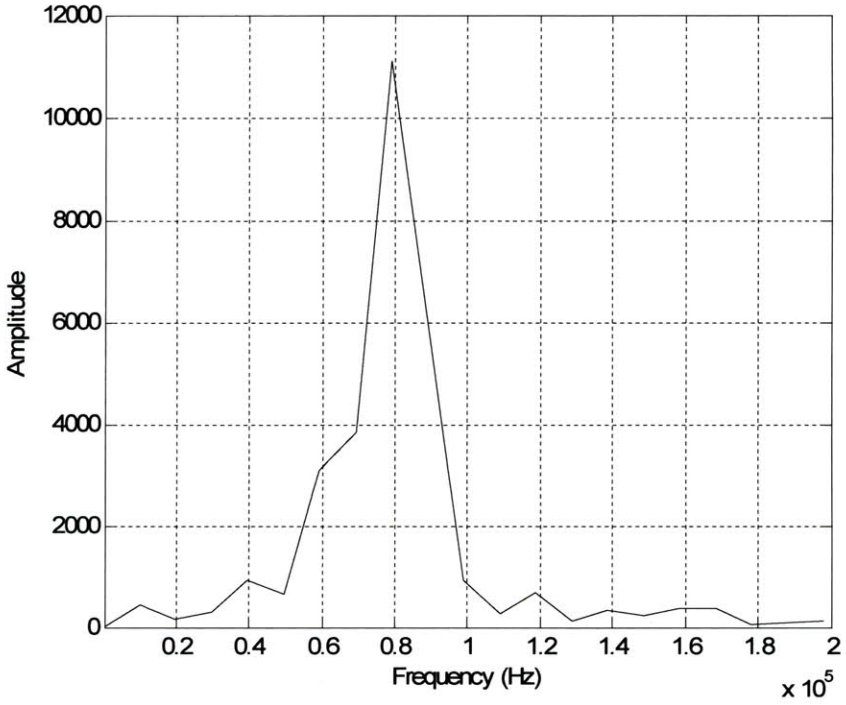

(b)

Figure 4-15: Seismoelectric signals of trace 12 in Fig, 4-13, which are excited by five-cycle sine burst with center frequency of 80 kHz in the time domain (a) and frequency domain (b).

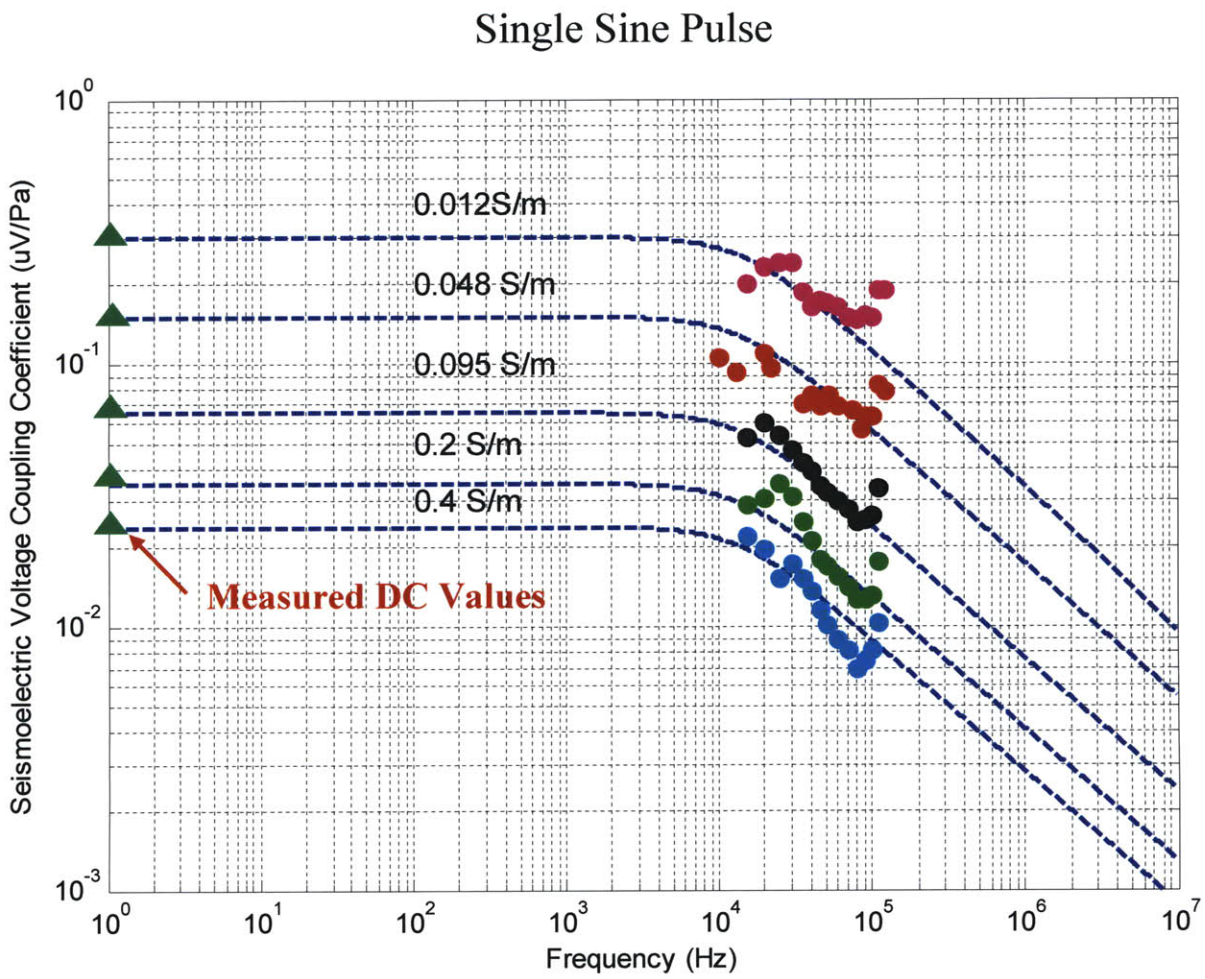

Figure 4-17: Seismoelectric voltage coupling coefficients (with the unit of $\mu V/Pa$) for Berea Sandstone 500 in DC and 10kHz to 120kHz frequency range using single sine pulse. The Berea Sandstone 500 core samples are saturated with NaCl brine with conductivities of 0.012 *S/m*, 0.048 *S/m*, 0.095 *S/m*, 0.2 *S/m* and 0.4 *S/m,* respectively. Dashed lines are the theoretical predictions of frequency dependent coupling coefficient using Eq. 4-2 and measured DC coupling coefficient (green triangles). Dots are the experimentally measured frequency dependent coupling coefficient.

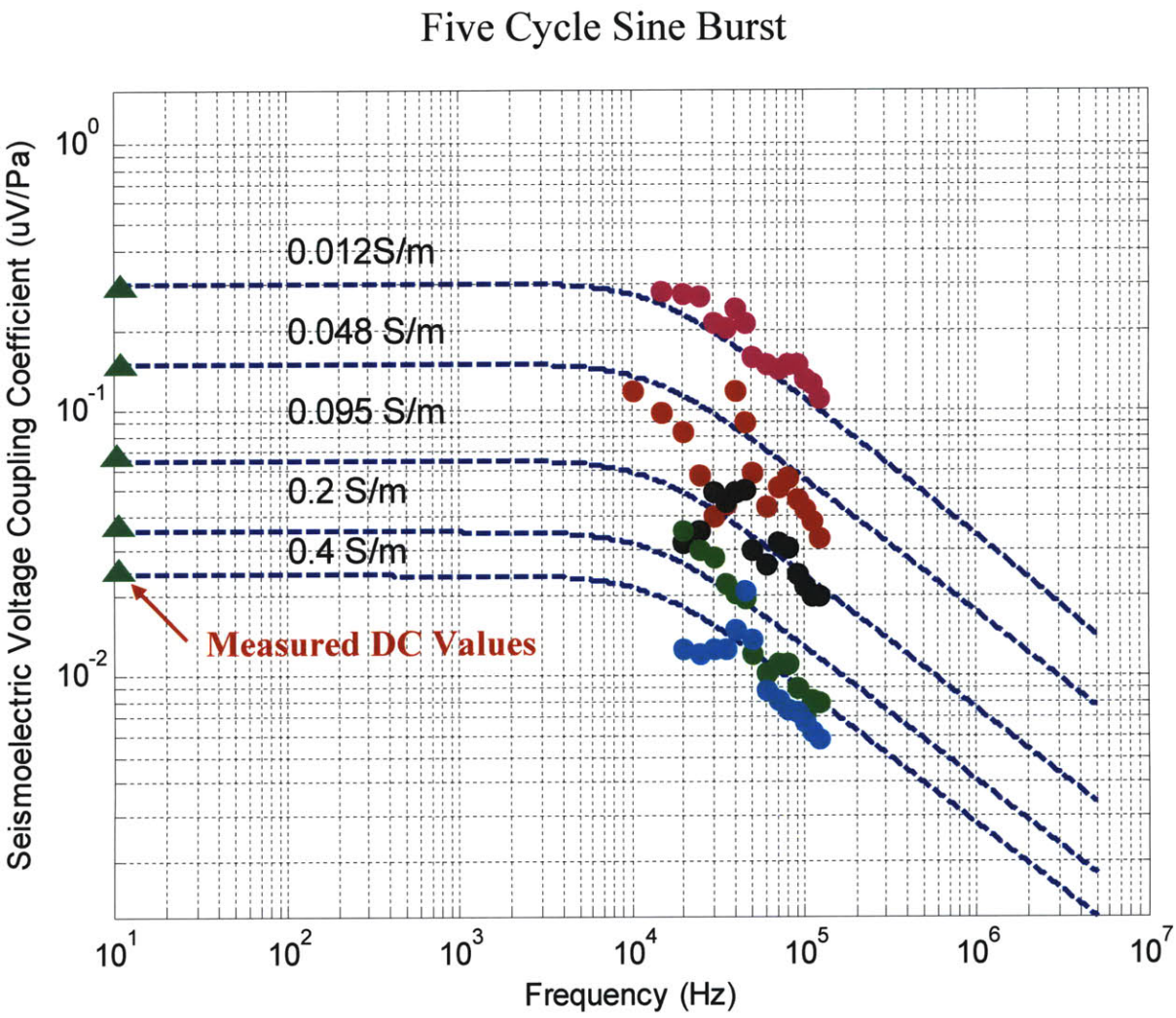

Figure 4-18: Seismoelectric voltage coupling coefficients (with the unit of $\mu V/Pa$) for Berea Sandstone 500 in DC and 10kHz to 120kHz frequency range using five-cycle sine burst. The Berea Sandstone 500 core samples are saturated with NaCl brine with conductivities of 0.012 *S/m*, 0.048 *S/m*, 0.095 *S/m*, 0.2 *S/m* and 0.4 *S/m,* respectively. Dashed lines are the theoretical predictions of frequency dependent coupling coefficient using Eq. 4-2 and measured DC coupling coefficient (green triangles). Dots are the experimentally measured frequency dependent coupling coefficient.

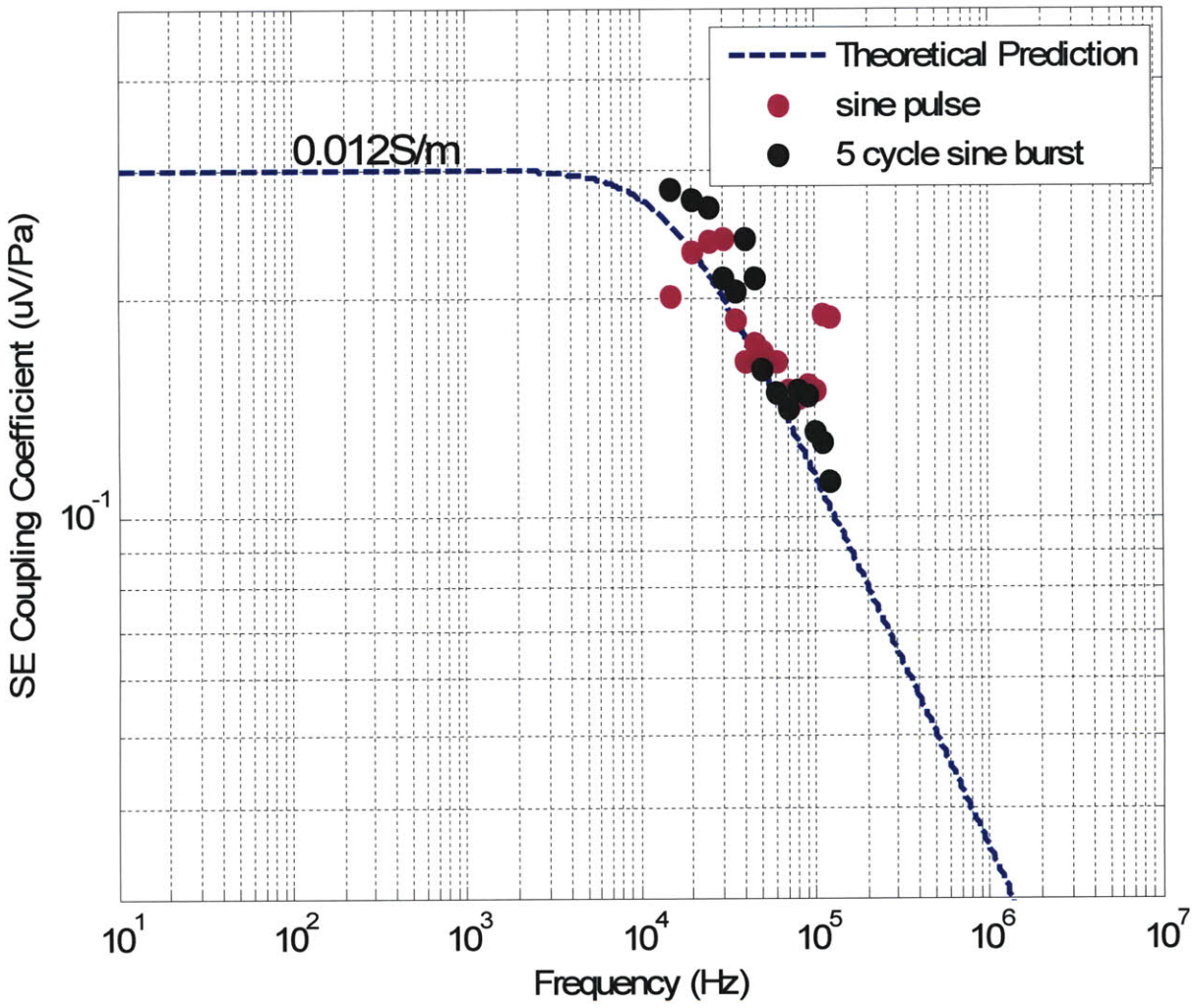

Figure 4-19: Seismoelectric voltage coupling coefficients (with the unit of $\mu V/Pa$) for 0.012 *S/m* NaCl using single sine wave and five-cycle sine burst, respectively.

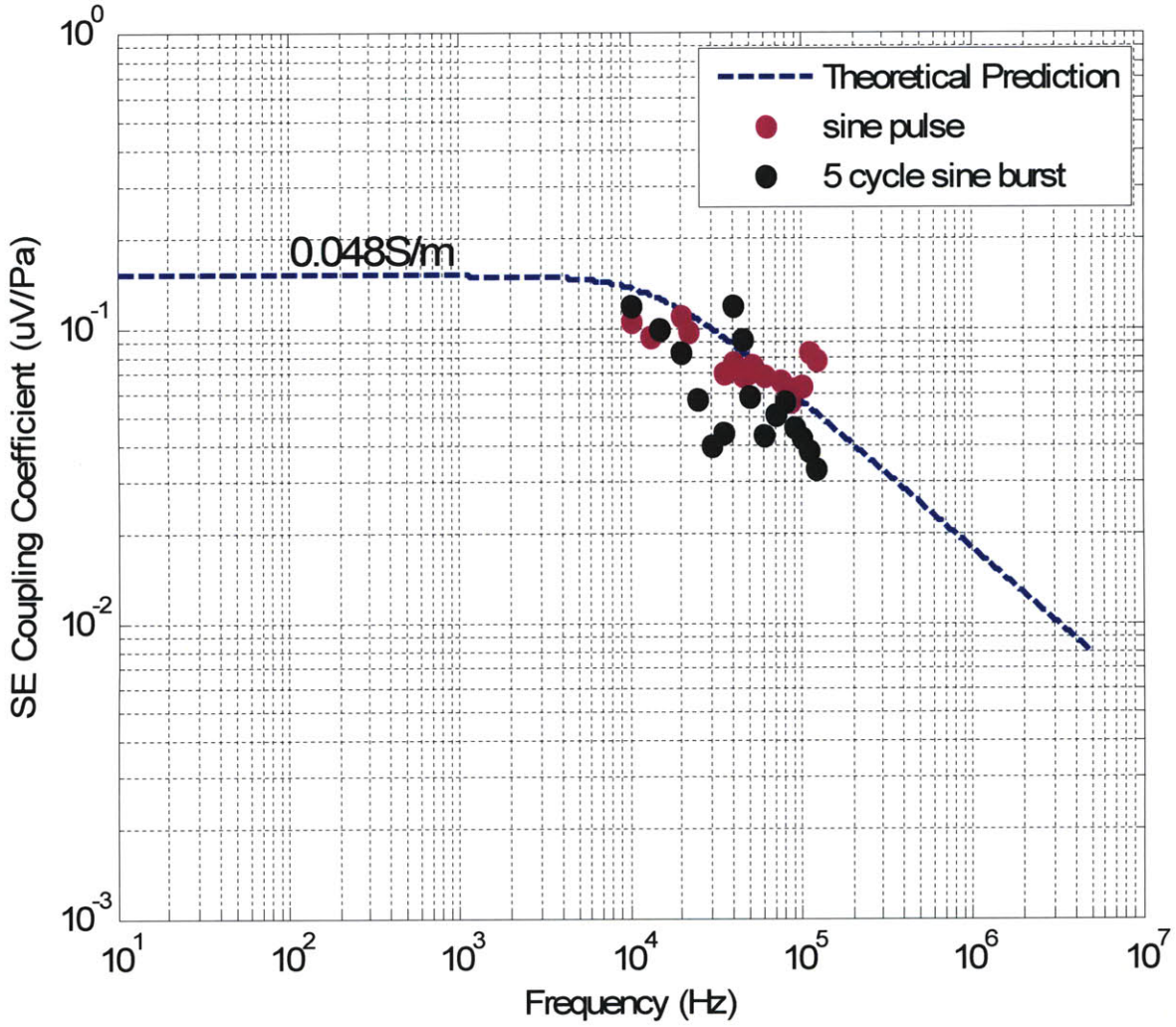

Figure 4-20: Seismoelectric voltage coupling coefficients (with the unit of $\mu V/Pa$) for 0.048 *S/m* NaCl using single sine wave and five-cycle sine burst, respectively.

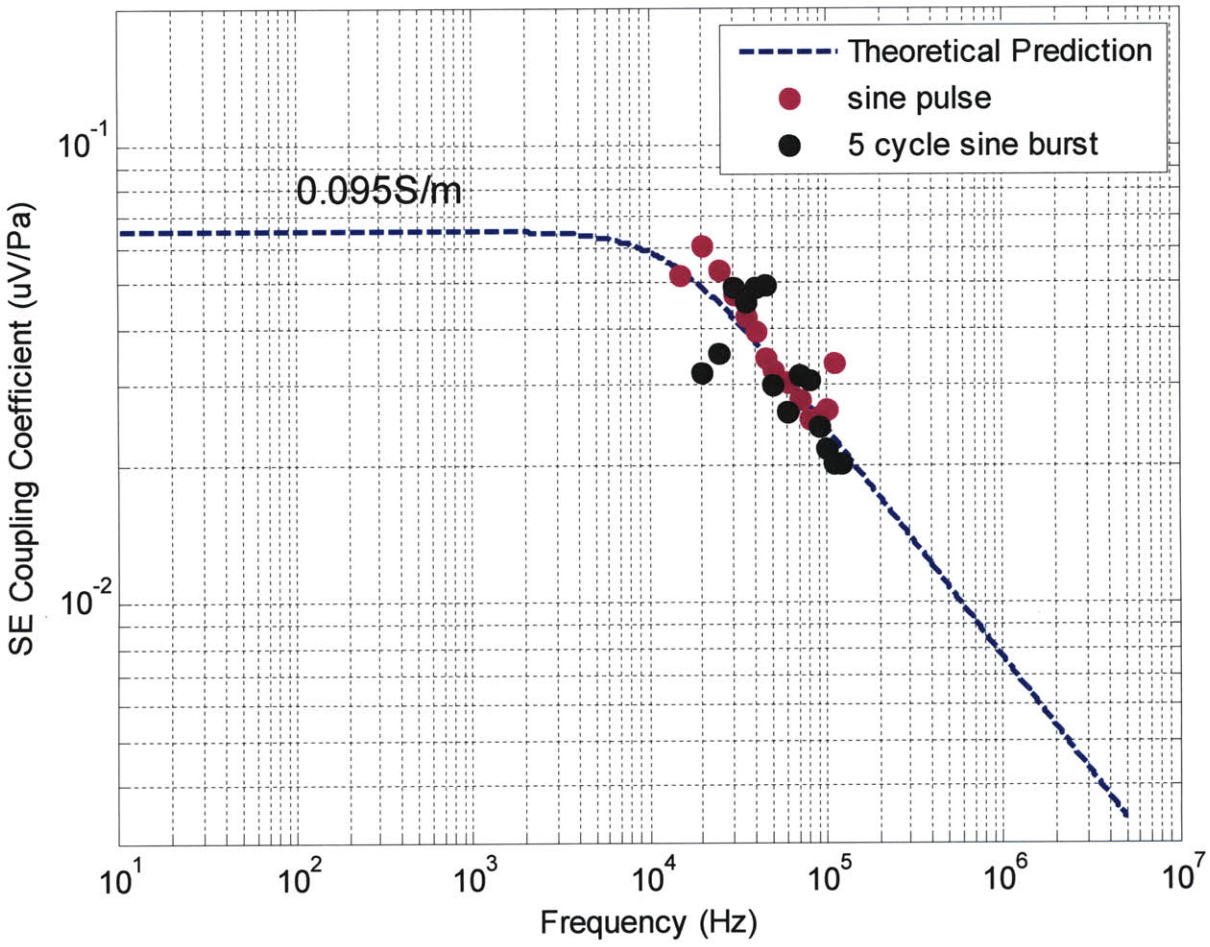

Figure 4-21: Seismoelectric voltage coupling coefficients (with the unit of $\mu V/Pa$) for 0.095 *S/m* NaCl using single sine wave and five-cycle sine burst, respectively.

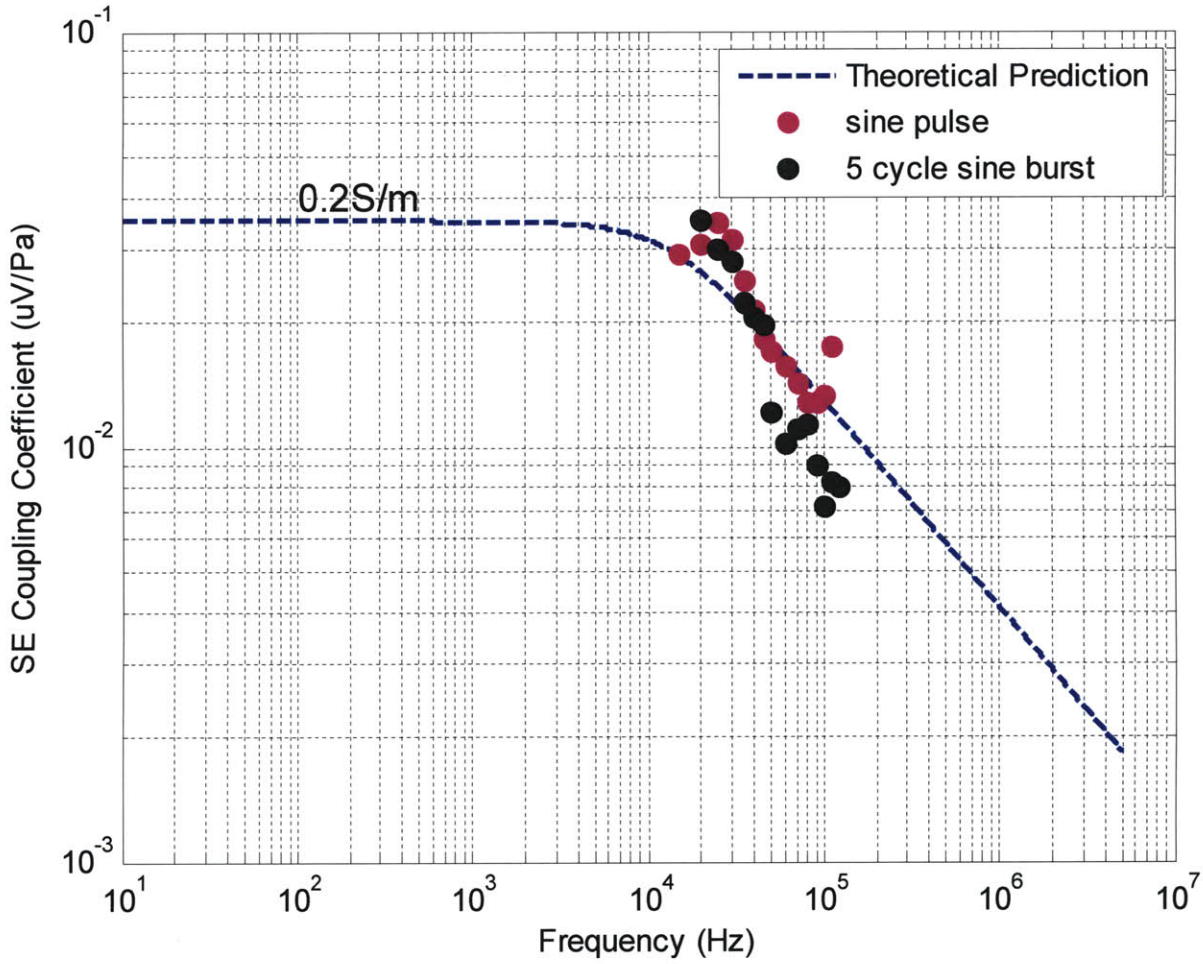

Figure 4-22: Seismoelectric voltage coupling coefficients (with the unit of $\mu V/Pa$) for 0.2 S/m NaCl using single sine wave and five-cycle sine burst, respectively.

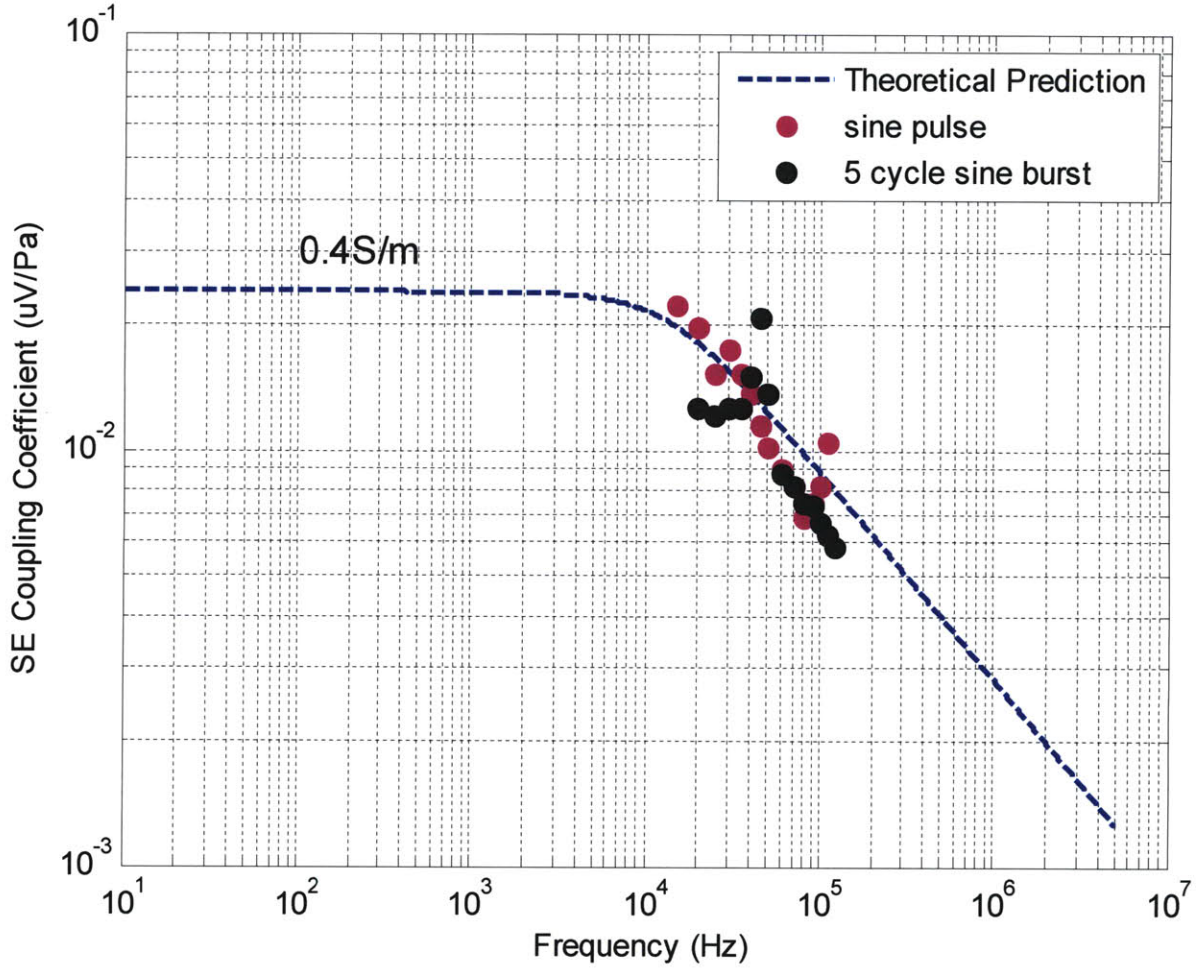

Figure 4-23: Seismoelectric voltage coupling coefficients (with the unit of $\mu V/Pa$) for 0.4 S/m NaCl using single sine wave and five-cycle sine burst, respectively.

Chapter 5

Conclusions

This thesis provides a systematic study of the transport and seismeolectric properties of porous permeable rock. Two basic scientific approaches, numerical modeling and laboratory measurements, are adopted to study the physics of the rock – fluid system. This work was divided into two parts to cover different aspects of the study.

I. Better understanding of transport and geometrical properties of fluid saturated rock from both pore scale modeling and laboratory measurements.

1. Numerical tools are built to compute different rock properties (e.g., porosity, electrical conductivity, surface conductivity, hydraulic permeability, pore surface area, Λ parameter) from 3-D microstructures.
2. Calculated results on synthetic sand pack (Finney pack) compare well with analytic solutions.

3. Computed values of porosity, surface area, electrical conductivity and hydraulic permeability compare well with laboratory measurements of the same properties for the Berea BS500 sandstone.
4. Reducing image resolution decreased calculated electrical conductivity and permeability. A large computation sample provides better representation of the rock.

II. Better understanding of the frequency dependent seismoelectric response of fluid saturated rock and its geophysical application – LWD SE – response from both numerical modeling and laboratory measurements.

1. Laboratory apparatus is designed to measure AC seismoelectric signal (10 kHz ~ 120 kHz) on BS500 samples with varying saturation brine conductivity.
2. Majority of the measured data were compared with Pride's theoretical model using transport and geometrical parameters of BS500 obtained from measurements and μCT image.

In the first part, numerical tools are built to compute different rock properties (e.g., porosity, electrical conductivity, surface conductivity, hydraulic permeability, pore surface area, Λ parameter) from 3-D microstructures. A staggered-grid finite difference (FD) scheme is applied to solve the Laplace equation for the electrical problem and Stokes equation for the hydraulic problem. The Laplace solver can handle different levels of conductivity contrast so that different saturations (gas, oil and brine) can be modeled. A three-phase conductivity

model developed on the binary representation of the microstructure, which is based on the geometric average of free electrolyte conductance and surface conductance in the EDL, is illustrated. Two different edge detection methods are applied to recognize surface voxel in binary image. One is a gradient based, first order differential method and the second one is a connectivity-number-based edge detection (CNED) method. The results from both edge detection methods are averaged to give the final surface area.

A family of synthetic sand packs – Finney pack with low, medium to high porosities is first applied to provide a benchmark of numerical methods with analytic solutions. Binary image of 200^3 Finney pack whose edge length equals $1/20$ of the original grain radius is generated for computation. Numerical results on 14 Finney packs with low, medium to high porosities compare well with the analytic rock physics models for formation factor, surface conductivity, permeability and specific surface area and Λ parameter. The effects of image resolution on computed physical properties are investigated using majority rule. Decreased resolution leads to decreased permeability and electrical conductivity. Image resolution has larger impact on low porosity microstructure than high porosity microstructure.

Then we implement all the numerical methods to the 3-D μCT micro tomography of a 23.6% porosity Berea Sandstone 500 (BS500) with 2.8 micron resolution. Five 400^3 sub-sets at different locations within the whole 1840^3 volume of BS500 μCT image are selected as representative computation units based on the porosity distribution. The computed physical properties varied between samples: formation factor by a factor of two (12 to 22), permeability by a factor of three (0.38 darcy to 1.05 darcy) and surface area from

$0.69\ m^2/g$ to $0.88\ m^2/g$. These variations are due to the heterogeneity of the BS500 at the *mm* scale. The average values of properties calculated for five samples compared well with laboratory measured values. To obtain representative values of physical properties, it is necessary to do calculations on several sub-samples. The effects of image resolution on computed physical properties were investigated. Decreased resolution leads to sharply decreased permeability and electrical conductivity. Optimization of our computation algorithm enabled us to perform calculations on a large (800^3) 3-D volume; this calculation gives better results for the electrical formation factor. Formation factor and permeability of five sub-sets are cross-correlated using surface area and Λ parameter. The three-phase conductivity model, which calculates surface conductivity on the rock μCT image, agrees with experimental data and provides a better fit than the Waxman-Smits equation.

In the second part, we present quantitative AC seismoelectric signal (10 kHz ~ 120 kHz) collected on the saturated BS500 plate in a solution tank. Both single sine pulse and five-cycle sine burst are adopted as source wavelets. Received acoustic and electric signals are analyzed in both time domain and frequency domain. Streaming potential is collected on freshly cut BS500 cylinder core samples saturated with different brine conductivities under the same experimental conditions as AC measurements. Frequency dependent coupling coefficient of BS500 is theoretically calculated using Pride's equation with the parameters previously obtained from μcT image and laboratory measurements. A majority of the experimental data between 40 kHz and 100 kHz frequency range is found to follow the theoretical curve. The

overall data quality is better for single sine pulse than five cycle sine burst due to its higher resolution and simplicity in time domain.

Appendix A

Finite Difference Scheme for Solving Laplace Equation

A.1 Finite Difference Form of Laplace Equation

The effective dc conductivity of a random medium can be calculated by Ohm's Law:

$$\vec{J}(r) = \sigma(r)\vec{E}(r), \tag{A-1}$$

where J is the current density, σ is the electric conductivity and E is the electric field strength at location r. For a steady state conductivity problem, where the currents are steady in time, the charge conservation equation:

$$\nabla \cdot \vec{J} + \frac{\partial \rho}{\partial t} = 0 \tag{A-2}$$

can be written in the form of Laplace equation (Zwillinger, 1995):

$$\nabla \cdot \vec{J}(r) = -\nabla \cdot \left(\sigma(r) \cdot \nabla \vec{V}(r)\right) = 0. \tag{A-3}$$

We can calculate the macroscopic conductivity of the random material by applying an electric potential gradient across the sample. The volume averaged current density can be used to compute the effective conductivity from Ohms' law, as given in Eq. A-1.

In a uniform conductivity region, the voltage at point (*i, j, k*) in 3-D is defined as *v*(*i, j, k*). To the second order in space, the potential at $i \pm 1$, $j \pm 1$ and $k \pm 1$ is written as:

$$v(i \pm 1, j, k) = v(i, j, k) \pm a\left(\frac{\partial \mathrm{v}}{\partial \mathrm{x}}\right)_{i,j,k} + \frac{1}{2}a^2\left(\frac{\partial^2 \mathrm{v}}{\partial^2 \mathrm{x}}\right)_{i,j,k}, \tag{A-4}$$

$$v(i, j \pm 1, k) = v(i, j, k) \pm b\left(\frac{\partial \mathrm{v}}{\partial \mathrm{y}}\right)_{i,j,k} + \frac{1}{2}b^2\left(\frac{\partial^2 \mathrm{v}}{\partial^2 \mathrm{y}}\right)_{i,j,k}, \tag{A-5}$$

$$v(i, j, k \pm 1) = v(i, j, k) \pm c\left(\frac{\partial \mathrm{v}}{\partial \mathrm{z}}\right)_{i,j,k} + \frac{1}{2}c^2\left(\frac{\partial^2 \mathrm{v}}{\partial^2 \mathrm{z}}\right)_{i,j,k}. \tag{A-6}$$

Here, *a,b,c* are the special increment in *x, y , z* direction, respectively. We have $\Delta x = a, \Delta y = b$ and $\Delta z = c$. Thus, there are six equations associated with the six nearest neighbors with respect to the central point (*i, j, k*). Adding the equations in pair will cancel out the first order derivatives and multiply *abc* on both sides, the Laplace's equation in the finite difference form at node m (the center of voxel (*i, j, k*)) becomes (Garboczi, 1998):

$$\sum_n \mathrm{C_{mn}}\,(v_n - v_m) = 0\,, \tag{A-7}$$

where $\mathrm{C_{mn}}$ is the conductance of the bond connecting node *m* to its nearest neighbor *n*, and the sum is over *n=1,6* nearest neighbors, where *1,2,3* correspond to the neighbors in (*x, y,z*) direction, *4,5,6* correspond to the neighbors in (*-x,- y-,z*) direction. We have $\mathrm{C_{m1}} = \mathrm{C_{m4}} = \sigma\frac{\mathrm{ab}}{\mathrm{c}}$, $\mathrm{C_{m2}} = \mathrm{C_{m5}} = \sigma\frac{\mathrm{ac}}{\mathrm{b}}$ and $\mathrm{C_{m3}} = \mathrm{C_{m6}} = \sigma\frac{\mathrm{bc}}{\mathrm{a}}$.

This finite difference scheme can handle rectangular voxel with arbitrary dimensions in three directions. For the 3-D μCT image, the grid interval in x-, y- and z- direction is exactly the same as the μCT image resolution. Thus, we have cubic voxel, where *a=b=c=l.* For each point *m*, we have Eq. A-7. A global equation could be formed as:

$$A_{mn} v_n = 0, \tag{A-8}$$

where A_{mn} is a sparse matrix composed of the conductances of all the bonds in the 3-D structure. We can solve Eq. A-8 by minimizing the quadratic form of $\frac{1}{2} vAv$. Without any applied electric field, the natural solution for the minimization of $\frac{1}{2} vAv$ would be $v=0$. A generalized conjugate gradient (CG) iterative method is applied to solve Eq. A-8. Conjugate gradient method appears to be especially efficient for solving real, linear, algebraic equations in forms of $Ax=b$, where A is a sparse matrix. It requires fewer restrictions on the matrix A for optimal behavior than do such methods and successive ovverrealxatioin (Concus and Golub, 1976).

The boundary conditions between phases with different conductivities are that the current density normal to the interface and the potential are continuous. The conductance of the bond between two adjacent voxels (m and n) of the same material property ($\sigma_m=\sigma_n$) is written as:

$$C_{mn=}\sigma_m \cdot l. \tag{A-9}$$

If node m and n posses different material properties, the conductance of that bond connecting m and n is written as:

$$C_{mn=}\left(\frac{1}{2\sigma_m} + \frac{1}{2\sigma_n}\right)^{-1} \cdot l. \tag{A-10}$$

As for the material properties, finite difference electrical conductivity programs can handle arbitrary diagonal conductivity tensors. The conductivity tensor $\sigma(r)$ is defined for each phase in the microstructure as a function of location. The 3D microstructure is redefined to a 1D label to be taken in the finite difference scheme. We can define an electric potential

gradient across the sample in x, y, and z directions respectively and calculate the current density in all three directions for each voxel. By doing the volume average of the local current densities, we can back out the full conductivity tensor as indicated in Fig. A-1.

There is an intrinsic challenge solving Laplace's equation when the conductivity contrast between the different phases is very high (high contrast boundaries). For our specific problem, the solid matrix is defined to be quartz with the conductivity of 10^{-14} S/m. As for the fluid phase, we want to have a conductivity range between 10^{-5} S/m and 10 S/m. Thus, the contrast between the two phases could be 7 to 13 orders in magnitude. To handle such a large contrast, we adopt a gradual relaxation method (Press et al., 1990). We can start from the low conductivity contrast and gradually relax the potential field, then gradually increase the conductivity contrast to make the result converge. A relatively loose convergence criteria for the gradient of the electric energy is applied first when the conductivity contrast is small. Then, we use a more strict criteria when the target contrast level is reached. Enough conjugate gradient cycles is run to make sure that the gradient is no longer changing. Overrelaxation needs to be prevented not to waste too much CPU time beyond the point where the answer no long changes significantly. Thus, numerical experimentation is needed to determine the convergence criteria for each specific problem.

A.2 Benchmark of the Finite Difference Program

To validate the finite difference code, we apply the code to a simple geometry and compare the calculated effective conductivity with an analytic solution. We also compare the

current density distribution from the FD code with the result from a commercial finite element software package, FEMLAB. The geometry we use is a spherical inclusion with a radius of 15 meters in the center of a 100 meter cube as shown in Fig. A-2. The spherical inclusion is defined to be phase 1 and cubic host is defined to be phase 2. The volume fraction of the spherical inclusion is $f_1 = 0.0141$, the conductivity of the sphere is set to be $\sigma_1 = 10^{-5} S/m$, and the conductivity of the cubic host is set to be $\sigma_2 = 0.06 S/m$. The porosity of the inclusion is low and we choose the conductivity value to be real number with decimal fraction to test the numerical accuracy of the FD program.

The analytic solution for a two-component material can be calculated by the Clausius-Mossotti formula (Markov, 1999; Hughes, 2000) as:

$$\frac{\sigma^* - \sigma_2}{\sigma^* + 2\sigma_2} = f_1 \cdot \frac{\sigma_1 - \sigma_2}{\sigma_1 + 2\sigma_2}. \qquad \text{(A-11)}$$

A unit electric field of 1V/m is applied in the x-direction across the cube (Fig. A-2). The effective conductivity calculated from FD code is 0.00589688. The number calculated from Clausius-Mossotti formula is 0.05935868. Difference between FD result and analytic solution is 0.656%.

We also compare the computed electric current density computed from our FD code and FEMLAB. Slice views of the current density distribution in the x-direction and from two programs are compared in Fig. A-3. The color bar represents the absolute value of the current density (with unit of A/m^2) in the direction of the electric potential gradient (x-direction). The relative and absolute magnitude of current density is close to each other in two figures.

A.3 3D Fontainbleau Sandstone μCT microtomography

We next apply the FD code on our Fontainbleau Sandstone CT microtomographic sample. The digital image we have is a 200^3 binary voxel. The pore space is coded to be '0' and grain material to be '1'. The voxel is close to a cube-shape with the resolution of $4.68 \times 4.68 \times 5.21$ μm in X, Y and Z direction respectively. The whole sample is ~$1mm^3$ in volume with 7.37% porosity, as shown in Fig. A-4.

In our calculation, the grain is considered to be quartz with the conductivity of 10^{-12} S/m instead of 0. We saturate the Fontainbleau Sandstone with gas, oil and saline water with different values of salinity. We assign all the '0's in the sample, which stands for the pore space, with the saturating phase conductivity and all the '1's with the quartz conductivity. The effective conductivity of the saturated Fontainbleau sandstone, σ_{eff}, is listed in the last row of Tab. A-1. For the saline water saturation, the effective conductivity σ_{eff} and brine conductivity σ_f obeys linear relationship described as Archie's law (Archie, 1942, Eq. 2-1).

To visually represent the sandstone saturated with different fluids, we also display the current density (with unit of A/m^2) distribution in a common (base 10) logarithm. Gas, oil and saline water (brine conductivity to be $10^{-6}S/m$) saturations are shown in Fig. A-5. From the current density distribution, we can resolve the pore space very well which corresponds to the hot spots in the map. With an increase of the conductivity contrast between the saturation phase and host grain phase, the boundary between the pore space and grain becomes sharper. It is obvious that larger contrasts can better resolve the details of the structure.

From the current density distribution, we can also resolve the pore geometry. Plotting the electrical current density by gradually lessening the criteria (plotting the current density larger than certain criteria), the pore geometry could be gradually resolved (Fig. A-6). The largest connected pore for this Fontainbleau sandstone core sample is 45 degree to the X-Y plane (indicated by the green circle in Fig. A-6). We can back out the formation factor by calculating the ratio σ_f/σ_{eff}. The computed formation factor is 0.003223. Due to the lack of the Fontainbleau sandstone core sample, we don't have any laboratory measurement to compare with the numerical calculation. However, this result is comparable to the value of 0.003172 obtained by Arns (Arns, 2001) on a 7.99% porosity Fontainbleau Sandstone μCT image (personal communication with Christoph Arns).

References

Arns, C. H.: 2001, The influences of morphology on physical properties of reservoir rock, *Ph.D. thesis, University of New South Wales.*

Concus, P. and Golub, G. H.: 1976, A generalize conjugate gradient method for nonsymmetrical systems of linear equations, *The energy research and development administration under contact,* No. E(04-3), 326 PA No.30.

Garbozi, E. J.: 1998, Finite Element and Finite Difference Programs for Computing the Linear Electric and Elastic Properties of Digital Image of Random Materials, *NISTIR* 6269.

Hughes, M. P.: 2000, AC electrokinitics: applications for nanotechnology, *Nanotechnology*, **11**, 124-132.

Markov, K. Z.:1999, Elementary micromechanics of heterogeneous media, *Birkhauser Boston*, 1-162.

Press, W.H., Flannery, B.P., Teukolsky, S.A. and Vetterling, W.T.: 1990, Numerical Recipes, *Cambridge University Press, Cambridge.*

Zwillinger, D, 1997, Handbook of Differential Equations, 3rd Ed: Academic Press, Boston, MA.

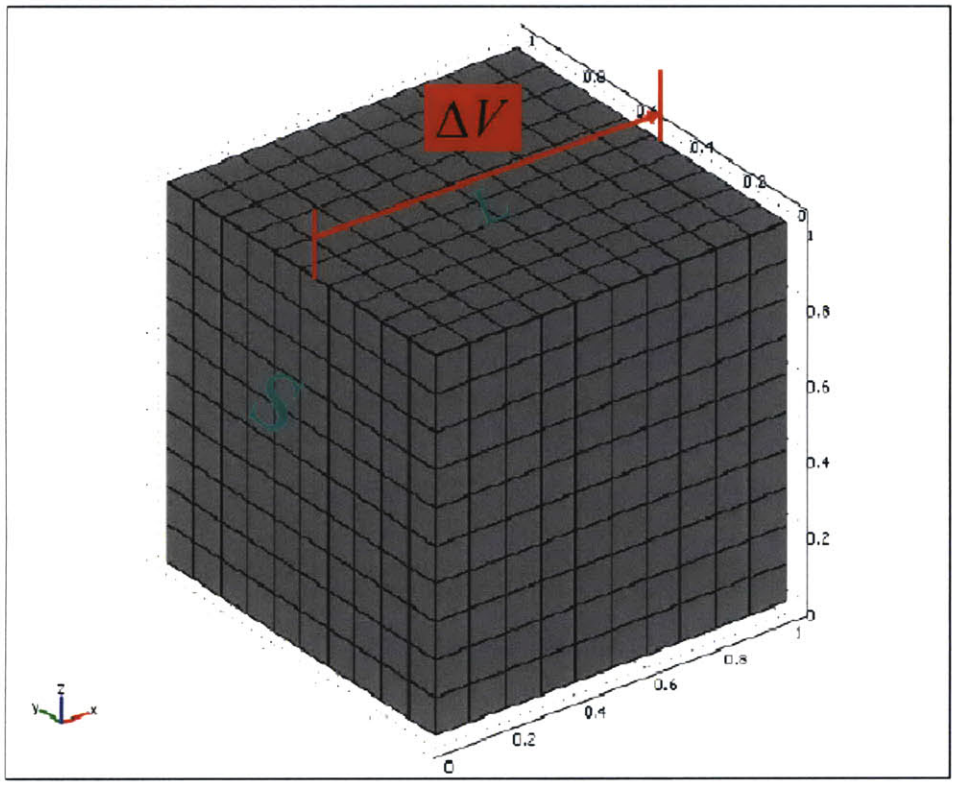

$$\sigma_{eff} = \left(\frac{L}{\Delta V}\right)\frac{1}{A}\iint_S \sigma(r)(-\hat{x}\cdot\vec{\nabla}V)dS$$

Figure A-1: Effective conductivity calculation of a random material using the finite difference scheme.

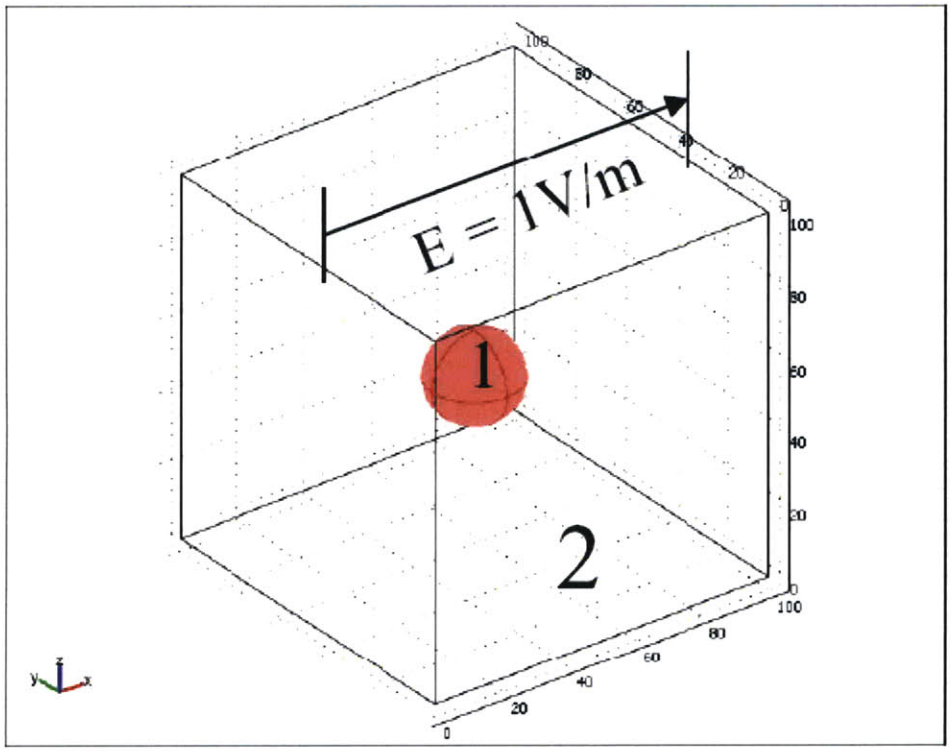

Figure A-2: The geometry of a spherical inclusion (phase 1, shown in red) in a cubic host (phase 2). The radius of the sphere is 15 and the cube length is 100. An electric potential gradient of 1 *V/m* is applied in x-direction.

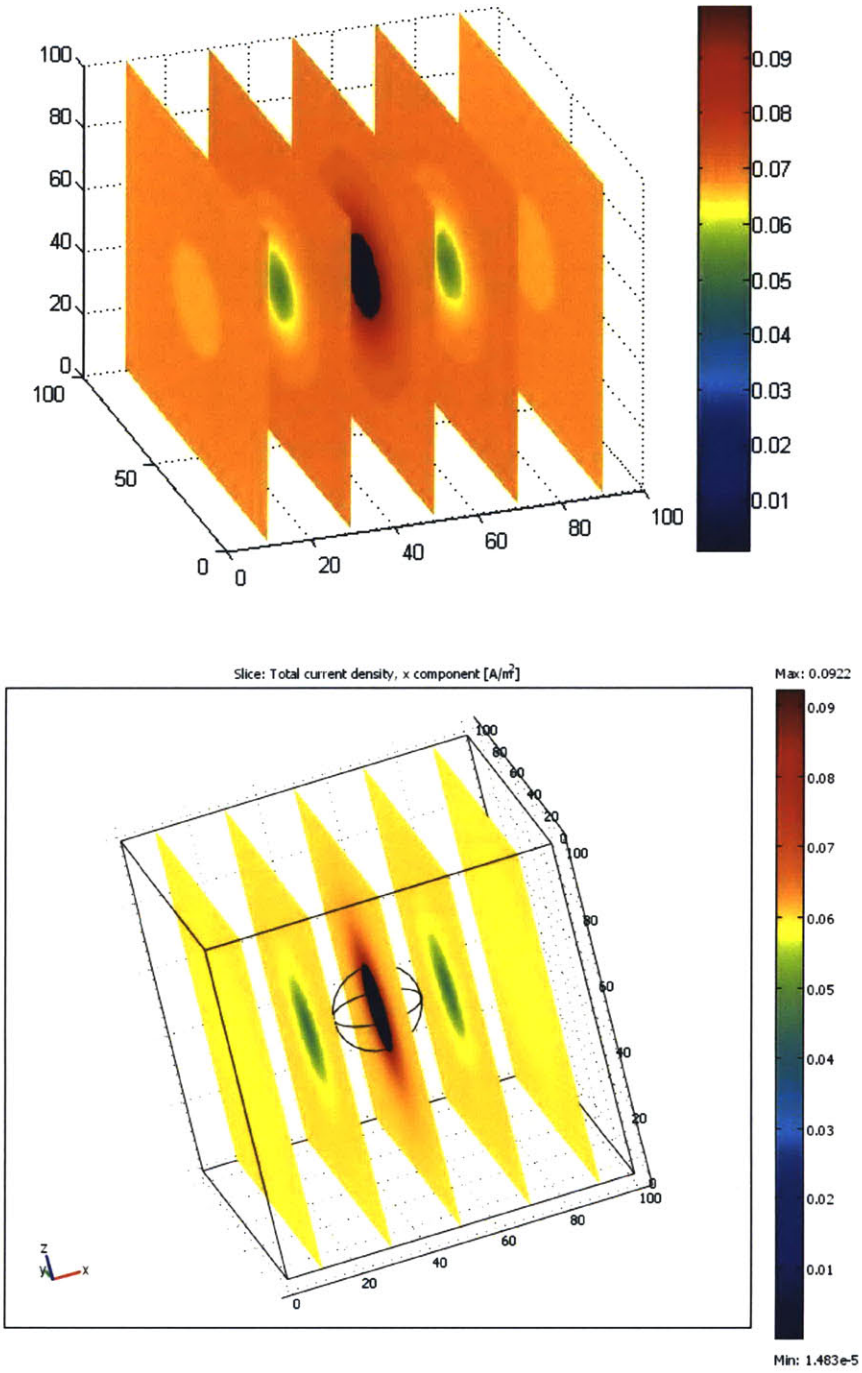

Figure A-3: The current density distribution (with unit of A/m^2) in x-direction of the spherical inclusion in a cubic host. Color bar indicates the magnitude of the current density. Above is the FD result and below is the FEMLAB result (directly taken form FEMLAB package).

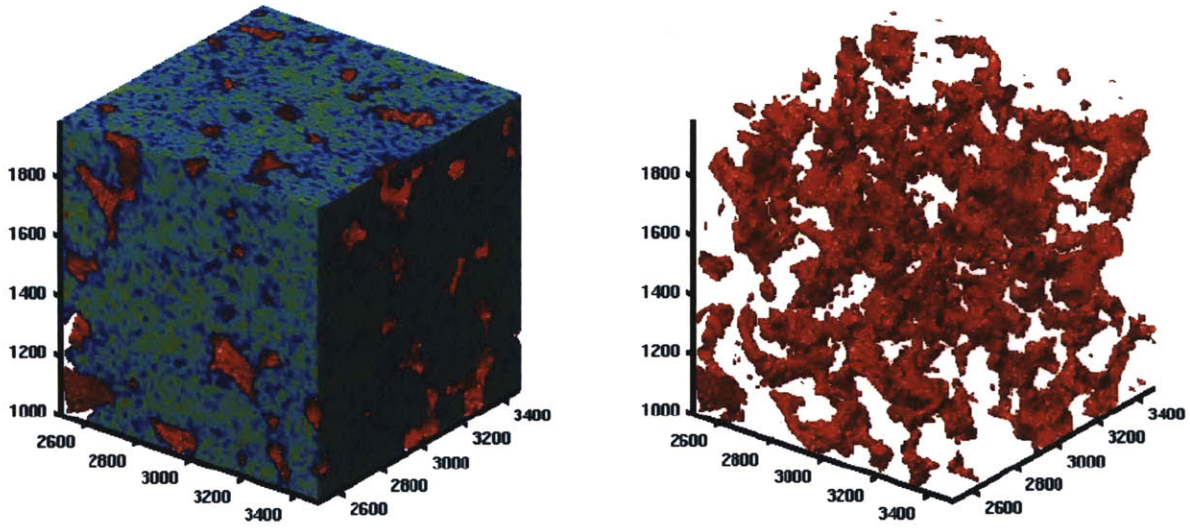

Figure A-4: The Fontainbleau Sandstone CT microtomogrphay. On the left panel, the red indicate the pore space and the blue indicate the grain. On the right panel, the grain space is eliminated and remain a 'pore cast'. The total volume is a 200^3 volume with $4.68 \times 4.68 \times 5.21$ μm resolution in X, Y, Z direction.

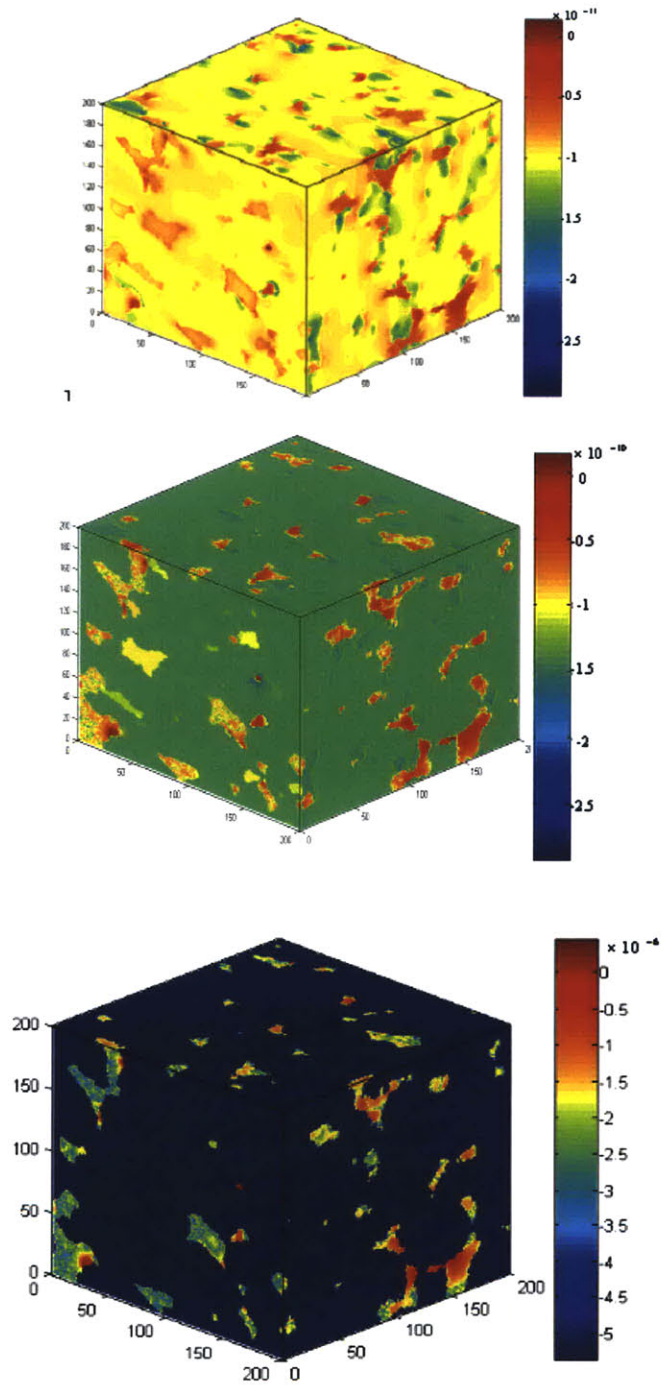

Figure A-5: The current density distribution when Fontainbleau Sandstone saturated with gas, oil and brine, respectively (from above to below). Color bar indicates the common (base 10) logarithm of the current density (with the unit of A/m^2).

Gas	Oil	Saline Water						
$1e^{-11}$ (S/m)	$5e^{-9}$ (S/m)	$1e^{-5}$ (S/m)	$1e^{-4}$ (S/m)	$1e^{-3}$ (S/m)	$1e^{-2}$ (S/m)	$1e^{-1}$ (S/m)	1 (S/m)	10 (S/m)
$7.016e^{-14}$ (S/m)	$1.128e^{-12}$ (S/m)	$3.06e^{-8}$ (S/m)	$3.12e^{-7}$ (S/m)	$2.98e^{-6}$ (S/m)	$3.23e^{-5}$ (S/m)	$3.18e^{-4}$ (S/m)	$3.23e^{-3}$ (S/m)	$3.03e^{-2}$ (S/m)

Table A-1: The conductivity of gas, oil and saline water as saturation phase and the effective conductivity of the saturated Fontainbleau Sandsonte.

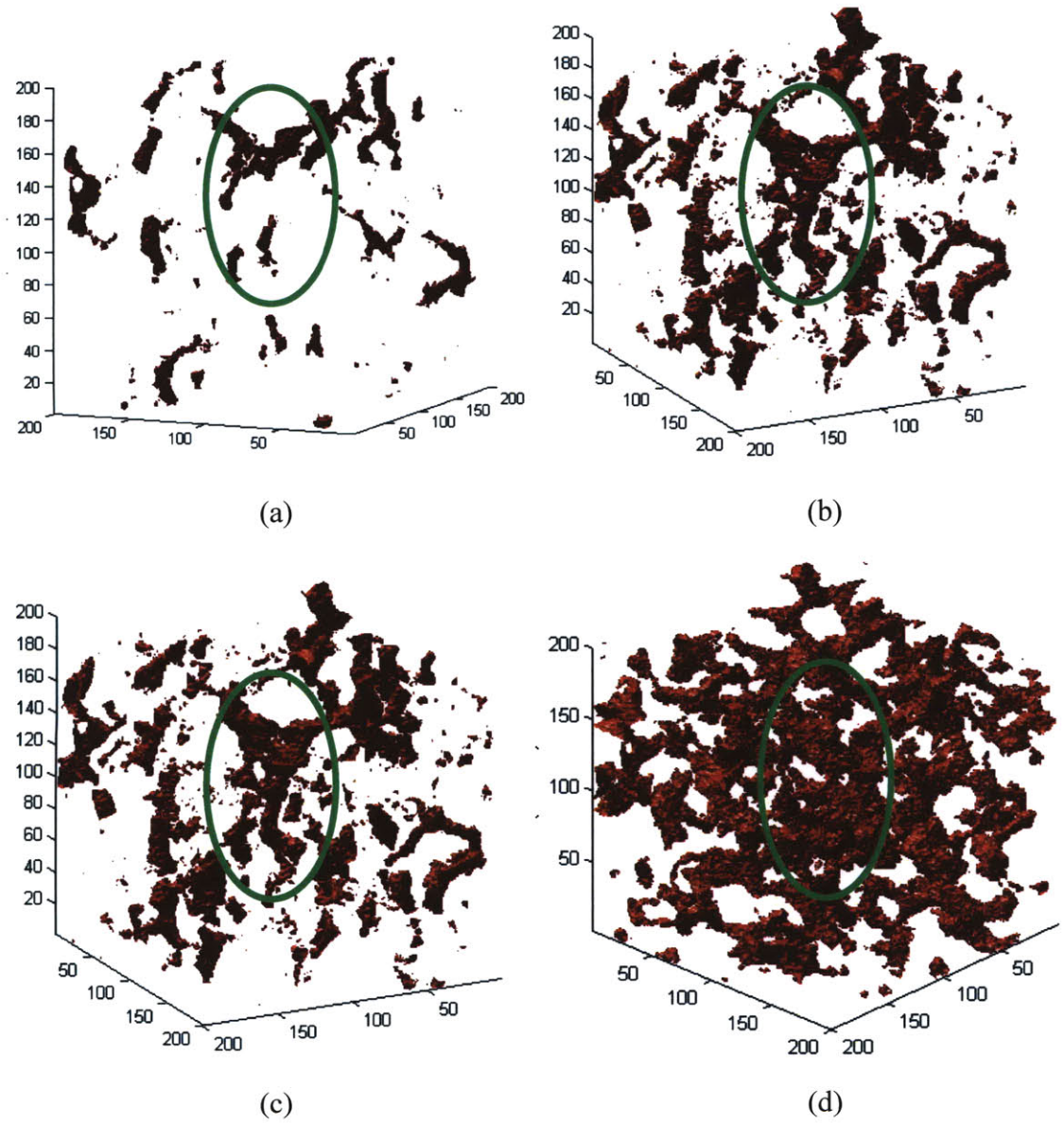

Figure A-6: The current density distribution when the current density is larger than $10^{-7}A/m^2$ (Fig. A-6.a), $10^{-9}A/m^2$ (Fig. A-6.b), $10^{-10}A/m^2$ (Fig. A-6.c), $10^{-12}A/m^2$ (Fig. A-6.d). The largest pore is 45 degree to X-Y plane (indicated by the green circle).

Appendix B

Finite Difference Scheme for Sovling Stokes Equation

B.1 Finite Difference Form of Stokes Equation

To solve the hydraulic problem, we use a modified finite difference Stokes solver based on an industry standard finite difference (FD) code developed at NIST (National Institute of Standards and Technology, Gaithersburg, MD 20899-8621, U.S.A; ftp://ftp.nist.gov/pub/bfrl/bentz/permsolver/; Bentz and Martys, 2007).

Permeability is a measure of the resistance to fluid flow under a pressure gradient of a given porous medium. The mechanism of fluid flow is given by the Navier-Stokes equation:

$$\frac{d(\rho\upsilon)}{dt} + \nabla \cdot (\rho\upsilon\upsilon) = -\nabla P + \eta\nabla^2\upsilon\,, \tag{B-1}$$

where ρ is fluid density, v is the fluid velocity, P stands for pressure and η is the fluid viscosity. The Navier-Stokes equation is based on the assumption that the fluid, at the scale of interest, is a continuum, in other word is not made up with descrete particles but ration a

continous substace. Another assumption is that all the fields such as pressure, velocity and density are differentiable.

For the case of laminar (slow, incompressible Newtonian) flow where advective inertial forces are small compared with viscous forces, the Navier-Stokes equation simplifies into linear Stokes equation:

$$\eta\nabla^2\vec{v}(r) = \nabla P(r), \tag{B-2}$$

$$\nabla \cdot \vec{v}(r) = 0, \tag{B-3}$$

Where Eq. B-3 is the conservation of mass. A Stokes flow has no depence on time other than through time-dependent boundary condctions.

NIST Stokes solver adopts a finite difference scheme in conjuction with the artificial compressibility relaxation algorithm (Peyret and Taylor, 1983; Martys and Garboczi, 1992; Schwartz et al., 1993). Pressure is defined at the nodes (center of the voxel) and fluid velocity components are defined along the center center of bonds connetcitn neighboring nodes (center of voxel edge). A non-centered finite difference realization of the ∇^2 operator is derived to maintain at least 2nd order accuracy in space.

The ∇^2 operator is divided into two parts as: $\nabla^2 = \nabla_{\parallel}^2 + \nabla_{\perp}^2$. $\nabla_{\parallel}^2$ operator corresponds to the direction parallel to the velocity and $\nabla_{\perp}^2$ operator corresponds to the direction transverse to the velocity. The discretization of $\nabla_{\parallel}^2$ operator takes the form:

$$\nabla_{\parallel}^2 \upsilon_i = \upsilon_{i+1} + \upsilon_{i-1} - 2\upsilon_i \tag{B-4}$$

at node *i*. of The discretization of $\nabla_{\perp}^2$ operator has six forms depending on the location of the nearest solid voxels in the transverse direction (Bentz and Martys, 2007).

Taking the geometry in Fig. B-1 for example, at node 2, we have the 3rd order Talyor expansion as:

$$v_1 = v_2 - \frac{1}{2}\left(\frac{\partial v_2}{\partial x}\right) + \frac{1}{8}\left(\frac{\partial^2 v_2}{\partial^2 x}\right) - \frac{1}{48}\left(\frac{\partial^3 v_2}{\partial^3 x}\right), \tag{B-5}$$

$$v_3 = v_2 + \left(\frac{\partial v_2}{\partial x}\right) + \frac{1}{2}\left(\frac{\partial^2 v_2}{\partial^2 x}\right) + \frac{1}{6}\left(\frac{\partial^3 v_2}{\partial^3 x}\right), \tag{B-6}$$

$$v_4 = v_2 + \frac{3}{2}\left(\frac{\partial v_2}{\partial x}\right) + \frac{9}{8}\left(\frac{\partial^2 v_2}{\partial^2 x}\right) + \frac{9}{16}\left(\frac{\partial^3 v_2}{\partial^3 x}\right). \tag{B-7}$$

The boundary conditions are fluid velocity vanishing at the fluid-solid interface and an applied pressure gradient across the inlet and outlet of the 3-D structure. With the non-slip boundary conduction, we have $v_1 = v_4 = 0$. Thus, the $\nabla_{\perp}^2$ operator for node 2, which is $\frac{\partial^2 \upsilon_2}{\partial x^2}$ (υ_2 is the y component of the velocity at node 2), could be written as:

$$\frac{\partial^2 \upsilon_2}{\partial x^2} = \frac{8}{3} v_3 - \frac{16}{3} v_2. \tag{B-8}$$

For all three velocity components in x, y, z direction, there're totally thirty six different forms of the $\nabla_{\perp}^2$ operator.

We can calculate the macroscopic permeability of the porous medium by applying a pressure gradient across the sample. The permeability, κ, of the porous medium is calculated by volume averaging the local fluid velocity (in the direction of the flow) and applying the Darcy equation:

$$u = -\frac{\kappa \Delta P}{\eta \; L}, \tag{B-9}$$

where u is the average fluid velocity in the direction of the flow for the porous media and L is the length of the sample porous medium across which there is an applied pressure gradient of ΔP.

B.2 Benchmark of the Finite Difference Program on Microstructure

The NIST FD Stokes solver has been validated by computing the permeability of circular and square tubes. The accuracy is claimed to be within 2% compared with analytic solution. Here we test the code on a 2D thin scanning electron microscope (SEM) image of San Gregorio Beach sand. We compare the calculated pressure and velocity field from NIST FD code with our Lattice Boltzmann code.

The Lattice-Boltzmann method (LBM) is a mesoscopic approach for computational fluid dynamics (Rothman and Zaleski, 1997; Chopard and Droz, 1998). The basic idea is to solve a discretized Boltzmann equation. The macroscopic dynamics of the system can be shown to obey the Navier-Stokes equation. Different from the traditional finite difference, finite element method, LBM is a bottom up method to reconstruct governing PDE from the collision rule of the particles (Fig. B-2).

For LBM, fluid is modeled by particle distributions that move on a regular lattice (Fig. B-3). In our implementation, we adopt the D2Q9 model in 2D (Rothman and Zaleski, 1997). At each lattice grid, a discrete velocity and density is defined. Hydrodynamic quantities such as density ρ and velocity v are obtained from the velocity moments of the distribution of the particle density f_i (Fig. B-3) in analogy with the kinetic theory of gases (Manwart et al., 2002). The non-slip boundary condition at solid-fluid interface is realized by the bounce-back rule in LBM (Manwart et al., 2002). Thus, the momentum of the particles that meet a solid wall are reversed (Fig. B-4).

A 2D thin SEM image of San Gregorio Beach sand is shown in Fig. B-5. The total size of the image is 551×496grids with 2.5 micron resolution. A unit pressure gradient of 1Pa/grid is applied from the left side of the image. Resolved velocity field and pressure field by LBM method and NIST finite difference code is shown in Fig. B-6. Gratifying agreement could be observed in the results from two different set of codes.

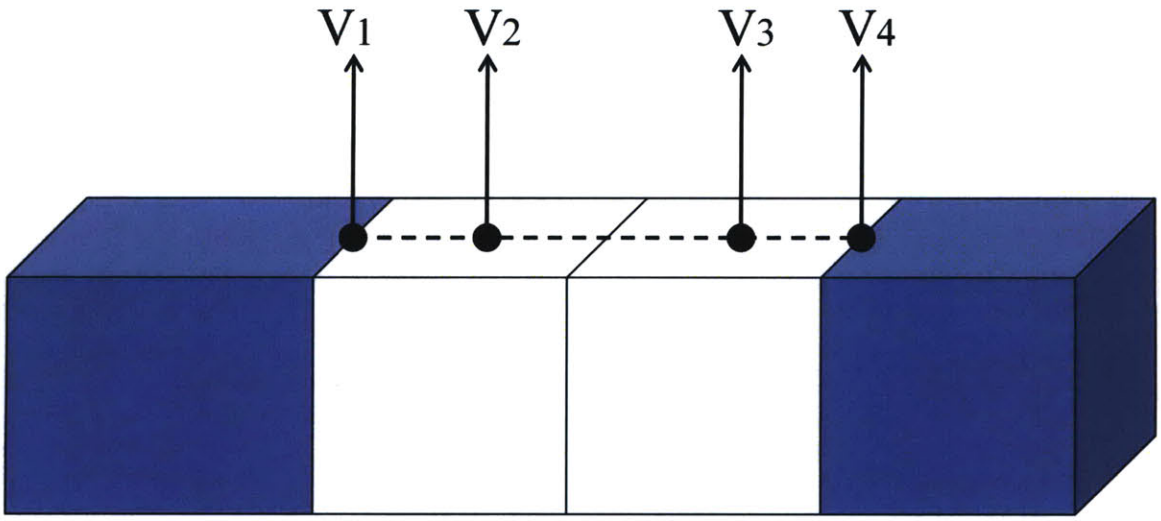

Figure B-1: Schematic for the non-centered difference solution for two adjacent pore voxel sandwiched by two solid voxel at two ends, solving for v_2. Blue voxels indicates solids and white voxels indicates pores (Bentz and Martys, 2007, Fig 2).

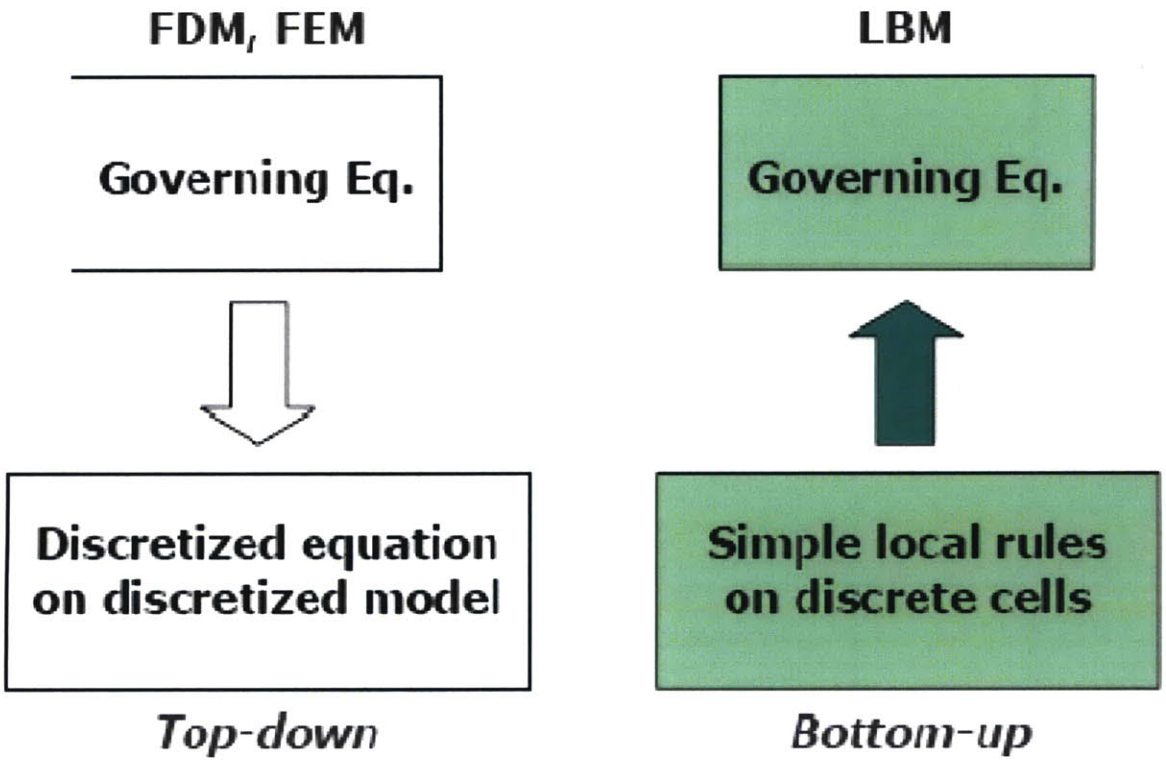

Figure B-2: Schematic for the major difference between traditional FEM, FD method and LBM method. FD and FEM are top-down methods, which are based on disretization of the governing PDE in time and space. LBM is a bottom-up method, which is based on the reconstruction of the governing PDE from the collision rule of particles.

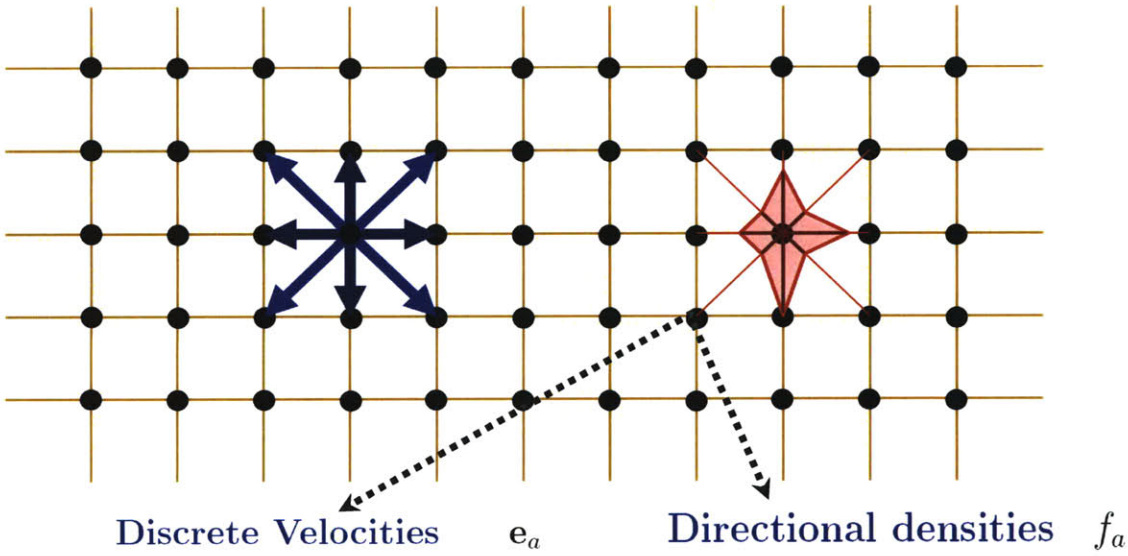

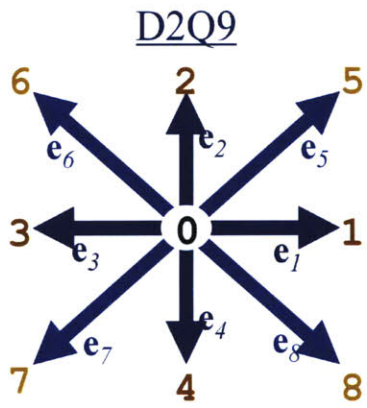

$$\textbf{Macroscopic density} \quad \rho = \sum_{a=0}^{8} f_a$$

$$\textbf{Macroscopic velocity} \quad \mathbf{u} = \frac{1}{\rho} \sum_{a=0}^{8} f_a \mathbf{e}_a$$

Figure B-3: Schematic for the LBM simulation of fluid dynamics. At each lattice grid, discrete velocity and density is defined. For implementation, D2Q9 model is adopted for 2D simulation. Each grid is connected to its 8 nearest and second-nearest neighbors in 2D. Hydrodynamic quantities such as density ρ and velocity v are obtained from the velocity moments of the distribution of the particle density f_i.

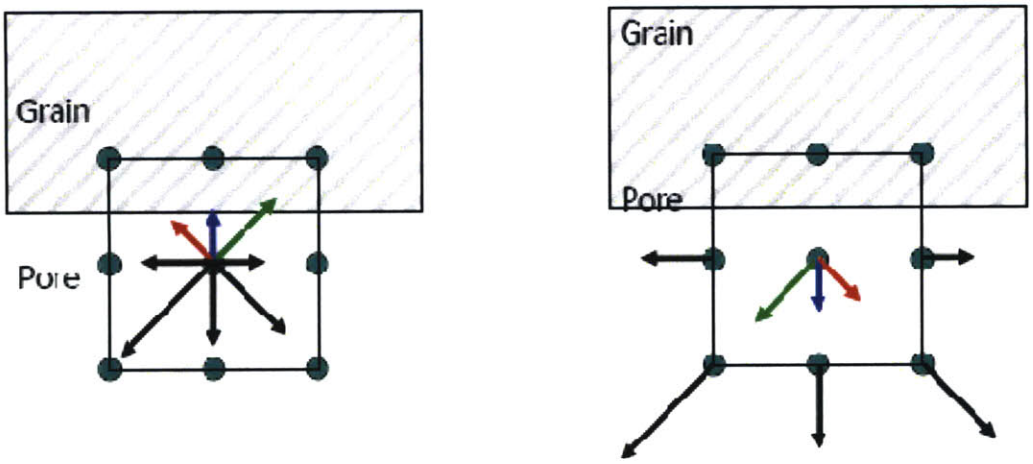

Figure B-4: Bounce-back collusion rule to realize the non-slip boundary condition. The momentum of the particles that meet a wall are simply reversed.

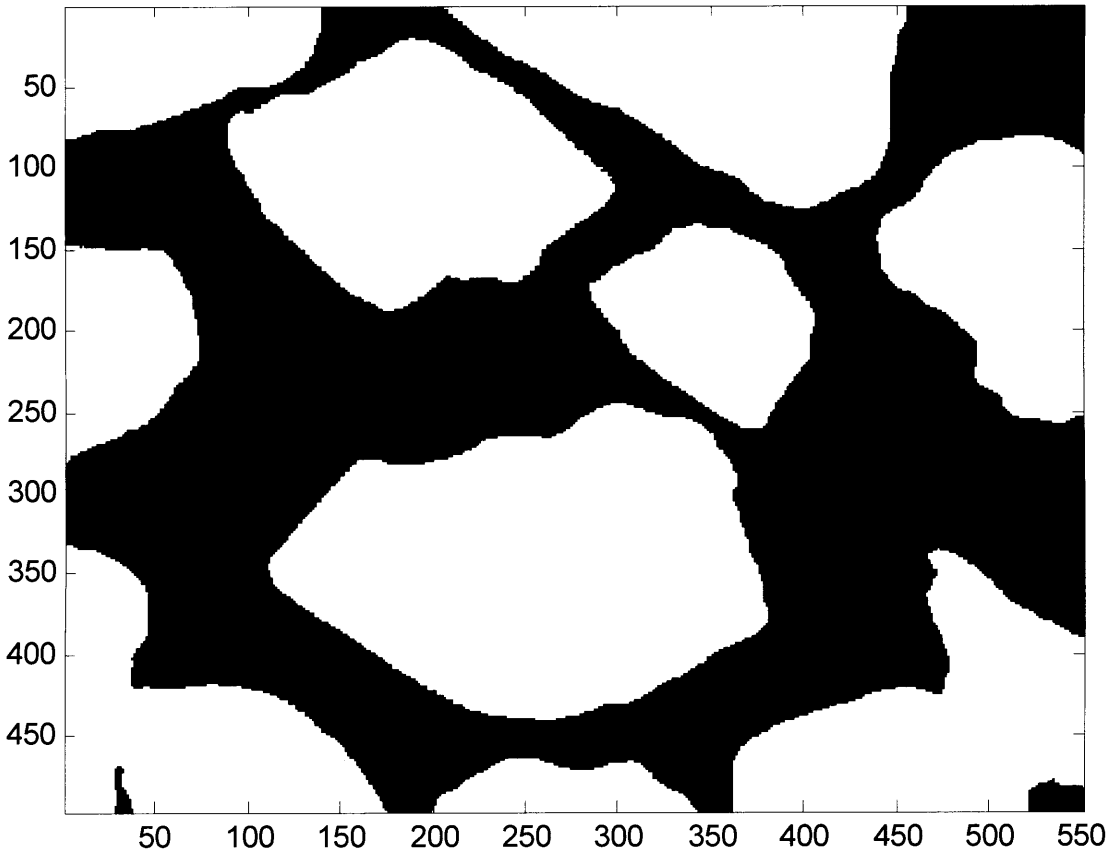

Figure B-5: 2D SEM image of San Gregorio Beach sand. Total size is 551×496grids. Pore space is shown in black and grains are shown in white.

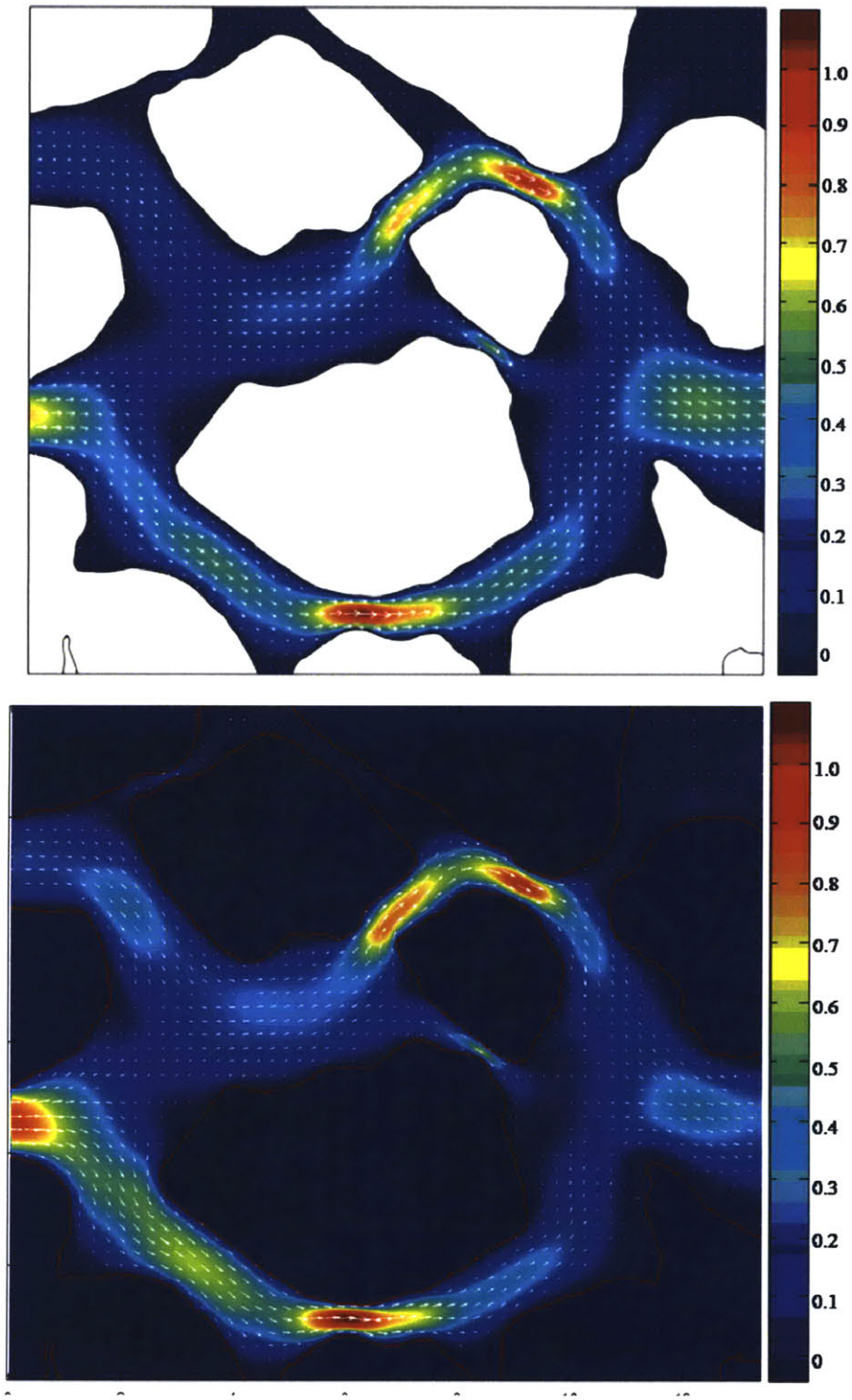

Figure B-6: Resolved pressure field (shown as the colored surface) and velocity field (shown in white arrow) from NIST FD Stokes solver (above) and LBM code (below) of 2D SEM image of San Gregorio Beach sand (Fig. B-5). Color bar indicates the amplitude of the pressure field.

References

Bentz, D. P. and Martys, N. S.: 2007, A stokes permeability solver for three-dimensional porous media, *National Institute of Standards and Technology*, NISTIR **7416**.

Chopard. B. and Droz. M.: 1998, Cellular automata modeling of physical systems, *Cambridge University Press, Cambridge*.

Manwart, C., Aaltosalmi, U., Koponen, A., Hilfer, R. and Timonen, J.: 2002, Lattice-boltzmann and finite-difference simulations for the permeability for three-dimensional porous media, *Physical Review E*, **66**, 016702-1.

Martys, N. and Garboczi, E. J.: 1992, Length scale relating fluid permeability and electrical conductivity in random two-dimensional model porous media, *Physical Review B*, **46**, 6080.

Peyret, R. and Taylor, T. D.: 1983, Computational methods for fluid flow, *Springer-Verlag, New York*.

Rothman, D. and Zaleski, S.: 1997, Lattice-Gas cellular automata: simple models of complex hydrodynamics, *Cambridge University Press, Cambridge*.

Schwartz, L. M., Martys, N., Bentz, D. P., Garboczi, E. J. and Torquato, S.: 1993, Cross property relations and permeability estimation in porous media, *Physical Review E*, **48**, 4584-4591.

Appendix C

Electrical Properties of Clay Minerals

The presence of clay in a reservoir has two effects on petrophysical logs: 1) it lowers resistivity, and 2) it reduces a reservoir's storage capacity by reducing effective porosity. The loss of resistivity is due to the high bound water content and greater conductance along the clay-brine interface. This bound water contributes to the electrical conductivity, but does not contribute to hydraulic conductivity because the bound water is immovable. Clay particles can fill pore space, reduce pore sizes and develop micropores within them. To achieve the same permeability, shaly sandstones must possess higher total porosity than quartzose sandstone since the micropores associated with clays don't contribute to permeability (Wu, 2004). As we have described in Chapter 3, as long as pore microtomography captures the effective porosity, the hydraulic permeability can be well estimated from rock CT microtomography.

The influence of clay on the electric response of reservoir rocks and problems associated with its interpretation, have been major issues of investigation in the petroleum industry for many years (Waxman and Smits, 1968; Juhász, 1981; Clavier et al., 1984; de Lima, 1995; Revil and Glover, 1997, 1998; Alkafeef and Alajmi, 2007). To quantify the surface

conductivity of rocks containing clay minerals, Q_v, which is the charge per unit pore volume of the sand needs to be determined for most conductivity models previously referenced. The cation-exchange capacity per unit pore volume, Q_v, is the usual parameter indicating the shaliness of sandstones (Asquith, 1990). The Q_v value for different clay species can vary by one or two orders. Morillonite can be two orders higher than kaolinite (de Lima and Sharma, 1990) and illite can be one order higher than kaolinite (Wu, 2004). For sandstone containing mixture of different clay minerals, Q_v value is an average value weighted by volume fraction of different components.

Q_v (in *meg ml* $^{-1}$) is usually converted from "cation exchange capacity" (*CEC*) (in *meg* g^{-1}), which indicates the maximum number of surface exchangeable cations per unit mass of rock (Patchett, 1975) using the following equation:

$$Q_v = \mathrm{CEC}[(1-\phi)/\phi]\rho_g, \qquad \text{(C-1)}$$

Here, ϕ is porosity and ρ_g is grain density (in *g* cm^{-3}). *CEC* value of the rock is chemically measured on the core sample. Two sets of experimental techniques (Burck, 1986; Sen, 1990) are adopted — destructive and nondestructive. Destructive method loads the exchange sites with measurable cations such as ammonium and barium on the grinded core sample (Ridge, 1983). The degree of grinding can change the geometry and the measured value of *CEC*. Nondestructive methods (such as membrane potential measurements) preserve the geometry and is claimed to give Q_v value better correlated with effective transport properties such as electrical measurements (Yuan and Diederix 1987; de Waal, 1987). However, the accurate determination of *CEC* is difficult even on core samples.

Empirical relationship between Q_v and other measurable parameter such as permeability, volume to surface ratio, proton NMR decay constant *T1* and clay content (*p*) has been well studied and established (Steward and Burck, 1986; Herron, 1987; Sen, 1990) on a wide range of sandstone samples. More than 100 sandstone data (Tab. C-1) from various parts of the world, which is also a subset of data used in Waxman-Smits model (Waxman and Smits, 1968) have been used to test these empirical cross-property relationships (Fig. C-1, Fig C-2). Q_v value in the range of 0.01 to 0.75 *meg/ml*. Especially in the borehole logging, estimating a physical parameter by using its statistical relationship with another measurable parameter is a common practice. With the absence of direct chemical laboratory measurement of *CEC* value, obtaining Q_v from other available property is a practical alternative. In this study, Q_v is estimated from the clay content (*p*), which can be obtained from the X-ray attenuation histogram. The intensity histogram before and after the anisotropic diffusion filter of BS500 core sample is shown as Fig. 3-1. Segmentation thresholds for separating different phases are: ~ 13500 belong to pore space, 14300~14800 belong to clay (which is part of the intermediate signal between the two peaks in the histogram), ~16000 belong to grain (criteria provided by Australian National University). Thus, the clay volume fraction is estimated to be 4.03% from the X-ray grey scale μCT image, which is close to 3.9% from the composition analysis (provided by Schlumberger Doll Research) in Tab. 3-1.

Q_v can be related to clay content *p,* which is the shaliness parameter, and the clay parameter $\frac{\beta}{a}$, which describe the clay type in the sand using the equation (de Lima, 1995):

$$Q_v = \frac{3p(1-\phi)(1-\phi_{sh})}{\phi_t}\left(\frac{\beta}{a}\right), \qquad \text{(C-2)}$$

β is the surface conterion density necessary to balance the immobile charges on the clay particles of radius *a*, ϕ_{sh} is the shale porosity, ϕ_t is the total porosity and ϕ is the effective porosity. Rock can be represented as a self-similar mixture of solid grains having a volumetric total current conductivity with the grains suspended in a continuous electrolyte (de Lima, 1995). Clay particle is represented as a charged sphere immersed in an electrolyte solution and charged particle-electrolytic film model is used to compute the clay conductivity. In general, ϕ_{sh} is small, especially for clean sand, and, for practical purposes, the difference between ϕ_t and ϕ is negligible. Thus, Eq. C-2 could be simplified as:

$$Q_v = \frac{3p(1-\phi)}{\phi}\left(\frac{\beta}{a}\right). \qquad \text{(C-3)}$$

The electrical conductivity of rocks containing clay minerals can be satisfactorily described using self-similar mixing models in which the clays occur as continuous coatings over the sand grains (de Lima and Sharma, 1990; 1992). The DC effective conductivity of rock containing clay minerals depend on: 1) formation factor of the sand; 2) a characteristic clay parameter $(\frac{\beta}{a})$ relating the charge density on the clay surface to the clay particle size; 3) the clay volume content (*p*) in the sand; 4) electrical conductivity of the interstitial electrolyte; 5) water saturation level in the rock (de Lima, 1995). Linear regression is done to fit the data set in Tab. C-1, which includes a Berea 500 sample (shaded in Tab. C-1) with similar permeability, slightly higher *CEC* value and lower surface area than our BS500 sample (Tab. 3-5). An "average sand" is found to be equivalent to the entire data set, where $\frac{3\beta}{a} \approx$

$\frac{1}{450}\ meg/ml$ (de Lima, 1995). These result is later applied to an oil production well from the Potiguar Basin, Rio Grande do Norte, Brazil to successfully relate different properties from various measurements, e.g., resistivity log, dielectric log (EPT), neutron and density log and gamma-ray log. The clay content p is normally between 5% to 20% and the Q_v value in the range of 0.01 to 0.92 *meg/ml*. Dominate clays are from the kaolinite and illite groups (de Lima, 1995), which is similar to our BS500 sample (Tab. 3-2).

The Q_v value of our BS500 core sample calculated from experimentally obtained *CEC* value using Eq. C-1 is 0.026 *meg/ml*, with 23.6% porosity and 2.65 g/cm^3 grain density. Taking the clay content 4.03% estimated from the X-ray grey scale μCT image and $\frac{3\beta}{a} \approx \frac{1}{450}\ meg/ml$ into Eq. C-3, we can get the Q_v value to be 0.0288 *meg/ml.* The difference in Q_v value obtained from directly measured *CEC* and deduction from clay content and clay parameter $(\frac{\beta}{a})$ is 10%. Thus, with the absence of *CEC* measurement on the core sample, we can still back out the Q_v value from the μCT image combined with the mineralogical information on the clay species. Estimating the clay content is another important application of the rock μCT image. It will further reduce the amount of measurements required for the electrical conductivity prediction.

References

Alkafeef S. F. and Alajmi, A. F.: 2007, The electric conductivity and surface conduction of consolidated rock cores, *Journal of colloid and interface science*, **309**, 253-261.

Asquith, G.: 1990, Log evaluation of shaly sandstones: a practical guide, *Am. Assoc. Petr. Geol.*, Course Notes #31.

Burck, L. J. S.:1986, A review of log and core methods of determining cation exchange capacity Q_v, *8th European Formation Evaluation Sym,* **Paper F**.

Clavier, C., Coates, G. and Dumanoir, J.: 1984, Theoretical and experimental bases for the dual-water model for interpretation of shaly sands, *Soc. Pet. Eng. J.*, **24**, 153-168.

de Waal, J. A.: 1987, Influence of clay distribution on shaly sand conductivity, *Ann. Fall Technical Conf. Soc. Petr. Eng., A. I. M.E.,* SPE, **Paper 16786**.

Herron, M.: 1987, Estimating the intrinsic permeability of clastic sediments from geochemical data, *28th Ann. Logging Sym,* SPWLA, **Paper HH**.

Juhász, I.: 1981, Normalized Qv – The key to shaley sand evaluation using Waxman-Smits equation in the absence of core data, *Trans. Soc. Prof. Well Log Analysts, 22nd Annual Logging Symposium,* **Paper Z**.

Lima, O. A. L. and Sharma, M. M: 1990, A grain conductivity approach to shaly sand, *Geophysics*, **50**, 1347-1356.

Lima, O. A. L. and Sharma, M. M: 1992, A generalized Maxwell-Wagner theory for membrane polarization in shaly sands, *Geophysics*, **57**, 789-799s.

Lima, O. A. L.: 1995, Water saturation and permeability from resistivity, dielectric and porosity logs, *Geophysics*, **60**, 1756-1764.

Revil, A. and Glover P. W. J.: 1997, Theory of ionic-surface electrical conduction in porous media, *Phys. Rev. B,* **55,** 1757-1773.

Revil, A. and Glover P. W. J.: 1998, Nature of surface electrical conductivity in natural sands, sandstone, and clays, *Geophysical Research Letters,* **25,** 691-694.

Ridge, M.: 1983, A combustion method of measuring cation exchange capacity of clay minerals, *Log Analyst*, **24**, no.3, 4-11.

Steward, H. E. and Burck, L. J. S.: 1986, Improved cation exchange capacity Q_v determination using the multi-temperature membrane potential test, *The Log Analyst,* **27,** no. 1, 25.

Waxman, M.H and Smits, L.J.M.: 1968, Electrical conduction in oil-bearing sands, *Society of Petroleum Engineers Journal*, **8**, 107-122

Wu, T.: 2004, Permeability prediction and drainage capillary pressure simulation in sandstone reservoirs, *Ph.D. thesis, Texas A&M University.*

Yuan, H. H. and Diederix, K. M.: 1987, The role of membrane potential measurements in shaly sand evaluation, 28^{th} *Ann. Logging Sym,* SPWLA, **Paper GG**.

Rock type	Porosity	T1 (ms)	CEC (meq/100g)	m	Density (g/cm^3)	k mD	S/M m^2/g
A1	0.190	208	0.3	1.69	2.65	311	0.597
A2	0.204	249	0.5	1.67	2.65	669	0.389
A3	0.205	192	0.6	1.73	2.65	508	0.356
A4	0.201	206	0.4	1.71	2.65	412	0.371
A5	0.186	60	1.4	1.8	2.65	7.5	2.21
A6	0.209	110	0.9	1.87	2.65	20.5	1.87
A7	0.217	112	1	1.81	2.65	52.5	1.76
A8	0.148	67	0.8	1.82	2.65	4.2	1.04
A9	0.185	179	0.6	1.66	2.65	308	0.295
A10	0.211	292	0.5	1.83	2.65	723	0.463
A11	0.199	243	0.6	1.67	2.65	323	0.585
A12	0.200	203	0.7	1.69	2.65	678	0.225
A13	0.176	139	1	1.82	2.65	10.9	0.774
A14	0.186	180	0.8	1.78	2.65	197	0.478
A15	0.194	201	0.9	1.74	2.65	353	0.616
A16	0.195	239	0.7	1.70	2.65	847	1.19
A17	0.181	181	0.4	1.73	2.65	279	0.536
Ar 13	0.209		5.2	2	2.58	0.41	8.22
Ar 14/1-B	0.173		3.5	2	2.65	0.03	6.64
Ar 14/1-T	0.215		5.4	2	2.63	0.13	7.47
Ar 15/2	0.180		3.1	2	2.54	0.48	3.43
Ar 16	0.212	167	4.5	2.14	2.64	0.17	4.91
Ar 18	0.230		4.9	2	2.63	0.19	6.18
Ar 28-B	0.129		2.4	2	2.64	1.94	0.828
Ar 30-S	–		2.1	2	–		0.991
Ar 31	0.149		2.4	2	2.62	5.21	1.26
Ar 40	0.087		1	2	2.62	0.02	0.908
Ar 41	0.103		1.2	2	2.62	0.04	0.968
Ar 41/2	0.105		1.7	2	2.63	0.06	1.18
Ar 43-T	0.088		2.3	2	2.66	0.01	3.88
Ar 61-B	0.127		1.3	2	2.64	0.13	0.814
Ar 62.02	0.312	166	1.9	2	2.62	2719	2.25
Ar 62.40	0.315		1.9	2	2.62	3553	1.86
Ar 63	0.117		2.2	2	2.61	0.54	1.38
Ar 63.22	0.272		1.7	2	2.62	2275	2.44
Ar 63.54	0.304	190	1.6	2	2.63	1382	1.88
Ar 64-B	0.082		6.4	2	2.69	0.02	6.26
Ar 64.21	0.248	34	2.6	2	2.62	3.3	8.3
Ar 64.45	0.269		1.5	2	2.62	332	10
Ar 64.65	0.285	183	1.9	2	2.62	215	1.73
Ar 64.94	0.280		1.9	2	2.63	262	4.97
Ar 65.32	0.278	147	2.1	2	2.63	151	2.11
Ar 65.58	0.276	198	1.7	2	2.64	426	1.65
ARC12849	0.092	37	1.9	1.73	2.67	0.39	2.07
ARC12863	0.303	203	1.7	1.62	2.62	1072	1.6
ARC12878	0.220	71	2.3	1.77	2.65	32.1	2.12
ARC12903	0.228	117	1.9	1.7	2.65	83.2	0.728
ARC12904	0.204	49	3.2	1.82	2.66	4.56	3.17
Bandera	0.219	51	3.5	2.15	2.68	6	3.46
Benoist E1	0.172	155	2.3	1.75	2.57	91.9	0.496
Benoist E2	0.167	222	3.5	1.71	2.63	190.4	1.37
Benoist E3	0.186	262	1.4	1.85	2.64	425	0.536
Benoist E4	0.183	242	1.8	1.67	2.64	270	0.668
Benoist E5	0.163	190	1.8	1.82	2.63	137	0.746
Benoist E6	0.156	138	2.1	1.77	2.63	28.5	0.617
Benoist E7	0.172	278	1.5	1.70	2.64	200	0.676
Benoist E8	0.164	157	1.9	1.81	2.62	36.5	
Benoist E9	0.183	204	1.4	1.76	2.64	243	0.562
Benoist E10	0.181	137	1.4	1.69	2.64	337	0.802
Benoist E11	0.149	203	1.9	1.73	2.64	39.9	1.25
Benoist E12	0.149	183	1.9	1.76	2.63	64.6	1.25
Benoist E13	0.196	295	1.3	1.65	2.63	670	0.473
Benoist E14	0.183	334	1.2	1.63	2.64	540	0.403

Rock type	Porosity	T1 (ms)	CEC (meq/100g)	m	Density (g/cm^3)	k mD	S/M m^2/g
Benoist E15	0.188	497	1.1	1.61	2.64	890	0.439
Benoist E16	0.178	314	1	1.62	2.64	430	0.574
Berea 100	0.205	214	0.87	1.88	2.65	45	0.88
Berea 200	0.239	358	0.61	1.79	2.64	685	0.57
Berea 350	0.238	361	0.9	1.83	2.66	591	0.6
Berea 400	0.229	359	1.01	1.82	2.66	511	0.7
Berea 500	0.216	416	0.59	1.79	2.65	478	0.63
Berea 600	0.222	332	1.01	1.90	2.66	131	0.67
Boise	0.262	249	12.6	2.00	2.61	601	1.4
Brown	0.101	72.3	1.7	2	2.65	0.03	1.14
C1	0.175	133	1.2	1.75	2.7	20.1	0.721
C2	0.181	113	1.9	1.86	2.7	110.5	1.226
C3	0.167	128	1.4	1.78	2.7	16.1	1.79
C4	0.165	121	1.3	1.79	2.7	12.7	1.103
C5	0.159	91	1.8	1.82	2.7	7	2.511
C6	0.152	95	1.6	1.86	2.7	6	1.422
C7	0.175	105	1.8	1.85	2.7	10.6	1.833
C8	0.164	57	2.2	1.87	2.71	2.3	2.414
C9	0.128	104	1.1	1.75	2.74	7.8	6.042
C10	0.167	93	1.6	1.82	2.72	7.4	1.198
C11	0.169	90	1.4	1.81	2.71	7.7	2.026
Coconino	0.139	135	1	1.88	2.64	62.5	0.96
EA 85	0.112	63	2.2	1.79	2.66	0.15	2.56
EA 22	0.132	53	0.61	1.92	2.67	0.39	0.43
EA 66	0.120	21	1.3	1.93	2.68	0.12	2.71
EA 21	0.102	15	1.6	1.86	2.69	0.01	3.5
EA 1	0.053				2.64		
EA 2	0.267				2.6	379	
EA 3	0.182				2.6	469	
EA 4	0.220				2.59	62.5	
Fountain A	0.223			1.64	2.64	1305	0.03
Fountain B	0.168			1.68	2.64	621	0.05
Fountain C	0.067			1.88	2.63	10.4	0.07
Gabon Shale	0.409	13.4	31	2.41	2.34	–	28.4
L1	0.161	15	2.9	2	2.71	0.011	8.55
L2	0.180	13	5	1.95	2.68	0.52	5.95
L3	0.166	14	4.4	1.95	2.67	0.52	7.22
L4	0.161	20	4.8	2	2.69	0.087	7.98
L5	0.172	150	1	1.76	2.67	12.1	0.94
L6	0.225	61	3	2.02	2.67	5.97	2.43
L7	0.196	27	4.2	2	2.69	1.72	3.89
L8	0.127	21	2.8	2.05	2.69	0.063	2.07
L9	0.152	58	1.3	2	2.68	0.93	1.38
L10	0.191	67	4.6	2	2.68	20.3	2.23
L11	0.148	43	4.6	2	2.68	4.72	2.35
Massillon 106	0.238	407	0.4	1.97	2.65	1242	0.5
Massilon 118	0.243	581	0.4	1.74	2.75	2590	0.5
Mesa 329	0.084	20.8	3.8	1.75	2.66	0.05	1.46
Mesa 356	0.078	42.7	3.1	1.67	2.65	0.02	0.968
Mesa 455	0.073	15.2	6.9	1.84	2.65	0.05	1.74
Mesa 490	0.039	6.6	6.2	1.70	2.69	0.01	2.96
Mesa 540A	0.119	38.5	4.6	1.85	2.66	0.12	
Mesa 876	0.088	35.2	2.6	1.81	2.66	0.01	1.69
Mesa 885	0.083	39.2	2.2	1.91	2.67	0.02	1.46
Mesa 935	0.120	28.8	6.1	1.97	2.65	0.04	2.22
Mesa 939	0.058	19.9	4.1	1.85	2.65	0.01	1.79
Milsap	0.204	54.4	2.6	1.95	2.65	3.2	1.95
Morrow 81	0.070	87.7	0.5	2	2.74	0.21	
Morrow 112	0.051	83.5	0.6	2	2.74	0.23	
Morrow 132	0.098	139.2	1	2	2.67	0.91	
Morrow 142	0.087	83.1	0.8	2	2.65	0.12	
Nugget	0.063	21	1.8	1.94	2.64	0.003	1.58
Portland	0.200	13	2.9	2.08	2.68	0.85	3.5

Table C-1: Rock properties for 126 sandstone samples (taken from Sen et al., 1990, Table 1).

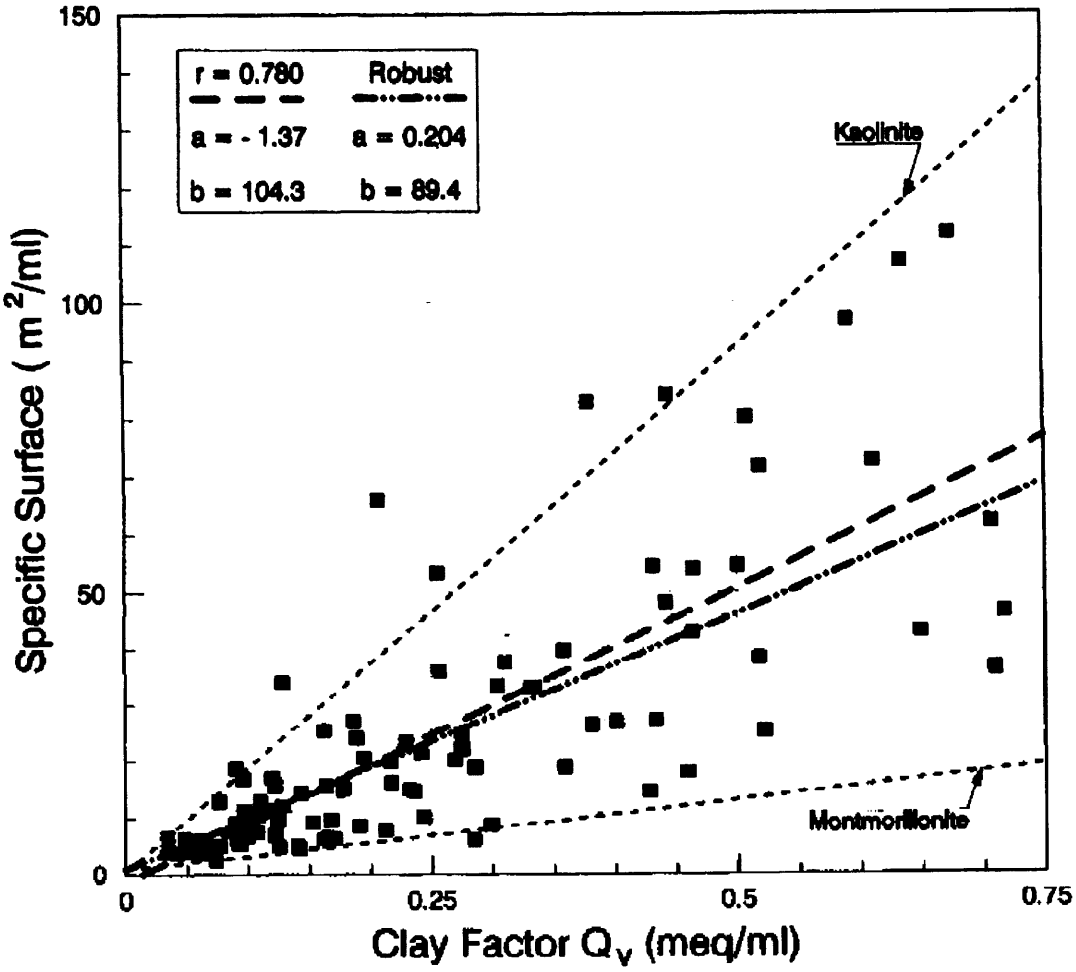

Figure C-1: Regression of S_{SC} and Qv for shaly sands. Samples with Qv in the range from 0.01 to 0.75 *meg/ml*. (Data from Sen et al., 1990) (figure taken from de Lima, 1995, Fig 2.). A linear equation $y=ax+b$ is used to regress the specific surface and Qv, r is the correlation coefficient.

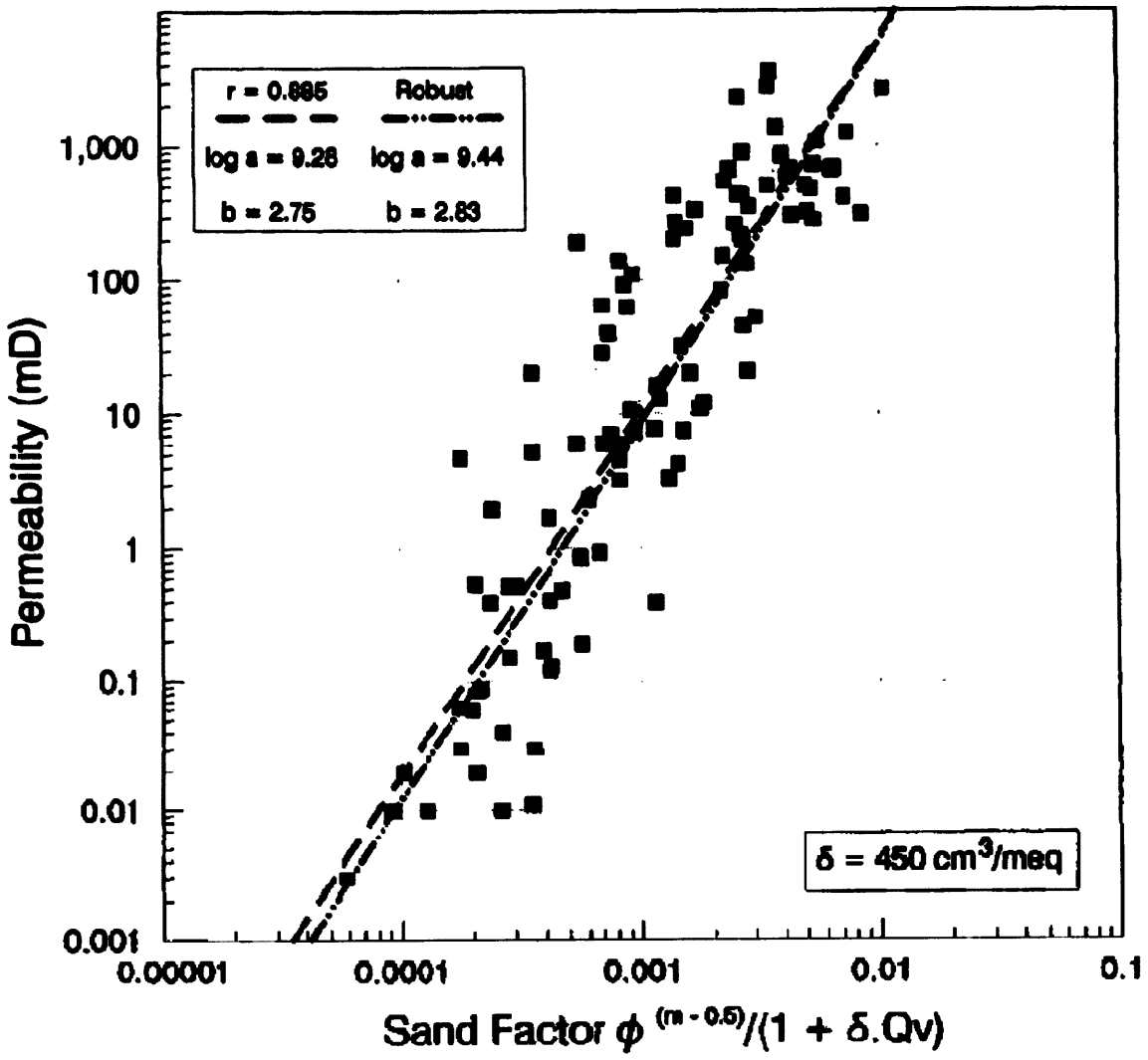

Figure C-2: Correlation of k versus $\phi^{(m-0.5)}/(1+\delta Q_v)$ for brine permeability of sandstones. $\delta = 450\ ml/meg$. (Data from Sen et al., 1990) (figure taken from de Lima, 1995, Fig 3.). A linear equation $y=ax+b$ is used to regress x and y axis, r is the correlation coefficient.

Appendix D

Governing Equations for the Coupled Eelctromagnetics and Acoustics of Porous Media

Coupled acoustic and electromagnetic fields in a homogeneous porous formation are described by Pride's governing equations (Pride, 1994). For a harmonic field with time dependence of exp (iωt), the coupling between mechanical motion and electric field is expressed as:

$$J = \sigma E + L(-\nabla p + \omega^2 \rho_f \mu) \tag{D-1}$$

$$-i\omega w = LE + (-\nabla p + \omega^2 \rho_f \mu)\, \kappa/\eta\,, \tag{D-2}$$

where J is the total electic current density, E is the electric field strength, μ is the solid frame displacement, w is the fluid filtration displacement and p is the pore fluid pressure. L is the coupling coefficient, ρ_f and η are the density and viscosity of the pore fluid, κ and σ are the permeability and conductivity of the porous medium respectively, ω is the angular frequency.

In the frequency domain, μ, w, and E obey the following set of equations (Pride and Haartsen, 1996):

$$\begin{gathered}(\mathrm{H}-\mathrm{G})\nabla\nabla\cdot\mu+\mathrm{G}\nabla^2\mu+C\nabla\nabla\cdot w+\omega^2\rho_{\mathrm{f}}\mathrm{w}=0\\ \mathrm{C}\nabla\nabla\cdot\mu+\omega^2\rho_{\mathrm{f}}\mu+\mathrm{M}\nabla\nabla\cdot w+\omega^2\tilde{\rho}\mathrm{w}-\mathrm{i}\omega\tilde{\rho}\mathrm{LE}=0,\\ \nabla\nabla\cdot E-\nabla^2E-\omega^2\mu\tilde{\varepsilon}\mathrm{E}+\mathrm{i}\omega^3\varepsilon\mu Lw=0\end{gathered}\tag{D-3}$$

where ε is the permittivity of the formation, $\tilde{\varepsilon}=\varepsilon+\mathrm{i}\sigma/\omega-\tilde{\rho}\mathrm{L}^2$ is the effective electrical permittivity of the formation, ρ is the density of the formation, $\tilde{\rho}=\mathrm{i}\eta/(\omega\cdot\mathrm{k})$ is the effective density for the relative flow, G is the shear modulus of the formation, and H, C, and M are porous medium moduli. The formation parameters ρ, H, C, and M can be expressed as:

$$\begin{gathered}\rho=(1-\phi)\rho_{\mathrm{s}}+\phi\rho_{\mathrm{f}}\\ \mathrm{H}=\mathrm{K_b}+4\mathrm{G}/3+(\mathrm{K_s}-\mathrm{K_b})^2/(\mathrm{D}-\mathrm{K_b})\\ \mathrm{C}=\mathrm{K_s}\,(\mathrm{K_s}-\mathrm{K_b})/(\mathrm{D}-\mathrm{K_b}),\\ \mathrm{M}=\mathrm{K_s}^2/(\mathrm{D}-\mathrm{K_b})\end{gathered}\tag{D-4}$$

where $\mathrm{D}=\mathrm{K_s}[1+\phi(\mathrm{K_s}/\mathrm{K_f}-1)]$, and ϕ is the formation porosity, $\mathrm{K_s}$ and $\mathrm{K_f}$ are the bulk moduli of the solid grain and the fluid, $\mathrm{K_b}$ is the bulk moduli of the 'frame of the grains' when the fluid is absent (Pride, 1994), ρ_{f} and ρ_{s} are the densities of the grain and fluid.

Once μ, w, and E are know, all the other quantities can be determined. The magnetic field can be determined by Faraday's law,

$$\mathrm{B}=-\mathrm{i}\,(\nabla\times\mathrm{E})/\omega\,.\tag{D-5}$$

And the magnetic field strength H can be obtained by

$$\mathrm{H}=\mathrm{B}/\mathrm{u}\ ,\tag{D-6}$$

where u is the magnetic permeability of the formation.

The dynamic permeability κ and the electrokinetic coupling coefficient L that appear in equations Eq. D-1 and Eq. D-2 are very important to the electrokinetic phenomena. Both are frequency dependent. When L goes to zero, Pride's equation separates to Maxwell's equations for an electromagnetic field, and Biot's equations (Biot, 1962) for a mechanical field in porous media. The expressions for L and κ are as follows:

$$\frac{L(\omega)}{L_o} = [1 - i\frac{\omega}{\omega_c}\frac{m}{4}(1 - 2\frac{\chi_d}{\Lambda})^2(1 - i^{\frac{3}{2}}\frac{\chi_d}{\delta})^2]^{-\frac{1}{2}} \tag{D-7}$$

$$\frac{\kappa(\omega)}{\kappa_o} = [(1 - i\frac{\omega}{\omega_c}\frac{4}{m})^{\frac{1}{2}} - i\frac{\omega}{\omega_c}]^{-1}, \tag{D-8}$$

where L_o is the low frequency linit of the coupling coefficient, $\omega_c = \phi\eta/\alpha_\infty \kappa_0 \rho_f$ is the so called transition frequency, ϕ is porosity, κ_0 is DC permeability, α_∞ is the tortuosity, η is the fluid viscosity, m is a dimensionless parameter defined as $m = \phi\Lambda^2/\alpha_\infty \kappa_0$, Λ is the weighted volume to surface ratio as introduced previously, $\delta = \sqrt{\eta/\omega\rho_f}$ is so called viscous skin depth, χ_d is the Debye length calculated as $\chi_d = \sqrt{\varepsilon_f \kappa_B T/e^2 z^2 N}$. ε_f is the fluid permittivity, κ_B is the Boltzman constant, T is the absolute temperature, e is the electric charge, z is the ionic valence of the solution, and N is the ion concentration defined as N = 6.022 x 10^{26} x molarity.

L_o is the low frequency limit of the coupling coefficient, which is usually obtained by laboratory measurement (Morgan et al., 1989; Pride and Morgan ,1991; Li et al., 1995), and defined as (Pride, 1994):

$$L_o = -\frac{\phi}{\alpha_\infty}\frac{\varepsilon_f \zeta}{\eta}[1 - 2\frac{\chi_d}{\Lambda}]. \tag{D-9}$$

where ζ is the zeta potential on the slipping plane. Despite the negative sign in its definition, L_o leads to positive streaming current densities for positive values of $-\nabla P$. This is because

the ζ potential is negative when the diffuse layer contains excess positive charge and positive when the diffuse layer contains excess negative charge. The correction term $1 - 2\frac{\chi_d}{\Lambda}$ is only valid under thin electric double layer (EDL) assumption and at most represens a correction of a few percent.

Pride and Morgan (1991) summerize the ζ vs. C relationship based on the experimental data by a variety of researchers as following:

$$\zeta = 0.008 + 0.026 \log_{10} C, \tag{D-10}$$

where C is the molarity of the solution. All data sets are for NaCl or KCl flowing past quartz of variying purity (Gaudian and Fuerstenau, 1955; Li and de Bruyn, 1996; Jednacak and Pravdic, 1974; Sidorova et al., 1975; Hifslho-Alverez et al., 1985).

References

Biot, M. A.: 1962, Mechanics of deformation and acoustic propagation in porous media, *J. Applied Phys.*, **33**, 1482-1489.

Gaudin, A. M. and Fuerstenau, D. W.: 1955, quartz flotation with anionic collectors, *Trans. AIME*, 66-72.

Hidalgo-alverez, R., De Las Nieves, F. J. and Pardo, G.: 1985, Comparative sedimentation and streaming potential studies for ζ potential determination, *J. Colloid Interface Sci*, **107**, 29E-300.

Li, H. C. and de Bruyn, P. L.: 1966, Electrokinetic and adsorption studies on quartz, *Surface Sci*, **5**, 203-220.

Li, S. X., Pengra, D. B. and Wang, P. Z.: 1995, Onsagers reciprocal relation and the hydraulic permeability of porous media. *Phys. Rev. E*, 51, 5748-5751.

Jednacak, J. and Pravdic, V.: 1974, The electrokinetic potential of glasses in aqueous electrolyte solutions, *J. Colloid Interface Sci*, **19**, 16-23.

Morgan, F.D., Williams, E.R. and Madden, T.R.: 1989, Streaming potential properties of westerly granite with applications, *Journal of Geophysical Research*, **94**, 12449-12461.

Pride, S. R. and Morgan, R. D.: 1991, Electrokinetic dissipation induced by seismic waves. *Geophysics*, **56**, 914-925.

Pride, S. R.: 1994, Governing equations for the coupled electromagnetics and acoustics of porous media, *Phys. Rev. B*, **50**, 15678-15696.

Pride, S. R. and Haartsen, M. W. (1996). Electroseismic wave properties. J. Acoust. Soc. Am., 100, 1301-1315.

Sidorova, M. P., Fazylova, M. and Fridrikhsberg, D. A.: 1975, Electrokinetic studies of some model systems: quartz-electrolyte solutions, Wolfram, E., Ed., Proc. Inter. Conf. Colloid Surf. Sci, *Elsevier Science Publ. Co., Inc.*

Appendix E

Geophysical Application of Seismoelectric Conversion: Seismoelectric Signal in Logging While Drilling[4]

Abstract

Borehole acoustic logging-while-drilling (LWD) for formation evaluation has become an indispensable part of hydrocarbon reservoir assessmen. However, the detection of acoustic formation arrivals over tool mode contamination has been a challenging problem in acoustic LWD technology. In this chapter, we propose a new method for separating tool waves from formation acoustic waves in acoustic LWD. This method is to measure the seismoelectric

[4] (the bulk of this Appendix is) Published as: Zhan X., Z. Zhu, S. Chi. and M. N. Toksöz.: 2009, Elimination of LWD (logging while drilling) tool modes using seismoelectric data, *Communications in Computational Physics,* **7**, 47-63.

signal excited by the LWD acoustic waves. LWD tool waves which propagate along the rigid string during the LWD process makes it impossible to accumulate any excess charge at the conductive tool – borehole fluid interface. Therefore, there should be no contribution by the tool modes to the recorded seismoelectric signals. We designed the laboratory experiments to collect simulated LWD monopole and dipole acoustic and seismoelectric signals in a sandstone borehole. The recorded acoustic and seismoelectric signals were analyzed in both time and frequency domains using a semblance method. To theoretically understand the seismoelectric conversion in the LWD geometry, we calculate the synthetic waveforms for the multipole LWD seismoelectric signals based on Pride's theory. Both experimental and numerical results confirm the absence of the tool mode in the electric field induced by the LWD-acoustic-wave along the borehole wall. By analyzing the spectrum of acoustic and electric signals, we can detect and filter out the difference between the two signals, which are the mainly tool modes and noise.

E.1 Introduction

Acoustic logging-while-drilling (LWD) technology was developed in the 1990's to meet the demand for real-time acoustic logging measurements for the purpose of providing seismic tie or / and acoustic porosity and pore pressure determination (Aron et al., 1994; Minear el al., 1995; Market et al., 2002; Tang et al., 2002; Cittá et al., 2004). As compared with wireline logging LWD has the advantage of measuring properties of a formation before drilling fluids invade deeply into it. Further, many wellbores prove to be difficult or even

impossible to measure with conventional wireline tools, especially highly deviated wells and deepwater wells. In these situations, the LWD measurement ensures that some measurements of the subsurface are captured in the event that wireline operations are not possible or become too expensive.

The LWD acoustic technology aims at measuring the compressional and shear wave velocities of an earth formation during drilling (Tang et al., 2002). Fig. E-1 is a schematic view of an LWD multipole acoustic source built into a drill collar. The LWD apparatus, with sources and receivers located close to the borehole wall and the drill collar taking up a large portion of the borehole, have some significant effects on borehole acoustic modes. Therefore, modeling wave propagation in the LWD environment has been the focus of several recent studies. The velocity dispersion characteristics for the formation and tool acoustic modes in LWD situations have been well studied by Rao et al., (1999, 2005) and Tang et al. (2002). The case of an off-center tool has been studied by Huang in 2003 (Huang, 2003).

The actual LWD measurement is complicated by several factors. One major influence is the noise caused by drilling and drilling mud circulation. The various vibrations of the drill string in its axial, radial, lateral, and azimuthal directions, together with the impact of the drill string on the borehole wall and the impact of the drill bit on the formation, generate strong drilling noise. Field measurements (Joyce et al., 2001) have shown that the frequency range of this noise influences the frequency range of the measurement of shear wave velocities in slow formations. The second problem is the impact of tool waves. The tool waves are strong in amplitude and always exist in the multipole LWD measurements. All these noise sources

contaminate the true formation acoustic waveform, causing difficulty in the recognition of formation arrivals. When the tool is not perfectly centered the tool modes become even more complex. Because of the complexity of collar movement during drilling, tool centralization is essentially unlikely. An off-centered quadrupole source inevitably generates some monopole and dipole components to excite tool waves along the collar (Tang et al., 2002). It is the difficulty in characterizing and removing the source of the noise that has motivated the research in this chapter.

The basis for seismoelectric conversion is the stronger electric double layer (EDL) that exists in most rock water systems (Ishido and Mizutani, 1981; Morgan et al., 1989; Loren et al., 1999). The EDL at the steel water interface of the tool, on the other hand, is rather weak (Hunter, 2001). In addition, the drilling string attached to the LWD tool is effectively grounded in field LWD operations. Therefore, there should be no contribution by the tool modes to the recorded seismoelectric signals.

Although borehole seismoelectric phenomena have been studied by several authors (Haartsen, 1995, 1997; Mikhailov et al., 2000; Zhu and Toksöz, 2003, 2005; Zhu et al., 2000, 2008) in recent years, the seismoelectric signal generated in the LWD process and their potential applications have not been investigated. This chapter represents the first attempt in this direction of research. We first designed physical LWD experiments in the lab to collect simulated LWD monopole and dipole acoustic and seismoelectric signals in a sandstone borehole. By analyzing the acoustic and electric signals in the time and frequency domains, we can observe different signal content, which are mainly tool modes and noise. Then we

applied a coherence method to pick out the common arrivals of the acoustic and seismoelectric signals, which is the pure formation modes. This method also has the side benefit of reducing the noise level in the acoustic LWD recording. This is very important for an actual field environment where the LWD recordings tend to be noisy.

E.2 Laboratory Measurement of LWD Acoustic and Seismoelectric Signal

E.2.1 Experiment Borehole Model

The experiment borehole we use is isotropic sandstone. The sandstone block has a length of 30cm, a width of 29cm, and a height of 23cm. The diameter of the borehole is 1.7cm. The P- and S- velocities are all higher than the borehole fluid velocity. The model parameters of our laboratory tool and the borehole, which is in a fast sandstone formation, are shown in Tab. E-1. The tool ID is $0.004m$, OD is $0.01m$ and borehole radius is $0.017m$. We use a scaling factor of 17 onto the laboratory tool compared with field LWD borehole and tool size. Schematics of the borehole model are shown in Fig. E-2. The porosity of sandstone is about 20% and permeability is about 100 millidarcy.

E.2.2 LWD Multipole Tool for Acoustic and Seismoelectric Measurement

In LWD multipole acoustic logging, both the source and the receiver transducers are tightly mounted on the drill collar. This attachment results in the receivers recording a tool mode propagating along the drill collar. The tool mode can interfere with the acoustic fields

propagating along the formation. To simulate the LWD measurement, we built a scaled multipole acoustic tool composed of three parts: the source, receiver, and a connector (Zhu et al., 2004). Our laboratory LWD tool includes three sections: the source, the receivers, and the connector. Both the source and receiver acoustic transducers are made of PZT crystal disks of 0.635cm in diameter and 0.37cm in thickness. The dimension of the tool is shown in Fig. E-3. For the scaled LWD tool, we use the equivalent composite tool velocity to indicate the steel tool has holes in it to embed acoustic transducers and electrodes. The tool ID is 0.4cm, OD is 1cm.

The source is made of four separate crystal disks shown in the B-B profile of Fig. E-3. The arrows on the disks indicate their piezoelectric polarization. Each disk has two electrodes attached to it; the eight electrodes are connected to a switch. Using the switch to change the electric polarization applied on each crystal disk, we can achieve a working combination to simulate a monopole or dipole source. The receiver section is composed of six pairs of crystal disks at six different locations. The polarizations of each disk pair are shown in the A-A profile of Fig. E-3.The connector section is made of a steel pipe threaded at each end. The source and receiver sections are tightly connected by this steel pipe to simulate the drill-string connection in LWD.

By changing the electric polarization of the source PZT disks and by combining the signals received by the receiver disk pairs, we are able to mimic a working system of acoustic logging sources. When the piezoelectric polarization of the source transducer is consistent with the positive pulse of the source signal, the phase of the acoustic wave is also positive.

The polarization of the received acoustic field is the same as the piezoelectric polarization of the receiver transducer. The working combinations of monopole and dipole systems are shown in Fig. E-4. During measurements, we used a switch to change the working mode from monopole to dipole. This allows us to conduct the multipole logging without changing or moving the tool position. Therefore, the experiment results can be compared under the identical conditions.

To measure the seismoelectric signal, we need to change the receiver section from acoustic transducers to electrodes. The electrodes used for this experiment are point electrodes of 1.0mm in diameter. Thus, each electrode on the electrode array can only detect the electric field around it. We replace the array of the six pairs of transducers by an array of six pairs of electrodes spaced at the same interval. The holes in which the electrodes are imbedded are filled with sand and glued by epoxy. The surface is covered with conducting glue and connected to the steel tool. The acoustic transducer is embedded in the logging tool as shown in Fig. E-3 to measure the acoustic pressure at the tool rim. The electrodes are protruding from the tool surface and are close to the borehole wall to measure the strength of the localized electric field at the borehole wall.

E.2.3 Experiment Mechanism and Procedure

It is generally accepted that the electric double layer (EDL) is the basis for the electrokinetic conversion (Morgan et al, 1989; Pride and Morgan, 1991; Loren et al., 1999). For our sandstone borehole model, an EDL is developed at the borehole wall. When the

acoustic waves hit the borehole wall, a localized electric field is generated and the electrode detects this electric field. Since the conductivity of the borehole fluid is very low, the recorded voltage between the electrode and ground can represent the electric field generated at the borehole wall. The difference between rock and metal is that the latter one is a conductor. By effectively grounding the drilling collar during the real LWD process, there would be no excess charge accumulated at steal tool surface. Though tool waves propagate along the rigid tool surface with large amplitude, no excess charge can be moved by the tool wave pressure to induce a localized electric field at the tool – borehole fluid interface. Thus, in the seismoelectric signals, what we record is purely the electric field excited by the formation acoustic waves propagating along the borehole wall and with the apparent velocities of formation acoustic modes. No electric component propagating at the apparent speed of tool wave can be observed in the electric signals.

The working system is shown in Fig. E-5. The source side is connected to a high voltage generator and the receiver side to a preamplifier and a filter before being displayed on an oscilloscope. The High Power Pulse Generator generates a square pulse with duration of 10us. This means that the source wavelet is a square wave with a center frequency of 100 kHz. The excitation voltages for the measurements vary between 5 volts and 750 volts. The sampling rate is 500 ns. For each trace we record 512 points. The filter range set from 300 Hz to 500 kHz is broad enough to include all the dominant acoustic and electric modes. We first take measurements in the borehole to record monopole and dipole acoustic waves. After finishing

recording of the measurements for the acoustic signals, the acoustic receiver transducers are replaced by electrodes to make the seismoelectric measurements.

E.3 Analysis of Recorded LWD Acoustic and Seismoelectric Signals

E.3.1 Array Processing Methods

Recorded LWD acoustic and seismoelectric signals are analyzed in both time domain and frequency domain. Array processing methods can be used to detect the various wave modes embedded in the waveform and calculate their velocity dispersion characteristics in a borehole. We use the semblance method to analyze the experimental data. This method can be applied in both time and frequency domains (Rao et al., 1999, 2005).

Time domain semblance algorithm searches for all arrivals received by the array and locates the appropriate wave arrival time and slowness values that maximize the coherent energy in the array waveforms. The coherence is defined as (Kimball and Marzetta, 1984):

$$\rho(s,t) = \frac{\int_T^{T+T_W} \left|\sum_{m=1}^{N} X_m(t+s(m-1)d)\right|^2 dt}{N \int_T^{T+T_W} \sum_{m=1}^{N} |X_m(t+s(m-1)d)|^2 dt}. \quad \text{(E-1)}$$

The acoustic array is composed of N receivers with a spacing of d. $X_m(t)$ represents the acoustic time signal at the mth receiver. A set of time windows defined by the center position T and length T_w is applied to the waveforms. The time window slides through the waveform at a certain time increment (usually half of the T_w). For a range of values of arrival time and slowness, the scalar semblance is computed for the windowed portion. We can find some

values of T and s, say ($s_{k,}$ $T_{k,}$), which maximize the semblance coherence function and obtain a semblance surface in the time-slowness plot. These peak semblance values mark the arrival time and the slowness of the acoustic wave modes in the array data (Tang and Cheng, 2004).

Frequency domain semblance is commonly used to estimate the velocity dispersion characteristics of the guided waves from array wave data. I use the method developed by Nolte et al. (1997) and Rao et al. (1999, 2005) to weight the semblance (or coherence function) of the array data. This method processes a frequency by weighting the data over neighboring frequencies and searches the peak of weighted semblance function over a range of slowness values to find the actual number of wave modes. The spectral semblance is defined as (Tang and Cheng, 2004)

$$\rho(\omega, s) = \frac{\left|\sum_{n=1}^{N} X_n^*(\omega) z^{n-1}\right|}{\sqrt{N \sum_{n=1}^{N} X_n^*(\omega) X_n(\omega)}}. \tag{E-2}$$

where, $z = \exp(-i\omega s d)$, $s(\omega)$is the slowness at frequency ω and d is the receiver spacing, the total expression for z denotes the wave propagation. The wave mode traveling at a distinct slow $s_k(\omega)$across each receiver in the array is $X_n(\omega) = h_k z_k^{n-1} = h_k(\omega) \exp(-i\omega s_k(n-1)d)$, where $h_k(\omega)$ is the amplitude of the kth wave mode. Maximizing $\rho(\omega, s)$ as a function of s_k for different frequencies will generate the dispersion curves. To enhance the data information and reduce noise, we first resample the spectral data to obtain denser data points and then try to maximize a weighted semblance function defined as:

$$F(\omega_t, s) = \sum_{j=l-m}^{l+m} W(\omega_j, \omega_m) \rho(\omega_m, s). \tag{E-3}$$

,where ω_l stands for the re-sampled frequency, $W(\omega_j, \omega_m)$is a Gaussian weight function given by

$$W(\omega_j, \omega_m) = \exp\left(-\frac{(\omega_m - \omega_j)^2}{2\sigma^2}\right). \quad \text{(E-4)}$$

The number of neighboring points to be weighted over is controlled by σ. Usually σ is set to be $4\Delta\omega$, where $\Delta\omega$ is the increment of re-sampled data.

E.3.2 Noise Reduction and Tool Waves

The electric data in the experiment is recorded by the point electrodes exposed in water. The signal is rather weak, therefore can be contaminated by the ambient electric fields (Butler and Russell, 1993, 2003; Russell et al., 1997). This ambient noise not only contaminates the electric waveforms but also reduces the ability of the semblance method to recognize the wave modes. In order to reduce noise and enhance the signal to noise ratio (SNR) of the electric signal, steps need to be taken both during the data collection process and during analysis.

To reduce random noise, we sum the repeated measurements. The averaging function of the oscilloscope is used for summing. Each trace in electric array data is the average of 512 sweeps. Good shielding to eliminate the outside noise is also very important for weak signal detection. Some good practices include the following: effectively grounding the computers, oscilloscope, and the shielding line of the point electrode; placing the transducers and electrodes completely in water; shutting down unnecessary electric sources; grounding the water tank, etc.

Besides random noise, we also have a large synchronous signal from the source and a DC component in the electric recordings. This synchronous signal is large in amplitude and appears in front of the wave train so that a lot of useful modes may be buried in the large noise. Fortunately, the source noise does not have a phase move-out over the receiver array, while the seismoelectric signals do. We can subtract the mean value of the six source – receiver offsets traces from each individual trace to eliminate this noise. The DC component can be eliminated with a high-pass filter for each trace separately.

In order to understand the properties of monopole and dipole tool modes of our specific scaled multipole tool, we first conduct measurements by putting the tool with and without the connector into the water tank, in the absence of a borehole and formation, as shown in Fig. E-5. Case A has been studied by Zhu et al. (2004) and we do not repeat it here. Since the acoustic impedance difference between the steel and water is large, no tool wave can be recorded when the connector is not present. In case B, we make the measurements in water tank with the connector and obtain the monopole tool wave (speed at 3500 *m/s*) and the dipole tool wave (speed about 800 *m/s*). The waveforms of monopole and dipole tool modes and their time domain semblances are shown in Fig. E-6.

E.3.3 LWD acoustic and seismoelectric signals in sandstone borehole

After we analyze the velocity of our LWD multipole tool, we test the absence of seismoelectric signal at the tool-electrolyte interface. To understand the EDL at the steel fluid interface more intuitively, we measure the seismoelectric signals by putting the scaled

multiple tool in the water tank. This is exactly the same setup as the measurement of tool waves in the water with the connector shown in (Fig. E-5 B). The electric records taken at the tool water interface are very weak due to the low density of the EDL at the steel water interface and the grounding of the steel tool. Almost no mode is observed from the recorded electric signals. Thus, the LWD seismoelectric signal should contain no tool mode contribution.

At this point, we have validated our scaled laboratory tool as a multipole acoustic source, studied the acoustic property of the laboratory tool, now we will focus on the difference between the LWD acoustic and seismoelectric signals in the sandstone borehole model. As pointed out previously, the seismoelectric signal excited in the acoustic LWD process should contain no signals with the apparent velocity of the tool modes.

We now examine the two kinds of signals for monopole (Fig. E-7) and dipole (Fig. E-8) excitations using time domain and frequency domain analysis. From the acoustic waveform we can clearly see a monopole tool wave coming between P and S wave and a low frequency dipole tool wave coming in the late part of the wave train. In the time domain semblance we can observe the peaks at the monopole and dipole tool waves. In the seismoelectric data, tool modes do not exist. This is especially clear in the frequency domain semblance, where the monopole and dipole tool modes are absent. These results show that by measuring the seismoelectric signal during the logging-while-drilling process, we can potentially eliminate the effect of tool modes.

E.3.4 LWD acoustic and seismoelectric signal Correlation

Based on the laboratory experiments we conclude the following:

LWD acoustic signal = Formation acoustic waves + Tool waves + Noise

LWD SE signal = Formation acoustic wave induced electric signals + Noise.

In field acoustic LWD operation, the tool modes can have velocities close to the formation velocities for some formations. Therefore, the detection of formation arrivals can be hampered by tool mode contamination. When the LWD tool departs from the centralized position, the tool contamination can be even more complex. The seismoelectric signal in the LWD process, do not contain tool mode induced electric signals. Given that the LWD acoustic and seismoelectric (SE) signals are different in content, we can use the SE signal to filter the acoustic signal to eliminate the tool modes.

We measure the similarity between the acoustic and SE signals using their respective spectra. There are several reasons for this to be done in the frequency domain instead of the time domain. (1) In the frequency range where the formation acoustic wave modes exist, the waveforms overlap better. In other frequency ranges where the waveforms differ greatly due to the different modes content, it is difficult to find the correlation between the two signals. (2) There are phase difference between the two signals due to the various circuit elements used in laboratory collection of the two signals and the seismoelectric coupling. (3) In the acoustic record, it takes time for the main acoustic energy to propagate from the borehole wall to the receiver transducer at the fluid acoustic velocity. While the propagation time for the electric

signal can be ignored due to the high EM wave speed. Thus, it is more difficult to compare the two signals in time domain than in the frequency domain.

We calculate the similarity coefficients of the two signals defined by:

$$r = \frac{\sum_m A_m B_m}{\sqrt{\sum_m (A_m)^2 (B_m)^2}}, \tag{E-5}$$

where A_m and B_m are the acoustic and electric amplitude spectrum, m is the index of the sampling point in frequency domain. A moving window is used to scan the spectra of the two signals simultaneously. The similarity coefficient of that window is set to be the similarity for the center frequency of the window.

The similarity curves and the filtered results are shown in Fig. E-9 for monopole excitation and Fig. E-10 for dipole excitation. In Fig. E-8, ST stands for Stoneley wave, T stands for monopole tool wave. In Figure Fig. E-10 F stands for dipole flexural wave, T stands for dipole tool wave. The monopole similarity curve is similar to a band stop filter. The dipole coherence curve is similar to a band pass filter.

After obtaining a coherence curve (Fig. E-9 b right, Fig. E-10 b right), we use it to design a zero-phase filter to be applied to the acoustic signal. A time domain semblance for the filtered data is then computed. We can see clearly that the filtered data contains only formation acoustic modes (Fig. E-9 c right, Fig. E-10 c right). Other benefits of this filtering method include the reduction of noise in the acoustic signal as well. To further demonstrate these benefits, we detect the peaks in the acoustic and seismoelectric signal spectra and calculate the corresponding wave velocity of those frequency peaks. We find that in the

frequency range with low similarity the wave velocities are also different, which means the wave modes are different.

The above analysis illustrates that by correlating the LWD seismoelectric signal with the acoustic signal, we can pick out formation acoustic modes from the LWD acoustic measurement and reduce the noise. This is a very significant result for extracting the formation arrivals from real-time LWD field data that may be contaminated by the complex tool modes and the drilling noise.

E.4 Numerical Simulation of LWD Acoustic and Seismoelectric Signal

In this section we develop a theoretical model to simulate the seismoelectric effect during the LWD process in a borehole. The modeling was performed for an isotropic, homogenous elastic formation and both axially symmetric (monopole) and axially non-symmetric (dipole) sources.

E.4.1 Modeling LWD Acoustic Wave Propagation

The presence of a logging tool in the borehole will modify the excitation and propagation characteristics of the borehole acoustic waves (Tang et al., 2002; Huang, 2003). To model the acoustic wave propagation in the logging-while-drilling (LWD) configuration, we use the acoustic theory for a multi-layered system. The tool body is made of steel, its elastic moduli and density are much higher than those of the borehole fluid. The dimension of the source on

the acoustic tool cannot be ignored, thus we use an acoustic ring source instead of point source in the LWD modeling.

The geometry and coordinate of the borehole and the logging tool is shown in Fig. E-11. The axial direction is z; radial direction is r. The borehole formation is a homogenous, elastic formation. The acoustic logging tool is modeled as a cylindrical structure with the outer radius (tool OD), r_2 a multipole ring source is constructed by a distribution of the point sources along the tool rim. Both the source and receivers are located at the tool outer radius, where $r_{source} = r_{receiver} = r_2$. By summing the contributions of all these point sources, the resulting radial displacement at the source location can be expressed in the wave-number domain as (Tang and Cheng, 2004):

$$u = \varepsilon_n\left(-n\,K_{n-1}(fr_2)/r_2 - fK_n(fr_2)\right)I_n(fr_2)\cos\left(n(\theta-\phi)\right). \quad \text{(E-6)}$$

Here, $\varepsilon_n$is 1 for $n = 0$, and 2 for $n > 0$ where n is the azimuthal order number with $n = 0, 1, 2$ corresponding to monopole, dipole and quadrupole source, respectively. I_n and $K_n\,(n = 0, 1, ..)$ are the modified Bessel functions of the first and second kind of order n. $f = (k^2 - k_f^2)^{1/2}$ is the radial wavenumber, where k is the axial wavenumber and $k_f = \omega/\alpha_f$; ω is the angular frequency and α_f is the fluid acoustic velocity. The cylindrical coordinate (r, θ, z) is used and ϕ is a reference angle to which those point source location are referred.

Finally, we apply the acoustic boundary conditions to the three boundaries (inner fluid tool inner layer, tool outer layer outer fluid, outer fluid borehole wall) and a Ricker wavelet of the form (Aki and Richards, 1980):

$$S(\omega) = (\frac{\omega}{\omega_0})^2 e^{i(\omega/\omega_0)^2} \quad \text{(E-7)}$$

to calculate the pressure waveform at the rim of the tool.

E.4.2 Converted Electric Field in LWD Geometry

The coupling between the acoustic and electromagnetic field in a porous media can be expressed as (Pride, 1994):

$$J = \sigma E + L(-\nabla p + \omega^2 \rho_f \mu) \quad \text{(E-8)}$$

$$-i\omega w = LE + (-\nabla p + \omega^2 \rho_f \mu)\, \kappa/\eta\,, \quad \text{(E-9)}$$

where J is the total electic current density, E is the electric field strength, μ is the solid frame displacement, w is the fluid filtration displacement and p is the pore fluid pressure. L is the coupling coefficient, ρ_f and η is the density and viscosity of the pore fluid, κ and σ is the permeability and conductivity of the porous medium respectively, ω is the angular frequency. The detailed expressions of L, κ are given in Appendix D derived by Pride (1994). The zeta potential we used in our simulation is calculated from Eq. D-10. The NaCl brine conductivity is 0.05S/m, which is the same as what we use in the laboratory experiment. In our numerical simulation, L value is calculated by using the experimental porous formation parameters listed in the Tab. E-2.

Taking the divergence of Eq. E-8 and using $E = -\nabla\Phi$ with gerneralized Ampere's law, we can obtain:

$$\nabla^2\Phi = (L/\sigma)(-\nabla^2 p + \omega^2 \rho_f \nabla^2 \varphi), \quad \text{(E-10)}$$

where φ is the displacement potential of the gradient field. To solve Eq. E-8 in the wavenumber domain, we get

$$\Phi = A \cdot K_n(kr) + (L/\sigma)(-p + \omega^2 \rho_f \varphi), \tag{E-11}$$

where k is the axial wavenumber, $K_n(kr)$ is the modified Bessel function of n*th* order and A is the unknown coefficient for the electric field to be decided by the electric boundary conditions.

In the LWD geometry, using the expression of the displacement potentials in the elastic formation, which is the 4th layer, can be expressed as:

$$\begin{aligned} \varphi_4 &= B_4 K_n(kp_4 r) \\ \chi_4 &= D_4 K_n(ks_4 r), \\ \Gamma_4 &= F_4 K_n(ks_4 r) \end{aligned} \tag{E-12}$$

where φ_4 is the compressional wave potential of the formatiom, χ_4 and Γ_4 are the vertically and horizontally polarized shear wave potential. In terms of potentials, the radial displacement component μ_r in the elastic formation can be expressed as:

$$\mu_r = \frac{\partial \varphi_4}{\partial r} + \frac{1}{r}\frac{\partial \chi_4}{\partial \theta} + \frac{\partial^2 \Gamma_4}{\partial r \, \partial z}. \tag{E-13}$$

Combining Eq. E-12 and Eq. E-13, we can get

$$\mu_r = B_4 K_n'(kp_4 r) + \frac{n}{r} D_4 K_n(ks_4 r) + iks_4 F_4 K_n'(ks_4 r). \tag{E-14}$$

Substituting Eq. E-12 into Eq. E-11 and Eq. E-13 into Eq. E-8, we can get the expression for the potentialΦ_{wall}, radial strength E_{rwall} and the streaming current density J_{wall} of electric field along the elastic borehole wall

$$\begin{aligned} \Phi_{wall} &= AK_n(kr) + (L/\sigma)\omega^2 \rho_f B_4 K_n(kp_4 r) \\ E_{rwall} &= -\frac{\partial \Phi_{wall}}{\partial r} = -AK_n'(kr) - (L/\sigma)\omega^2 \rho_f B_4 K_n'(kp_4 r), \\ J_{wall} &= -\sigma AK_n'(kr) + L\omega^2 \rho_f \left[\frac{n}{r} D_4 K_n(ks_4 r) + iks_4 F_4 K_n'(ks_4 r)\right] \end{aligned} \tag{E-15}$$

where σ is the rock conductivity. Under the quasi-static assumption, the electric field in the borehole satisfies the Laplace's equation (Hu and Liu, 2002), the solution for the potential Φ_{flu}, radial strength E_{rflu} and the streaming current density J_{flu} is:

$$\begin{aligned} \Phi_{flu} &= \mathrm{BI_n(kr)} + \mathrm{CK_n(kr)} \\ \mathrm{E}_{rflu} &= -\frac{\partial \Phi_{flu}}{\partial \mathrm{r}} = -\mathrm{BI_n'(kr)} - \mathrm{CK_n'(kr)}, \\ \mathrm{J}_{flu} &= -\sigma \frac{\partial \Phi_{flu}}{\partial \mathrm{r}} = -\sigma\left[\mathrm{BI_n'(kr)} + \mathrm{CK_n'(kr)}\right] \end{aligned} \tag{E-16}$$

where B and C are the coefficients to be determined by the electric boundary conditions.

E.4.3 Acoustic and Electric Boundary Conditions

To solve the three coefficients *A, B* and *C* in the above expressions for the converted electric fields along the borehole wall (Eq. E-15) and in the borehole fluid (Eq. E-16), we apply the following boundary conditions.

For acoustic boundary conditions, we have the continuity of the radial displacement μ and stress element σ_{rr} , and the vanishing of the other two shear stress elements $\sigma_{r\theta}$ andσ_{rz}. For the electric boundary conditions, we have $\Phi_{wall} = \Phi_{flu}$, $\mathrm{J}_{wall} = \mathrm{J}_{flu}$ at the borehole wall, and the radial current density or the radial electric field strength (since they only differ in the multiplication of a conductivity) is equal to zero at the tool surface. At the tool surface, no current flowing between borehole fluid and tool surface. Thus, the radial current density or equivalently radial electric field strength should be set to zero.

Substituting equation Eq. E-15 and Eq. E-16 into the three boundary conditions, we could rewrite the boundary conditions in the matrix formation as following:

$$\begin{bmatrix} \frac{-I_n'(kr_2)}{K_n'(kr_2)}K_n(kr)+I_n(kr) & -K_n(kr) \\ \frac{-I_n'(kr_2)}{K_n'(kr_2)}K_n'(kr)+I_n'(kr) & -K_n'(kr) \end{bmatrix} \begin{bmatrix} B \\ A \end{bmatrix} = \begin{bmatrix} (L/\sigma)\omega^2\rho_f B_4 K_n(kp_4 r) \\ -(L/\sigma)\omega^2\rho_f \left[\frac{n}{r}D_4 K_n(ks_4 r)+iks_4 F_4 K_n'(ks_4 r)\right] \end{bmatrix}$$

. (E-17)

From Eq. E-17, we could get A, B and C after we solve the acoustic coefficients B_4, D_4 and F_4 by applying the LWD acoustic boundary conditions. Once A, B and C are all determined the electric field both along the borehole wall and within the borehole fluid can be determined.

E.4.4 Synthetic Waveforms of LWD acoustic and seismoelctric signal

The formation properties are the same as the lab formation. The four layer model we use to simulate the LWD process is listed in the Tab. E-1. A scaling factor of 17 is used to scale the lab tool to the field scale. The source wavelet in the experiment is a square wave with a center frequency of 100 kHz. Scaling the 100 kHz center frequency to the modeling, we use a Ricker wavelet with the center frequency of 6 kHz as a source. The formulae in both acoustic and electric calculations are expressed in the wavenumber domain, thus we use the discrete wavenumber method (Bouchon and Schimitt, 1989; Bouchon, 2003) to do the modeling.

Fig. E-12 and Fig. E-13 show the calculated monopole and dipole waveforms using the formation parameters of our lab experiment. Solid curves are the acoustic signals and the dotted curves are the electric signals. (A-A) is the radiating electromagnetic wave in both

figures. The figures are scaled back to the real lab borehole tool scale with the first trace located at $z = 0.098m$ and the spacing is $0.012m$.

In Fig. E-12, (B-B) is the formation compressional wave, (C-C) is the monopole tool wave and (D-D) represents the formation shear wave, (E-E) is the Stoneley wave. We use the same semblance method to analyze the wave modes in the acoustic and electric waveforms as we did for the experiment data. The time domain semblances for the monopole acoustic and electric waveforms are shown in Fig. E-14 and Fig. E-15, respectively. The absence of the monopole tool mode which is indicated by the first big block in Fig. E-14 can be observed very clearly in the semblance of the electric signal (Fig. E-15).

The same phenomena can be observed for the dipole case. In Fig. E-13, (B-B), (C-C), (D-D) are the 2^{nd} order dipole formation flexural wave, dipole tool wave and 1^{st} order dipole formation flexural wave, respectively. The absence of the dipole tool mode, which is indicated by the second big block in Fig. E-16, can be observed very clearly in the semblance of the electric signal (Fig. E-17). These observations are consistent with the laboratory measurements. Both the experimental and theoretical study proves that LWD seismoelectric signals do not contain contributions from tool modes.

E.5 Summary

In this work, we studied the electric fields induced by borehole monopole and dipole LWD acoustic waves both theoretically and experimentally. We developed laboratory experimental set-up and procedures as well as processing methods to enhance the recorded

seismoelectric signal. A suite of acoustic and seismoelectric measurements are made to demonstrate and understand the mechanism of the borehole seismoelectric phenomena, especially under LWD acoustic excitation. A Pride-theory-based model for the acoustic wave induced electric field in the LWD geometry can also be used to calculate the electric field strength excited by the acoustic pressure.

Summarizing the whole chapter, the following two conclusions can be reached:

1. LWD seismoelectric signals do not contain contributions from tool modes.

2. By correlating the LWD seismoelectric and acoustic signals, we can effectively separate the real acoustic modes from the tool modes and improve the overall signal to noise ratio in acoustic LWD data.

Laboratory experiments with good control of noise level and medium salinity brines are ideal settings compared to the field measurements. In practice, during drilling, a pressure difference between formation and borehole creates mud invasion and pressure transients can also generate seismoelectric signals. In well drilled with oil-based mud, seismoelectric potential will also exist if the mud contains a water fraction. In the case of bottom hole pressure to be a few *kpsi*, streaming potential signal could be at the order of tens of *mv*. This indicates the feasibility of collecting seismoelectric signal in real drilling environment

This work has taken the first step towards understanding borehole LWD seismoelectric phenomena. With future improvements in both theory and instrumentation, seismoelectric LWD might evolve into a new logging method in the future.

Acknowledgement

We thank Dr. Shihong Chi from ConocoPhillips for his direction on the numerical modeling of LWD acoustic wave propagation.

References

Aki, K. and Richards, P. G.: 1980, Quantitative Seismology, Theory and Methods. W. H. Freeman and Co., San Francisco.

Aron, J., Chang, S., Dworak, R., Hsu, K., Lau, T., Masson, J., Mayes, J., McDaniel, G., Randall, C., Kostek, S., and Plona, T.: 1994, Sonic compressional measurements while drilling, SPWLA 35th Annual Logging Symposium.

Bouchon, M. and Schimitt, D.: 1989, Full-wave acoustic logging in an irregular borehole, *Geophysics*, **54**, 758-765.

Bouchon, M.: 2003, A review of the discrete wavenumber method, *Pure and Applied Geophysics*. **160**, 44E-465.

Butler, K. E. and Russell, R. D.: 1993, Subtraction of powerline harmonics from geophysical records, *Geophysics*, **58**, 889-903.

Butler, K. E. and Russell, R. D.: 2003, Cancellation of multiple harmonic noise series in geophysical records, *Geophysics*, **68**, 1083-1090.

Cittá, F., Russell, C., Deady, R., and Hinz D.: 2004, Deepwater hazard avoidance in a large top-hole section using LWD acoustic data, *The Leading Edge*, **23**, 566-573.

Huang, X.: 2003, Effects of tool positions on borehole acoustic measurement: a stretched grid finite difference approach, *Ph.D. thesis*, Massachusetts Institute of Technology.

Hu, H. S. and Liu, J. Q.: 2002, Simulation of the converted electric field during acoustoelectric logging, *SEG Int'l Exposition and 72nd Annual Meeting.*

Hunter, Robert J.: 2001, Foundations of colloid science, *Oxford University Press*, New York

Ishido, T. and Mizutani, H.: 1981, Experimental and theoretical basis of electrokinetic phenomena in rock-water systems and its applications to geophysics, *J. Geophys Res.*, **86**, 1763-1775.

Kimball, C. V., and Marzetta, T. L.: 1984, Semblence processing of borehole acoustic array data, *Geophysics*, **49**, 274-281.

Joyce, B., Patterson, D., Leggett, J. V., and Dubinsky, V.: 2001, Introduction of a new

omni-directional acoustic system for improved real-time LWD sonic logging-tool design and field test results, *SPWLA 42nd Annual Logging Symposium.*

Loren, B., Perrier, F., and Avouac, J. P.: 1999, Streaming potential measurements 1. Properties of the electrical double layer from crusted rock samples, *J. Geophys Res.*, **104**, 17857-17877.

Market, J., Althoff, G., Barnett, C., and Deady, R.: 2002, Processing and quality control of lwd dipole sonic measurements, *SPWLA 43rd Annual Logging Symposium, Osio, Japan.*

Mikhailov, O. V., Queen, J., and Toksöz, M. N.: 2000, Using borehole electroseismic measurements to detect and characterize fractured (permeable) zones, *Geophysics*, **65**, 1098-1112.

Minear, J., Birchak, R., Robbins, C., Linyaev, E., and Mackie, B.: 1995, Compressional wave slowness measurement while drilling, *SPWLA 36th Annual Logging Symposium.*

Morgan, F.D., Williams, E.R. and Madden, T.R.: 1989, Streaming potential properties of westerly granite with applications, *Journal of Geophysical Research*, **94**, 12449-12461.

Nolte B., Rao, V. N. R., and Huang, X.: 1997, Dispersion analysis of split flexural waves, *Borehole Acoustic and Logging / Reservoir Delineation Consortia Annual Report*, MIT.

Pride, S. R. and Morgan, R. D.: 1991, Electrokinetic dissipation induced by seismic waves. *Geophysics*, **56**, 914-925.

Pride, S. R.: 1994, Governing equations for the coupled electromagnetics and acoustics of porous media, *Phys. Rev. B*, **50**, 15678-15696.

Rao, V. N. R., Burns, D. R., and Toksöz, M. N.: 1999, Models in LWD applications. *Borehole Acoustic and Logging / Reservoir Delineation Consortia Annual Report*, MIT.

Rao, V. N. R. and Toksöz, M. N.: 2005, Dispersive wave analysis – method and applicatoins. *Borehole Acoustic and Logging / Reservoir Delineation Consortia Annual Report*, MIT.

Russell, R. D., Butler, K. E., Kepic, A. W., and Maxwell, M.: 1997, Seismoelectric exploration. *The Leading Edge*, **16**, 1611-1615.

Tang, X. M. and Cheng, C. H.: 1993, Effects of a logging tool on the Stoneley waves in

elastic and porous boreholes, *Log Analyst*, **34**, 46-56.

Tang, X. M., Dubinsky, V., Wang, T., Bolshakov, A., and Patterson, D.: 2002, Shear-velocity measurement in the logging-while-drilling environment: modeling and field evaluations. *SPWLA 43rd Annual Logging Symposium*, **paper RR**.

Zhu, Z. and Toksöz, M. N.: 2003, Seismoelectric measurements in cross-borehole models with fractures, *Proceedings of 6th SEGJ International Symposium*, 342-347.

Zhu, Z., Rao, V. N. R., and Burns, D. R., and Toksöz, M. N.: 2004, Experimental studies of multipole logging with scaled borehole models, *Borehole Acoustic and Logging / Reservoir Delineation Consortia Annual Report*, MIT.

Zhu, Z. and Toksöz, M. N.: 2005, Seismoelectric and electroseismic measurements in fractured borehole models, *Geophysics*, **70**, F4E-F51.

Zhu, Z., Toksöz, M. N. and Burns, D. R.: 2008, Electroseismic and seismoelectric measurements of rock samples in a water tank, *Geophysics*, **73**, E153-E164.

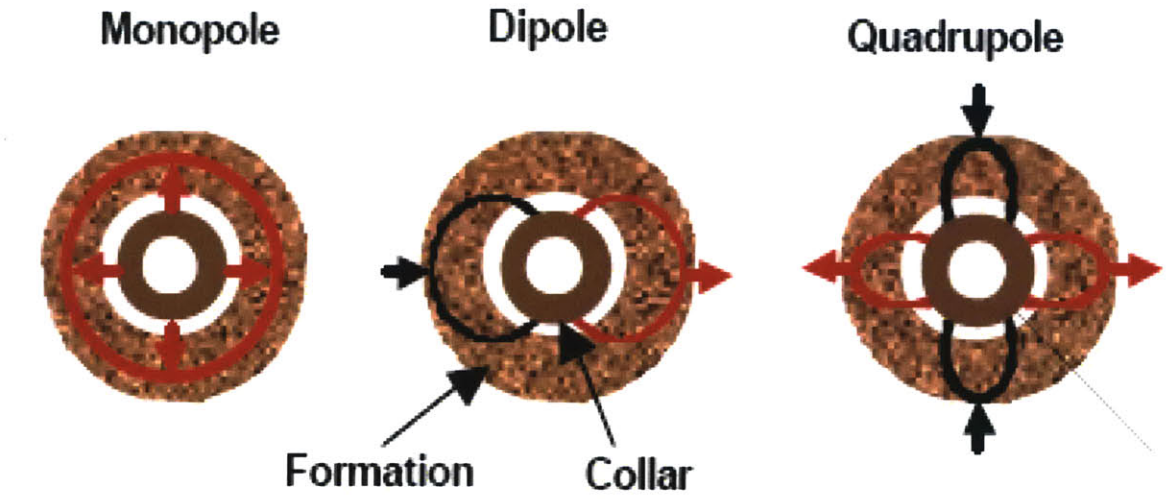

Figure E-1: Azimuthal wave-amplitude variation pattern for the monopole, dipole and quadrupole sources in connection with the LWD model (Tang et al., 2002).

	P-velocity	S-velocity	Density	Outer radius
Inner fluid	1500 *m/s*	-------	1000 kg/m^3	0.024m
Tool (Composite)	4185 *m/s*	2100 *m/s*	7700 kg/m^3	0.085m
Outer fluid	1500 *m/s*	-------	1000 kg/m^3	0.11m
Formation	4660 *m/s*	2640 *m/s*	2100 kg/m^3	∞

Table E-1: Laboratory sandstone borehole model.

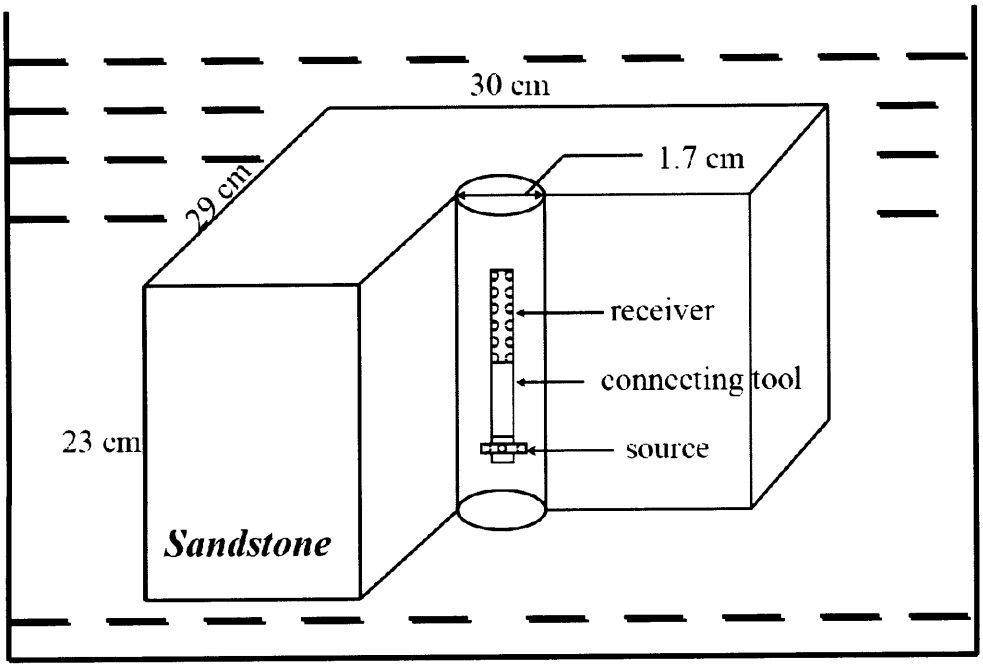

Figure E-2: Schematics of the borehole model in laboratory measurement.

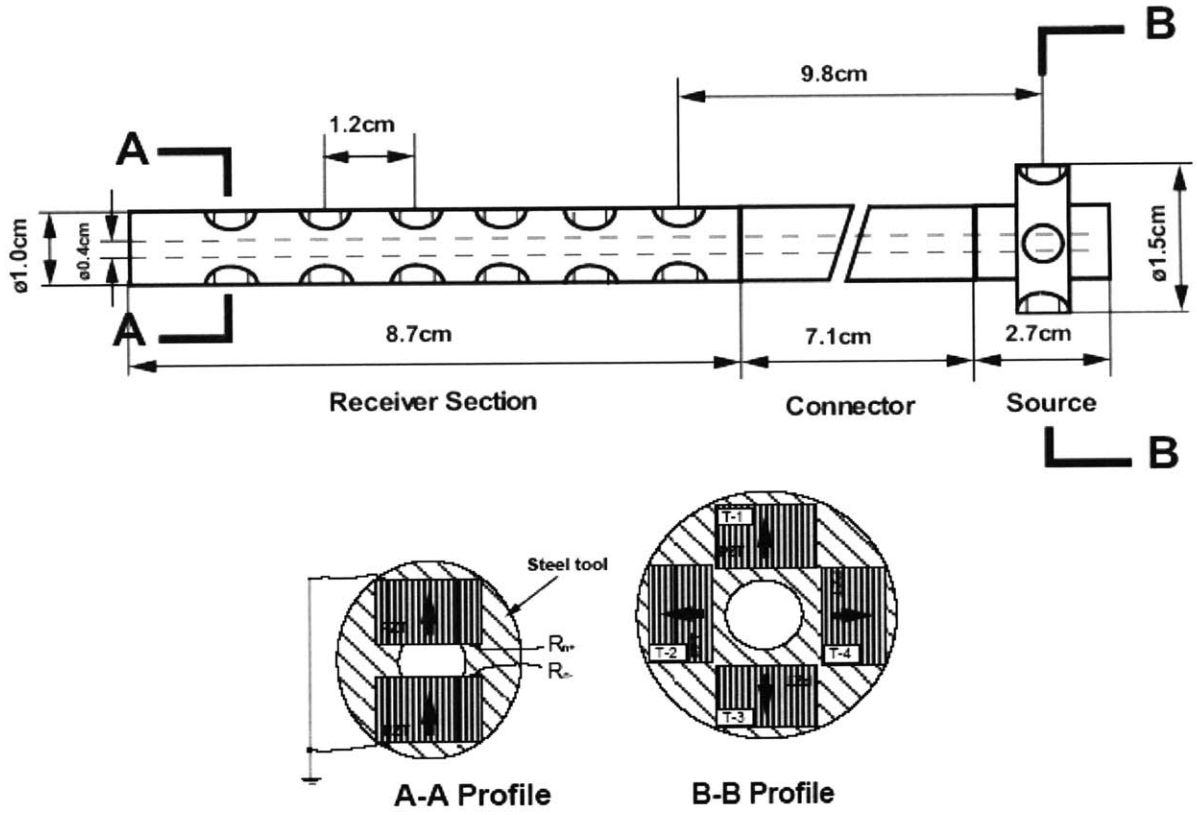

Figure E-3: Schematics of the borehole model in laboratory measurement.

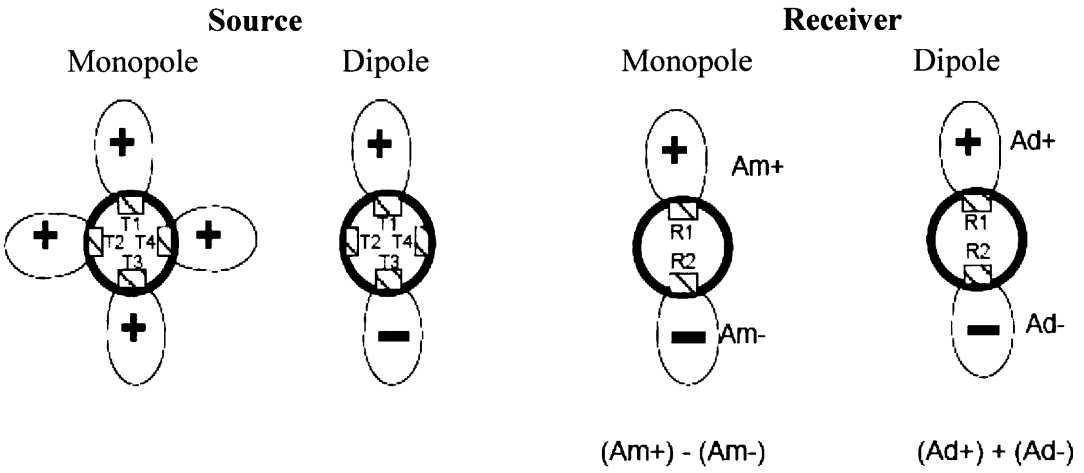

Figure E-4: Schematic diagram of the working modes of the multipole logging tool. The "+" and "-" indicate the polarization of the electric signals in the source and the polarization of the PZT crystals in the receiver (Zhu et al., 2004).

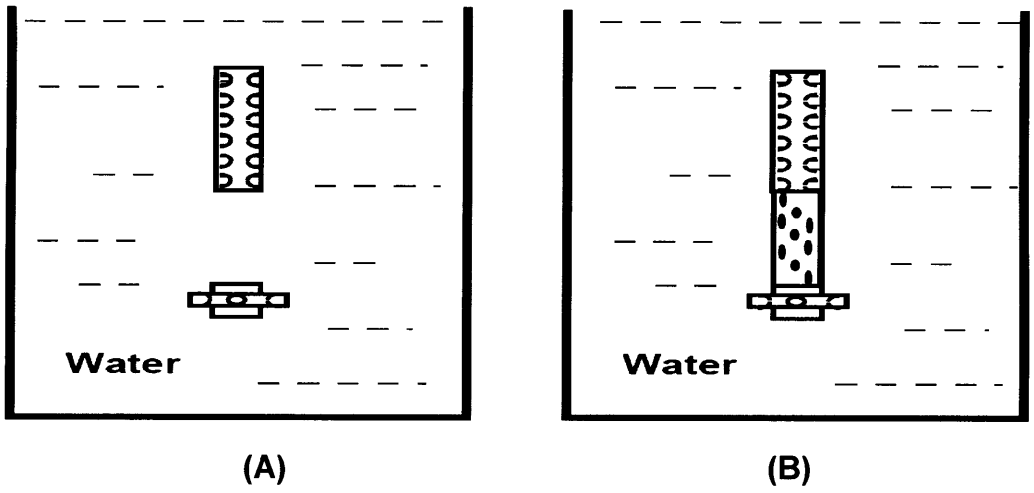

Figure E-5: Measurements in the water tank without (A) and with (B) connector (Zhu et al., 2004).

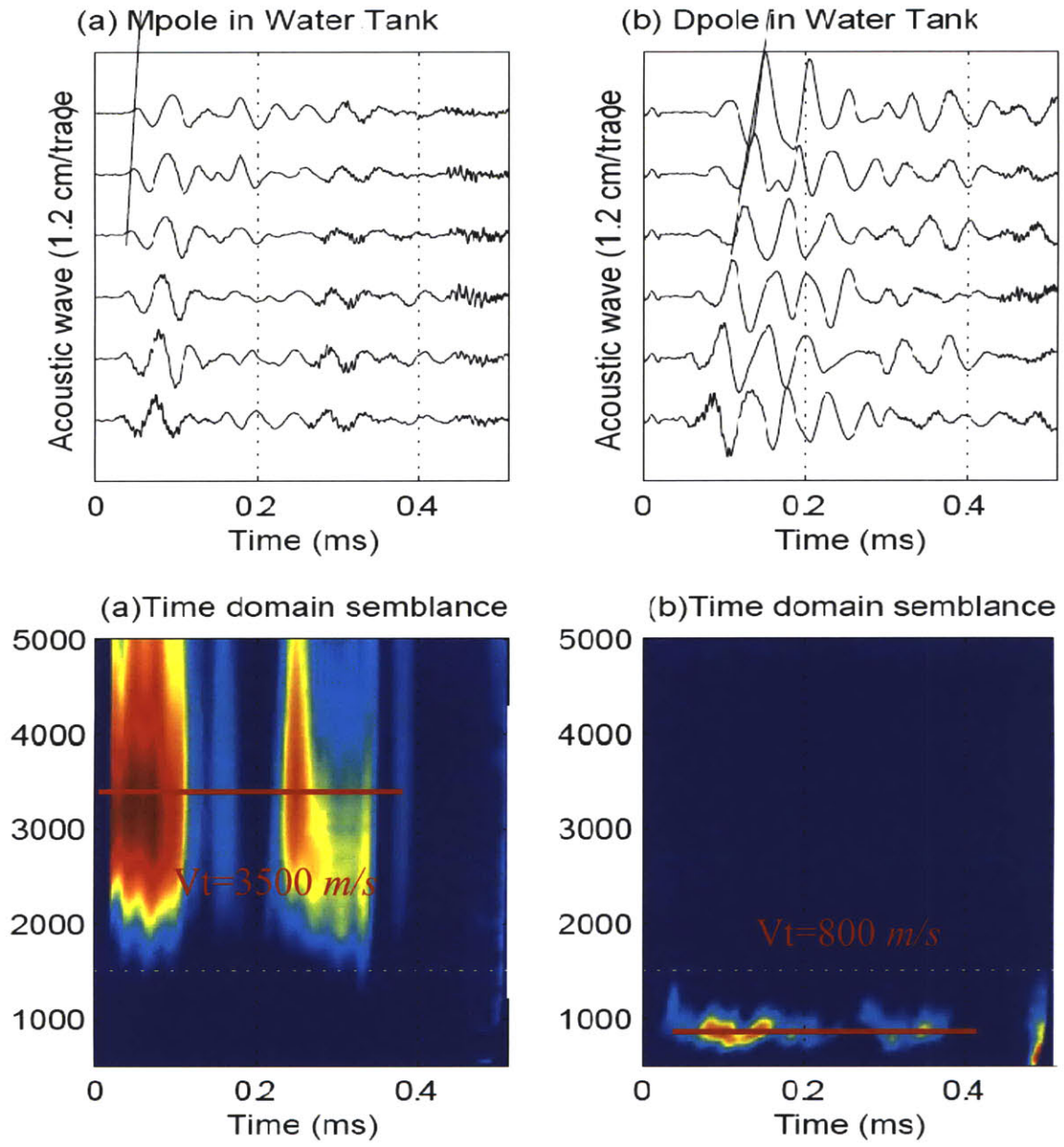

Figure E-6: Monopole (a) (left) and Dipole (b) (right) tool wave waveforms and their time domain semblance. (Vt stands for lab tool wave velocity.)

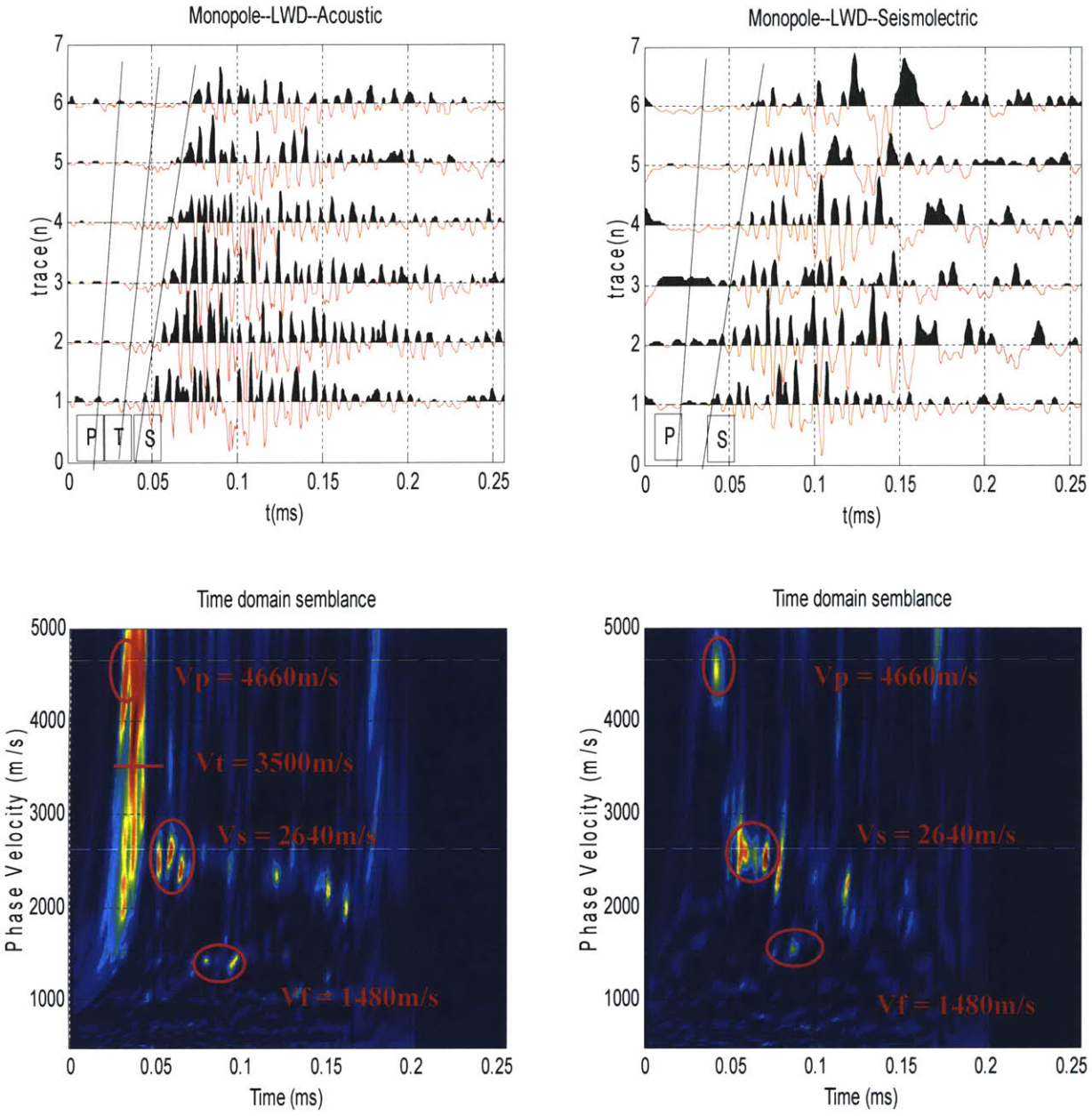

Figure E-7. Monopole LWD acoustic (left) and seismoelectric signal (right) comparison. (Vp stands for formation P wave velocity, Vs for formation S wave velocity, and Vf for fluid velocity; Vt for tool wave velocity, P means P wave, S means S wave, T means tool wave.)

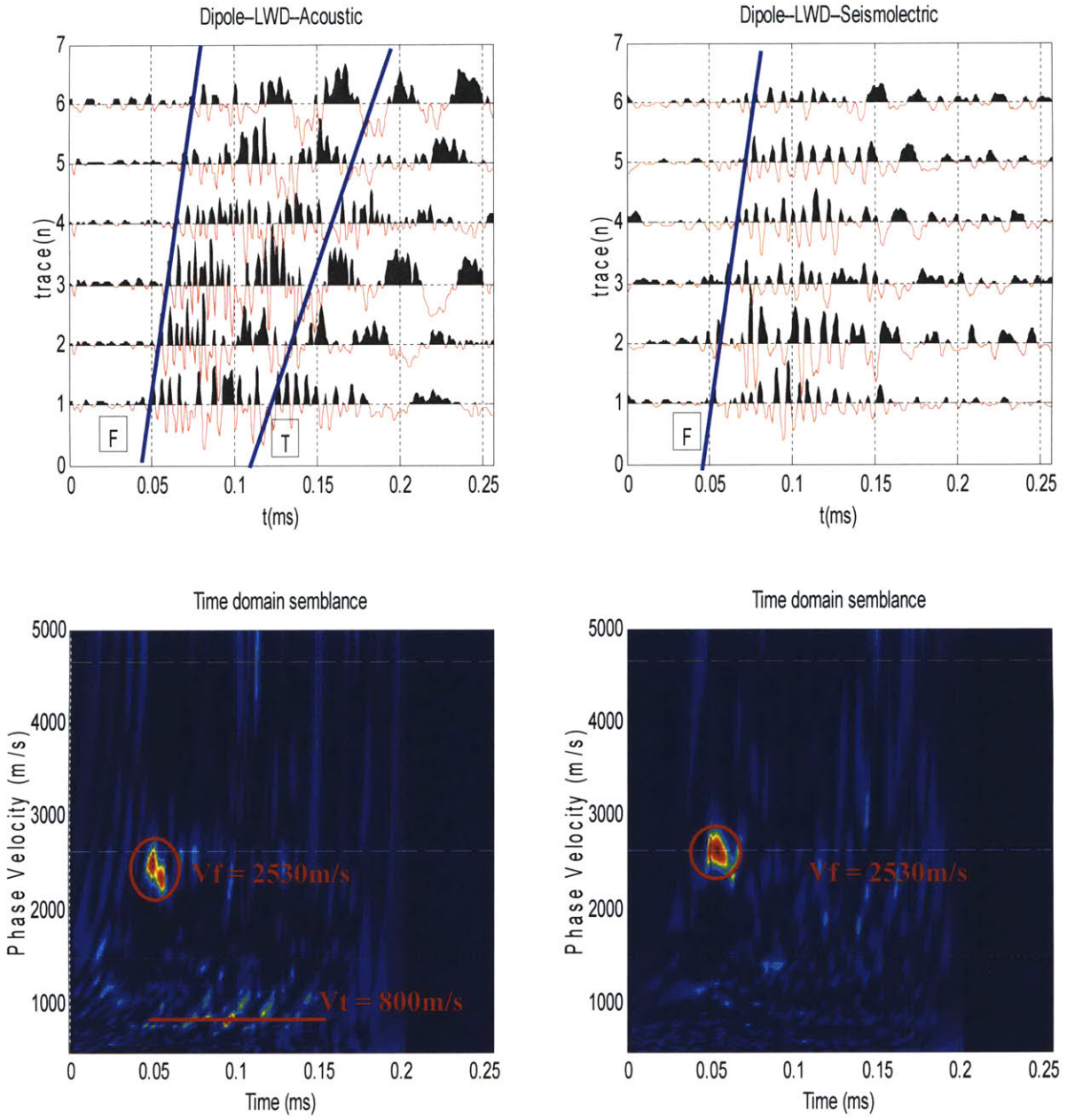

Figure E-8. Dipole LWD acoustic (left) and seismoelectric signal (right) comparison. (Vf stands for flexural wave velocity, Vt for tool wave velocity; F means formation flexure wave, T means tool wave.)

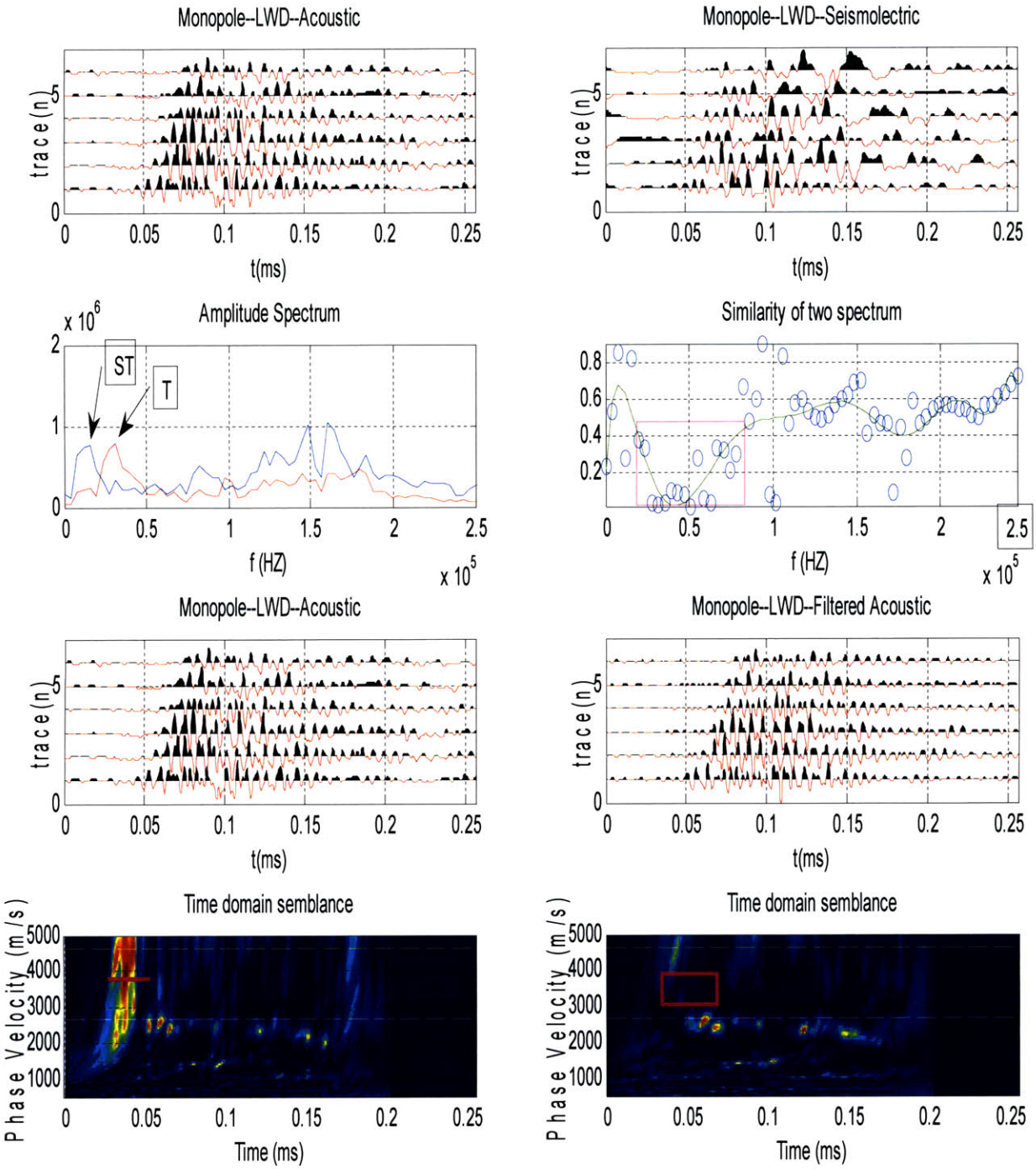

Figure E-9 (a) Monopole acoustic (left) and seismoelectric (right) waveforms; (b) monopole acoustic (line with arrow "T") and seismoelectric (line with arrow "ST"). Fourier amplitude spectra (left) and coherence as a function of frequencies (right); (c) monopole unfiltered acoustic (left) and filtered (right) waveforms; and (d) their time domain semblances. (T means frequency peak due to tool wave, ST stands for Stoneley wave).

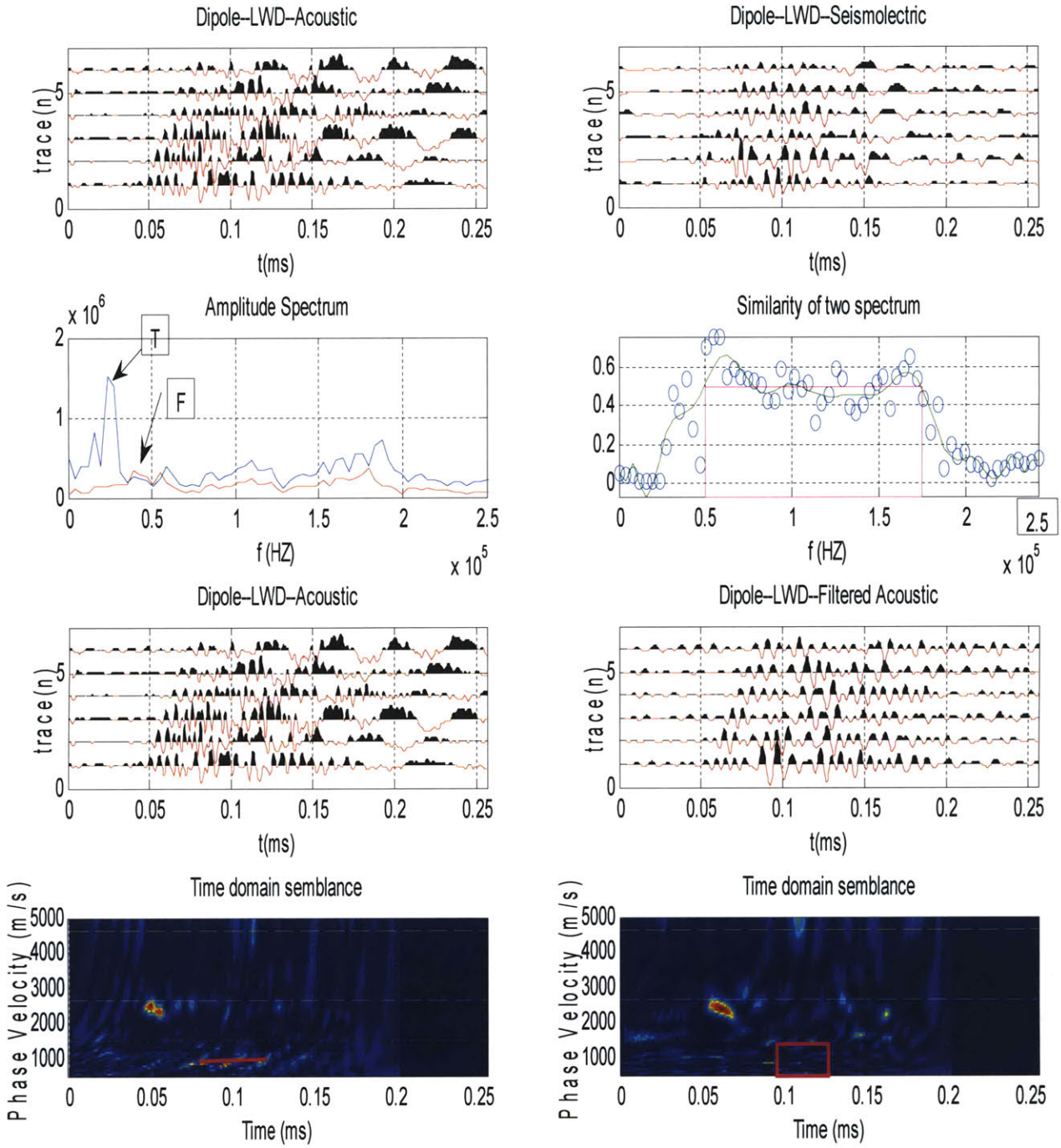

Figure E-10. (a) Dipole acoustic (left) and seismoelectric (right) waveforms; (b) dipole acoustic (line with arrow "T") and seismoelectric (line with arrow "F") Fourier amplitude spectra (left) and coherence as a function of frequencies (right); (c) dipole unfiltered acoustic (left) and filtered (right) waveforms; and (d) their time domain semblances. (T means frequency peak due to tool wave, F stands for Flexural wave).

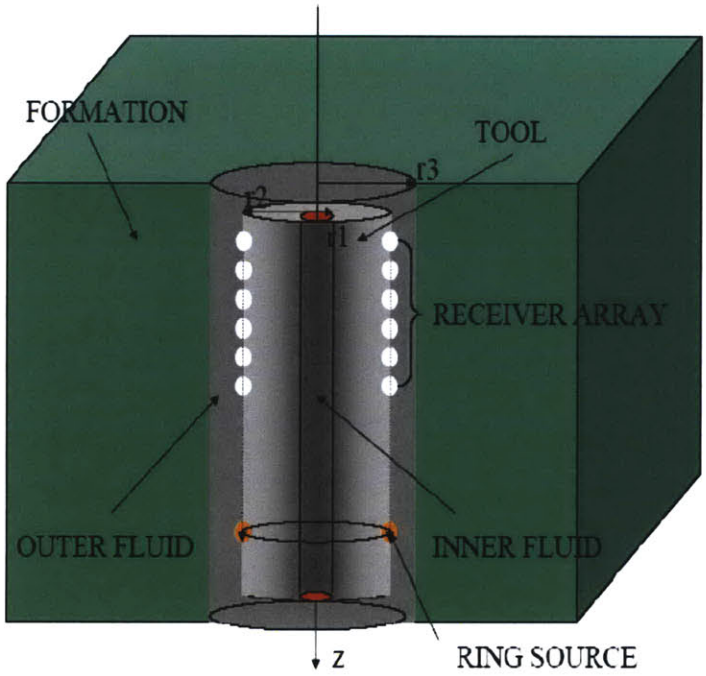

Figure E-11. Geometry and coordinate of the borehole and logging tool in the numerical modeling (r_1, r_2 and r_3, indicates the inner fluid , tool outer layer and borehole radius respectively).

	Porosity (%)	Ks (GPa)	Solid density (kg/m^3)	Solid Vp (m/s)	Solid Vs (m/s)	Permeability (Darcy)
Formation	20	35	2600	4600	2640	0.1
Pore fluid density = 1000 (kg/m^3)			Pore fluid viscosity =0.001 Pa .S			
Pore fluid permittivity = $80\varepsilon_0$			Formation permittivity = $4\varepsilon_0$			

Table E-2: Medium properties used in the numerical simulation, where ε_0 is the permittivity in the vacuum.

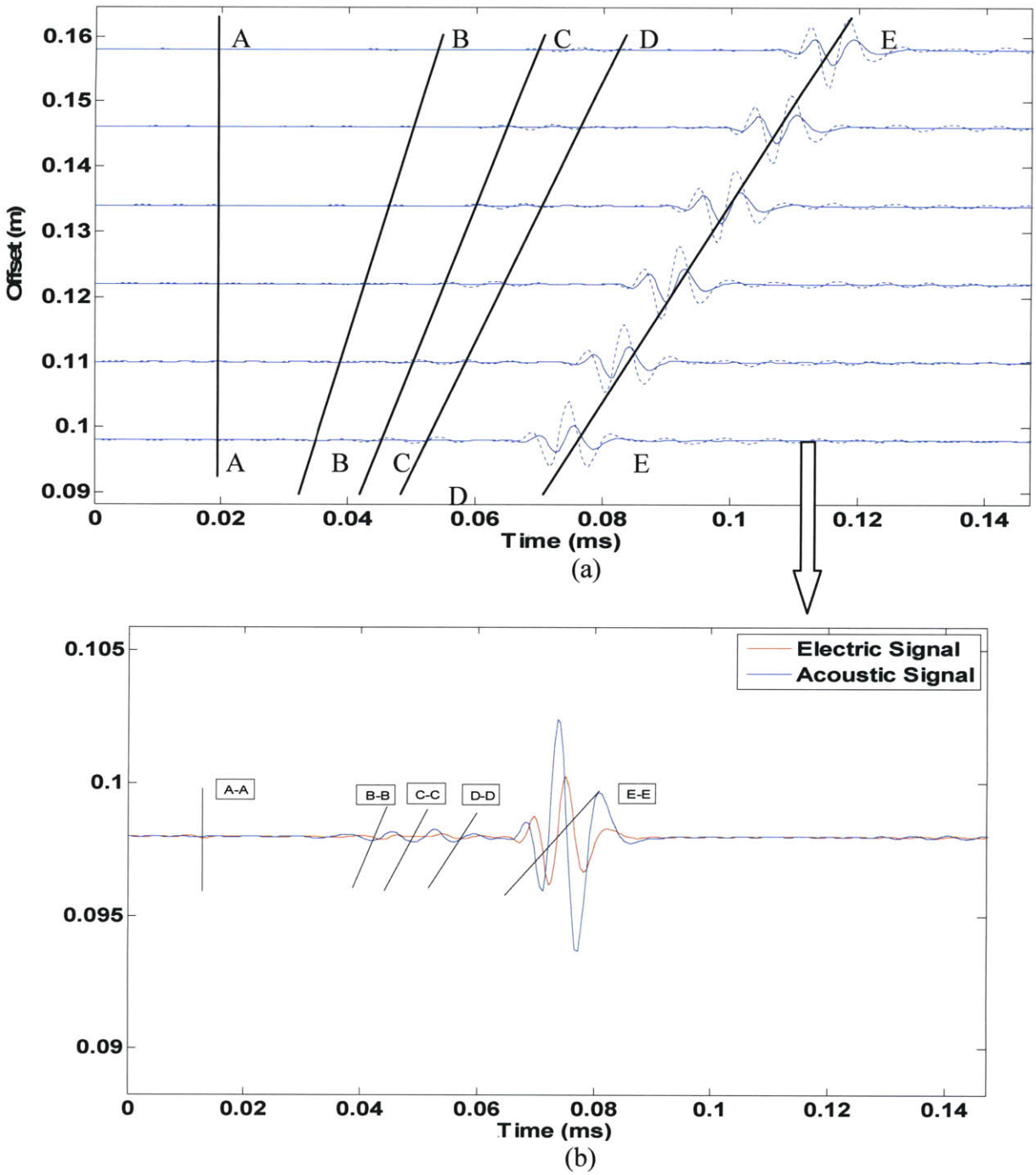

Figure E-12. (a) The monopole waveforms of the normalized acoustic pressure (solid curves) and the normalized electric field strength (dotted curves) for laboratory fast formation. A-A is the radiating electromagnetic wave, B-B is formation compresional wave, C-C is monopole tool wave, D-D is the formation shear wave, E-E is the Stoneley wave, which has the largest amplitude in the waveforms. (b) Enlarged view of first trace in (a).

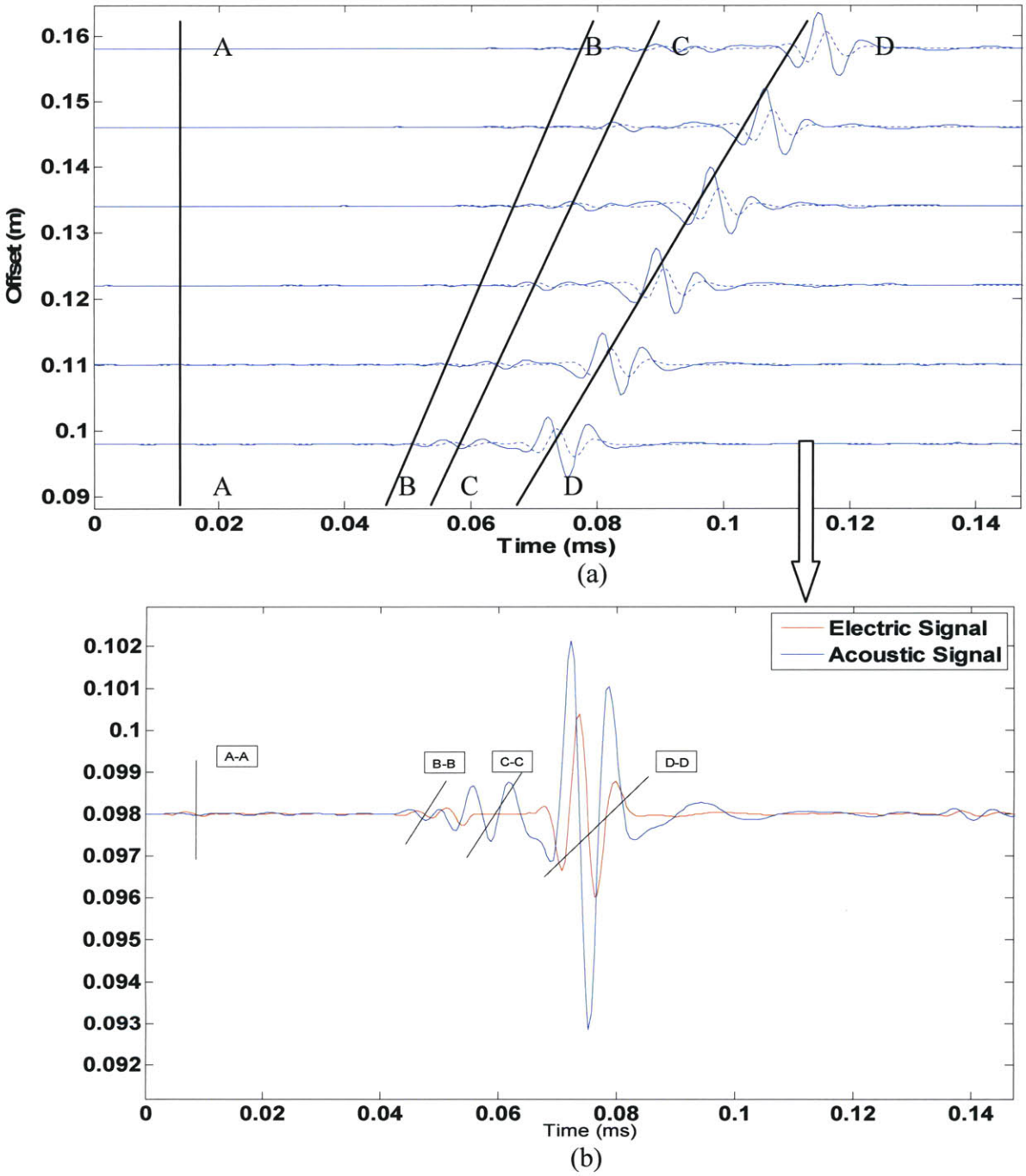

Figure E-13. (a) The dipole waveforms of the normalized acoustic pressure (solid curves) and the normalized electric field strength (dotted curves) for laboratory fast formation. A-A is the radiating electromagnetic wave, B-B is the 2nd order dipole formation flexural wave, C-C is dipole tool wave, D-D is the 1st order diple formation flexural wave. (b) Enlarged view of first trace in (a).

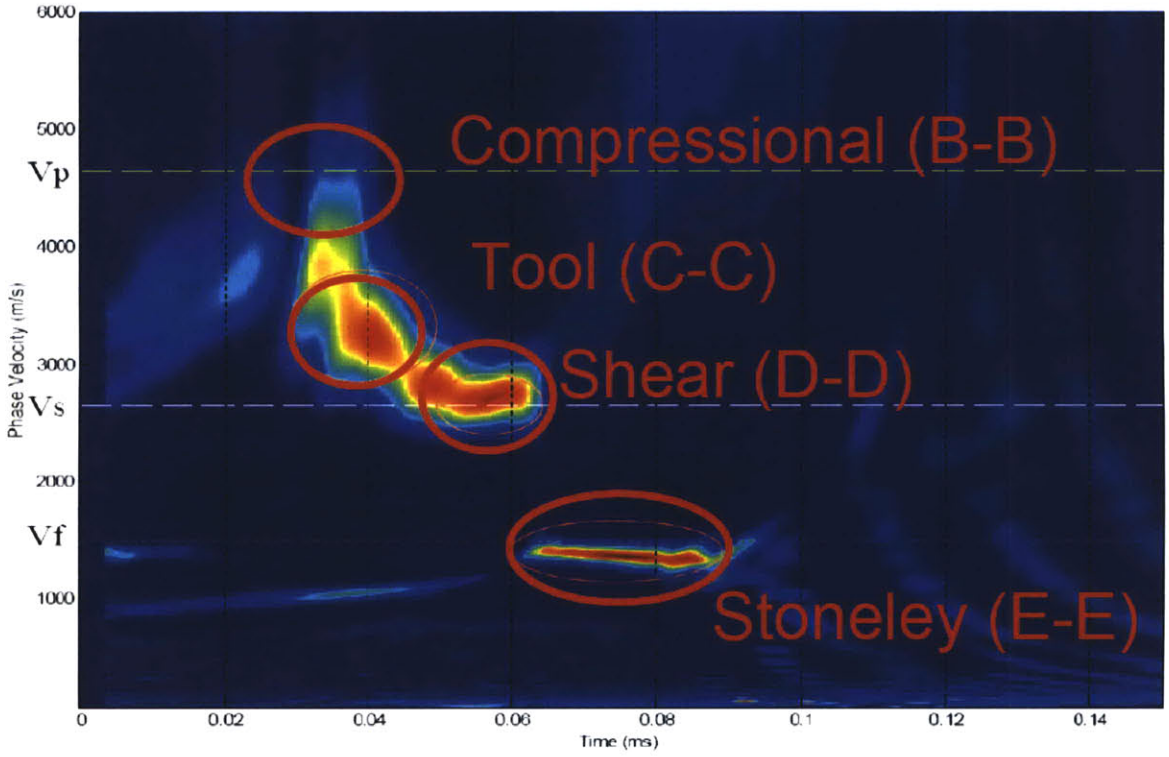

Figure E-14. The time domain semblance of the monopole acoustic waveforms in Figure E-12. (The three circles indicates the monopole tool wave, shear wave and stonely wave respectively from top to bottom.Compressional wave is not very clear in this figure. Vp stands for the formation P wave velocity, Vs for S wave velocity, Vf for fluid wave velocity.)

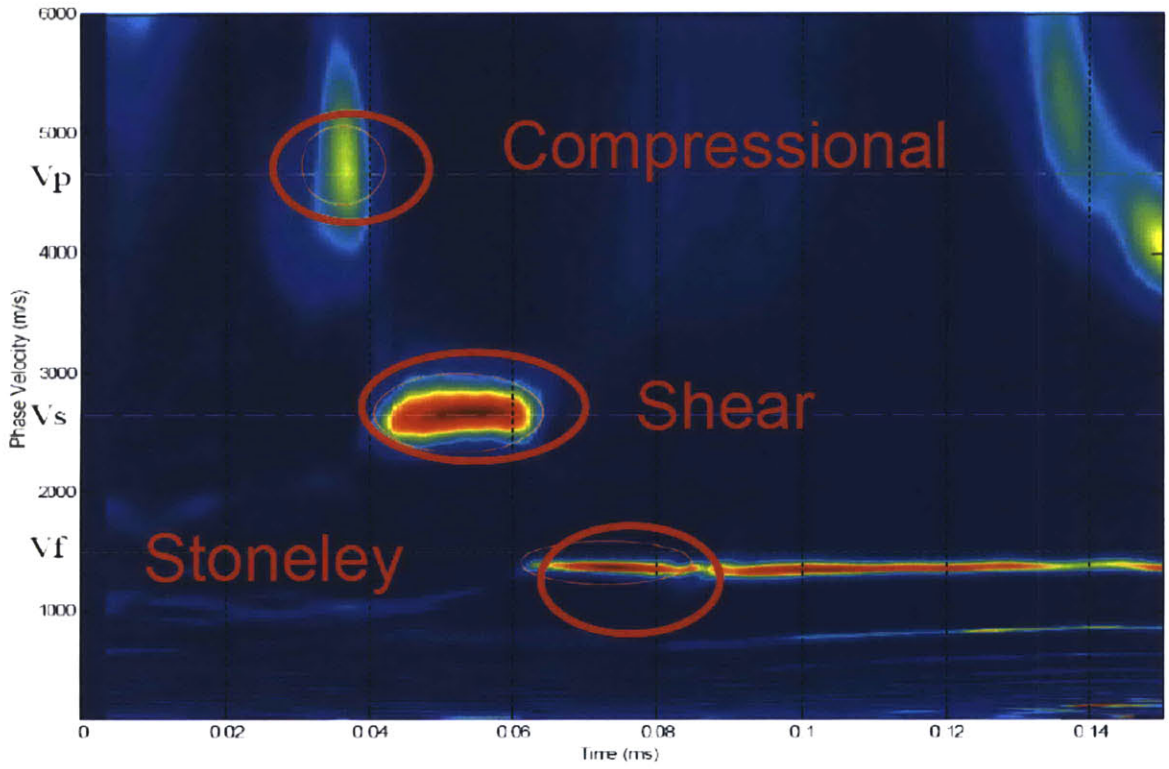

Figure E-15. The time domain semblance of the monopole electric waveforms in Figure E-12. (The three circles indicates the monopole compressional wave, shear wave and stonely wave respectively from the top to bottom. Vp stands for the formation P wave velocity, Vs for S wave velocity, Vf for fluid wave velocity.)

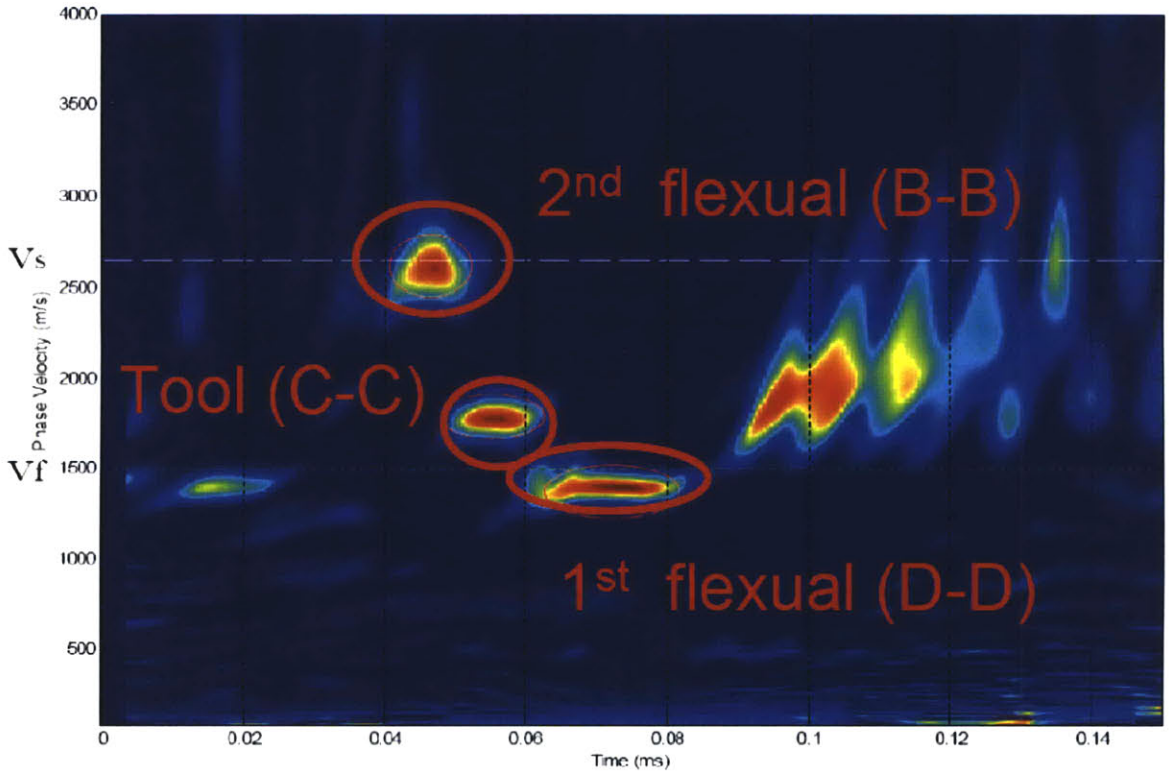

Figure E-16. The time domain semblance of the dipole acoustic waveforms in Figure E-13. (The three circles indicates the 1st order dipole formation flexural wave, tool wave and 2nd order formation flexuraly wave respectively from the above to the bottom. Vs stands for formation S wave velocity. Vf for fluid wave velocity.)

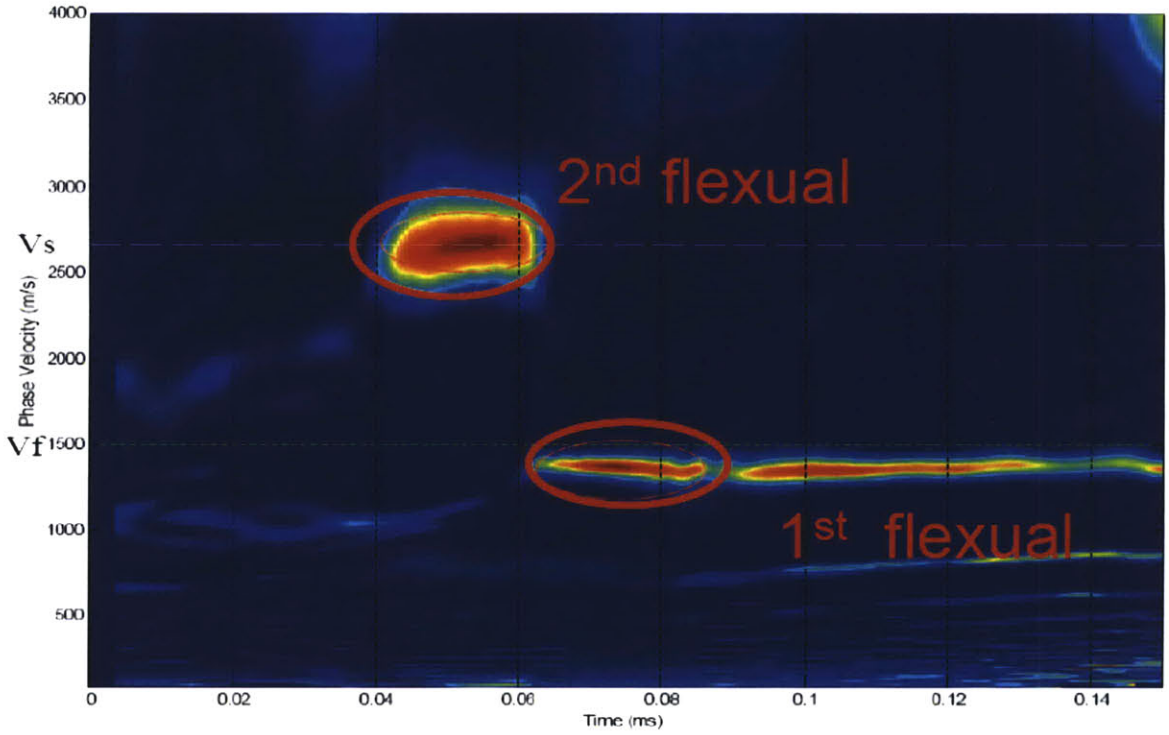

Figure E-17. The time domain semblance of the dipole electric waveforms in Figure E-13. (The two circles indicates the 1st order dipole formation flexural wave and 2nd order formation flexural wave respectively from the above to the bottom. Vs stands for formation S wave velocity, Vf for fluid wave velocity.)